UNIVERSITAT AUTONOMA DE BARCELONA

FACULTAD DE CIENCIAS

P H D T H E S I S

by the Universitat Autonoma de Barcelona

Specialty : Astrophysics

Some observational and theoretical aspects of cosmic-ray diffusion

Defended by

Elsa de Cea del Pozo

Thesis Advisor: Diego F. Torres

prepared at Institut de Ciencies de l'Espai, IEEC - CSIC

defended on July 2011

To those who believed in me, despite myself.

Acknowledgments

Esta tesis nunca habría sido posible sin mi "jefe". Diego me ha abierto las puertas al mundo de la investigación, enseñándome el compromiso que implica, tanto a nivel personal como profesional. Por su dedicación y esfuerzo, por acompañarme durante mis primeros pasos en la dura carrera científica, quiero darle las gracias. No sólo me ha aportado su experiencia y conocimientos científicos, sino que también me ha brindado la oportunidad de trabajar con estupendos colaboradores, de los que espero seguir aprendiendo en el futuro.

I want to acknowledge my great group-mates: those who are, and those who were. They have helped me through the hardest parts, being patient many many times, and always trying to teach me something. They even consent to go with me outside the working world, and shared a few laughs! Agni, Ana Y.: I miss you girls, thanks for putting up with me in my clueless first years. Nanda, Andrea, Ana and Gio: I have nothing but smiles and huge thanks to you all, I'll see you on the road, I'm sure. Also, I sent my gratitude to those whom I have the pleasure to work with and that have taught me a great deal of useful things: Stefano and Olaf, thanks a lot.

I have met wonderful people inside the MAGIC Collaboration, and I would like to thank them, too. Working with you has been a really interesting experience. Moreover, I had a really nice time with many of you outside the work, both in La Palma and in any city we had a meeting or a school. I hope to be in close contact in the future, no matter where I end up being.

> "I almost wish I hadn't
> gone down that rabbit-hole
> — and yet — and yet —
> it's rather curious, you know,
> this sort of life!"
>
> Lewis Carroll, *Alice's Adventures in Wonderland*

He tenido la suerte de conocer a gente estupenda en estos cuatro años en Barcelona. Sin ellos, mi vida aquí habría sido insoportable, y es a ellos a los que más echaré de menos cuando me haya ido. Siempre había pensado que conseguiría escribir algo especial para cada uno de ellos, pero dado que soy un poco desastre y que, bueno, no me estoy muriendo, sólo me voy un poco más lejos, pues tendrán que conformarse con lo que hay.

Empezaré por mis compis en desdichas: los ciberianos. Esa extraña población de estudiantes capaz de trabajar en un lugar sin puertas ni ventanas, y aún así reír y animarse mutuamente. Por orden alfabético: Ane, Antonio, Carlos, Dani, Diego, Felipe, Jacobo, Jonatan, Jorge(s), Jose, Juan Carlos, Nataly, Pris, Santi. Ser ciberiano se lleva en el corazón, recordadlo. Y si me he dejado a alguien, no me

peguéis muy fuerte en la cabeza, que estoy estudiando. Gracias por hacer mi día a día menos gris, y mis fines de semana más ajetreados.

En esta categoría entran también un buen puñado de gente del IFAE, 'los del instituto de al lado'. A los seniors, gracias por aguantar estoicamente mis incesantes dudas, ruegos y preguntas, en especial a Stefan, Daniel y Abelardo. De los niños no me olvido, por supuesto, también les doy las gracias: Manel (por darme collejas y animarme, todo a la vez: volveré a visitarte y es una amenaza), Ignasi (por hacerme temer más que antes los petardos y adorar más que antes la montaña), Roberta (mi 'criatura' y compañera en desgracias, la tesis se acaba pero nosotras no), sin olvidar a las recientes incorporaciones, Alicia (a.k.a. la piraña más dicharachera, ojalá nos hubiéramos encontrado antes, niña) y Adiv (compi de piso durante 6 meses, que tiene su mérito). Y ya que estoy, también aprovecho a mandar un abrazo enorme a esa comunidad de italianos que me han hecho conocer más lugares de esta ciudad que cualquier persona local: me alegro de que nos hayáis *invadido*.

Y antes de que deje de hablar del trabajo, quiero reconocer aquí la labor de Isabel, Delfi y Josep. Desde la administración, la gestión o la informática, se han ocupado de mí y me han ayudado con la mejor de las intenciones siempre que han podido, y más allá de lo que les tocaba. Y a Alina, que no se me olvida, gracias por nuestras charlas diarias aguantando tormentas y tempestades, y por ser la primera en leerse esta tesis y corregir mi inglés para que fuera más facilmente legible. Los errores que queden son míos.

Llegados a este punto, tengo que parar de hacer listas. En los concursos y entregas de premios se llama a esta categoría 'menciones especiales', y como tal deben considerarse. Ellos me han cambiado para bien, espero, y gracias a ellos he llegado a donde estoy. Escribir esta tesis no ha sido sólo acumular conocimientos en astrofísica. Mi salud mental se ha visto claramente resentida, y de no ser por ellos, llevaría ya una bonita camisa blanca, con mangas atadas a la espalda. Gracias por estar a mi lado todos estos años, y por cuidar, como bonus extra, de mi salud emocional. A Carlos, le doy las gracias por nuestras inacabables conversaciones sobre libros, películas, comics y demás, pero sobre todo por recordarme que valgo más de lo que reconozco, y por tratar de enseñarme a quererme un poco más. Tengo tus palabras en la mente, aplicarlas me llevará tiempo, pero que sepas que tendrás una gran parte de culpa cuando lo consiga. A Delfi, por ser mi amiga y compartir conmigo el trocito de su vida que he tenido la suerte de presenciar, peluquera incluida. Suya es la culpa de que en estos agradecimientos incluya una de las frases con más sinsentido de la historia: gracias por ayudarme a apreciar el inestimable uso de una bola de demolición, por mostrarme la verdad que esconde la palabra perro como definición de jornada laboral, y por hacerme entender que la vida sería mucho más triste sin pingüinos ni ovejas. Recuerda lo que dijo el telar del destino... A Daniela, por convertirse en mi *maligna aprendiz* y sufrir cuando he sufrido y reir cuando yo he reído. Pink girl, loca-loca-loca, no defraudes al LOC (que te ayude Alicia, es su deber pirañil). Volveré y tendremos fiesta, salsa y elefantitos de colores.

Cambio de ciudad y me vuelvo a Madrid, aunque sea sólo con la mente: mis

amigos no me han olvidado en este tiempo, y como en cada separación me he dado cuenta de la suerte que tengo conociendo gente. Con cada regreso, he podido robaros minutos, risas y muchos ánimos. Desde aquí, os doy las gracias: a los del master, por ser los *afectados* que mejor saben salir de cena y bares (Cris, Álvaro, Ignacio, Pablo y Juan-ito), a los del barrio, por acogerme con tanto cariño desde el primer día (Jewi, Riki, Guille, Fer, *et al.*), y a los de la carrera, porque ya sois mis amigos de verdad y cuento con vosotros (Arturo, Carmen, Ele-rizos, Fer, Juan, Marta, Sol, Super-Ele, váis por orden alfabético, ea). Y ya para terminar, agradecer de todo corazón, y me da igual que suene cursi, a la piedra angular en mi vida que constituyen las tres: Ana, Isa y Elena. Cada una guardáis una parte diferente de mí, sois las mejores amigas que podría haber soñado, y cualquier cosa que diga sonará a poco. Gracias, de verdad.

> Everyone seems quite relieved, though,
> considering they all knew I'd get off.
>
> J. K. Rowling, *Harry Potter and the Order of the Phoenix*

Por último, y por tanto más importante, quiero darles las gracias a mi familia. Tanto a los que me acogieron a mi llegada a Barcelona como a una más, como a los que me han seguido animando desde Madrid. Tengo mucha suerte de teneros, y está claro que seguiremos unidos sin importar dónde esté. De todos ellos quiero destacar a mi padre, a mi madre y a mis hermanos. Mis palabras no van a ser suficientes, pero lo voy a intentar. Mis padres han sido y seguirán siendo mi lugar seguro en el mundo. Desde el principio me han apoyado en mi elección, aunque ello supusiera mandarme a 600 km de casa – que era 600 km más lejos de lo que ellos hubieran deseado. Pero siempre han estado ahí para mí, y siempre los he sentido cerca. Estoy orgullosa de la forma en la que me habéis criado, y espero que vosotros lo estéis de mí. A mi hermano Pablo le doy las gracias por seguir confiando en mí, aunque me fuera lejos... justo después de embarcarle en la locura de la Física. Y a mis enanitos, Jorge y Luis, que después de tanto tiempo ya no son tan pequeños, también les quiero dar las gracias por llenarme de abrazos y besos con los que llenar mis largas ausencias. Os quiero mucho, a todos. Gracias.

> "There's no place I can be
> since I found *serenity*.
> You can't take the sky from me."
>
> Joss Wheddon, *Firefly*

Contents

Chapter 1

Introduction

Contents

1.1 Connecting CR and gamma rays

Gamma-ray astronomy appeared as a mean to obtain an answer for the long-standing problem of the origin of cosmic rays (CR). Those CR particles were discovered by Victor Hess in 1912, who observed an ionizing radiation impacting on nuclei in the Earth's atmosphere [Hess 1912]. The CR spectrum, shown in Figure 1.1, extends over an energy range of 13 orders of magnitude.

Below $E = 1\,\mathrm{GeV}$, the CR flux is affected by the solar wind, via the 11 yrs modulation of its magnetic field. At higher energies the differential spectrum can be described by a power law $\mathrm{d}N/\mathrm{d}E \propto E^{-\Gamma}$ with a spectral index $\Gamma \approx 2.7$ up to $\mathrm{E} = 10^{15.5}\,\mathrm{eV}$ and $\Gamma \approx 3.0$ above that energy. The transition region is called 'knee'. The spectrum hardens again at about $E = 10^{18}\,\mathrm{eV}$ (the so-called 'ankle'). It is believed that CRs below the 'knee' are produced at galactic sites like supernova remnants, pulsars, or binary systems, while CRs with higher energies are more likely extragalactic. Due to galactic and intergalactic magnetic fields, charged cosmic rays up to $10^{19}\,\mathrm{eV}$ are isotropized. Therefore, their arrival direction at Earth does not point back to their origin. Only at even higher energies, in the regime of the ultra high energy cosmic rays, the rigidity $R = E/(Ze)$ of the particles is so high that they are not deflected by extragalactic or galactic magnetic fields ($r_{gyro} = R/B$).

The cosmic-originated particles can be electrically charged (electrons, protons, heavy nuclei, ...), but there is also photons. Since photons do not have charge, they are not deflected by the interestellar magnetic fields, thus providing direct

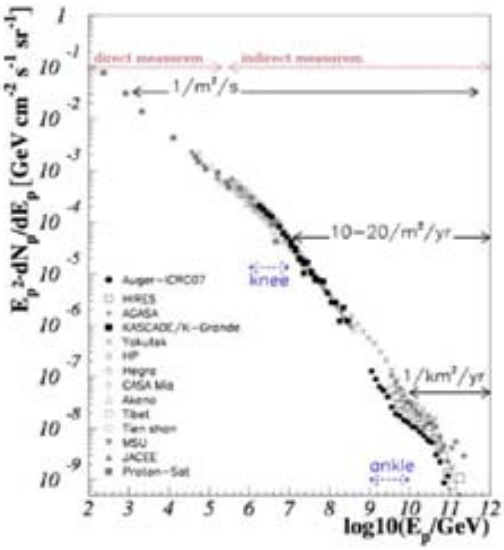

Figure 1.1: All-particle cosmic ray spectrum. From [Becker 2008].

information on the location of the original source. These energetic photons are produced through several non-thermal processes and, depending on the nature of the parental cosmic-ray particle, they can be either leptonic (mostly electrons) or hadronic (mostly protons and nuclei) processes.

The main physical processes that contribute to gamma-ray creation by electrons and other particles alike are: synchrotron radiation, cuvature radiation, inverse Compton interactions, relativistic bremsstrahlung and electron-positron annihilation. Whereas for proton-originated gamma rays there are: photomeson production and neutral pion decay from proton-proton (pp) interactions. For a comprehensive study on the details of these processes see [Ginzburg & Syrovatskii 1964], a general sketch can be seen in Figure 1.2. Essentially the processes can be briefly described as follows.

Synchrotron radiation

Extremely energetic particles moving in a strong magnetic field will emit gamma-ray photons within an angle $\theta \sim mc^2/E$ of its direction of motion. Synchrotron radiation usually generates seed photons for inverse Compton scattering (see below). Moreover, ultra-high energy CRs can emit synchrotron photons directly in the gamma-ray energy domain.

Curvature radiation

Inside strong magnetic fields charged particles move along the field lines and are accelerated (because the curvature radius of the field is small) and then radiate.

Inverse Compton interaction

Relativistic electrons are scattered on soft photons, transfering part of their energy, thus being able to produce gamma rays. Two regimes can be considered

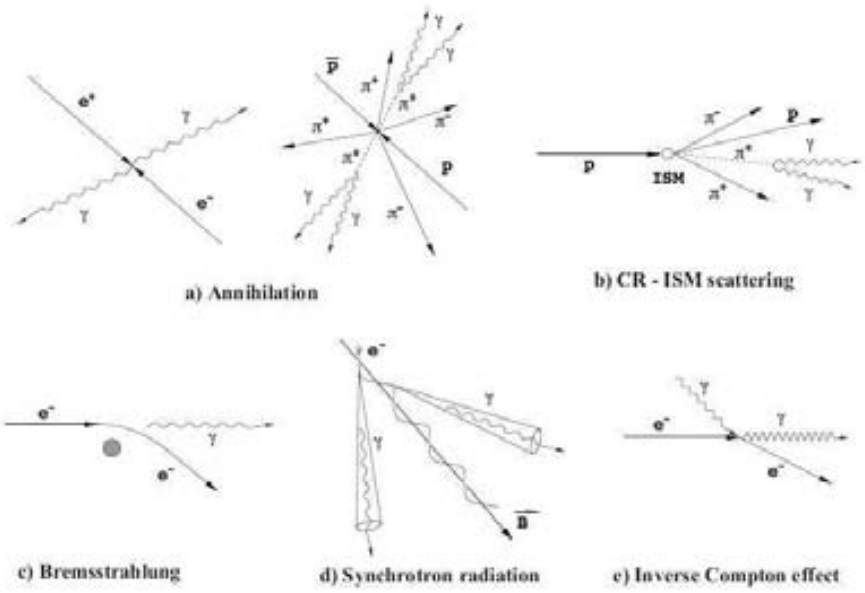

Figure 1.2: Main physical processes that can generate gamma-ray photons through different interactionsm, both hadronic (b) and leptonic (c, d, e). Annihilation can take place among leptons or hadrons.

for the cross-section of the interaction: the Thompson (for $E_e E_\gamma \ll m_e^2 c^4$) and the Klein–Nishina (for $E_e E_\gamma \gg m_e^2 c^4$) approximation. For $E_e E_\gamma \approx m_e^2 c^4$, the exact Klein-Nishina formula should be used, see (Weinberg 1995, pp.362).

$$\sigma_T = \frac{3}{8}\pi r_e^2 \tag{1.1}$$

$$\sigma_{KN} = \pi r_e^2 \frac{1}{\varepsilon}\left(\ln(2\varepsilon) + 0.5\right) \, , \varepsilon = \frac{E_\gamma}{m_e c^2} \tag{1.2}$$

Photomeson production

Interaction of a very relativistic proton with a photon produce pions. This process is responsible for the GZK cut-off at distances above 100 Mpc.

Relativistic bremsstrahlung

A relativistic electron is accelerated in the electrostatic field of a nucleus or a charged particle, radiating energetic photons. The emitted photon spectrum can be expressed with a power law with the same index as the accelerated electron.

Hadronic gamma-ray emission

The collision of two protons (or proton – antiproton) produce neutral and charged particles. The neutral pions decay inmediately ($\sim 10^{-16}$) in two gamma-ray photons. The charged pions also decay fast ($\sim 10^{-8}$), generating muons and neutrinos. The former secondaries, the muons, also decay producing electrons (or positrons, depending on the charge of the original muon and

pion) and neutrinos (or antineutrinos). This neutrino signature is characteristic and unique for hadronic interactions.

$$\begin{aligned} \pi^0 &\rightarrow 2\gamma \\ \pi^{\pm} &\rightarrow \mu^{\pm} + \nu \\ \mu^{\pm} &\rightarrow e^{\pm} + \nu + \overline{\nu} \end{aligned}$$

Electron-positron annihilation

Two gamma rays are produced when an electron and a positron collide and annihilate.

1.2 Gamma-ray Astronomy, There and Back Again[1]

In the early years of gamma-ray astronomy, the success of a mission over its precedents was quantified by the number of photons, rather than the sources detected. The first experiments devoted to observe energetic photons in the MeV–GeV range were placed in balloon- and space-borne detectors. However, gamma rays above hundreds of GeV could not be detected by these detectors mainly due to their small collection area. Ground-based telescopes cover this range of energies, for instance, profiting from the imaging Cherenkov technique, or detecting other secondary particles that carry information of the primary cosmic ray.

1.2.1 Observing photons of GeV energies

Although several gamma-ray detectors were placed into space in the 1950's and 1960's, the first succesful – scientific – mission dedicated to the study of gamma rays was launched in 1972. The second Small Astronomy Satellite (SAS-2) only operated for 7 months, but in that short time it detected photons above 30 MeV from the Crab and Vela pulsars, and confirmed the Galactic center as a source of gamma rays. Shortly afterwards, in 1975, the COS-B satellite started taking data at energies above 50 MeV. For the first time, the COS-B mission completed a skymap of the Galactic plane between 100 MeV and 6 GeV, allowing the study of the large-scale gamma-ray diffuse emission. This diffuse emission was supposed to be originated from cosmic rays interacting with the interestellar medium and, in fact, a correlation with gas distribution (both in HI and CO maps) was found. Emission could be resolved from cloud complexes as Ophiuchus and Orion-Monoceros. Moreover, the Crab and Vela pulsars were confirmed as gamma-ray sources, as well as the yet-unidentified Geminga source and the Cygnus region [Hermsen 1990]. Moreover, the first extragalactic source at these high energies was detected: the quasar 3C 273. However, the large positional uncertainty – from 0.4 to 1.5 degrees, depending on the energy – prevented further identification of point-like sources.

[1] *The Hobbit, or There and Back Again*, better known by its abbreviated title *The Hobbit*, is a fantasy novel by J. R. R. Tolkien, published in 1937.

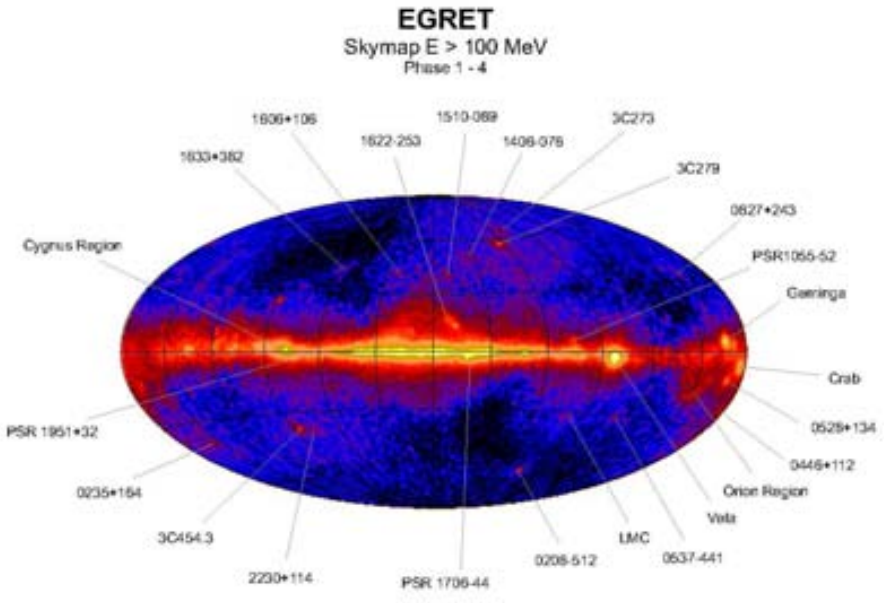

Figure 1.3: Skymap above 100 MeV from our Galaxy by the entire EGRET mission (phases 1 to 4), with the main sources detected in gamma rays. Credit: EGRET Team/NASA.

Following these encouraging results, other satellites were launched during the next decade. The next gamma-ray experiment, the Energetic Gamma-Ray Experiment Telescope (EGRET), on board of the Compton Gamma-Ray Observatory (CGRO), was launched in 1991. After nine years of observations between 30 MeV and 30 GeV, EGRET left behind a catalog containing 271 sources [Hartman *et al.* 1999]. Blazars were established as the more numerous gamma-ray emitters. Pulsars were also established as a source class by adding 5 new members, including the identification of Geminga, a radio-quiet pulsar. The skymap of the Galaxy is shown in Figure 1.3 and presents some of the principal identified sources. Among them, the Large Magellanic Cloud (LMC) is the first galaxy detected in gamma rays without having an active galactic nuclei (AGN). Moreover, the radio galaxy Centaurus A (Cen A) is also detected. Nonetheless, 60% of the sources in the Third EGRET Catalog ($\sim$ 170) are unidentified. Studies on the galactic diffuse emission were carried on thanks to the performed all-sky survey. Together with this, the telescope allowed determining the isotropic nature of the extragalactic diffuse emission. Another scientific contribution provided by EGRET was the prolonged GeV emission (or high energy tail) detected from gamma-ray bursts. Regarding caveats of this instrument, the decrease of detection efficiency at high energies and the large error boxes that prevented from finding counterparts for some of the unidentified sources are among the most importants.

Almost a decade after the end of the CGRO mission in 2000, AGILE and *Fermi*

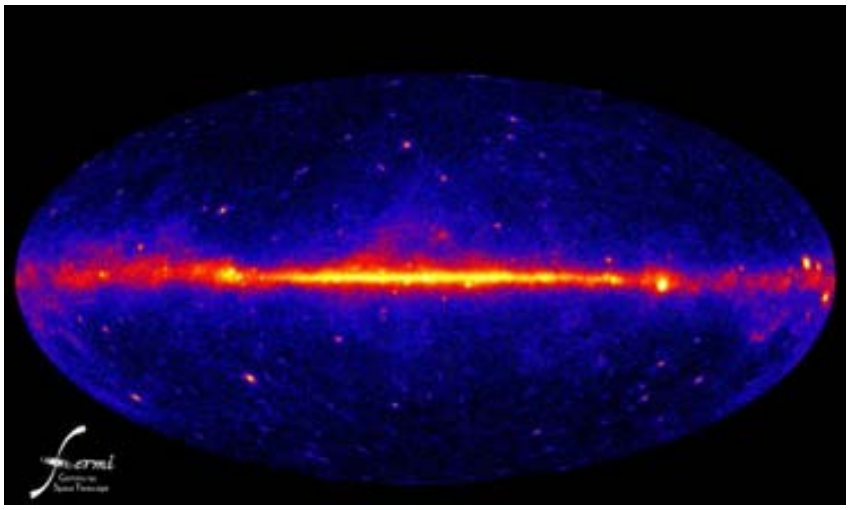

Figure 1.4: All-sky map above 300 MeV during the first year of the *Fermi* LAT telescope. Credit: NASA/DOE/*Fermi* LAT Collaboration.

Table 1.1: Mission parameters of the three latest space telescopes in the MeV – GeV range: EGRET, AGILE and *Fermi* LAT. The sensitivity above 100 MeV is considered for a 2-year survey at high latitudes.

	EGRET	AGILE	*Fermi* LAT
Energy range	30 MeV – 30 GeV	30 MeV – 50 GeV	20 MeV – 300 GeV
Energy resolution	20 – 25%	$\Delta E/E = 1$	18 – 6%
Effective area (peak)	1500 cm^2	700 cm^2	10000 cm^2
Field of view	0.5 sr	3 sr	2.4 sr
Angular resolution	5.5° at 100 MeV	4.7° at 100 MeV	3.5° at 100 MeV
	0.5° at 10 GeV	0.2° at 10 GeV	0.15° at 10 GeV
Sensitivity > 100 MeV	$10^{-7}\,\mathrm{cm}^{-2}\,\mathrm{s}^{-1}$	$5 \times 10^{-8}\,\mathrm{cm}^{-2}\,\mathrm{s}^{-1}$	$2 \times 10^{-9}\,\mathrm{cm}^{-2}\,\mathrm{s}^{-1}$
Mass	1800 kg	60 kg	3000 kg

have been launched in 2007 and 2008, respectively. AGILE (Astrorivelatore Gamma a Immagini LEggero) contains an X-ray monitor observing from 18 to 60 keV and a gamma-ray telescope that covers the sky in the energy range from 30 MeV to 50 GeV. The two instruments on board of *Fermi* are a Gamma-ray Burst Monitor (GBM), sensitive to hard X-rays and soft gamma-rays, and a Large Area Telescope (LAT) that observes in sky-survey mode from 20 MeV to 300 GeV. Table 1.2.1 compares the parameters of the latest three satellite telescopes. Already in the first year of observation (Figure 1.4), *Fermi* LAT detected around 1451 sources, including new types of gamma-ray emitters, i.e., pulsar wind nebulae, supernova remnants, X-ray binaries, starburst galaxies and globular clusters. The increased angular resolution has finally allowed to carry on morphological and spectral studies of individual sources. Key results provided by these latest experiments are discussed in the next section.

The detection technique common to SAS-2, COS-B, EGRET, AGILE and *Fermi* LAT consist in pair-production telescopes with a tracker, a calorimeter and an anticoincidence detector. The electron and positron generated by the original gamma ray hits the silicon-trip detector, and the paths are tracked through the different layers. The pair conversion signature is also used to distinguish the signal from the more abundant background of cosmic rays. The energy of the particle is measured in the calorimeter, when it is totally absorbed. The ultimate defense against the CR background is the anticoincidence detector that covers the tracker. Flashes of light are produced whenever a charged particle hits on it. All the information collected from the previous components is handled by the data acquisition system (DAQ), which also tells apart CRs from gamma rays for the first time.

1.2.2 Observing photons of TeV energies

Above 100 GeV, the flux of gamma rays is too low for the small collection area of the space-borne telescopes to detect them. Nonetheless, the Earth's atmosphere, that prevents the primary gamma-ray photons to arrive at ground level, also acts as a calorimeter where a cascade of particles – created by energetic cosmic particles – develops. The secondary particles that are generated in this way can be detected from ground-based telescopes and provide information from the primary particle, like the arrival direction and the primary energy. One of the existing techniques profits from the Cherenkov radiation: when the gamma-ray photon enters the atmosphere, it generates an electromagnetic cascade (electron-positron pair), then, the secondary particles propagate at a faster-than-light speed in the medium, generating a flash of Cherenkov light that reaches ground level (see Chapter 6 for more details in Cherenkov technique and detection).

Gamma rays and charged cosmic rays can both produce particle cascades in the atmosphere, being the latter several orders of magnitude more numerous and thus producing an overall background. The imaging technique tries to discriminate among both kind of particles through geometric considerations on the shape of the cascade when it arrives at the detector. In 1989, the 10-meter Whipple telescope pioneered this technique and detected the Crab Nebula at TeV energies [Weekes *et al.* 1989]. The second generation of Cherenkov telescopes in the 90's was leaded by the High Energy Gamma Ray Astronomy (HEGRA) and Cherenkov Array at Th'emis (CAT) experiments. They were responsible of detecting the first extragalactic source at TeV energies, the blazar Mkn 421 [Punch *et al.* 1992], and a few other galactic and extragalactic sources (like, for instance, the SNR Cas A and the blazar Mkn 501).

The Imaging Air Cherenkov (IAC) telescopes improved the background rejection through stereoscopic observations. The introduced progress relied on the better determination of the point of the atmosphere where the primary photon impact, the direction where it came from and the original energy. At present, the three main IAC telescopes are:

- High Energy Stereoscopic System (H.E.S.S.) operating since 2004 with 4 tele-

Table 1.2: Performance of the three main Cherenkov experiments in the GeV – TeV range: H.E.S.S., MAGIC and VERITAS. In the title: ♯ Tels. stands for number of telescopes, Tels. Area is the area of each telescope, f.o.v. is the field of view, Tot. Area is the total area of the array of telsecopes, E_{th} is the energy threshold, Ang. res. means angular resolution, and Sensitivity 50 h conveys the source flux in 50 hours of observation respect to the Crab Nebula flux with a significance of 5 sigma. From [De Angelis 2011].

Instrument	♯ Tels.	Tels. Area (m^2)	f.o.v. (°)	Tot. Area (m^2)	E_{th} (TeV)	Ang. res. (°)	Sens. 50 h (% Crab)
H.E.S.S.	4	107	5	428	0.1	0.06	0.7
MAGIC	2	236	3.5	472	0.05 (0.025)	0.07	0.8
VERITAS	4	106	4	424	0.1	0.07	0.7

scopes, of 13 m diameter each, in Namibia (South Africa).

- Major Atmospheric Gamma-ray Imaging Cherenkov Telescope (MAGIC) consisted on a single-dish telescope by 2004, and then become a stereoscopic system by adding a second telescope in 2009. Both telescopes have a diameter of 17 m and are located in La Palma (Canary Islands, Spain).

- Very Energetic Radiation Imaging Telescope Array System (VERITAS) observing with 4 telescopes, 12 m diameter each, since 2007. The recent rearrangement of the array improved significatively its sensitivity.

Further information on their perfomance are displayed in Table 1.2.2.

In addition to these experiments, there are other ways to observe at TeV energies from ground level: for instance, detecting the secondary particles generated in the mentioned atmospheric cascades. These experiments have higher energy thresholds and longer duty cycles than IAC telescopes (which cannot observe during full Moon). Tibet and Milagro are the best examples of air shower detectors.

1.3 Recent scientific impact

In the past few years, the latest instruments mentioned in the previous section have provided the scientific community with key results from the gamma-ray astronomy, from GeV to TeV energies.

1.3.1 A brief summary of galactic highlights

Supernova remnants (SNRs) have always been the most favoured candidates for accelerating cosmic rays, and thus an expected source of gamma rays at high and very high energies (HE and VHE, respectively). In fact, such emission has been

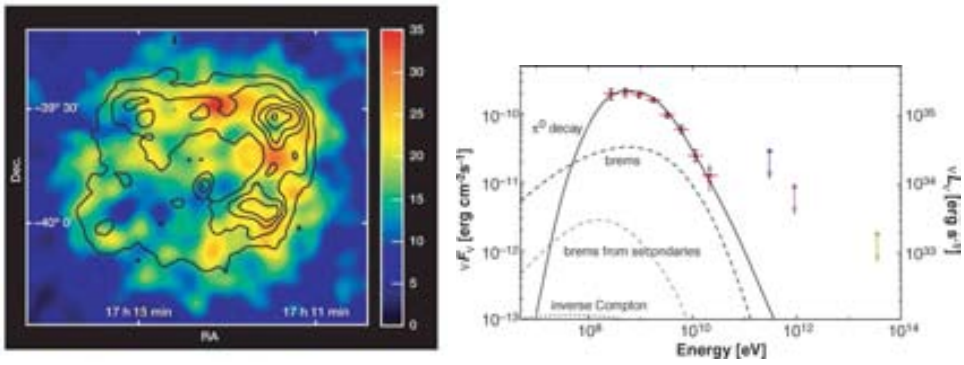

Figure 1.5: Left: Skymap RX J1713.7-3946 by H.E.S.S., black contours overplotted show the X-ray brightness that ASCA detectes from 1 to 3 keV. From [Aharonian *et al.* 2004b]. Right: *Fermi* LAT spectral energy distribution (SED) of the SNR W44, each curve corresponds to π^0 decay (solid), electron bremsstrahlung (dashed), inverse Compton scattering (dotted) and bremsstrahlung from secondary electrons and positrons (thin dashed). From [Abdo *et al.* 2010f]

reported, although the nature of the parental cosmic-ray particles that are accelerated (protons or electrons) still remains a subject of debate. The biggest step towards the disentanglement of hadronic/leptonic scenarios has been the spatial resolution of shell-like SNR, reported both at GeV and TeV energies. RX J1713.7-3946 [Aharonian *et al.* 2004b] and W44 [Abdo *et al.* 2010f] constituted the pioneering sources in each energy regime.

The first confirmed shell-like SNR, RX J1713 in short, was detected and spatially resolved by H.E.S.S. [Aharonian *et al.* 2004b]. The unprecedently well-resolved shell morphology, acquired thanks to the stereoscopic imaging technique, coincides with the X-ray morphology, as can be seen in Figure 1.5 (left). The observed TeV spectrum (without signs of a cutoff up to several TeVs) indicates that particles are being accelerated in the shell of the SNR to energies up to 100 TeV. To further distinguish between protons or electrons as the parent particles producing gamma rays, observations of SNRs on the GeV energy range are needed. The Fermi LAT detector resolved the shell morphology of the SNR W44 [Abdo *et al.* 2010f], and presented its spectrum with a low energy cut-off (around 2 GeV), as seen in Figure 1.5 (right). Subsequent detections of both young and middle-aged SNRs continue to provide information on their emission mechanism.

Not only expected gamma-ray emitters have been detected and studied, but also other type of objects have surprised the scientific comunity by showing gamma-ray emission. This has been the case of the nova that was found in the symbiotic binary V407 Cygni (a binary system consisting on a pulsating red giant and a white dwarf companion). The *Fermi* LAT reported HE emission coinciding with the maximun optical emission from a nova outburst [Abdo *et al.* 2010e]. The GeV emission lasted for 2 weeks, by that time, the X-ray emission reported by Swift started rising. The gamma-ray spectrum suggest for the emission to be produced

either by neutral pion decay or by inverse Compton scattering of infrared photons from the red giant. A prediction for novas in the gamma-ray sky was previously made by [Tatischeff & Hernanz 2007, Tatischeff & Hernanz 2008], although the position on the sky of the studied souce prevented observations of gamma rays with ground-based detectors. Notwithstanding, these gamma-ray novae are thought to be rare events.

Another class of long expected gamma-ray generators are the X-ray binaries (XRBs). The first one ever detected was Cygnus X-3 (Cyg X-3), by SAS-2. But it was only recently that it has been confirmed as a gamma-ray source between 100 MeV and 100 GeV by the *Fermi* satellite [Abdo *et al.* 2009g]. Furthermore, the first XRB detected at TeV energies was PSR B1259−63 [Aharonian *et al.* 2005a], very closely followed by the detection of LS 5039 by H.E.S.S. [Aharonian *et al.* 2005c]. The next year, another TeV object was added to this class when LS I +61 303 [Albert *et al.* 2006] was detected by the MAGIC telescope. In each case, the gamma-ray emission appear to be modulated by the orbit of the system. The acceleration site of the parental cosmic ray particles – that produce the gamma-ray emission – seems to be geometry dependent and confined inside the binary system. Nonetheless, one of the open discussions regarding XRBs is the nature of the compact object: wheter it is a black hole or a neutron star. In the former scenario, the binary system is called *microquasar* and it displays relativistic radio jets. Hence, the VHE gamma rays may be produced in the jet via inverse Compton scattering. In the case of the pulsar binary system, the VHE gamma rays are expected to be generated in the wind-wind collisions between the pulsar and the massive companion star. The multiwavelength approach to solve the puzzle would be either detecting the jet in radio, or pulsations from the compact object. Up to date, 7 XRBs have reported either at GeV or TeV energies, adding PSR B1259−63 [Abdo *et al.* 2010i], Cyg X-3 [Abdo *et al.* 2009g], Cyg X-1 [Albert *et al.* 2007a, Sabatini *et al.* 2010], 1FGL J1018.6-5856 [Corbet *et al.* 2011] and HESS J0632+057 [Ong 2011, Mariotti 2011] to the already mentioned binary systems. It is worth noting that, of these sources, only LS I +61 303, LS 5039 and PSR B12594−63 have been detected at both GeV and TeV energies.

Diffuse emission from the Galactic Center has been observed since the begining of the space-borne missions. This emission was associated with interactions of CR with the interestellar medium. Thanks to the scan of the Galactic Plane performed by H.E.S.S. [Aharonian *et al.* 2005b], eight new sources were discovered. In deeper and longer observations, the afforementioned association – specifically, to dense molecular clouds – could be successfully proved [Aharonian *et al.* 2006e]. Therefore, hadronic processes are favoured as the origin of the gamma-ray emission in the center of our Galaxy.

The latest flares measured in the Crab Nebula [Abdo *et al.* 2011], defy the definition of this object as the 'standard candle' both in X-ray and gamma-ray astronomy. In X-rays, variation in the flux of the Crab Nebula have been reported for the last years. The gamma-ray flares detected by the *Fermi* and AGILE satellites, however, are not correlated with the emission in the keV energy regime.

Pulsars, the first established source-class in gamma-rays, are starting to be studied as a population in gamma rays. *Fermi* LAT detected more than 60 of these objects, from which 8 were millisecond pulsars (MSPs) [Abdo *et al.* 2009e], and 16 new gamma-ray pulsars were found through blind[2] searches [Abdo *et al.* 2009a]. The starting point of these discoveries was starred by the pulsar found inside the SNR CTA [Abdo *et al.* 2008]. CTA-1 belongs to a certain type of radio-quiet, but gamma-ray-loud pulsars, like Geminga.

The MSPs are usually found in binary systems and thougth to be spun up by the torque resulting from accretion of mass from their companion. They are significantly more stable than younger pulsars, although their basic emission mechanism seems to be the same. The globular cluster 47 Tucanae [Abdo *et al.* 2009f] belongs to another class of predicted source of gamma rays, but it had eluded detection until very recently. Globular clusters contains a large amount of MSPs, and in fact their GeV emission is largely explained by the cumulative gamma-ray emission from these young pulsars.

Furthermore, in 2008, MAGIC opened the window of the detection of pulsars from ground-based telescopes: the Crab pulsar was seen above 25 GeV [Aliu *et al.* 2008b], thanks to a special trigger setup. This re-opened a discussion on models that were trying to explain the emission and mechanism of pulsars. Very recently, the Crab pulsar as been detected by VERITAS at the *Fermi* Symposium (2010) at energies as high as 100 GeV, thus constraining even more the model for the mechanism of gamma-ray production.

1.3.2 A brief summary of extragalactic highlights

Blazars are the most numerous population of gamma-ray sources, and are included in the category of active galactic nuclei (AGN) objects. They allow studies on the extragalactic background light (EBL), test general relativity, and shed some light on the jet processes occuring next to their central black holes.

The starlight emitted by galaxies and accumulated over time is largely assumed to be the main contributor for EBL. Another possible source of this diffuse extragalactic emission was thought to be the emission coming from the first stars, that were formed in the early Universe: metal-free massive stars, known as *population III*. Given that direct measurements are not straightforward, observing distant objects – specifically, their absorbed spectra – like blazars seems a better approach. Those absorption features are a consequence of photon-photon collision and pair production. The original spectrum of the source (named intrinsinc spectrum) is thus modified and depends on the spectral energy distribution (SED) of the EBL. This spectral change (steepening above 1 TeV) becomes more pronounced at larger redshifts. For instance, the H.E.S.S. experiment discovered gamma-ray emission from the distant blazars H 2356-309 and 1ES 1101-232, at redshifts z = 0.165 and 0.186, respectively [Aharonian *et al.* 2006f]. By assuming an intrinsic and reasonable spectrum for both blazars, an upper limit on the EBL could be derived. The EBL flux was

[2]None of them were detected previously in any other lower frequency

constrained to lower values, consistent with the limit provided by the integrated light of resolved galaxies, and it excluded a major contribution from the first stars. Up to date, continued observations of these objects is further constraining the shape of the EBL.

Blazars owe their large number of detections to the fact of having their jets pointing towards us. Their TeV emission is due to the photons emitted in the jet being boosted by relativistic effects. Besides blazars, there have also been gamma-ray emission reported from other AGNs, like the radio galaxies M87 and Cen A and far-away radio quasar 3C 279.

In the GeV regime, Cen A was detected by the EGRET satellite [Hartman *et al.* 1999], and later on the *Fermi* LAT telescope confirmed and imaged its giant radio lobes [Abdo *et al.* 2010d]. Cen A is the nearest and one of the brightest radio galaxies, and has also been monitored at radio wavenlenghts.

M87 is one of the best studied radio galaxies in almost every wavelength, with a resolved jet (in radio, optical and X-ray) inclined 30° from the our line of sight. It is one of the best candidates to study the jet connection to the observed gamma-ray emission. A first hint of detection was claimed by the HEGRA experiment [Aharonian *et al.* 2003] and was finally confirmed above 730 GeV by H.E.S.S. [Acciari *et al.* 2009c]. The fast TeV variability – in a daily scale – reported in 2005 already pointed to a small emission region for the VHE radiation, in the immediate vicinity of the central supermassive black hole. Another rapid and strong outburst in 2008 was reported by the MAGIC telescope, subsequently followed by the VERITAS and H.E.S.S., a response that allowed a dense sampling of the event [Aharonian *et al.* 2006d]. All the previous VHE gamma-ray detections, together with the simultaneous high-frequency radio coverage provided by the Very Long Baseline Interferometry (VLBI), further constrained the VHE emission site to take place within the jet collimation, in a region small even for the highly resolved radio images.

The more distant extragalactic object – detected in gamma rays – is the radio quasar 3C 279. Its detection in flaring state by the MAGIC experiment implied not only the first report at VHE of a quasar, but also that the Universe was more transparent to gamma-ray radiation than what was previously thougth [Albert *et al.* 2008a].

The year 2009 brought to the gamma-ray astronomy the addition of a new class of source: starburst galaxies were found to emit both at GeV and TeV energies (see below). These long predicted gamma-ray emitters are located at intermediate distances between the already detected LMC close to our Galaxy and the distant blazars, and are supposed to have intermediate gamma-ray luminosities. The producion of gamma rays in these galaxies was predicted to come from the acceleration of CRs in SNRs and subsequent collision with interestellar gas. An excess in gamma rays is expected at the central region of starburst galaxies due to the characteristic enhanced SN explosion rate, enhanced star formation rate and rich molecular gas regions. More discussion on this topic is provided in Chapter 5.

The two closest starburst galaxies that have been detected are M82, by

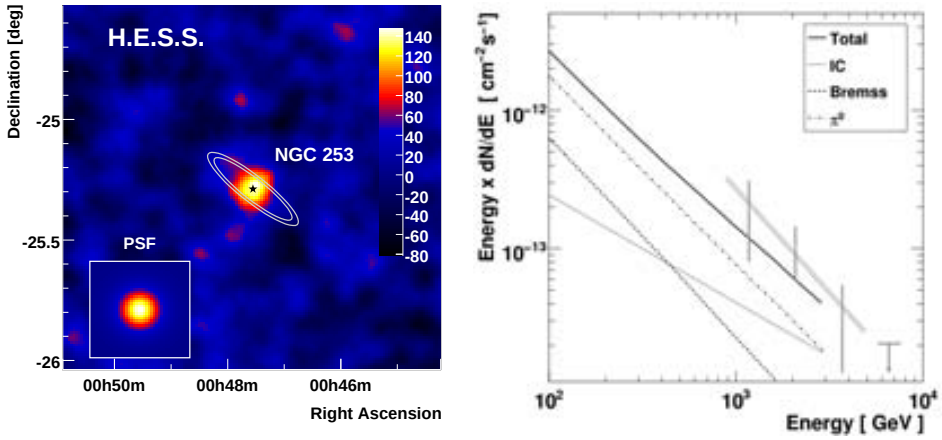

Figure 1.6: Left: Skymap NGC 253 by HESS. Right: Spectrum M 82 by VERITAS.

VERITAS [Acciari *et al.* 2009a], and NGC 253, by H.E.S.S. [Acero *et al.* 2009] in the TeV range, and both of them were detected by *Fermi* in the GeV range [Abdo *et al.* 2010c]. The VERITAS Collaboration presented a spectrum above 700 GeV, see Figure 1.6 (left). H.E.S.S. showed that the gamma-ray emission comes from the central part of the starburst galaxy, see Figure 1.6 (right).

Gamma-Ray Bursts (GRBs) were established as extragalactic transient sources, due to its isotropic distribution on the sky by BATSE, on board of CGRO. Their spectra helps constraining EBL [Abdo *et al.* 2009h] and, recently, quantum gravity [Abdo *et al.* 2009b]. The GRB 090510 at a redshift z = 0.903 was detected by *Fermi* over a very broad energy range (from 8 keV to 31 GeV). Despite its distance, the rising edge time of the burst varied less than 1 s over the entire energy range. Many theories on quantum gravity predict Lorenz invariance violation (LIV) that should be detected as a delay: an energy-dependent variation in the rising edge time of the burst. This delay was not detected in this GRB 090510 and set the strongest constrain on the Lorenz invariance up to now: less than the Planck length divided by 1.2 at 99% confidence level.

1.4 Multimessenger astronomy

Neutrinos are the ideal astronomical messenger. Since they interact weakly with matter, they travel long distances without being deflected by magnetic fields and carrying almost unbiased information of the source that produces them. However, their detection on Earth is not so easy, basically for the same reason: their lack of electric charge results in very scarce interactions. Therefore, the neutrino dectectors need to be inmense enough to collect sufficient statistics.

One of the strongest motivations to promote neutrino astronomy – from the gamma-ray astronomer perspective – is that detecting neutrinos from an astrophysical source would provide univocal evidence for the hadronic production of gamma-

rays (see section 1.1). The gamma-ray and neutrino astronomy shared a couple of common aims:

- the study of the type of sources and mechanisms responsible of the cosmic-ray acceleration,
- and the nature and distribution of dark matter.

The most prominent km^3 neutrino experiments are about to open this window. The IceCube Neutrino Observatory, in the Antartica, has been completed recently [Halzen & Klein 2010], thanks to the success of its predecessor, Antarctic Muon and Neutrino Detector Array (AMANDA). On the other side of the Earth, the Cubic Kilometer Neutrino Telescope (KM3NeT) will soon continue the efforts made by the Astronomy with a Neutrino Telescope and Abyss Environmental Research (ANTARES) experiment in the Mediterranean sea. Being placed in different hemispheres, they will be both complementary. As has been mentioned, the inmense particle detectors IceCube and KM3NeT have their performance previously tested in smaller detectors, (namely AMANDA and ANTARES respectively).

The neutrino detection technique is based on capturing Cherenkov light, which is produced when these particles interact with a nucleus in the ice or in the water. The few interactions that take place create muons, electrons and hadrons in a cascade of particles. The charged secondary particles are the ones that radiate Cherenkov light and penetrate deep into the ice/water. The direction of the neutrino can be derived from the light pattern, that is recorded by photomultipliers (PMTs). The time of arrival and the digitized waveforms of the light contains the information to reconstruct the energy of the neutrino events, as well as their arrival directions. The largest source of background for cosmic neutrinos are the so-called "atmospheric neutrinos": they come from the decay of pions and kaons that were produced in pp interactions in the atmosphere. The undesired radiation is present up to 1000 TeV, but its flux can be calculated. The good angular resolution is provided thanks to the big size of the detectors (in the ice, the mean free path for muons can reack 10 km).

IceCube contains a total of 5160 digital optical modules, deployed on 86 vertical strings, with 60 digital optical modules (DOMs) attached at depths around 2000 m. The conceptual design is ilustrated in Figure 1.7. The bulk of IceCube is sensitive to neutrinos with energies above 100 GeV; the DeepCore infill array may observe neutrinos with energies as low as 10 GeV. The IceTop surface array, located on the ice above IceCube, consists of 160 ice-filled tanks, each instrumented with two DOMs. It observes cosmic-ray air showers with a threshold of about 300 GeV. The early data from IceCube are very promising, and the detector is observing over 10 000 neutrino events per year.

Also profiting from the Cherenkov radiation and containing water detectors is the Auger Project, named after Pierre Auger, the French scientist who first investigated air showers. Actually, Auger is a hybrid experiment that combines particle and fluorescence detectors. The particle detector part of the array consists of a total

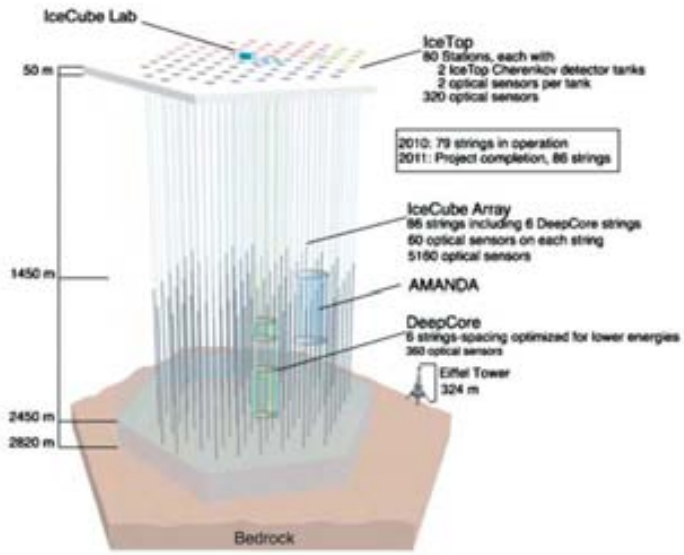

Figure 1.7: Actual design of the IceCube neutrino detector with 5160 optical sensors viewing a kilometer cubed of natural ice. The signals detected by each sensor are transmitted to the surface over the 86 strings to which the sensors are attached. IceCube encloses its smaller predecessor, AMANDA. From IceCube Science Team - Francis Halzen.

of 1,600 tanks of water, of large capacity and sealed from external light contamination. It is dotted with PMTs to detect the passage of air shower particles through their emission of Cherenkov light. The tanks are spaced in a huge grid as to allow detection of a single air shower by five to ten detector tanks. There is a set of four arrays of fluorescence detector telescopes interspersed among the water tank grid. There is one telescope array in the center of the particle detector grid, with the other three eyes around the rim of the grid.

1.5 On this Thesis

This Thesis contains some studies on aspects related to cosmic-ray diffusion. It is presented in two parts, one describing models on the phenomenology of CR diffusion (Chapters 2 to 5), and another that shows observations using the MAGIC experiment and simulations of the future Cherenkov Telescope Array, CTA (Chapters 6 to 9). In the first part, the general accepted theory on CR diffusion is introduced in Chapter 2. From this starting point, a model is presented for the environment of the SNR IC 443 – on Chapters 3 and 4 – in order to explain the high-energy phenomenology, and it is contrasted with current observations of the source. The Chapter 5 contains a multi-messenger model for the diffuse emission of the starburst galaxy M82. The gamma-ray predictions are compared with the recent detections in the GeV and TeV energy range. In the second part,

the Cherenkov technique and the MAGIC experiments is described. The upper limits obtained with the MAGIC-I telescope from two Milagro-detected Brigth Fermi sources in the region of the SNR G65.1+0.6 are presented on Chapter 7. The Chapter 8 contains simulations of CTA and initial spectral studies on particular science cases. Observations with MAGIC stereo on IC 443, together with preliminar studies performed with CTA can be found in Chapter 9. Finally, the Chapter 10 contains conclusions and advances some future work.

Part of the work in this Thesis has already been published in refereed journals:

"Diffusion of cosmic-rays and the Gamma-ray Large Area Telescope: Phenomenology at the 1-100 GeV regime", [Rodríguez Marrero *et al.* 2008].

"MAGIC J0616+225 as delayed TeV emission of cosmic-rays diffusing from SNR IC 443", [Torres *et al.* 2008].

"The GeV to TeV view of SNR IC443: predictions for Fermi", [Rodríguez Marrero *et al.* 2009].

"The GeV to TeV connection in the environment of SNR IC 443", [Torres *et al.* 2010].

"Multi-messenger model for the starburst galaxy M82", [de Cea del Pozo *et al.* 2009b].

"MAGIC Upper Limits for two Milagro-detected, Bright Fermi Sources in the Region of SNR G65.1+0.6" (as one of the corresponding authors), [Aleksić *et al.* 2010].

Moreover oral and poster contributions have also been presented by the PhD student:

"Diffusion of cosmic-rays and gamma-ray sources", oral talk, VIII Reunión Científica de la Sociedad Española de Astronomía, 2008, Santander (Spain).

"Model analysis of the very high energy detections of the starburst galaxies M82 and NGC 253", poster, Fermi Symposium, 2009, Washington DC (USA) [de Cea del Pozo *et al.* 2009a].

"First exploration of the spectral CTA response on molecular clouds near supernova remnants", oral talk, General CTA Meeting, 2010, Zeuthen (Germany).

More contributions displaying several simulations with CTA can be found in the following address:

http://www.cta-observatory.org/ctawpcwiki/index.php/PHYS-TLs-work.

PART I:

Studies on the phenomenology of cosmic-ray diffusion

Chapter 2

Diffusion of cosmic-rays

Contents

It is commonly accepted that supernova remnants (SNR) are one of the most probable scenarios of leptonic and hadronic cosmic-ray (CR) acceleration. The particle acceleration mechanism in individual SNRs is usually assumed to be diffusive shock acceleration, which naturally leads to a power-law population of relativistic particles. In the standard version of this mechanism, e.g. [Bell 1978], particles are scattered by magnetohydrodynamic waves repeatedly through the shock front. Electrons suffer synchrotron losses, producing the non-thermal emission from radio to X-rays usually seen in shell-type SNRs.

The maximum energy achieved depends on the shock speed and SNR age as well as on any competing loss processes. In young SNRs, electrons can easily reach energies in excess of 1 TeV, and they produce X-rays. Non-thermal X-ray emission associated with shock acceleration has been clearly observed in many SNRs. But in order to have an observational confirmation of protons and other nuclei being accelerated, particularly, in order to be able to distinguish this from leptonic emission, one should try and isolate the multi-messenger effects of the secondary particles produced when the accelerated hadrons interact in nearby molecular clouds through *pp* collisions. These ideas go back, for instance, to the works by [Dogel & Sharov 1990, Naito & Takahara 1994, Drury *et al.* 1994, Sturner *et al.* 1997, Gaisser *et al.* 1998, Baring *et al.* 1999], among others. In fact, more than 30 years ago, [Montmerle 1979] suggested that SNRs within OB stellar associations, i.e. star forming regions with plenty of molecular gas, could generate observable gamma-ray sources. A molecular cloud being illuminated by particles that escaped from a nearby SNR could then act as a target for *pp* interactions, greatly enhancing the gamma-ray emission, see, e.g., the recent works by [Gabici & Aharonian 2007, Gabici *et al.* 2009, Casanova *et al.* 2010, Rodríguez Marrero *et al.* 2008]. Furthermore, observing gamma rays from clouds nearby SNRs, can provide feedback on our knowledge of the diffusion characteristics of the environment.

As investigated by [Aharonian & Atoyan 1996], the observed gamma rays can have a significantly different spectrum from that expected from the primary particle population at the immediate vicinity of source (the SNR shock). For instance, a standard diffusion coefficient in the range $\delta \sim 0.3 - 0.6$ can explain gamma-ray spectra as steep as $\Gamma \sim 2.3 - 2.6$ in sources with particles accelerated to a power-law $J_p(E_p) \propto E^{-2}$ if the target that is illuminated by the π^0-decays is sufficiently far away from the accelerator. Measuring gamma-ray emission around SNRs would then allow to acquire knowledge of the diffusion environment in which the CRs propagate at several kpc from Earth.

EGRET was unsuccessful in performing detailed studies of the gamma-ray sky above 10 GeV, partly due to back-splash of secondary particles produced by high-energy gamma rays causing a self-veto in the monolithic anti-coincidence detector used to reject charged particles, and partly due to a non-calibrated detector response. *Fermi* is not strongly affected by this effect since the anti-coincidence shield was designed in a segmented fashion [Moiseev *et al.* 2007]. The effective area of *Fermi* is roughly an order of magnitude larger than that of EGRET leading to an increased sensitivity, see figure 1 of [Funk *et al.* 2008].

This Chapter presents the general theory that up to day tries to explain the diffusion of cosmic rays in the interestellar medium, ISM. In section 2.2, possible astrophysical scenarios that were predicted to be detected at the high-energy end of the observations with *Fermi* have been analyzed. Those scenarios have been published in [Rodríguez Marrero *et al.* 2008], previous to the *Fermi* launch, and are thought to occur as result of CR diffusion in the ISM.

2.1 The role of diffusion

When CR protons interact with ambient nuclei, several types of particles are produced. One of these products are neutral pions, π^0, which naturally decay in two gamma-ray photons. Above hundreds of MeVs, the π^0-decay gamma-ray emission dominates over bremsstrahlung and inverse Compton (IC) in the galactic plane [Fichtel *et al.* 1976, Bertsch *et al.* 1993]. The π^0-decay gamma-ray flux from a source of proton-density n_p is

$$F(E_\gamma) = 2 \int_{E_\pi^{\min}}^{\infty} \frac{F_\pi(E_\pi)}{\sqrt{E_\pi^2 - m_\pi^2}} \, dE_\pi, \tag{2.1}$$

where

$$F_\pi(E_\pi) = 4\pi n_p \int_{E_p^{\min}}^{E_p^{\max}} J_p(E) \frac{d\sigma_\pi(E_\pi,\ E_p)}{dE_\pi} \, dE_p, \tag{2.2}$$

and $d\sigma_\pi(E_\pi,\ E_p)/dE_\pi$ is the differential cross-section for the production of π^0, e.g., [Domingo-Santamaría & Torres 2005, Kelner *et al.* 2006]. The limits of integration in the last expression are obtained by kinematic considerations. Any possible gradient of CR or gas number density in the target has been implicitly neglected. The CR

spectrum, which is essentially mimicked by π^0-decay gamma rays at high energies, is given by:

$$J_p(E,\ r,\ t) = \left[\frac{c\beta}{4\pi}\right] f, \tag{2.3}$$

where $f(E,\ r,\ t)$ is the distribution function of protons at an instant t and a distance r from the source.

The distribution function f satisfies the radial-temporal-energy dependent diffusion equation, [Ginzburg & Syrovatskii 1964], which in the spherically symmetric case has the form:

$$\frac{\partial f}{\partial t} = \frac{D(E)}{r^2}\frac{\partial}{\partial r}r^2\frac{\partial f}{\partial r} + \frac{\partial}{\partial E}\left(Pf\right) + Q, \tag{2.4}$$

where $P = -dE/dt$ is the energy loss rate of the particles, $Q = Q(E,\ r,\ t)$ is the source function, and $D(E)$ is the diffusion coefficient, for which a dependence only on the particle's energy is assumed. The energy loss rate are due to ionization and nuclear interactions, with the latter dominating over the former for energies larger than 1 GeV. The nuclear loss rate is $P_{\rm nuc} = E/\tau_{pp}$, with $\tau_{pp} = (n_p\, c\, \kappa\, \sigma_{pp})^{-1}$ being the timescale for the corresponding nuclear loss, $\kappa \sim 0.45$ being the inelasticity of the interaction, and σ_{pp} being the cross section (Gaisser 1990). [Aharonian & Atoyan 1996] presented a solution for the diffusion equation with an arbitrary diffusion coefficient, and an impulsive injection spectrum $f_{\rm inj}(E)$, such that $Q(E,r,t) = N_0 f_{\rm inj}(E)\delta\bar{r}\delta(t)$. For the particular case in which $D(E) \propto E^{\delta}$ and $f_{\rm inj} \propto E^{-\alpha}$, above 1 – 10 GeV, where the cross-section to pp interactions is a weak function of E, it reads

$$f(E,r,t) \sim \frac{N_0 E^{-\alpha}}{\pi^{3/2} R_{\rm dif}^3}\exp\left[-\frac{(\alpha-1)t}{\tau_{pp}} - \left(\frac{R}{R_{\rm dif}}\right)^2\right], \tag{2.5}$$

where

$$R_{\rm dif} = 2\left(D(E)t\frac{\exp(\frac{t\delta}{\tau_{pp}})-1}{t\delta/\tau_{pp}}\right)^{1/2} \tag{2.6}$$

stands for the radius of the sphere up to which the particles of energy E have time to propagate after their injection. In case of continuous injection of accelerated particles, $Q(E,\ t) = Q_0 E^{-\alpha} T(t)$, the previous solution needs to be convolved with the function $\mathcal{T}(t-t')$ in the time interval $0 \le t' \le t$ [Atoyan *et al.* 1995].

$$f(E,r,t) \sim \frac{N_0 E^{-\alpha}}{4\pi D(E) R}\mathrm{erfc}\left[\frac{R}{R_{\rm dif}(E,\ t)}\right], \tag{2.7}$$

where

$$\mathrm{erfc}(z) = \frac{2}{\pi}\int_z^{\infty}\exp(-x^2)\,dx \tag{2.8}$$

is the error function.

In the following section, typical values, $\alpha = 2.2$ and $\delta = 0.5$, will be assumed.

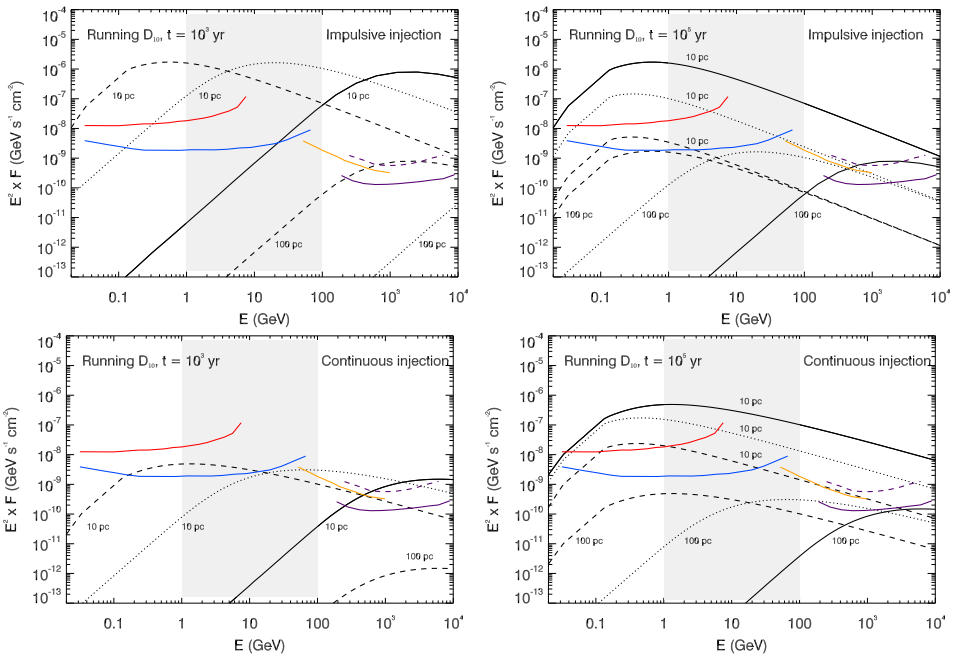

Figure 2.1: SEDs generated by CR propagation in ISM with different properties. Fluxes correspond to a cloud with $M_5/d_{kpc}^2 = 0.5$. Curve for $D_{10} = 10^{26}$, 10^{27}, and 10^{28} cm^2 s^{-1} are shown with solid, dotted, and dashed lines respectively. Sensitivities of EGRET (red) and *Fermi* (blue) (both for different directions in the sky with different background contribution), H.E.S.S. (magenta) (survey mode and pointed observations with typical integrations), and MAGIC (yellow), are shown for comparison purposes (see figure 1 of [Funk *et al.* 2008] for details on sensitivities).

2.2 Astrophysical scenarios in the Pre-Fermi era

In the case of energy-dependent propagation of CRs, a large variety of γ-ray spectra is expected, e.g., [Aharonian & Atoyan 1996, Gabici & Aharonian 2007, Torres *et al.* 2008]. This study presents – systematically and numerically produced – more than 2000 E^2F distributions, and their dependences with the involved parameters. Table 2.1 summarizes the results both for an impulsive and a continuous accelerator. The most surprising dependences are related with the age of the accelerator and the diffusion coefficient, see Figure 2.1. These parameters have a direct impact on the CR distribution. As the diffusion increases in speed, high energy CR cover larger distances. The source (cloud) is parameterized in units of $M_5 = M_{Cl}/10^5 M_\odot$ and $d_{kpc} = d/\ 1\,\mathrm{kpc}$. The $t_{transition}$ parameter, defined in the case of an impulsive accelerator, is the age for which the timescale for the corresponding nuclear loss becomes comparable to the age of the accelerator itself. $D_{transition}$ is the value of the diffusion coefficient for which the SEDs stop displacing in energy keeping approximately the same flux, as inferred from Figure 2.1.

Setting, as an example, reasonable parameters for the energy injected by the

Table 2.1: Dependence of the SED (E^2F vs. E) on various parameters. *Imp.* (*cont.*) stands for the impulsive (continuous) accelerator case. Dependences upon cloud parameters such as density (n_{Cl}), mass (M_{Cl}), and radius (R_{Cl}) are obvious and related.

Parameter symbol and meaning	Effect on the E^2F distributions versus E
Accelerator	
W_p: total energy injected as CRs	*imp.:* overall scaling, small effects in the range if in the typical range 10^{50}–10^{51} erg
L_p: energy injected per unit time	*cont.:* overall scaling, small effects in the range if in the typical range 10^{37}–10^{38} erg s^{-1}
increasing t: age of the accelerator	*imp.:* peak displaces to smaller energies for a fixed distance, until $t > t_{transition}$, and the peak displaces to smaller fluxes *cont.:* peak displaces to smaller energies and larger fluxes, for a fixed distance
Interstellar medium	
n: density	negligible effects in the typical range 0.5–10 cm^{-3}, since $\tau_{pp} \gg t$.
increasing D_{10}: diffusion coefficient of the medium (at 10 GeV)	**for a fixed age**: displacement to smaller energies until $D_{10} > D_{transition}$ where peaks generated by clouds at large separation, R, displace up and peaks generated by clouds at smaller R displace down in the SED **for a fixed distance**: displacement to smaller energies until $D_{10} > D_{transition}$ where peaks generated by older accelerators (larger t) displaces down and peaks generated by younger accelerators (smaller t) displaces up

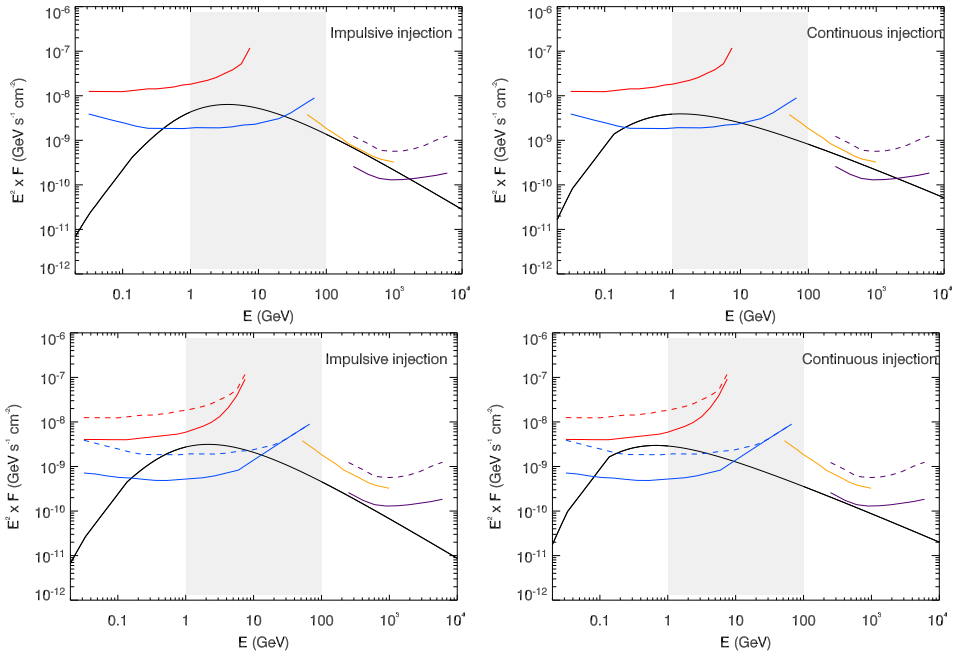

Figure 2.2: Examples of the model predictions for a hadronic maxima in the $1-100\,\mathrm{GeV}$ regime. The left top (bottom) panel shows the predictions for a cloud scaled at $M_5/d^2_{kpc} = 0.025$ (0.04), located at 20 (30) pc from an accelerator of 10^4 (3×10^4) yr, diffusing with $D_{10} = 10^{27}\,\mathrm{cm^2\,s^{-}1}$. The right top (bottom) panel curve shows the predictions for a cloud scaled at $M_5/d^2_{kpc} = 0.08$ (0.06) located at 10 (20) pc from an accelerator of 10^3 (10^4) yr, diffusing with $D_{10} = 10^{28}\,\mathrm{cm^2\,s^{-}1}$. Increasing the ratio M_5/d^2_{kpc}, the curves move up maintaining all other features.

accelerator into cosmic-rays (e.g., $W_p = 5\times10^{49}$ erg for an impulsive source and $L_p = 5\times10^{37}\,\mathrm{erg\,s^{-1}}$ for a continuous one) and for the interstellar medium density (e.g., $n = 1\,\mathrm{cm^{-3}}$), several scenarios for the appearance of hadronic maxima produced by diffusion are found. Some examples are shown in Figure 2.2, for the two types of accelerators. Two kinds of peaks at this energy regime are possible: those that are not to be detected by an instrument with the sensitivity of EGRET or MAGIC, and those that are not to be detected by an instrument like H.E.S.S. or VERITAS. The impulsive accelerator produces a more narrow peak maxima. A maxima in the SED, hadronically produced as an effect of diffusion of CRs, is possible and not uncommon at the high-energy end, where they produce a level of flux detectable by *Fermi* LAT.

Figure 2.3 displays, as contour plots, the energy at which the maximum of the SED is found for the cases of impulsive acceleration of cosmic rays, at different distances, ages of the accelerator, and diffusion coefficients. The impact of the diffusion is clearly shown by this figure, which changes are due to pure energy-dependent propagation effects. The diffusion radius, for $t \ll \tau_{pp}$, is $R_{\mathrm{dif}}(E) = 2\sqrt{D(E)t}$, so that at a fixed age and distance, only particles of higher energy will be able to compensate a

smaller D_{10}, producing SED maxima at higher E-values. The smaller values of D_{10} are expected in dense regions of ISM, e.g., [Ormes *et al.* 1988, Torres *et al.* 2008]. It is interesting to note that for many, albeit not for all, of the SEDs studied, the maximum is found at energies beyond the *Fermi* acceptance. On the other hand, Figure 2.3 interpretes a *Fermi* observational discovery of a $1-100\,\mathrm{GeV}$ maximum, and provides interesting clues about the nature of the astrophysical system that generates the gamma rays. First, these SEDs are found in cases where the scenario does not predict detectable emission at the EGRET sensitivity, so that they will represent new phenomenology. Second, the range of accelerator-target separations and ages of the accelerator that would produce such a $1-100$ GeV maximum is rather limited (see in Figure 2.3 the narrow contours for maxima at such energies). This would lead to a direct identification of the source.

Another interesting possibility is the case of two unresolved sources. Two separate accelerator-cloud complexes are considered close to the line of sight, such that they would be observed as a single source. This kind of scenarios would produce an inverted spectrum. Figure 2.4 shows four possible inverted spectra. The two figures in the top (bottom) panel are generated by an impulsive (continuous) accelerator. The SED created by the oldest (youngest) accelerator is shown by dashed (dot-dashed) lines in each of the scenarios. For the left cases, EGRET should have been able to weakly detect the source producing fluxes at smallest energies. In any case, EGRET could not conclusively relate it to such phenomenon due to its large low-energy PSF. The counterpart at higher energies is a bright source potentially detectable by ground-based telescopes. Due to continuous energy coverage, *Fermi* is a prime instrument to track this phenomenology, although none has been reported up to now. The right panel cases show particular examples in which the detection of the source by an instrument with the sensitivity of EGRET is not possible at all. The inverted spectrum is less deep in these scenarios. Less pronounced V-shaped spectra can be obtained with concomitantly lower fluxes at TeV energies.

2.2.1 Discussion

Compton peaks (which first example could have been found already, [Aharonian *et al.* 2006c]) are not the only way to generate a maximum in a SED. A large variety of parameters representing physical conditions in the vicinity of a CR accelerator could produce a rather similar effect. Distinguishing between these cases would require multiwavelength information, search for counterparts, and modelling. If such a maximum is interpreted hadronically, as a result of diffusion of CR in the ISM and their subsequent interaction with a nearby target, the results presented herein constrain, given the energy at which the maximum of the SED is reached, the characteristics of the putative accelerator, helping to the identification process. Indeed, one of the most distinguishing aspects of this study is the realization that these signatures (in particular, peaks at the $1-100\,\mathrm{GeV}$ energy region) is indicative for an identification of the underlying mechanism producing the gamma rays that occurs in nature: which accelerator (age and relative position to the target cloud)

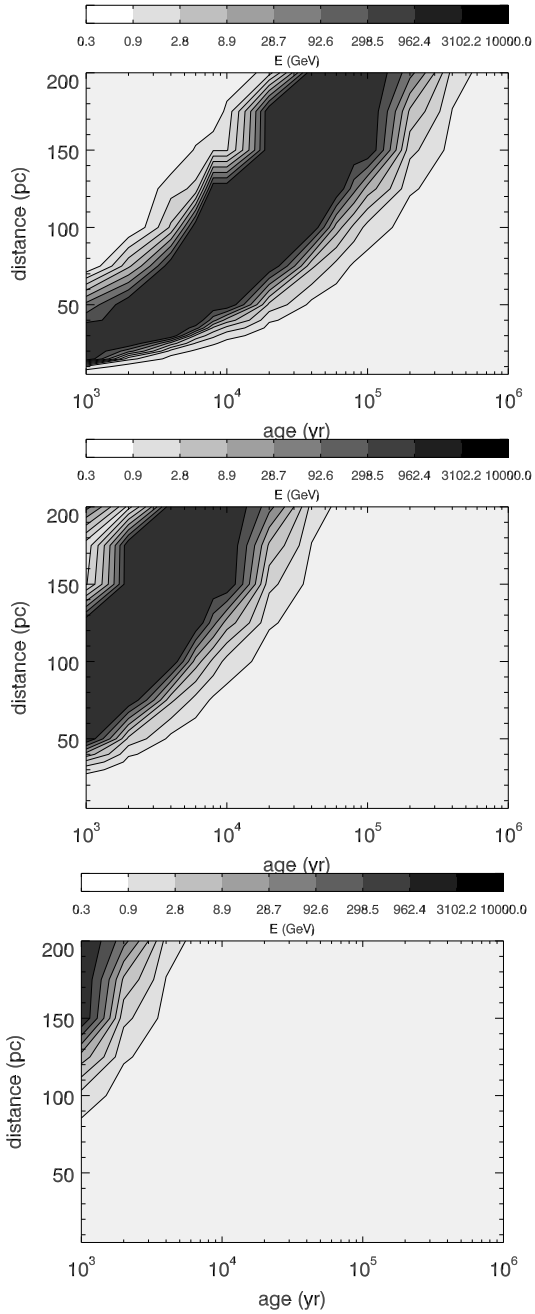

Figure 2.3: For each combination of age and accelerator-target separation, for which more than two thousand spectra where numerically produced, the energy of the maximum of such spectra are shown in a contour plot. The color of the different contours corresponds to the range of energy where the maximum is found according to the color bar above each figure. From top to bottom, plots are created for the case of an impulsive source injecting protons in a medium with D_{10}=10^{26}cm^2 s^{-1}, 10^{27}cm^2 s^{-1} and 10^{28}cm^2 s^{-1}.

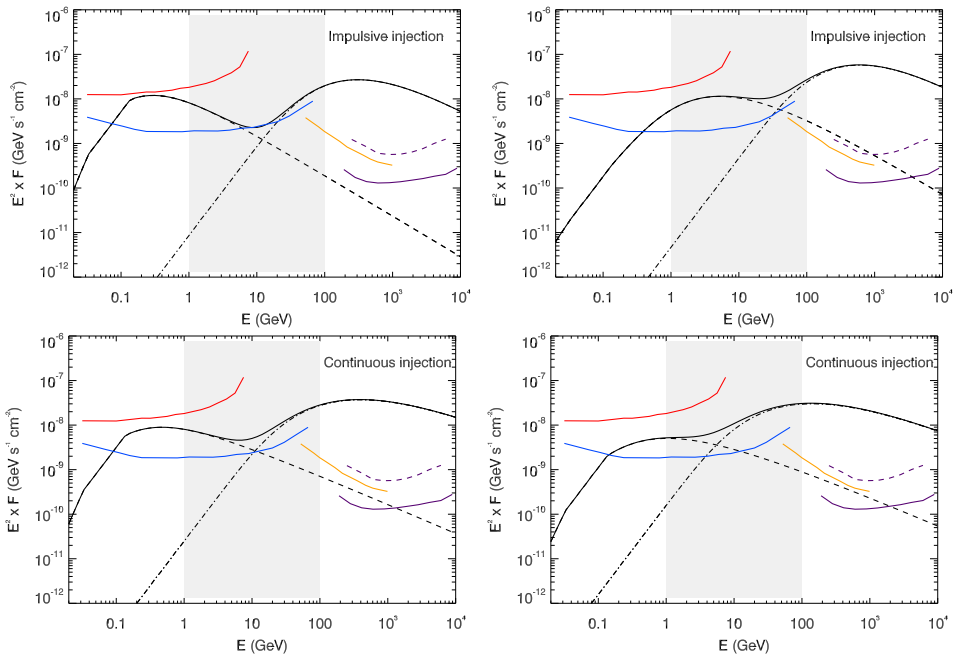

Figure 2.4: The parameters for the plots are as follows, (top left) the dashed curve on the left: $t = 4{\times}10^5$ yr, $R = 5$ pc, $M_5/d^2_{kpc} = 0.01$; the dashed curve on the right: $t = 10^4$ yr, $R = 20$ pc, $M_5/d^2_{kpc} = 0.1$; (top right) the dashed curve on the left: $t = 2{\times}10^6$ yr, R=100 pc, $M_5/d^2_{kpc} = 3$; the dashed curve on the right: $t = 4{\times}10^3$ yr, $R = 15$ pc,$M_5/d^2_{kpc} = 0.1$; (bottom left) the dashed curve on the left: $t = 2{\times}10^6$ yr, R=15 pc, $M_5/d^2_{kpc} = 0.004$; the dashed curve on the right: $t = 10^3$ yr, $R = 5$ pc, $M_5/d^2_{kpc} = 1$; (bottom right) the dashed curve on the left: $t = 2{\times}10^6$ yr, $R = 40$ pc, $M_5/d^2_{kpc} = 0.017$; the dashed curve on the right: $t = 6{\times}10^4$ yr, $R = 30$ pc,$M_5/d^2_{kpc} = 2.5$. D_{10} is set to 10^{26} cm^2 s^{-1}. R is the accelerator-cloud separation.

and under which diffusion properties CR propagate, as it is exemplified in Figure 2.3. In a survey mode such as the one *Fermi* LAT performs, it is also possible to find rather unexpected, tell-tailing SEDs, like those V-shaped presented here, if observed with instruments having a limited PSF, predictably leaving many Galactic sources unresolved.

2.3 Molecular clouds illuminated by CRs from SNRs

Non-thermal emission is expected to come from molecular clouds, due to interactions of CR that penetrate the cloud. This emission would be enhanced whenever the molecular cloud is in the proximity of a SNR [Gabici *et al.* 2009], [Rodríguez Marrero *et al.* 2009]. The molecular clouds provide a dense target for the CR that escape and subsequently diffuse away from the accelerator (i.e., the SNR). When both sources of CR are close with respect to the line of sight, a concave spectrum appears in gamma rays, reflecting the shape of the underlying CRs. This alternative V-shaped spectrum of CRs was thouroghly studied in [Gabici *et al.* 2009].

A hadronic scenario, where gamma rays mainly appear as a result of neutral pion decay produced in *pp* interactions, would be favoured if spatial correlation were found between TeV gamma rays and dense gas. A molecular cloud, situated close to a SNR, would appear illuminated by the CR escaping the SNR and produce gamma rays. This association was already presented as the possible source of unidentified TeV sources detected by ground based Cherenkov telescopes [Gabici & Aharonian 2007]. The model explored in [Gabici *et al.* 2009] includes not only the hadronically produced photons, but also the secondary electrons generated in the cloud, together with the bremsstrahlung and IC emission. The diffusion coefficient inside the cloud is assumed to be similar to the Galactic one, in order to have a free penetration of the CRs.

The total CR spectrum considered therein has two contributions: one coming from the Galactic background and the other from the CRs that escape the accelerator. The first contribution is characterized by a steep spectrum that peaks in the GeV energy region, and it is not supposed to change with time. On the other hand, the runaway CRs will be variable in time and their spectrum is hard. At the highest energies, in the TeV range, this second peak decreases and moves to lower energies. This effect comes from the fact that CRs diffuse earlier and faster away from the accelerator at PeV energies than at lower energies (GeVs, TeVs). Taking into account both contributions, the CR spectrum acquires a concave shape, which is reflected in gamma rays. The afforedmentioned evolution in time is proportional to the square of the separation between the molecular cloud and the SNR. The CR spectrum presents a cut-off, which position depends on the last particles with energy enough that have time to reach the cloud.

The detection of such a shape could prove the presence of a CR accelerator close to molecular clouds, and maybe clarify the nature of up-to-now unidentified TeV sources. One possibility to achieve this goal would be covering the whole

energy range with joint observations of *Fermi* and the next generation of ground based Cherenkov telescopes (CTA). An initial study on this direction is explored in Chapter 8.

Chapter 3

Applications to the environment of SNR IC443: Pre-*Fermi* study

Contents

Of all supernova remnants (SNRs) that were found to be positionally coincident with gamma-ray sources in the MeV range in the EGRET era, IC 443 was one of the most appealing for subsequent observations with higher sensitivity instruments (see the case-by-case study by [Torres *et al.* 2003]). It was, together with W28, the only case in which the molecular environment - as mapped for instance with CO observations - showed a peak in density close by, but separated in sky projection, from the SNR center, as shown in Figure 3.1. This would allow distinguishing possible cosmic-ray (CR) diffusion effects, in case the gamma-ray emission observed would be hadronically produced. Several observations of the IC 443 environment have been made at the highest energies, and in this Chapter, these are used in the setting of a theoretical model in which CRs from the SNR IC 443 are diffusing away from it and interacting with clouds nearby. This model has been originally presented in [Torres *et al.* 2008].

3.1 IC443 placed into context

IC 443 is an asymmetric shell-type SNR with a diameter of ∼45' (e.g., [Fesen & Kirshner 1980]). Two half shells appear in optical and radio images, e.g, [Braun & Strom 1986, Leahy 2004, Lasker *et al.* 1990]. The interaction region, with evidence for multiple dense clumps, is also seen in 2MASS images, e.g. [Rho *et al.* 2001]. In radio, IC 443 has a spectral index of 0.36, and a flux density of 160 Jy at 1 GHz [Green 2004]. [Claussen *et al.* 1997] reported the presence of maser emission at 1720 MHz at $(l, b) \sim (-171.0, 2.9)$. Later on, [Hewitt *et al.* 2006] confirmed these measurements and discovered

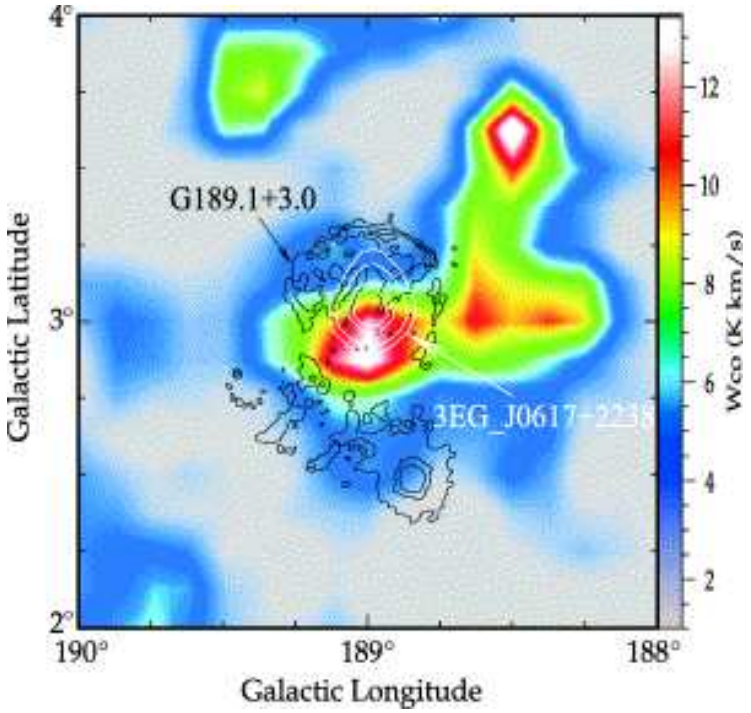

Figure 3.1: CO distribution around the remnant IC 443 (G189.1+3.0). The 3EG gamma-ray source J0617+2238 is plotted with white contours. The optical boundary of the SNR is superimposed as a black contour [Lasker *et al.* 1990]. The optical emission seems to fade in regions where CO emission increases. This indicates that the molecular material is likely located on the foreground side of the remnant, absorbing the optical radiation. Plot taken from [Torres *et al.* 2003], figure 10.

weaker maser sources in the region of interaction. IC 443 is a prominent X-ray source, observed with Rosat [Asaoka & Aschenbach 1994], ASCA [Keohane *et al.* 1997], XMM [Bocchino & Bykov 2000, Bocchino & Bykov 2001, Bocchino & Bykov 2003, Bykov *et al.* 2005, Troja *et al.* 2006], and Chandra [Olbert *et al.* 2001, Gaensler *et al.* 2006]. The works by [Troja *et al.* 2006] and [Bykov *et al.* 2008] summarize these observations. Some additional features of IC 443 are presented next, due to their relevance for the model.

Age

A small ($\sim 1000\,$yr) age was determined by [Wang *et al.* 1992] and seconded by [Asaoka & Aschenbach 1994] and [Keohane *et al.* 1997], although IC 443 is now agreed to have a middle-age of about $3 \times 10^4\,$yrs. This age has been initially advocated by [Lozinskaya 1981] and was later consistently obtained as a result of the SNR evolution model [Chevalier 1999]. Observations by [Bykov *et al.* 2008] confirm that there are a few X-ray-emitting ejecta fragments, a number much smaller than that expected for a younger SNR.

Distance

Kinematical distances from optical systemic velocities span from 0.7 to 1.5 kpc, e.g., [Lozinskaya 1981]. The assumption that the SNR is associated with a nearby HII region, S249, implies a distance of $\sim 1.5 - 2.0\,$kpc. Several authors claimed that the photometric distance is more reliable, e.g, [Rosado *et al.* 2007], and concurrently with all other works on IC 443, a distance of 1.5 kpc is adopted here (thus, 1 arcmin corresponds to 0.44 pc).

Energy of the explosion

There is no clear indicator for E_{51}, a term defined as the energy of the explosion in units of $10^{51}\,$erg. [Chevalier 1999] obtains a lower limit of $4 \times 10^{50}\,$erg, whereas lower estimations are provided by [Dickman *et al.* 1992], based on [Mufson *et al.* 1986], albeit the latter assumed an age of $\sim$5000 yr. Lacking a strong reason for other numerical assumptions, in the following model it will be assumed $E_{51} = 1$, although to be conservative, it will subsequently be assumed that only 5% of this energy is converted into relativistic CRs. Reasonable differences in this assumed value of E_{51} are not expected to have any impact on the model.

The molecular environment

[Cornett *et al.* 1977] and [De Noyer & Frerking 1981] were among the first to present detailed observations of molecular lines towards IC 443. Later on, [Dickman *et al.* 1992], [Seta *et al.* 1998], [Butt *et al.* 2003] and [Torres *et al.* 2003] among others, presented further analysis. These works conform the current picture for the environment of IC 443: a total mass of $\sim 1.1 \times 10^4$ $M_\odot$ mainly located in a quiescent cloud in front of the remnant (with linear scales of a few parsecs and densities of a few hundred particles cm^{-3}) that is absorbing optical and X-ray radiation, e.g.,

[Lasker *et al.* 1990, Troja *et al.* 2006], a scenario already put forward by [Cornett *et al.* 1977]. [Dickman *et al.* 1992] estimated that $500-2000\,\mathrm{M}_{\odot}$ are directly perturbed by the shock in the northern region of interaction, near the SNR itself. [Huang *et al.* 1986] found several clumps of molecular material along this interacting shell, with subparsec linear scales. [Rosado *et al.* 2007] found inhomogeneities down to 0.007 pc. As a first approximation to the problem, these latter inhomogeneities are neglected when considering the propagation of CRs in the ISM, i.e. it is assumed an homogeneous medium of typical ISM density where CRs diffuse. Then, the molecular mass scenario is a main giant cloud in front of the SNR containing most of the quiescent molecular material found in the region, and smaller cloud(s) totalizing the remaining mass located closer to the SNR.

3.2 MAGIC and EGRET observations of the region

The first gamma-ray emission coming from the SNR IC 443 was labeled as the EGRET source 3EG J0617+2238 [Hartman *et al.* 1999]. The EGRET flux was $(51.4 \pm 3.5) \times 10^{-8}\,\mathrm{ph\,cm^{-2}\,s^{-1}}$, with a photon spectral index of 2.01 ± 0.06 [Hartman *et al.* 1999]. The EGRET source was classified as non-variable by [Torres *et al.* 2001a, Nolan *et al.* 2003]. An independent analysis of GeV photons measured by EGRET ended up being the source GeV J0617+2237 [Lamb & Macomb 1997], also at the same location of 3EG J0617+2238 at the center of the SNR.

Later on, MAGIC observations towards IC 443 yielded the detection of J0616+225 nearby, but displaced from the center of the SNR IC 443, with centroid located at (RA,DEC)$_{J2000}$=($06^{\mathrm{h}}16^{\mathrm{m}}43^{\mathrm{s}}$, $+22°31'\ 48''$), $\pm\,0.025^{\circ}_{stat} \pm 0.017^{\circ}_{sys}$ [Albert *et al.* 2007b]. The MAGIC Collaboration showed that the very high energy (VHE) source is located at the position of a giant cloud right in front of the SNR. A simple power law was fitted to the measured spectral points:

$$\frac{\mathrm{d}N_{\gamma}}{\mathrm{d}A\mathrm{d}t\mathrm{d}E} = (1.0 \pm 0.2_{stat} \pm 0.35_{sys}) \times 10^{-11} \left(\frac{E}{0.4\mathrm{TeV}}\right)^{-3.1\pm0.3_{stat}\pm0.2_{sys}} \mathrm{cm^{-2}s^{-1}TeV^{-1}} \qquad (3.1)$$

with quoted errors being statistical. The systematic error was estimated to be 35% in flux and 0.2 in spectral index. The integral flux of MAGIC J0616+225 above 100 GeV is about 6.5% of the Crab Nebula. No variability was found along the observation time (over one year). No significant tails or extended structure was found at the MAGIC angular resolution. These results were confirmed by observations with the VERITAS array [Humensky & the VERITAS Collaboration 2008]. In addition, consistent upper limits were reported by Whipple $\mathrm{d}N_{\gamma}/(\mathrm{d}A\mathrm{d}t) < 6 \times 10^{-12}\mathrm{cm^{-2}s^{-1}}$ (0.11 Crab) above 500 GeV [Holder *et al.* 2005] and by CAT $\mathrm{d}N_{\gamma}/(\mathrm{d}A\mathrm{d}t) < 9 \times 10^{-12}\mathrm{cm^{-2}s^{-1}}$ above 250 GeV [Khelifi 2003].

MAGIC J0616+225 is displaced with respect to the position of the lower energy source 3EG J0617+2238. Indeed, the EGRET central position is located directly towards the SNR, whereas the MAGIC source is south of it, close to the 95% CL contour of the EGRET detection. As [Albert *et al.* 2007b] showed, the MAGIC source is located at the position of a giant cloud in front of the SNR. The aim of the model presented here is to show evidence of them being related. Extrapolating the spectrum of the EGRET source into the VHE regime, a higher flux and a harder spectrum than the one observed for MAGIC J0616+225 would be obtained, supporting the view that a direct extrapolation of this and other EGRET measurements into the VHE range is not valid [Funk *et al.* 2008].

3.3 A model for MAGIC J0616+225

A theoretical model is presented in this Chapter and the previous one, explaining the high energy phenomenology of IC 443 (see [Aharonian & Atoyan 1996, Gabici & Aharonian 2007]), placing an emphasis on the displacement between EGRET and MAGIC sources. MAGIC J0616+225 is interpreted as a delayed TeV emission of CRs diffusing from the SNR. This model is compared with other contemporary studies, together with a discussion on how it can be tested using observations with the *Fermi*-LAT instrument (at that time still to come).

The model [Torres *et al.* 2008] is based on the scenario of CR diffusion, as described in the previous Chapter. The parameters have been adjusted here for this specific source. CRs are accelerated at the SNR site and end up interacting with the nuclei present in the interestellar medium (ISM), producing a set of particles, including both charged and neutral pions. Gamma rays are generated through π_0-decay. The CR spectrum of the protons is given by a distribution function that satisfies the radial-temporal-energy dependent diffusion equation of [Ginzburg & Syrovatskii 1964]. Details on this issue are given in Chapter 2. Two assumptions are considered: a diffusion coefficient dependent only on the energy, $\mathrm{D(E)} \propto E^{-\delta}$, and a power-law for the distribution function of the injected proton spectrum ($\propto E^{-\alpha}$). Both impulsive and continuous injection of CR protons from the accelerator are considered (equations 2.5 and 2.7) in the following results. Finally, $\alpha = 2.2$ is assumed.

3.3.1 Results of the model

Figure 3.2 shows the current CR spectrum generated by IC 443 at two different distances from the accelerator, 10 (solid) and 30 (dashed) pc. The SNR is considered both as a continuous and an impulsive accelerator. In the continuous case, a relativistic proton power of $L_p = 5 \times 10^{37}\,\mathrm{erg\,s^{-1}}$ is assumed, and the proton luminosity is such that the energy injected into relativistic CRs through the SNR age is 5×10^{49} erg. If an impulsive injector is considered, then it has the same total power but the injection of high energy particles occur in a much shorter timescale than the SNR age. The horizontal line in Figure 3.2 marks the CR spectrum near Earth,

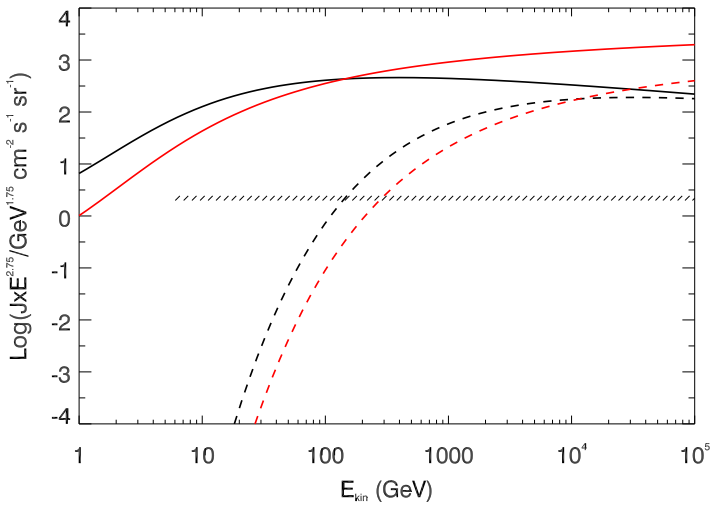

Figure 3.2: CR spectrum generated by IC 443 at two different distances, 10 (solid) and 30 (dashed) pc, at the age of the SNR. Two types of accelerator are considered, one providing a continuous injection (black) and other providing a more impulsive injection of CRs (red). The horizontal line marks the CR spectrum near the Earth. The Y-axis units have been chosen to emphasize the excess of CRs in the SNR environment.

so that the excess of CRs in the SNR environment can be seen. For this case, the diffusion coefficient at 10 GeV, D_{10}, was chosen to be $10^{26}\,\mathrm{cm}^2\,\mathrm{s}^{-1}$, with $\delta = 0.5$. CRs propagate through the ISM, which is assumed to have a typical density, e.g. $n_{ISM} = 0.5, 1, 5$, and $10\,\mathrm{cm}^{-3}$. In the scale of Figure 3.2, curves for this set of values would be superimposed, so that n_{ISM} becomes an irrelevant parameter in this range. The reason for this is that the timescale for nuclear loss τ_{pp}, obtained with the densities considered for the ISM, is orders of magnitude larger than the age of the accelerator. Differences between the different kind of accelerators assumed are also minimal for the SNR parameters.

Figure 3.3 shows the result for the gamma-ray emission coming from the cloud located at the position of the MAGIC source, when it is assumed that the source lies at different distances in front of IC 443. The giant cloud mass is assumed (consistently with observations) to be $8000\,\mathrm{M}_\odot$. The accelerator properties and power of IC 443 are those shown in Figure 3.2, for each case. Fluxes are given for an ISM propagation in a medium of $n = 1\,\mathrm{cm}^{-3}$, although this is not a relevant parameter, as it has been discussed beforehand. Clouds located from ∼20 to ∼30 pc produce an acceptable match to MAGIC data. In the case of a more impulsive accelerator, the VHE predicted spectra is slightly steeper than that produced in the continuous case at the same distance, providing a correspondingly better fit to the MAGIC spectrum. Figure 3.3 also shows, apart from MAGIC data, EGRET measurements of the neighborhood of IC 443. As it has been stated previously, these two sources are not located at the same place, highlighted with different symbols in

the plot. Figure 3.3 shows that there is plenty of room for a cloud the size of the one detected in front of IC 443 to generate the MAGIC source and not a co-spatial EGRET detection.

The existence of a VHE source without a counterpart at lower energies is the result of diffusion of the high-energy CRs from the SNR shock, which is an energy dependent process leading to an increasing deficit of low energy protons as the distance from the accelerator becomes larger. To clarify this assertion, and since the solution to the diffusion-loss equation is a function of time, the evolution of the flux along the age of the SNR is shown in Figure 3.4. The integrated photon flux coming from the position of the giant cloud is presented as a function of time above 100 MeV and 100 GeV in the impulsive case. Different qualities of the accelerator (impulsive or continuous) produce a rather comparable picture. At the age of the SNR, *Fermi* is predicted to see a source only for the closest separations. On the contrary, the integrated photon fluxes above 100 GeV present minimal deviations, and a MAGIC source is always expected.

Figure 3.3 also presents the results of this theoretical model focusing in the energy range of EGRET. At these low energies, the CR spectrum interacting with a local-to-the-SNR cloud is obtained assuming an average distance of interaction of $3 - 4\,\mathrm{pc}$. A few hundred $\mathrm{M}_\odot$ located at this distance ($\sim$700 $\mathrm{M}_\odot$ in the case of an impulsive, and $\sim$300 $\mathrm{M}_\odot$ for a continuous case) produce an excellent match to the EGRET data, without generating a co-spatial MAGIC source. As defended in [Gaisser *et al.* 1998], the lowest energy data points in the EGRET range (below 100 MeV) are produced by bremsstrahlung of accelerated electrons.

The present model imposes some constraints provided by the observed phenomenology, like e.g., the molecular environment and the position of the gamma-ray sources. One of the consequences is that D_{10} should be low, of the order of $10^{26}\,\mathrm{cm}^2\,\mathrm{s}^{-1}$, whereas the characteristic value on the Galaxy is $\sim 10^{28}\,\mathrm{cm}^2\,\mathrm{s}^{-1}$. By varying the diffusion coefficient, its influence in the results can be studied. If the separation between the giant cloud and the SNR is > 10 pc, a slower diffusion ($D_{10} > 10^{26}\,\mathrm{cm}^2\,\mathrm{s}^{-1}$) would not allow sufficient high energy particles to reach the target material; thus, the MAGIC source would not be there. On the other hand, if the separation between the main cloud and the SNR is $< 10\,\mathrm{pc}$, the EGRET source would have been detected at the position of the cloud, which is not the case. The value of D_{10} established in this study, at 1.5 kpc from Earth, has been defined by combining MAGIC and EGRET observations. Such low values of D_{10} are expected in dense regions of ISM [Ormes *et al.* 1988, Gabici & Aharonian 2007].

3.4 Discussion

In this section, the discussed model is placed in the context of others. [Bykov *et al.* 2000] suggested that the GeV emission seen towards IC 443 is mostly due to relativistic bremsstrahlung. As noted by [Butt *et al.* 2003], who already favor a hadronic emission of gamma-rays, the synchrotron radio emission seen towards the

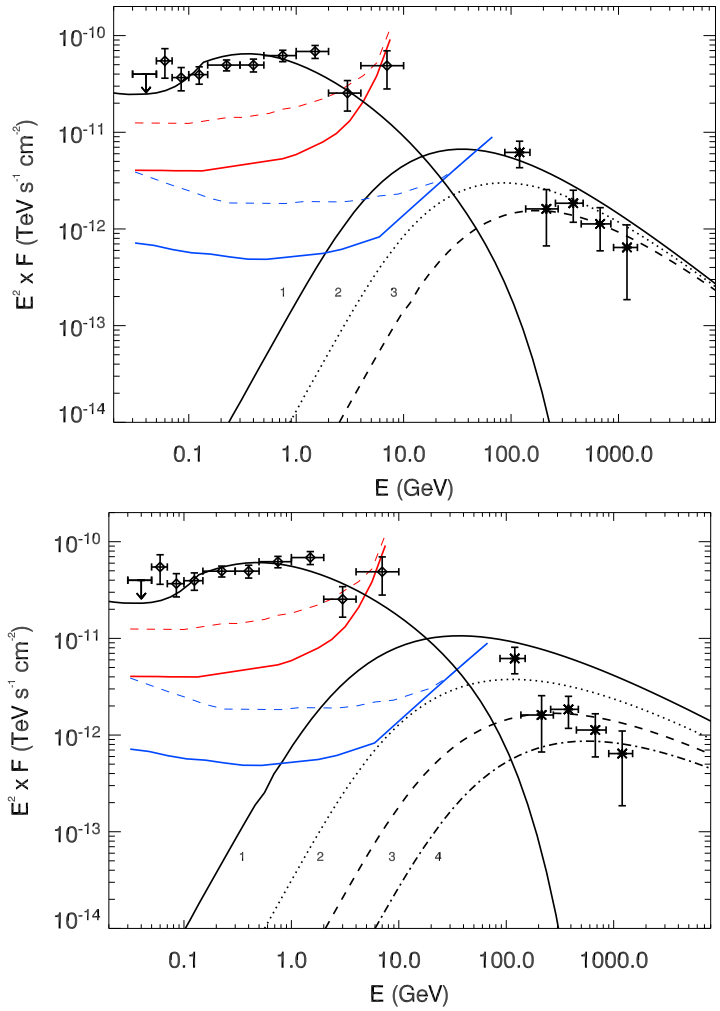

Figure 3.3: MAGIC and EGRET measurement of the neighborhood of IC 443 (stars and squares, respectively) as compared with model predictions. The top (bottom) panel shows the results for an impulsive (continuous) case. At the MAGIC energy range, the top panel curves show the predictions for a cloud of 8000 $M_\odot$ located at 20 (1), 25 (2), and 30 (3) pc, whereas they correspond to 15 (1), 20 (2), 25 (3), and 30 (4) pc in the bottom panel. At lower energies, the curve shows the prediction for a few hundred $M_\odot$ located at $3 - 4$ pc. The EGRET sensitivity curves (in red) are shown for the whole lifetime of the mission for the Galactic anti-centre (solid), which received the largest exposure time and has a lower level of diffuse gamma-ray emission, and for a typical position in the Inner Galaxy (dashed), more dominated by diffuse gamma-ray background. The *Fermi* sensitivity curves (in blue) show the simulated 1-year sky-survey sensitivity for the Galactic North pole, which corresponds to a position with low diffuse emission (solid), and for a typical position in the Inner Galaxy (dashed). These curves were taken from http://www-glast.slac.stanford.edu/software/IS/glast_latperformance.html. From [Rodríguez Marrero *et al.* 2009].

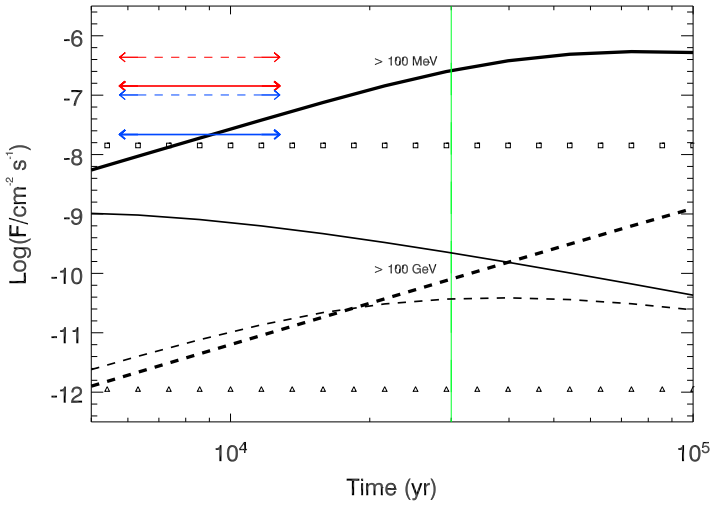

Figure 3.4: Integrated photon flux as a function of time above 100 MeV and 100 GeV, solid (dashed) lines correspond to the case of the cloud located at 10 (30) pc. The horizontal lines represent the values of integrated fluxes in the case that the CR spectrum interacting with the cloud is the one found near Earth. The vertical line stands for the SNR age. EGRET and *Fermi* – initially predicted – integral sensitivity are shown, consistent in value and color coding with those in Figure 3.3.

rim of the SNR and the centrally located EGRET source must then be associated. Judging from the localization of the multiwavelength emissions, this does not seem to be the case. An unavoidable (but subdominant at high energies) bremsstrahlung component coming from primary and secondary electrons can however play a role at the lowest energies in the EGRET range, as already shown by [Gaisser *et al.* 1998] and Figure 3.3.

[Bocchino & Bykov 2001] suggested that the systematic errors in the EGRET location contours could yield the pulsar CXOU J061705.3+222127 discovered by [Olbert *et al.* 2001] and its nebula, as the source of the GeV emission. As discussed above, this contradicts current observations. The same assumption (i.e., that the positions of the measured EGRET and GeV sources are wrong by half a degree) was taken by [Bartko & Bednarek 2008]. The pulsar nebula is also displaced from the MAGIC detection by 20 arcmin, but these authors suggested that they may be connected if a pulsar with a velocity of 250 km s^{-1} moves along the SNR age. This implies that the pulsar CXOU J061705.3+222127 should have been born at the SNR center and should have traveled to its current position while accelerating particles that interact with the cloud, giving rise to the MAGIC source. This scenario does not seem to match the observed phenomenology: the EGRET source should be on top of the current position of the pulsar and not where it actually is, and physically, it should be the result of pulsed emission (like in Vela), although pulses were not reported during the EGRET era. The only argument supporting the latter assumption is that the flux and spectrum of 3EG J0617+2238 are similar to that of PSR

1706-44, also observed by EGRET. This would apply to dozens of other EGRET sources but can not be sustained as circumstantial evidence of physical similarity, e.g., [Romero *et al.* 1999, Reimer 2001, Torres *et al.* 2001b, Torres *et al.* 2003]. Still within the same scenario, the MAGIC source is considered to be generated by inverse Compton from electrons accelerated at an initial phase of the pulsar and travelling towards the cloud. The localization and size of the MAGIC source are not explained since the difference in target photon fields in the region surrounding the cloud should not be significant, and the target field should even be larger at the position of the interacting shock in the northeast.

[Zhang & Fang 2008] presented an alternative model for IC 443, in which a fraction of the SNR shell evolves in the molecular cloud, and other in the ambient interstellar environment, encountering different matter densities. In this model, the gamma-rays observed by EGRET are mainly produced via *pp* interactions with the ambient matter in the clouds, similar to that found in the MAGIC source. Although this may sound similar to the present model, there is a key difference between them: in Zhang and Fang scenario, both EGRET and MAGIC sources should be at the same position. The reason for this lies in the fact that, in their model, the radial dependence of the CR spectrum is not considered. [Gabici & Aharonian 2007] noted in general that an old SNR cannot confine multi-TeV particles in their shells, as it has also been shown in the IC 443 results of this Chapter.

3.5 Summary

In this Chapter, MAGIC J0616+225 is found to be consistent with the interpretation of CR interactions with a giant molecular cloud lying in front of the remnant, producing no counterpart at lower energies. Moreover, the nearby EGRET source can be explained as produced by the same accelerator, and in this case, a co-spatial MAGIC source is not expected. In the present model, the displacement between EGRET and MAGIC sources has a physical origin. It is generated by the different properties of the proton spectrum at different locations, in turn produced by the diffusion of CRs from the accelerator (IC 443) to the target.

At high energies, a morphological and spectral change should come from the position of the cloud (i.e. the center of MAGIC J0616+225) towards the center of IC 443. At a morphological level, the lower the energy, the more coincident with the SNR the radiation will be detected. At a spectral level, sufficient statistics should show that the lower the gamma-ray energy the harder the spectrum is. In addition, *Fermi* LAT measurements are predicted to be sensitive enough to detect the same cloud that shines at higher energy.

All these predictions will be discussed in the following Chapter, combining the MAGIC stand-alone data with the new observations by *Fermi* and AGILE at HE, and by VERITAS at VHE. Related to this topic, preliminar observations made with the MAGIC stereo system at VHE will be presented in Chapter 9, together with prospects on the forthcoming Cherenkov Telescope Array (CTA).

Chapter 4

The GeV to TeV connection in SNR IC 443

Contents

In the previous Chapter 3, the source MAGIC J0616+225 has been interpreted as a result of delayed TeV emission of cosmic rays (CR) diffusing from the supernova remnant (SNR) IC 443 and interacting with a cloud in the foreground of the remnant. This model was used to make predictions for observations with the *Fermi* satellite. Recently, AGILE, *Fermi* LAT, and VERITAS released new results from their observations of IC 443. In this Chapter, those results are compared with the predictions of the model, exploring the GeV to TeV connection in this region. *Fermi* LAT data is used to consider the possibility of constraining the cosmic-ray diffusion features of the environment. Moreover, the cosmic-ray distributions, their interactions, and a possible detection of the SNR environment in the neutrino channel are analyzed. The study presented here was published as [Torres *et al.* 2010].

4.1 New high and very high-energy observations

Recently, the Very Energetic Radiation Imaging Telescope Array System (VERITAS) presented further observations towards IC 443 [Acciari *et al.* 2009b]. Regarding the position of the centroid, it was found to be at (RA, DEC)$_{J2000}$ = ($06^{\rm h}\,16^{\rm m}\,51^{\rm s}$, $+22^\circ\,30'\,11''$), $\pm\,0.03^\circ_{stat} \pm\,0.08^\circ_{sys}$ thus, consistent with that of MAGIC.

Evidence of a very-high-energy (VHE, $E > 100\,\mathrm{GeV}$) extended gamma-ray emission was also found. The extension derived was $0.16^\circ \pm 0.03^\circ_{stat} \pm 0.04^\circ_{sys}$. The VHE spectrum was well fit by a power law ($dN/dE = N_0 \times (E/\mathrm{TeV})^{-\Gamma}$) with a photon index of $2.99 \pm 0.38_{stat} \pm 0.3_{sys}$ and an integral flux above 300 GeV of $(4.63 \pm 0.90_{stat} \pm 0.93_{sys}) \times 10^{-12}\,\mathrm{cm}^{-2}\,\mathrm{s}^{-1}$. Thus, the spectral determination is consistent with the MAGIC measurements; both present a steep slope, with VERITAS finding a slight overall increase in the flux level. No variability of the gamma-ray emission was claimed by VERITAS either.

Moreover, AGILE results on IC 443 has been recently reported [Tavani *et al.* 2010]. AGILE discovered a distinct pattern of diffuse emission in the energy range 100 MeV–3 GeV coming from the SNR, with a prominent maximum localized in the Northeastern shell, displaced (as it was the case with EGRET) respect to the MAGIC/VERITAS sources. The latter are $\sim 0.4^o$ apart from the maximum of the AGILE emission (which is also separated from the position of the nearby pulsar wind nebula (PWN), as discussed below). Finally, *Fermi* has also recently presented an analysis of its first 11 months of observations towards the region of SNR IC 443 [Abdo *et al.* 2010g]. These results reinforce those obtained by AGILE, given the better instrument sensitivity. Therefore, *Fermi* LAT measurements will be preferably used when analyzing GeV results in this Chapter. The source has been detected in a broad range of energies, from 200 MeV up to 50 GeV, with a SED that rolls over at about 3 GeV to seemingly match in slope that found at the highest energies. The spectrum can be represented, for instance, with a broken power law with slopes of 1.93 ± 0.03 and 2.56 ± 0.11, with a break at 3.25 ± 0.6 GeV. This is one important difference with the previously discussed EGRET data. The spectral energy distribution (SED) could not unveil back then neither that the emission would maintain a hard spectrum up to such tens-of-GeV energies, nor the existence of a roll over in the spectrum at the energies found. The flux above 200 MeV resulted in $(28.5 \pm 0.7) \times 10^{-8}\,\mathrm{ph\,cm}^{-2}\,\mathrm{s}^{-1}$, thus allowing for a very significant detection in *Fermi*. The centroid of the emission is consistent with that of EGRET 3EG J0617+2238.

4.1.1 Relative localization of sources

[Abdo *et al.* 2010g] report that the centroid of the *Fermi* LAT emission is displaced more than $5 \times \theta_{68}^{error}$(MAGIC error) from that of MAGIC (J0610+225), and more than $1.5 \times \theta_{68}^{error}$ (VERITAS error) from that of the VERITAS source. These numbers are obtained assuming that the systematic and statistical errors in localization add up in quadrature, and considering the worse error of each of the pairs of measurements (*Fermi*–MAGIC, *Fermi*–VERITAS), which in both cases correspond to the imaging air Cherenkov telescopes (IACTs). The significance of the centroid separation greatly improves when a) the best measured position is considered (i.e., the error by *Fermi* LAT), for which both pairs of measurements are about 5σ away, and/or b) when only statistical errors are considered for VERITAS (the systematic errors in this latter measurement is about a factor of 3 larger than the statistics

and significantly different from all others; but of course, one can not necessarily assume it to approach the detection in the direction of the *Fermi* LAT source). Thus, albeit current measurements are not conclusive about energy dependent morphology, they are consistent with it. [Abdo *et al.* 2010g] report that the centroid of the *Fermi* LAT emission moves towards that of the VERITAS source as the energy band changes from $1 - 5\,\mathrm{GeV}$ to $5 - 50\,\mathrm{GeV}$. However, the significance of this displacement is low: only $\sim 1.5\sigma$. It might be that the angular resolution and/or sensitivity and/or the separation of the real molecular mass distribution on sky projection are not enough to distinguish when such nearby energy ranges are considered. New measurements from MAGIC (using the just-obtained stereoscopic capability) could provide continuous coverage from 50 GeV up.

4.1.2 Possible relationship between gamma-ray emission and the PWN

In all energy bands, the centroid of the correspondingly detected sources is inconsistent with the PWN (and the putative pulsar) CXOU J061705.3+222127, discovered by [Olbert *et al.* 2001], and lying nearby. Both the 3EG and the GeV source in the catalogs of [Hartman *et al.* 1999] and [Lamb & Macomb 1997], which are co-spatial, are inconsistent with the PWN location. Similarly, the position of the PWN is separated from *Fermi* LAT source by 0.26^o, or $\sim 11\sigma$ away from the localization of the *Fermi* LAT peak.

Also at higher energies, the gamma-ray emission observed by VERITAS and MAGIC is offset from the location of the PWN by $10 - 20$ arcmin. This latter fact could be understood in case the PWN is a gamma-ray emitter, like in HESS J1825-137 [Aharonian *et al.* 2006b] or HESS J1908+063 [Aharonian *et al.* 2009] where similar offsets were found, see also [Abdo *et al.* 2010h]. The emission could be consistent with a scenario in which the VHE emission arises from inverse Compton scattering off electrons accelerated early in the PWN's life.

However, if one would assume that the PWN CXOU J061705.3+222127 is producing the emission (note that pulsed radiation from this object has not been found at any frequency), the highest energy TeV-band radiation should peak there: it could be extended, but due to losses, as the energy increases, the emission should be maximum towards the PWN. Moreover, the GeV radiation should be an unresolved pulsar emission: it should also peak there and be pulsed, see [Bartko & Bednarek 2008]. Therefore, *Fermi*/VERITAS data guarantee that the GeV and TeV emissions detected do not originate in the PWN.

4.2 Comparison with nominal model

First of all, the predictions made in Chapter 3 are compared to/with the most recent results obtained by VERITAS and *Fermi*. In the case of VERITAS, given that their measured SED is compatible with the earlier one obtained by MAGIC, no significant difference in the response of the models is expected. In the case of

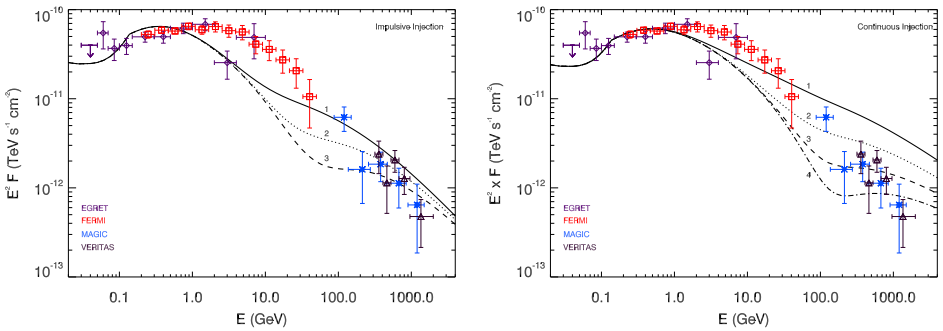

Figure 4.1: Earlier MAGIC and EGRET (stars and diamonds, respectively), and recent *Fermi* LAT and VERITAS (squares and upper trianges, respectively) measurements of the neighborhood of IC 443 as compared with model predictions for an impulsive and a continuous accelerator, as considered in Chapter 3. The nominal values of parameters for these models are the same as in Figure 3.3, although here the different contributions are summed up. See the text for details.

Fermi, the situation is different because *Fermi* LAT results have extended the energy domain of the SED much beyond what was possible for EGRET. Thus, the explored models in Chapter 3 were unconstrained for that energy range.

In the model presented in Chapter 3, IC 443 was considered both as a continuous and an impulsive accelerator, as explained in Section 3.3.1. CRs were assumed to propagate with a diffusion coefficient at 10 GeV, e.g., $D_{10} = 10^{26}\,\mathrm{cm^2\,s^{-1}}$, and $\delta = 0.5$ in a medium of typical density. In this medium, the timescale for nuclear loss τ_{pp} is orders of magnitude larger than the age of the accelerator. The nominal models also explored the possibility of having different distances between the SNR shock and the interacting clouds, together with assumptions on the molecular mass affected by the CRs. These assumptions were based on the observations of molecular lines towards the region IC 443 made by, e.g., [Cornett *et al.* 1977, De Noyer & Frerking 1981, Dickman *et al.* 1992, Seta *et al.* 1998] and [Torres *et al.* 2003]. From these studies, the overall picture emerges: a total mass of $\sim 1.1 \times 10^4$ $M_\odot$ placed mostly at the foreground of the remnant, since the optical and X-ray radiation appear absorbed, with smaller cloud(s) located closer to the SNR. However, there are several uncertainties at play: whether there is one or several foreground clouds, the distance between the foreground cloud(s) and the SNR shell, the number and specific location(s) of the foreground cloud(s), and their mass distribution if more than one cloud is present. *Fermi* LAT data is expected to elucidate some of these parameters by a posteriori comparison with data, regarding not only the molecular environment but also the diffusion properties of the medium.

Figure 4.1 shows the result of the nominal model predictions (theoretical curves are exactly as in Figure 3.3, from Chapter 3, except for the fact that all contributions are summed up), compared with the newest data. The electron bremsstrahlung contribution, visible only at the smallest energies, can hardly explain

the whole of the observed IC 443 gamma-ray emission, a conclusion also reached by [Abdo *et al.* 2010g], and previously by [Butt *et al.* 2003] but with EGRET data. In the present model, the bremsstrahlung contribution is considered for primary particles with a proton to electron ratio of 150, following [Torres 2004] formulae. The cross section of bremsstrahlung and pion production are similar at the *Fermi* LAT range. Hence, the bremsstrahlung to pion ratio can be approximated with the ratio of CR electron and proton fluxes (which is almost 0.01). The observed gamma-ray flux is too high for bremsstrahlung to be the dominant process, although it has likely a non-negligible contribution below 200 MeV.

The curves in Figure 4.1 are based on assuming 8000 $M_\odot$ at the different distances enumerated in the plot and a few hundred $M_\odot$ located closer to the SNR (as for example, $\sim$700 $M_\odot$ for the case of an impulsive, and $\sim$300 $M_\odot$ for a continuous case, located at $3-4$ pc). What is striking to the eye is that the previous good agreement between theory and the observations performed by EGRET and MAGIC (and obviously VERITAS), particularly in the case of the impulsive accelerator, is now in disagreement with *Fermi* LAT data. The spectrum is harder than that suggested by EGRET, presenting an almost flat SED up to 10 GeV, with a roll-over in the spectrum between 10 and 100 GeV. The models in Chapter 3 are unable to reproduce the details of these trends. In fact, the case of continuous acceleration was already disfavored in Chapter 3 due to both, the middle age of the remnant and the behavior at the highest energies, which were producing a much harder SED than that observed. This case is now definitely ruled out, and will not be considered any further. In the case of impulsive acceleration, it is at the earlier unexplored region of energies, between 10 and 100 GeV, where significant deviations between theory and data are found. There is no model among the ones explored above which can accommodate at the same time a SED that is both, sufficiently steep at VHEs to concur with MAGIC/VERITAS observations and sufficiently flat at lower energies to concur with *Fermi* LAT data.

4.3 Using *Fermi* LAT data to constrain model parameters

Although the previous section seems to present a difficult-to-solve failure of the scenario, the actual failure comes only from some numerical values of parameters. In particular, differences in the location and masses of the overtaken clouds can move the peaks of their corresponding contributions, see [Aharonian & Atoyan 1996, Gabici & Aharonian 2007, Rodríguez Marrero *et al.* 2009] and this Chapter for detailed analysis of the dependences. Certainly, kinematic distance estimations are not accurate enough to obtain the exact separation of the cloud(s) from the SNR shell. Thus, *Fermi* observations hold the key to make some precisions on the assumptions made in this sense, given that the unknowns can affect the final results on the predicted spectra. Using *Fermi* LAT results, we find that a closer less massive giant cloud (e.g., $\sim$5300 $M_\odot$ at 10 pc) is being overtaken by CRs diffusing away

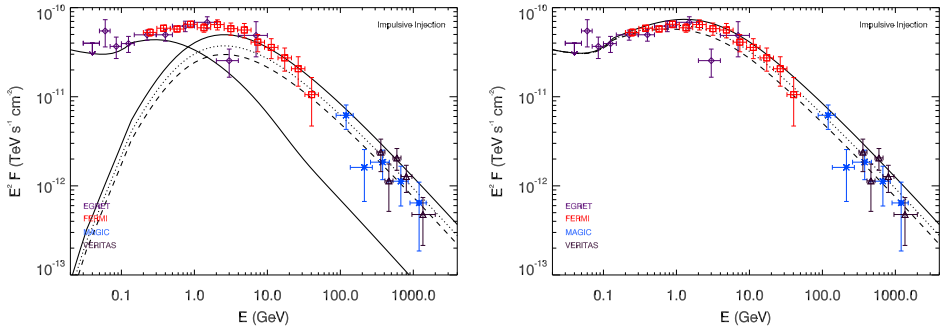

Figure 4.2: As in Figure 4.1, summed results (right) are produced by two main components (left) coming from a giant cloud in front of the SNR, which is at least partially overtaken by the diffusing cosmic rays ($\sim$5300 $M_\odot$ at 10 pc) and a closer-to-the-shell cloud (at 4 pc, with 350 $M_\odot$), similar to the previous examples. The dotted and dashed lines at the VHE range corresponds to different normalizations, which can also be understood as interacting masses of $\sim$4000 and $\sim$3200 $M_\odot$ at the same distance. The diffusion coefficient is as before, $D_{10} = 10^{26}\,\mathrm{cm^2\,s^{-1}}$.

from IC 443. In addition, a smaller amount of molecular material in cloud(s) closer to the SNR shell (e.g., at 4 pc, with 350 $M_\odot$). The combination of both produce an excellent match to the whole range of observations, see Figure 4.2. A smaller amount of mass – than the total quoted: $1.1 \times 10^4\,M_\odot$ – in the foreground giant molecular cloud(s) being overtaken by diffusing CRs from IC 443 is perfectly possible, despite the various uncertainties in the absolute position of the cloud, its real number, and the velocity model used; and essentially, due to the fact that the total amount of mass corresponds to a larger projected sky area. Whereas this implies no substantial change to the model, it allows a match with data at all high-energy frequencies, as shown in Figure 4.2. In this Figure, the non-solid lines at the VHE range corresponds to different normalizations, which can also be interpreted as different interacting masses, of $\sim$4000 and $\sim$3200 $M_\odot$ (dotted and dashed, respectively), at the same distance. The diffusion coefficient is as before, $D_{10} = 10^{26}\,\mathrm{cm^2\,s^{-1}}$.

4.4 Cosmic-ray distributions and their effects

In Figure 4.3, the distribution of CRs appears as generated by the impulsive accelerator (IC 443) at the two different distances considered for the molecular mass distribution in the model of Figure 4.2 (solid black line). Moreover, the ratio of these distributions with respect to Earth's cosmic-ray distribution is also shown. The key issue extracted from these plots is that the cosmic-ray energy density is greatly enhanced – along the energy range of interest – as compared to that in our vicinity, described with a spectrum of the form $J_\odot(E) \sim 2.2 E_{\mathrm{GeV}}^{-2.75}\,\mathrm{cm^{-2}\,GeV^{-1}\,s^{-1}\,sr^{-1}}$ (e.g. [Dermer 1986]. Another relevant aspect is that significant deviations of the cosmic-ray density are obtained when the diffusion is slower (i.e., D_{10} is larger). At a fixed SNR age of 30 kyrs, increasing D_{10} produces a displacement of the gamma-

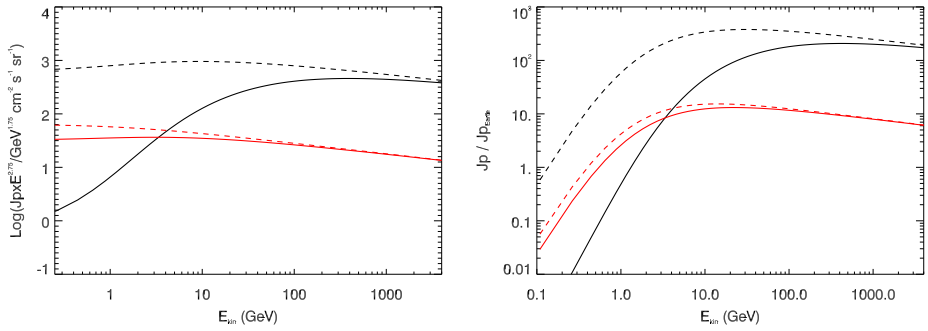

Figure 4.3: Cosmic-ray spectrum generated by the impulsive accelerator (IC 443) at the two different cloud distances considered in Figure 4.2: 10 (solid) and 4 pc (dashed), at the age of the SNR, as a function of energy. Different colors show results for different diffusion coefficients (black, $D_{10} = 10^{26}\,\mathrm{cm^2\,s^{-1}}$; and red, $D_{10} = 10^{27}\,\mathrm{cm^2\,s^{-1}}$). The right panel shows the ratio between the cosmic-ray spectra of the left panel, and the cosmic-ray spectrum near Earth, as a function of energy.

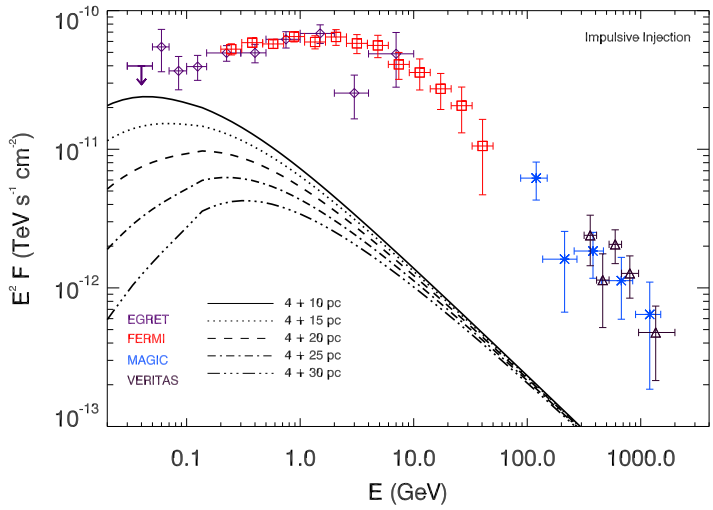

Figure 4.4: Example of a model output with $D_{10} = 10^{27}\,\mathrm{cm^2\,s^{-1}}$. The different curves represent results for the location of the giant molecular cloud at 10, 15, 20, 25, 30 pc from the SNR shell, whereas the close-to-the-SNR cloud is at 4 pc. Neither in this nor in any other of the studied models, the VHE source spectrum can be reproduced by varying the parameters with such a diffusion coefficient scale. Furthermore, the resulting SED in the *Fermi* LAT range is not hard enough to match the data.

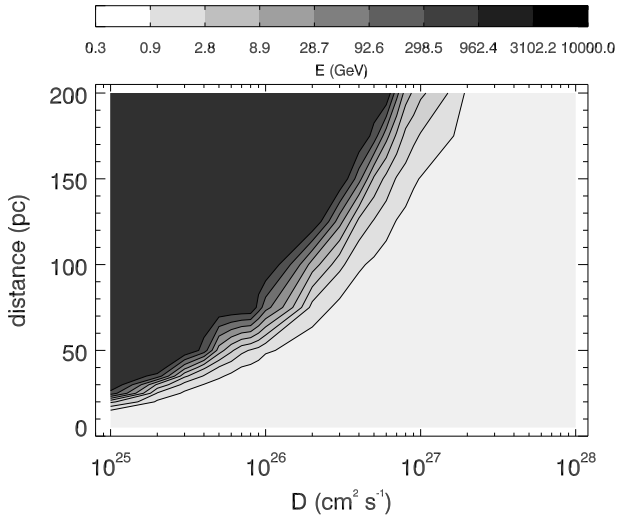

Figure 4.5: Contour plot depicting the position of the peak of the SED generated by a 30 kyrs old injection interacting with clouds at different distances, for a range of diffusion coefficient scale, D_{10}.

ray emission prediction to smaller energies, typically, up to $D_{10} > D_{transition}$, where peaks generated by clouds at large separation (e.g, 100 pc) shift up and peaks generated by clouds at smaller separation (e.g., 10 pc) shift down in the SED (e.g., [Rodríguez Marrero *et al.* 2009] and references therein). This fact implies that, for the range of distances considered for the giant and close-to-the-SNR molecular clouds (10 – 30 pc and 2 – 6 pc, respectively), there is no solution with large D_{10} able to fit the whole range of data. This was already suggested in Chapter 3, where it was possible to set a strong constraint over the diffusion timescale, using MAGIC data only. D_{10} should be of the order of $10^{26}\,\mathrm{cm^2\,s^{-1}}$. If the separation between the giant cloud and the SNR is greater than 10 pc, a slower diffusion would not allow sufficient high energy particles to reach the target material and it would be impossible to reproduce the VHE data. On the other hand, the separation between the foreground cloud(s) and the SNR shell can not be much smaller than 10 pc, given that there is a displacement between the centroid positions of EGRET/*Fermi* and VHE sources and that molecular material is absorbing lower frequency emission from the remnant. The current *Fermi* LAT data emphasizes this conclusion. Figure 4.4 shows an example of a full range of models constructed with $D_{10} = 10^{27}\,\mathrm{cm^2\,s^{-1}}$, and its disagreement with data. Note that even if the curves are rescaled and assuming, for instance, a much higher molecular mass (which would itself be in conflict with multi-frequency observations), it is not possible to obtain a good fit across the whole range of observations.

Figure 4.5 presents a contour plot of the energy at which the maximum of the SED is found for the cases of impulsive acceleration of CRs. The age corresponds to a SNR like IC 443, and the CRs are interacting with clouds at different distances, for a range of diffusion coefficient scale, D_{10}, from 10^{25} to $10^{27}\,\mathrm{cm^2\,s^{-1}}$. This plot is useful

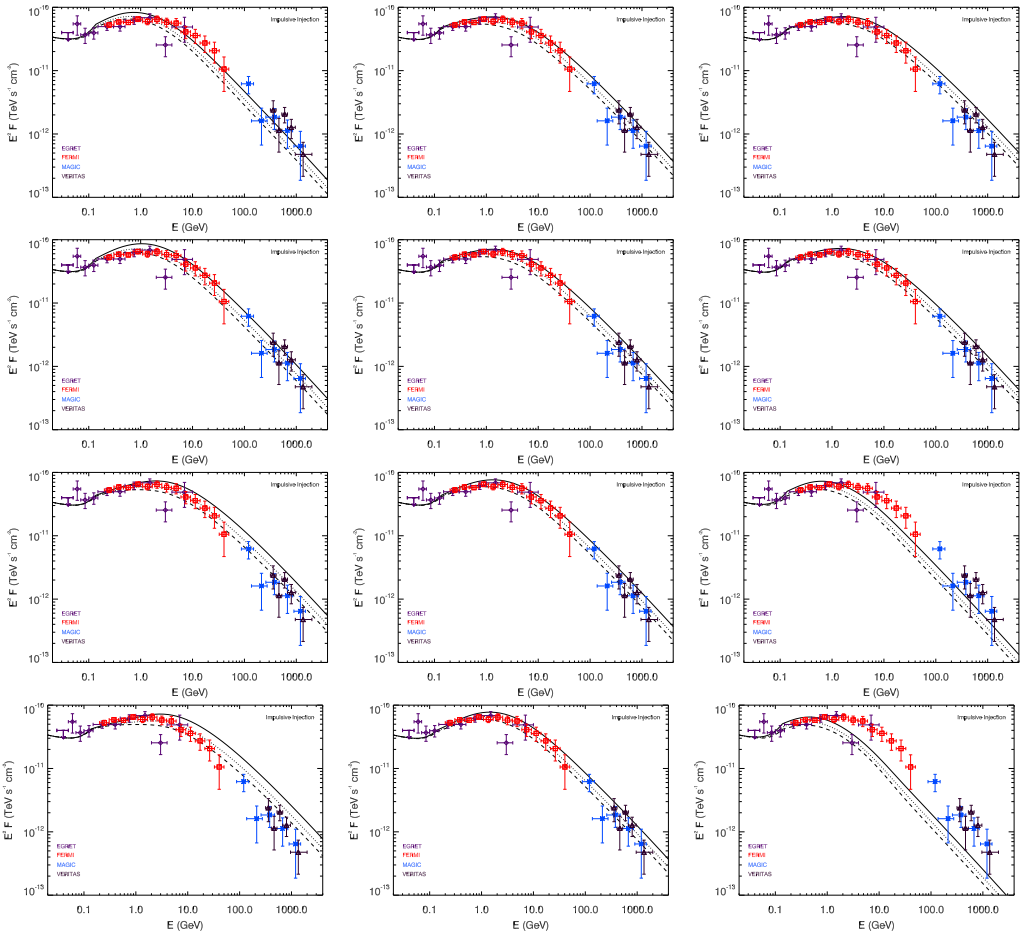

Figure 4.6: Examples of solutions around the discussed main values, exploring the degeneracies (or uncertainties) in determining the numerical values of model parameters matching the observational data. The order of the panels in this plot, top to bottom and left to right, corresponds with the parameters described in Table 4.5, being each column one of the three groups therein. Adapted from [Torres *et al.* 2010].

to understand which is the favored solution and its degree of uncertainty/degeneracy. In order to fit the combined MAGIC/VERITAS and *Fermi* LAT data, a giant cloud is needed to produce a peak at about the *Fermi* spectral turnover. This implies that, by looking at the plot, there is either a very large separation between the cloud and the SNR shell for a high D_{10}, or a smaller distance with a faster diffusion, i.e. a lower D_{10}. The first option is discarded because it is not possible to fit the VHE data in this configuration, whereas the latter is the favored solution in this study.

4.5 Degeneracies and uncertainties

Figure 4.6 explores the range of parameters around the solutions matching the observational data. The aim is to show the degeneracies (or uncertainties) within

which this model provides a reasonable agreement with observations. Given the distances to each of the clouds, the values of masses and diffusion coefficients used in Figure 4.6 to obtain good data-matching are displayed in Table 4.5. Fits could be considered good for distances to the giant molecular cloud, D_{GMC}, between 9 and 11 pc. For an average distance of 10 pc, the mass in the close-to-the-SNR cloud (or clouds) decreases the farther the cloud is, as shown in the second column of Figure 4.6. For these cases, good solutions with D_{GMC} between 9 and 11 pc (i.e., 10 pc) can always be found, adjusting other parameters, an example of which appears in the second column of Figure 4.6. The average model explored in Figure 4.2 corresponds to the model 3 in Table 4.5 with: $D_{GMC} = 10$ pc, $d_{snr} = 4$ pc, and the three curves constructed with ∼5300, ∼4000, ∼3200 $M_\odot$, and $M_{snr} = 350\,M_\odot$.

The results in the third column of Figure 4.6 and bottom group in Table 4.5 show that the smaller the diffusion coefficient, the worse is the fit at VHEs, overpredicting the data. Correcting this via a mass adjustment would in turn make for a poor fit at lower energies. Thanks to this, a lower limit to the diffusion coefficient D_{10} can be imposed. On the other hand, when D_{10} increases, the VHE spectra is quickly underpredicted, and again, correcting this via a mass adjustment would not provide a good fit at lower energies.

In summary, in order for this model to match the multi-frequency observational data, the range of variation in the parameters becomes constrained as $9 \lesssim D_{GMC} \lesssim 11$ pc; $3 \lesssim d_{snr} \lesssim 6$ pc, and $D_{10} \sim 10^{26}\,\mathrm{cm^2\,s^{-1}}$. Therefore, these parameters constitute a direct estimation of D_{10} and the molecular environment in the IC 443 vicinity, under the assumed validity of this model.

As mentioned before, the gamma-ray emissivity was assumed to be constant within the clouds; i.e., there is no significant cosmic-ray gradient in the target. This assumption is an approximation, and it improves whenever the size of the cloud is less than the distance to the accelerator and the diffusion coefficients inside and outside the cloud are not significantly different (or even if they are, the proton-proton timescale is larger than the time it takes for cosmic rays to overtake the whole cloud). In the case of IC 443, these conditions can be accommodated for the solutions in Table 4.5, except perhaps for the very massive cloud located close to the SNR at d_{snr}=2 pc. For this massive close-to-the-SNR cloud, it would imply an average density higher than that usually found, although even this might also be possible given the small scale clumps found therein, see e.g., [Rosado *et al.* 2007].

4.5.1 Influence of the δ-parameter

In addition, other parameters of the model are explored, particularly those influencing the way in which the diffusion coefficient varies with energy (the parameter δ), or the injection spectrum of cosmic rays (referred to as α). Their corresponding values appear to be rather constrained. For instance, the δ parameter is expected to be around $\delta = 0.4 - 0.7$, e.g., [Berezinskii *et al.* 1990], and a typical value of 0.5 is usually assumed. Figure 4.7 gives account on how small variations in δ change the slope of good-fitting solutions to the high and very-high energy data. One can see

Table 4.1: Main model parameters for solutions shown in Figure 4.6, except model 3, which instead is shown in Figure 4.2. D_{GMC} and d_{snr} are the distance to the GMC and the closer-to-the-SNR molecular clouds. The three quoted f values define $M_{GMC} = (1/f)\ 8000\,\mathrm{M}_\odot$. The three groups explore different degeneracies: in the position of the GMC, in the position of the smaller cloud, and on the diffusion coefficient.

Model	D_{GMC} pc	d_{snr} pc	D_{10} $\mathrm{cm^2\ s^{-1}}$	f ...	M_{snr} $\mathrm{M}_\odot$
1	8	4	10^{26}	3.0 – 4.0 – 5.0	350
2	9	4	10^{26}	1.8 – 2.5 – 3.2	350
3	10	4	10^{26}	1.5 – 2.0 – 2.5	350
4	11	4	10^{26}	1.0 – 1.4 – 1.8	350
5	12	4	10^{26}	0.7 – 1.0 – 1.3	350
6	10	2	10^{26}	1.5 – 2.0 – 2.5	1750
7	10	3	10^{26}	1.5 – 2.0 – 2.5	580
8	10	5	10^{26}	1.5 – 2.0 – 2.5	250
9	10	6	10^{26}	1.5 – 2.0 – 2.5	195
10	10	4	8×10^{25}	1.5 – 2.0 – 2.5	350
11	10	4	9×10^{25}	1.5 – 2.0 – 2.5	350
12	10	4	2×10^{26}	1.5 – 2.0 – 2.5	350
13	10	4	3×10^{26}	1.5 – 2.0 – 2.5	350

that for steeper δ-parameters, steeper gamma-ray spectra are found. If the masses of the molecular clouds are maintained and δ is larger, in order to have a good fit one would need an even lower D_{10} (lower than $D_{10} = 10^{26}\,\mathrm{cm^2\,s^{-1}}$, see Figure 4.6), obtaining a less plausible solution.

4.5.2 Uncertainties due to the cross section parameterization

Another check is performed to find out whether changes in the cross section parameterization can produce significant variance in the results. In the appendix of [Domingo-Santamaría & Torres 2005], the different predicted yields in gamma-rays obtained when using alternate cross section parameterizations (known back then) were compared among themselves and with the data. The considered parameterizations therein were: the one introduced by [Kamae *et al.* 2005], the δ-functional form by [Aharonian & Atoyan 1996] that is used above, the one by [Stephens & Badhwar 1981], and [Blattnig *et al.* 2000a, Blattnig *et al.* 2000b]. It was found that Kamae's and the δ-functional form matched quite well. Figure 11 of that study showed this by plotting the gamma-ray emissivities obtained with the corresponding use of each of the parameterizations of the cross section. In addition, it was also found that neither the parameterizations from [Stephens & Badhwar 1981] nor from [Blattnig *et al.* 2000a, Blattnig *et al.* 2000b] were appropriate for their use in broad-band high-energy modeling such as the one pursued here. More recently,

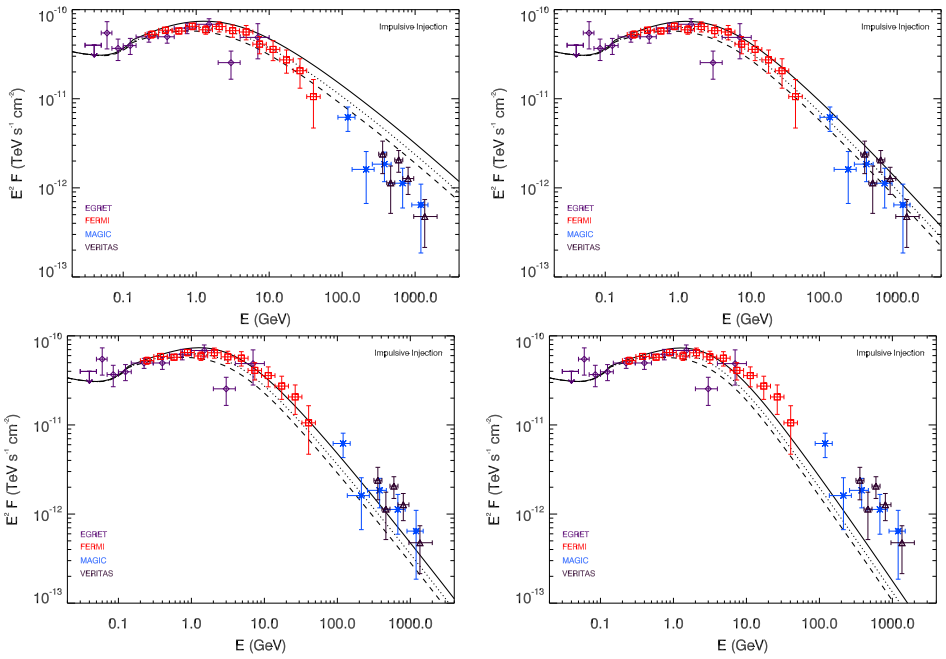

Figure 4.7: Comparing gamma-ray yields with different δ parameters, from left to right $\delta = 0.4$, 0.5, 0.6, and 0.7. The other parameters are as in Figure 4.2.

[Kelner *et al.* 2006] presented a new approach for obtaining the cross section in *pp* interactions. These authors used two shapes for representing the cross section, separated in energy. At low energies (up to 100 GeV), Kelner et al. approach uses a slightly modified but similarly-shaped δ-functional form. At higher energies, the approach is different, and presents an analytical shape that fits the results of the simulations of the energy distribution of π mesons by the SYBILL code. Figure 4.8 shows a comparison of the cross section parameterizations used in the previous figures, the δ-functional form by [Aharonian & Atoyan 1996], with that of [Kelner *et al.* 2006]. Differences are within 20%, with the δ-functional approximation being larger.

Hence, the concomitant change in flux predictions, due only to different cross section parameterizations, can be reabsorbed as part of the uncertainty in the determination of the model. Figure 4.9 shows the impact of this in two ways. The left panel shows several alternatives for the position of the large (TeV-producing) cloud in the model, located at 10, 15, and 20 pc. Here, the mass of this cloud is maintained fixed, and only the shape of the curves for different distances is important. It is clear that the change in cross section parameterization does not enable any of the previous models to be feasible. Also, it singles out a distance of about 10 pc from the SNR shell to the giant TeV-producing cloud for obtaining a good fit. The right panel assumes this distance of 10 pc and explores the uncertainty in the determination of the giant cloud mass. The parameters therein shown are 4 pc and 350 $M_\odot$ for the close-to-the-remnant cloud (the same as in the left panel), and 10 pc and 7272, 5333, 4210 $M_\odot$ for the TeV-producing giant cloud.

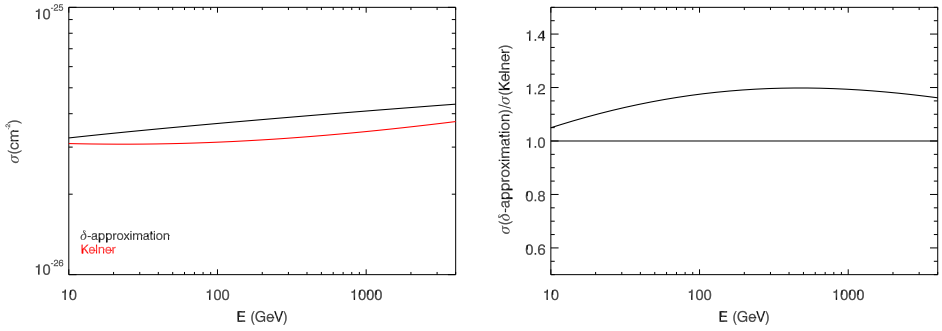

Figure 4.8: Comparison (left) and ratio (right) of the cross section parameterizations used in the previous Figures, the δ-functional form by [Aharonian & Atoyan 1996], with that of [Kelner *et al.* 2006].

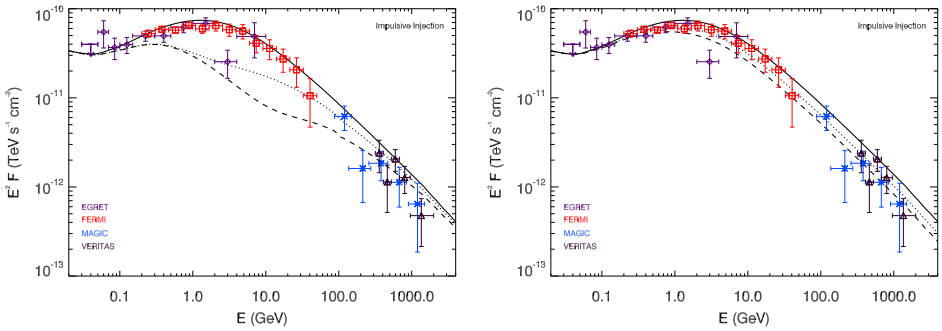

Figure 4.9: Left: Gamma-ray flux results using the [Kelner *et al.* 2006] approximation for different distances from the shell to the TeV-producing cloud, 10 (solid), 15 (dotted) and 20 (dashed) pc. The close-to-the-remnant cloud is fixed at 4 pc and contains 350 $M_\odot$ – changes in this latter value do not improve the overall fit. Right: Gamma-ray flux results using the parameterization from [Kelner *et al.* 2006] for different values of the giant cloud mass placed at a fixed distance of 10 pc (see text for details).

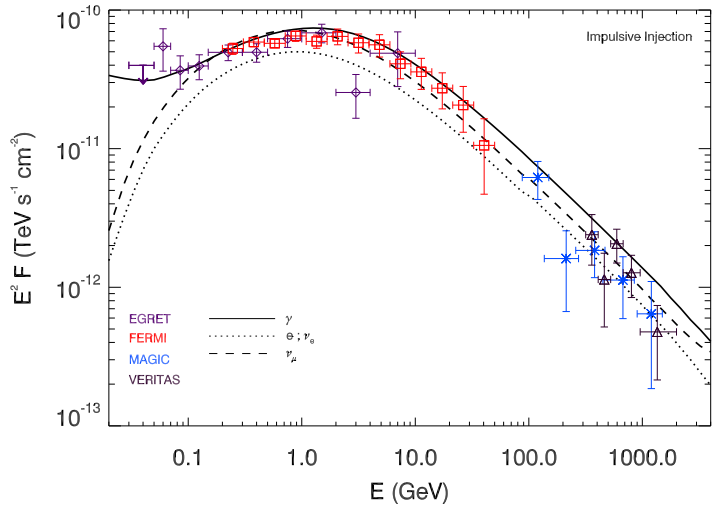

Figure 4.10: Electrons (electrons and positrons are shown together), photons and two flavors of neutrinos produced within the clouds considered nearby IC 443, using a set of parameters shown in Figure 4.9 (right panel) with mass of the giant cloud equal to 7272 $M_\odot$. The ν_μ and ν_e neutrino curves show both the particle and the anti-particle flux. Data should only be compared with the photon curve.

4.6 Computation of secondaries other than photons

Using the parameterization from [Kelner *et al.* 2006], secondary particles other than photons can be readily computed, and this is shown in Figure 4.10. [Gabici *et al.* 2009] showed, by testing a wide range of parameters, that secondary electrons produced within clouds can escape without being affected by significant losses. In other words, that the propagation time through the cloud for cosmic-ray electrons is shorter than the energy loss time for particle energies between ~ 100 MeV and few hundreds of TeV. Thus, there would be little effect of the secondary electrons produced on the non-thermal emission from the cloud. In addition, for typical densities of clouds, in the several hundred to several thousand particles per cm^3, the dominant energy loss from ~ 100 MeV and ~ 10 TeV would be bremsstrahlung and not synchrotron.

Nonetheless, a conclusive proof of the hadronic nature of the gamma-ray emission could come from the detection of neutrinos, ν. Neutrino telescopes search for up-going muons produced deep inside the Earth, and are mainly sensitive to the incoming flux of muonic neutrinos, ν_μ, and their antiparticles, $\bar{\nu}_\mu$. The finished IceCube experiment, for example, will consist on 4800 photomultipliers, arranged on 80 strings placed at depths between 1400 and 2400 m underneath the South Pole ice, e.g., [Halzen 2006]. The strings will be located in a regular space grid covering a surface area of 1 km^2. Each string will have 60 optical modules (OM) spaced 17 m apart. The number of OMs which have seen at least one photon is called the channel multiplicity, N_{ch}. Note that each photon comes from Cherenkov radiation

that has been produced by the muon which, in turn, results from the interaction of the incoming ν inside the earth and ice crust. The multiplicity threshold is set to $N_{\rm ch} = 10$, which corresponds to an energy threshold of 200 GeV. The angular resolution of IceCube will be around $\sim 0.7^\circ$.

A first estimation of the event rate of the atmospheric ν-background that will be detected in the search bin can be obtained, e.g., [Anchordoqui *et al.* 2003], as:

$$\left.\frac{dN}{dt}\right|_{\rm B} = A_{\rm eff} \int dE_\nu \, \frac{d\Phi_{\rm B}}{dE_\nu} \, P_{\nu\to\mu}(E_\nu) \, \Delta\Omega \,, \tag{4.1}$$

where $A_{\rm eff}$ is the effective area of the detector, $\Delta\Omega \approx 1.5 \times 10^{-4}$ sr is the angular size of the search bin, and $d\Phi_{\rm B}/dE_\nu \lesssim 0.2\,(E_\nu/{\rm GeV})^{-3.21}\,{\rm GeV}^{-1}\,{\rm cm}^{-2}\,{\rm s}^{-1}\,{\rm sr}^{-1}$ is the $\nu_\mu + \bar\nu_\mu$ atmospheric ν-flux [Volkova 1980, Lipari 1993]. Here, $P_{\nu\to\mu}(E_\nu)$ denotes the probability that a ν of energy E_ν on a trajectory through the detector, produces a muon. For $E_\nu \sim 1-10^3$ GeV, this probability is $\approx 3.3\times10^{-13}\,(E_\nu/{\rm GeV})^{2.2}$, whereas for $E_\nu > 1$ TeV, $P_{\nu\to\mu}(E_\nu) \approx 1.3 \times 10^{-6}\,(E_\nu/{\rm TeV})^{0.8}$ [Gaisser *et al.* 1995]. On the other hand, the ν-signal is similarly obtained as

$$\left.\frac{dN}{dt}\right|_{\rm S} = A_{\rm eff} \int dE_\nu \, (F_{\nu_\mu} + F_{\bar\nu_\mu}) \, P_{\nu\to\mu}(E_\nu) \;\; , \tag{4.2}$$

where $(F_{\nu_\mu} + F_{\bar\nu_\mu})$ is the incoming ν_μ-flux. In the previous integrals, both expressions for $P_{\nu\to\mu}(E_\nu)$ are used according to the energy, and integrated from 200 GeV up to 10 TeV. The effect of ν-oscillations is taken into account following table 2 of [Cavasinni *et al.* 2006], where the oscillation probability in the average vacuum oscillation hypothesis is given. The inter-conversion probability between flavours and between anti-flavours is assumed to be the same.

As an effect of oscillations, the flavour composition of all the expected fluxes for each flavour are within 50% of each other. Using the former equations and the secondary computation shown in Figure 4.10, the number of muon neutrino signal events is found to be 0.6 per year of observation. This is still significantly below the estimation of the number of background events, which under the previous provisions is 6.4 along the same period with the full IceCube array. If only events above 1 TeV are considered, the expected signal is $0.25\,{\rm yr}^{-1}$, and the computed background is $1.92\,{\rm yr}^{-1}$. IceCube does not seem to be able to distinguish this signal in reasonable integration times, at least within the reach of this simplified treatment of the detector.

4.7 Concluding remarks

The recent observations of the IC 443 environment made by AGILE, *Fermi* LAT, and VERITAS at the GeV and TeV energies, are spectrally consistent with the interpretation of cosmic-ray interactions with a giant molecular cloud lying in front of the remnant. This scenario would be producing no significant counterpart at lower energies at that location, and thus would be leading to a natural interpretation of

the displacement between the centroids of the detections at the different energy bands. Using the latest data, the diffusion characteristics in this environment were estimated, within the assumed validity and framework of this model. The results show that the diffusion coefficient is lower and the cosmic-ray density is higher than the Earth-values of both magnitudes. Uncertainties in the amount and the localization of the target molecular mass still remains. Just as well, the density at which this molecular material is found remains unknown. For instance, the uncertainty in the cosmic-ray-overtaken mass discussed in the previous sections is about 100% for matching models at the extremes of this parameter. But even allowing for such a wide range, the model could accommodate some but not all variations in other parameters, with the values of D_{10} and distances from the SNR shell seemingly being solid constraints.

Chapter 5

Starburst galaxies

Contents

5.1 Introduction

Starburst galaxies have been anticipated as gamma-ray sources [Paglione *et al.* 1996, Blom *et al.* 1999, Torres 2004, Torres *et al.* 2004, Domingo-Santamaría & Torres 2005, Persic *et al.* 2008], provided sufficient instrumental sensitivity. Such galaxies have an enhancement both in the star formation and supernova (SN) explosion rate, and dense (gas and dust enriched) environments. These characteristics suggest that they should emit gamma rays, and their luminosity would be greater than normal galaxies. SN remnants (SNR) and shock winds from massive stars are supposed to accelerate cosmic rays (CR). Very energetic gamma rays are produced due to CRs collisions with ambient nuclei and subsequent π^0 decay. Those gamma rays can be detected both with space-born and ground-based imaging atmospheric Cherenkov telescopes.

With the arrival of the *Fermi* satellite, and the second-generation of Cherenkov telescopes (H.E.S.S., VERITAS, MAGIC) at their full potential, it is important to have the most detailed model for these astronomical objects to obtain a proper feedback from observations and improve our knowledge of the cosmic-ray population and the physical environment of nearby starbursts. Furthermore, with the recent on-going discussions [Loeb & Waxman 2006, Stecker 2007, Anchordoqui *et al.* 2008] about the starbursts contribution to the neutrino background, it is important to have consistent and detailed models of neutrino production in specific galaxies. The

assumptions made in previous studies are dissected, while observational detectability with, e.g., km^3-observatories is considered.

Recently, the detection of M82 was reported by the VERITAS collaboration, while gamma rays above hundreds of GeVs coming from the fainter NGC 253 were claimed by the H.E.S.S. collaboration. During the same epoch, the *Fermi* experiment presented the data collected at lower energies coming from the direction of both starburst galaxies [Abdo *et al.* 2010c]. Minor and reasonable variations in the parameter space of already published models [Domingo-Santamaría & Torres 2005, de Cea del Pozo *et al.* 2009b] can fully account for the high and very high energy emission coming from both galaxies, while agreeing with previous data detected from radio to infrared (IR). This Chapter presents the model that, prior to the detections, predicted the gamma-ray emission from M82 [de Cea del Pozo *et al.* 2009b], and the possible parameter variations to better acknowledge those detections [de Cea del Pozo *et al.* 2009a].

5.2 Theoretical model

The aim of this study is to obtain multi-frequency/multi-messenger predictions for the photon and neutrino emission coming from the central region of M82, where the inner starburst is located. The model seeked is intended to be consistent, with all the different components of the emission – from radio to TeV photons and neutrinos – tracked to one and the same original cosmic-ray population. This population is a consequence of all electromagnetic and hadronic channels from the primary and subsequently-produced secondary particles. With this model at hand, a range of uncertainties in the parameters can be explored, correspondingly shifting upwards or downwards the high energy end of the spectrum.

In order to perform such study, the code $\mathcal{Q}$-DIFFUSE [Torres 2004] has been adapted in several ways. $\mathcal{Q}$-DIFFUSE solves the diffusion-loss equation for electrons and protons and finds the steady state distribution for these particles subject to a complete set of losses in the interstellar medium (ISM). Subsequently, it computes secondary particles from hadronic interactions (neutral and charged pions) and Coulomb processes (electrons), and gives account of the radiation or decay products that these particles produce. Secondaries (photons, muons, neutrinos, electrons, and positrons) that are in turn produced by pion decay are also calculated. Additional pieces of the code provide the dust emissivity, and the IR-FIR photon density, which is consistently used both as target for inverse Compton scattering and for modeling the radiation at lower frequencies. For radio photons, synchrotron radiation, free-free emission, and absorption are computed using the steady distribution of electrons. Finally, and using the radiation transport equation, opacities to $\gamma\gamma$ and γZ processes, as well as absorbed gamma-ray fluxes, are calculated. The implementation of $\mathcal{Q}$-DIFFUSE includes several upgrades. Some are strictly technical, allowing for a more versatile and automatic input-output interaction. Some are physical: neutrino-production subroutines have been developed for all neutrino

channels in the decay of positively and negatively charged pions and a recent parameterization of pp interactions by [Kelner *et al.* 2006] has been used. The flow of the $\mathcal{Q}$-DIFFUSE code is shown in Figure 5.1. Several loops can be distinguished there: they are used in order to determine a self-consistent set of parameters, such that all predictions for the different bands of the electromagnetic spectrum are consistent with the data.

Previous studies of diffuse high energy emission, and of electron and positron production, with different levels of detail and aims, go back to the early years of gamma-ray astronomy. A summary of these first efforts is summarized by [Fazio 1967, Ginzburg & Syrovatskii 1964] and [Ramaty & Lingenfelter 1966], then followed by [Maraschi *et al.* 1968, Stecker 1977], among many others. Secondary particle computations have a similarly long history see, e.g., [Stecker 1970, Orth & Buffington 1976]. Relatively more recent efforts include [Drury *et al.* 1994, Moskalenko & Strong 1998, Strong & Moskalenko 1998, Markoff *et al.* 1999] and [Fatuzzo & Melia 2003]. The general ideas followed in those works were already used by [Paglione *et al.* 1996] and [Blom *et al.* 1999] when modeling nearby starbursts galaxies. On the other hand, the present study closely tracks ideas from [Brown & Marscher 1977] and [Marscher & Brown 1978], regarding their studies of close molecular clouds.

An important aspect of this approach is that it lacks detail in modeling single sources. Isolated SN explosions, or SNRs, or even the implication of those SN exploding within the wind bubbles of their progenitors and the concurrent losses in these environments are not treated by themselves. On the contrary, the emphasis lies on average properties of the whole starburst region, seen as a CR injector. Mixing these two aims would require an effort that is beyond current observational capabilities of what is known in starburst galaxies, as well as beyond what is possible for this work. Essentially, to make quantitative estimates in such small-scale detail, one would need to understand the features of each and all the SN explosions in these kind of galaxies, and model them individually and accurately. From that point (i.e., from a stacking of a source-by-source modeling), an averaged scenario could be built. This has not been achieved even for our own Galaxy. Similarly, the present approach to the modeling of the super-wind is also simple, in order to encompass it with the rest of the components of the model. See [Everett *et al.* 2008] for a more detailed analysis of the properties of the Galactic super wind, and also [Gallagher & Smith 2005].

The assumption of a uniform distribution of accelerators in the inner region of the starburst justifies having a steady state distribution therein. Also, this distribution can be computed via solving the full diffusion-loss equation. Particles with energies of 100 TeV have a range comparable to or greater than the size of the Galaxy, whereas the distances travelled by hadronic particles injected with energies of the order of tens of GeV do not exceed $1 - 2\,\mathrm{kpc}$. For electrons, the situation is even more complicated (see later in this section), due to the more significant losses they suffer. TeV-energy electrons cool down so quickly due to synchrotron and inverse Compton losses that they cannot diffuse beyond few hundred parsecs from

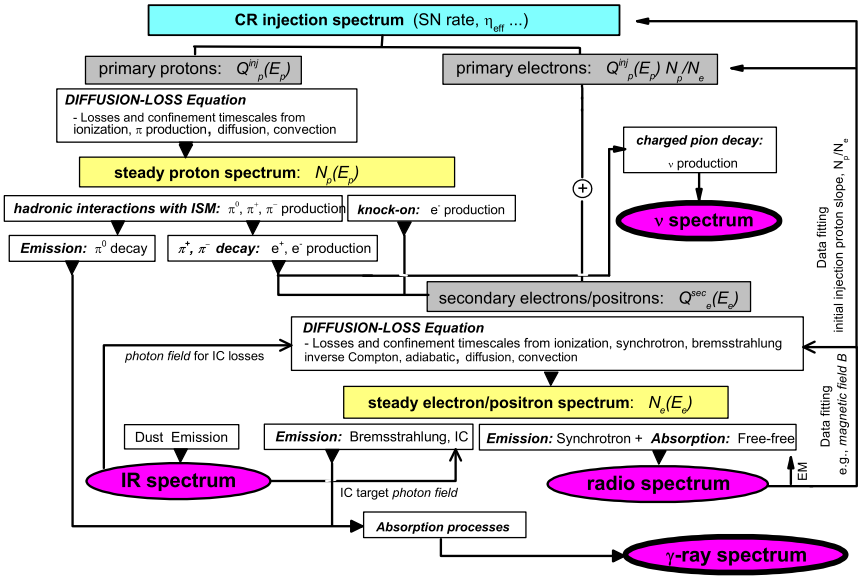

Figure 5.1: Code flow of $\mathcal{Q}$-DIFFUSE, adapted from [Torres & Domingo-Santamaría 2005] to take into account new updates developed for this work.

their injection site, for typical values of the diffusion coefficient and of the interstellar magnetic/radiation fields. Nonetheless, the limited size and compactness of the starburst region is compatible with a steady state electron distribution in that central region.

The steady-state particle distribution is computed as the result of an injection distribution being subject to losses and secondary production in the ISM. At sufficiently high energies, the injection proton emissivity is assumed to have the following form as a function of proton kinetic energies:

$$Q_{\rm inj}(E_{\rm p,\,kin}) = K \left(\frac{E_{\rm p,\,kin}}{\rm GeV}\right)^{-p} \exp\left(\frac{-E_{\rm p,\,kin}}{E_{\rm p,\,cut}}\right) \tag{5.1}$$

where p is a power-law index, K is a normalization constant, $E_{\rm p,\,cut}$ is an energy cutoff in the accelerated particles that are injected (assumed as 100 TeV, with a range explored below). Units are $[Q] = {\rm GeV}^{-1}\ {\rm cm}^{-3}\ {\rm s}^{-1}$. To get a numerical initial value for the normalization, K, its value is assumed to come from the total power transferred by supernovae into CRs kinetic energy within a given volume. Thus, the supernova rate is essential to fix the level of the cosmic-ray sea:

$$\int_{E_{\rm p,\,kin,\,min}}^{E_{\rm p,\,kin,\,max}} Q_{\rm inj}(E_{\rm p,\,kin}) E_{\rm p,\,kin} dE_{\rm p,\,kin} \equiv \frac{\eta \mathcal{P} \mathcal{R}}{V}. \tag{5.2}$$

$\mathcal{R}$ is the rate of supernova explosions, V corresponds to its volume, and η is the transferred fraction of the supernova explosion power ($\mathcal{P} \sim 10^{51}$ erg) into CRs. The

average rate of power transfer is assumed to be 10%. The assumption of the p value in 5.1 is not a-priori, but rather an a posteriori choice. That choice is made in order to get a – slightly – better fit to all the multi-wavelength data, and acts as an average description of the injected cosmic-ray sea in the star forming region, where multiple nearby shocks could contribute.

As noted by [Domingo-Santamaría & Torres 2005], the distribution of cosmic rays is probably flatter at low energies, e.g., it would be given by equation (6) of [Bell 1978], correspondingly normalized. Neglecting this difference at low energy has been numerically verified to not produce any important change in the computation of secondaries, and especially on gamma-rays at the energies of interest. As in [Berezhko *et al.* 2006], electrons are assumed to be injected into the acceleration process at the shock fronts. The electron injection rate is chosen such that the electron-proton ratio is a constant to be determined from the synchrotron observations. The diffusive transport equation takes care of the changes produced after injection onto this distribution.

The diffusion-loss equation (see, e.g.,[Ginzburg & Syrovatskii 1964] p. 296; [Longair 1994], p. 279) is given by:

$$-D\bigtriangledown^2 N(E) + \frac{N(E)}{\tau(E)} - \frac{d}{dE}\left[b(E)N(E)\right] - Q(E) = -\frac{\partial N(E)}{\partial t} \tag{5.3}$$

In this equation, D is the scalar diffusion coefficient, $Q(E)$ represents the source term appropriate to the production of particles with energy E, $\tau(E)$ stands for the confinement timescale, $N(E)$ is the distribution of particles with energies in the range E and $E + dE$ per unit volume, and $b(E) = -(dE/dt)$ is the rate of loss of energy. The functions $b(E)$, $\tau(E)$, and $Q(E)$ depend on the kind of particles considered. In the steady state, $\partial N(E)/\partial t = 0$, and when the spatial dependence is considered to be irrelevant: $D\bigtriangledown^2 N(E) = 0$. Then, the diffusion-loss equation can be numerically solved by using the corresponding Green function, G, such that for any given source function or emissivity, $Q(E)$, the solution is:

$$N(E) = \int_E^{E_{\max}} dE' Q(E') G(E, E') \tag{5.4}$$

The confinement timescale will take into account that particles can be diffusing away, carried away by the collective effect of stellar winds and supernovae, or affected by pion production (for CRs). Pion losses are catastrophic, since the inelasticity of the collision is about 50%. They produce a loss timescale in the form of:

$$\tau_{\rm pp}^{-1} = \frac{(dE/dt)^{\rm pion}}{E} \tag{5.5}$$

(see, e.g., [Mannheim & Schlickeiser 1994]. Thus, in general, for energies higher than the pion production threshold:

$$\tau^{-1}(E) = \tau_D^{-1} + {\tau_c}^{-1} + \tau_{\rm pp}^{-1}. \tag{5.6}$$

The convective timescale, τ_c, is $\sim R/V$, where V is the collective wind velocity. [Strickland *et al.* 1997] found a value of $600\,\mathrm{km\,s^{-1}}$ for the wind velocity, and this value is used below. However, the response of the model to an arbitrary doubling or halving of this value has been studied. The uncertainty introduced by varying the velocity is smaller than that produced by other parameters. Finally, assuming a homogeneous distribution of accelerators in the central hundreds of parsecs of the starburst galaxy, the characteristic escape time corresponds to the homogeneous diffusion model value ([Berezinskii *et al.* 1990], p. 50-52 and 78):

$$\tau_D = \frac{R^2}{2D(E)} = \frac{\tau_0}{\beta(E/\mathrm{GeV})^\mu} \tag{5.7}$$

where β is the velocity of the particle in units of c, R is the spatial extent of the region from where particles diffuse away, and $D(E)$ is the energy-dependent diffusion coefficient, whose dependence is assumed $\propto E^\mu$ with $\mu \sim 0.5$, and τ_0 is the characteristic diffusive escape time at $\sim 1\,\mathrm{GeV}$. The results contained in this Chapter use $\tau_0 = 10\,\mathrm{Myr}$, but a range was explored to judge uncertainties. For electrons, the total rate of energy loss considered is given by the sum of that involving ionization, inverse Compton scattering, adiabatic, bremsstrahlung, and synchrotron radiation. The Klein-Nishina cross section is used.

5.3 M 82

M82 is a near starburst galaxy. It can be seen nearly edge-on (77°, [Mayya *et al.* 2005]) and has a gas content mostly concentrated in the inner 2 kpc. This galaxy presents a high luminosity both in the far infrared and X-ray domain: $10^{44}\,\mathrm{erg\,s^{-1}}$ and $10^{40}\,\mathrm{erg\,s^{-1}}$ respectively, e.g., [Ranalli *et al.* 2008].

As part of the M81 group, M82 shows hints of an encounter with some of its members 1 Gyr ago, specifically with the dwarf galaxy NGC 3077 and the former M81, materialized in an intergalactic gas bridge of 20 kpc. Up to 10 kpc above the plane of M82, galactic superwinds can be detected. Following HI streamers, the external part of the disk (>5 kpc) presents a warped form. On the other hand, the inner part (300 pc) harbours a starburst. Around this region, a molecular ring of 400 pc radius and a near-IR bar of $\sim 1\,\mathrm{kpc}$ length can be detected [Telesco *et al.* 1991]. From the tips of this bar, two symmetrical arms emerge [Mayya *et al.* 2005]. This led to a change in the morphological classification. At first, an irregular shape was assumed due to optical appearance: bright star-forming knots interspersed by dusty filaments [O'Connell & Mangano 1978]. Nowadays, it seems more likely that M82 is a SBc galaxy. [Freedman *et al.* 1994] established a distance for M81 of $3.63 \pm 0.34\,\mathrm{Mpc}$, thanks to the discovery of new Cepheids by the Hubble Space Telescope (HST) in this galaxy. A few years later, [Sakai & Madore 1999] found a distance of $3.9\ (\pm 0.3)_{random}(\pm 0.3)_{systematic}\,\mathrm{Mpc}$ for M82, based on the detection of the red giant branch stars using HST photometry. Both distances are consistent within errors, the latter is the one used in this work. The starburst region is located in

the inner part of the galaxy, with a radius of ∼300 pc, height of ∼200 pc, e.g., see [Völk *et al.* 1996] and references therein, and [Mayya *et al.* 2006]. Meanwhile, the rest of the emission extends to a thin disk up to 7 kpc, see e.g., [Persic *et al.* 2008], and references therein.

A significant amount of molecular material has been found in the central region, where most of the starburst activity is located. A discussion on the supernova explosion rate can be found in the section 5.3.2. The content of the gas mass in the whole galaxy range from $2.9\times10^9 M_\odot$ (HI) by [Crutcher *et al.* 1978] and $2.9\times10^8 M_\odot$ (H_2) by [Young & Scoville 1984] to the more recent results found by [Casasola *et al.* 2004] $7\times10^8 M_\odot$ (HI) and $1.8\times10^9 M_\odot$ (H_2), where different assumptions for distance and the normalization of luminosity were made. [Weiß *et al.* 2001] report for the starburst region around $2\times10^8 M_\odot$ (H_2), using separate methods for the determination of CO and H_2 densities. This value essentially agrees with those estimated from 450 μm dust continuum measurements [Smith *et al.* 1991] and from CO($2\rightarrow1$) intensities [Wild *et al.* 1992], and is, therefore, the one used in the determination of the uniform density for the model of this Chapter ($\sim 180\,\mathrm{cm}^{-3}$).

5.3.1 Comparison with previous studies

A natural comparison can be made between this approach and previous studies of the central starburst region of M82, in particular, [Akyüz *et al.* 1991, Völk *et al.* 1996, Paglione *et al.* 1996], and [Persic *et al.* 2008].

The earlier work made by [Akyüz *et al.* 1991] focused on gamma-ray emission at the GeV regime (integral flux above 100 MeV) and basically provides a simple order of magnitude estimation with data available at that time. [Völk *et al.* 1996] also did not provide a multi-frequency model, but rather consider only neutral pion decay from protons to obtain an order of magnitude estimation of the flux at high and very-high gamma-rays. This approach was also taken (with minor differences) by [Pavlidou & Fields 2001] and [Torres *et al.* 2004]. These studies do not include a computation of secondaries and their emission at low energies. Their aim is different than the one in the present work, which is providing a consistent model along the entire electromagnetic spectrum. The work by [Paglione *et al.* 1996] is more complex, and it was discussed in detail, in particular, when compared with results by $\mathcal{Q}$-DIFFUSE on Arp 220 and NGC 253, by [Torres 2004] and [Domingo-Santamaría & Torres 2005] respectively. There are several different physical and methodological considerations embedded in their model compared to those assumed here. Moreover, high-energy (TeV) predictions are not provided. None of these works consider neutrino emission.

The most recent study on M82, from [Persic *et al.* 2008], also differs from the present work in some key parameters and, most importantly, in the method and assumptions for the modeling. Among the physical parameters, which values are given by Persic et al., the distance (3.6 Mpc, which is actually the one to M81), the dust emissivity index ($\sigma = 1$), the proton to electron primary ratio ($N_p/N_e = 200$), the magnetic field (180 μG) and the slope of primary injection spectrum (2.4) are

all different from the ones used or derived in the present Chapter. The difference between these (latter) values in [Persic *et al.* 2008] comes from the method used to fix them. For instance, Persic et al. obtained the magnetic field by assuming equipartition with primary particles, while the magnetic field in this work is found by a multi-frequency analysis that also takes into account produced secondary particles. As Figure 5.2 (left panel) shows, the steady population of electrons that would result after solving the diffusion loss equation, injecting only primary and only secondary[1] particles, are comparable. This fact was also found in the cases of other highly-dense environments, and it implies that it is not a safe assumption to consider that the primary population dominates when computing the equipartition field.

The path of the numerical treatment by [Persic *et al.* 2008] is inverse to the one presented in this Chapter. In the former study, the normalization of the proton spectrum is fixed starting from an assumed N_p/N_e factor from equipartition, with the normalization for electrons N_e in turn obtained from the radio spectrum. In the present case, protons are the starting point, with the supernova explosions injecting primaries which are left to interact through all possible processes, producing electrons which in turn generate synchrotron emission. It is this non-negligible contribution from secondary electrons what is taken into account when computing B and N_p/N_e, in order for the data to consistently match at all frequencies (see Figure 5.1 for further clarification). Neither equipartition is a priori assumed, nor the primary electron population is a priori fixed from the radio spectrum in the present approach. Finally, neutrino emission is scaled from gamma-ray fluxes by Persic et al., whereas it is computed using correspondingly parameterized cross sections up to tertiary particles interactions in this work. The two approaches – the one herein presented and that of [Persic *et al.* 2008] – are in any case complementary and provide consistent results.

5.3.2 Results and Discussion

The steady population of protons and electrons of the starburst galaxy M82 computed in the model is shown in Figure 5.2 (right), where a power-law index $p = 2.1$ for the injection of primary relativistic hadrons is used. An exponential cutoff is set to 100 TeV, although no significant difference is observed if it is changed to half this value, even at energies as high as 10 TeV. Moreover, a range of values is studied for the normalization factor for the hadronic injection spectrum, as it depends on other sensitive parameters subject to uncertainties. For instance, the rate of SN explosion per year was assumed to be 0.3 in earlier studies, but recently it is more commonly referred to as $\sim$0.1 SN yr^{-1}. In the present work, both a high and a low value for the SN rate are studied, revealing a range of uncertainties. This has been represented in Figure 5.4, where other exponential cutoffs are also considered.

Indeed, the discussion about the supernovae explosion rate is on-going. The highest value of 0.3 SN yr^{-1} is used by, e.g., [Völk *et al.* 1996] and other authors

[1] The secondary particles in this study are those electrons and positrons that result from knock-on and pion decay processes in the inner region of M82.

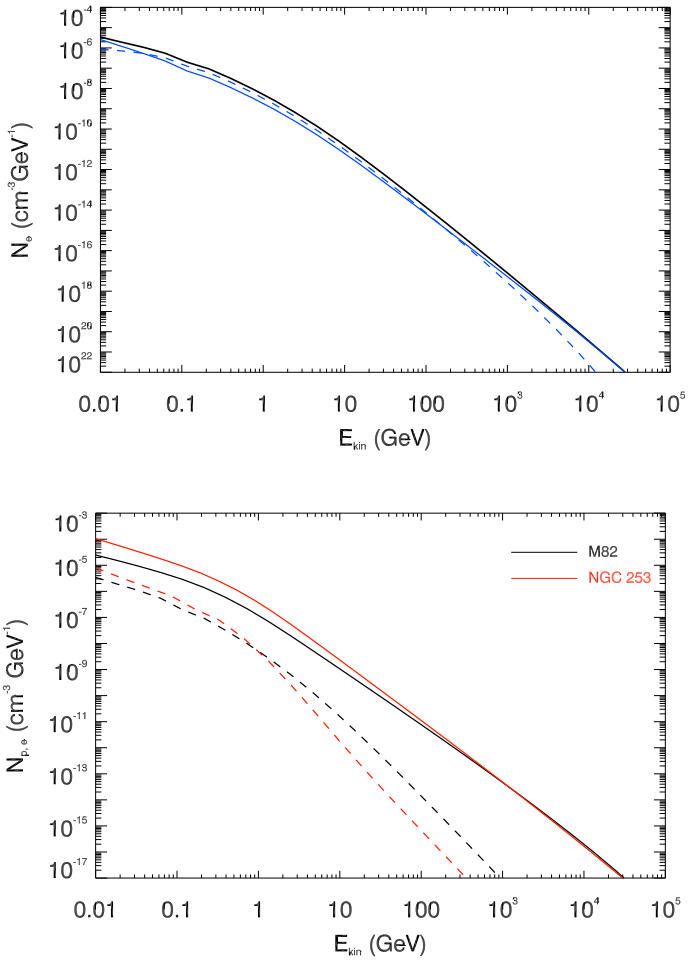

Figure 5.2: Left: Comparison of the steady population of electrons that would result after solving the diffuse loss equation injecting only primary (solid blue) and only secondary (dashed blue) particles – from knock-on and pion decay – in the inner region of M82. The total steady electron population (solid black), resulting from the injection of both primary and secondary electrons, is also shown. Parameters used in this Figure coincide with those presented later within the same model (Figures 5.3 – 5.4). Right: Steady proton (solid) and electron (dashed) distributions in the innermost region of both M82 (black) and NGC 253 (red).

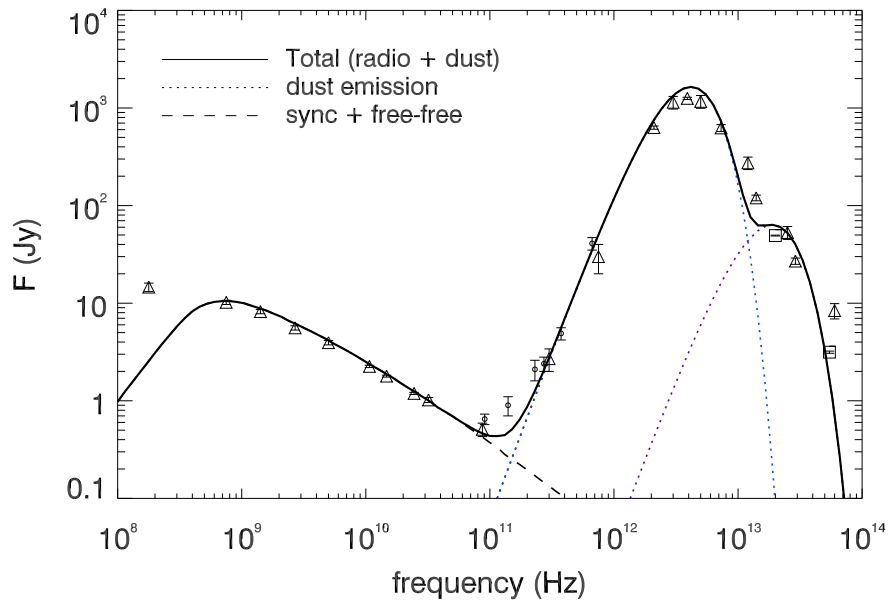

Figure 5.3: Multi-frequency spectrum of M82 from radio to infrared. The observational data points correspond to: [Klein *et al.* 1988] (triangles), [Hughes *et al.* 1994] (circles) and [Förster *et al.* 2003] (squares), and references therein in each case. The results from modelling correspond to: synchrotron plus free-free emision (dashed), dust emission (dotted) splitted in a cool (blue, $T_c = 45\,K$) and a warm (purple,$T_w \simeq 200\,K$) component, and the total emission from radio and IR emission (solid).

thereafter, and it is based on [Kronberg *et al.* 1985]. The latter study has compiled different estimations, starting from $0.1\,SN\,yr^{-1}$ by [Kronberg & Wilkinson 1975], based on the total non-thermal emission; going up to $0.16\,yr^{-1}$, based only on IR excess; then 0.2 – 0.3 by [Kronberg & Sramek 1985], based on direct monitoring of variability of discrete sources; and still going higher up to $0.3\,SN\,yr^{-1}$ in [Rieke *et al.* 1980], based on estimating the number of new radio sources. But critics to [Kronberg & Sramek 1985], and in general to high values of the supernova remnant rate, have arised mainly because the rate of detection of new radio sources does not correspond to those values, e.g., see de [de Grijs *et al.* 2001, McLeod *et al.* 1993, Bartel *et al.* 1987]. Lower values for the rates $(0.07 - 0.08\,SN\,yr^{-1})$ have also been recently favored by Fenech et al. (2008), who made an 8-days deep MERLIN radio imaging of SNR in the starburst and use two different methods to compute the explosion rate. On one side, they assumed that the more radio luminous SNRs in M82 are younger than Cas A. On the other, they assumed that the SNR are in free expansion and used the measured $N(< D) - D$ plot.

The primary electron population is taken to be proportional to the injection proton spectrum, scaled by the ratio between protons and electrons, N_p/N_e. The

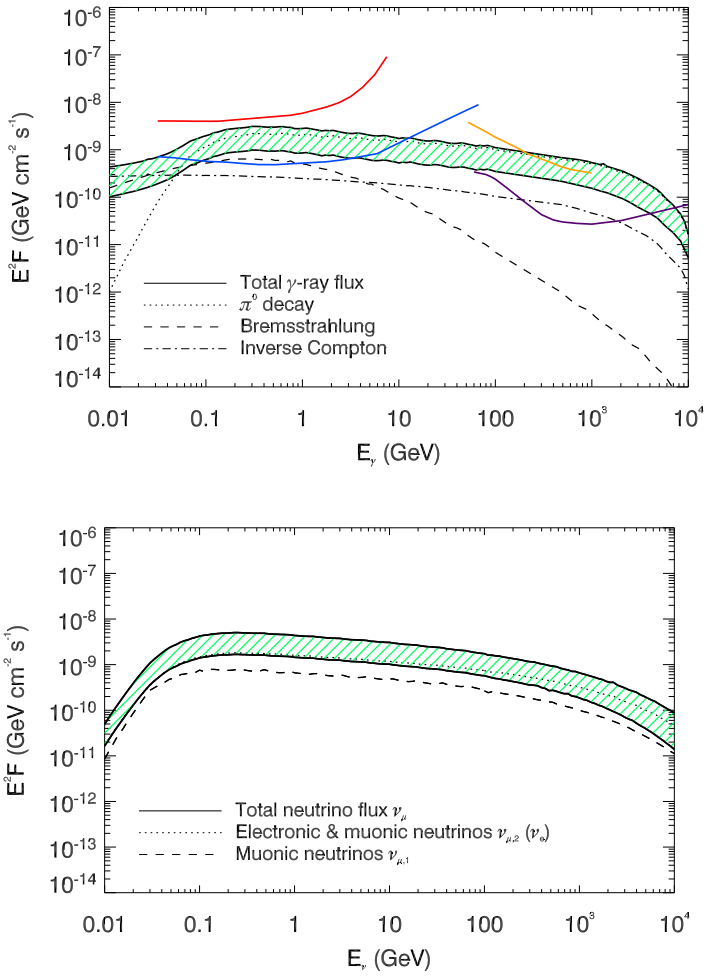

Figure 5.4: Left: Energy distribution of the differential gamma-ray fluxes, exploring a range of uncertainties in supernova explosion rate and cutoffs in the primary energy, as it is explained in the text. The sensitivity curves for EGRET (red), *Fermi* (blue), MAGIC (purple), all from [Funk *et al.* 2008], and the intended one for the forthcoming Cerenkov Telescope Array (CTA, violet) are shown. Right: Differential neutrino flux predictions from the inner region of M82, total and separated in different channels. The neutrino predictions make use of the same explored parameters already presented in the left panel and explained in the text.

value is set later on, in a recursive application of this model, as a fit to radio data. The same applies to other values, like the magnetic field. Together with the primary electron population, all the produced secondary electrons are taken into account when computing the steady state. For comparison, in Figure 5.2 (right), the steady particle populations present in M82 are plotted together with the ones present in NGC 253, from [Domingo-Santamaría & Torres 2005]. The curves for electron and proton distribution display a similar behavior and level than those corresponding to M82, emphasizing the similaritity of the initial characteristics of these two starbursts as possible high-energy sources. With the steady electron population determined, a multi-frequency spectrum (from radio up) can then be computed and compared with experimental data.

Multifrequency spectrum

Figure 5.3 shows the best match from this model: a multifrequency spectrum is overplotted to previous radio and IR data (see the caption for details). At the lowest frequencies, radio data is no longer reduced to the central starburst region. Due to angular resolution of the observing instrument, emission at this frequency comes from the whole galaxy and cannot be separated from that coming only from the inner region. Therefore, this model contribution is just a component of the total radiation below a few 10^8 Hz. In the region of the spectrum where synchrotron emission dominates, several parameters can be determined through repeated iterations: magnetic field, EM, slope of proton injection, and N_p/N_e ratio. In the range of uncertainty mentioned before, the lowest value for the magnetic field, 120 μG, corresponds to the highest steady distribution (i.e., with the highest supernovae explosion rate assumed, and a value $N_p/N_e = 30$). Inversely, a low steady distribution implies the need for greater losses by synchrotron in order to match the data, thus pumping the magnetic field up to 290 μG. The general fit to observations is quite good in each case. These values of magnetic field are in agreement with previous results in [Völk *et al.* 1989] and are also similar to the ones found for the disk of Arp 220 [Torres 2004] or NGC 253 [Domingo-Santamaría & Torres 2005], as well as compatible with measurements in molecular clouds [Crutcher 1988, Crutcher 1994, Crutcher 1999]. On the other hand, the slope of the proton injection p is determined in this step by matching the corresponding slope for radio emission. The range of uncertainties does not seem to affect p significantly.

[Tabatabaei *et al.* 2007] confirm, in a study of M33, that non-thermal emission is spatially associated with star forming regions and propose that the contribution of localized structures (SNRs) become more important as the (synchrotron photon) energy shifts to higher values. Although this may be true, the spatial correlation by itself is not really a proof of it, since star forming regions also have an enhanced cosmic ray sea, and thus an increase in the production of secondary electrons, which emit non-thermally. In fact, [Bressan *et al.* 2002]

have shown that the contribution of radio SNRs to the non-thermal emission cannot be dominant in galaxies, concluding that, for our Galaxy in particular, it cannot be more than about 6%. In any case, the uncertainty in determining the magnetic field in this model must be carefully taken into account: most of the radio emission is considered to come from cosmic ray electrons that have been either injected by SNRs (primaries) or other accelerators, or produced in cosmic-ray interactions (secondaries). If there is a contribution to the total non-thermal radio signal made by unresolved SNRs, this would diminish the estimation of the average magnetic field in the starburst. However, this distinction cannot be made with the data on M82 so far.

Regarding the far IR emission, starbursts data generally require a dust emissivity law, $\nu^{\sigma} B(E,T)$, where typically $\sigma = 1.5$ and $B(E,T)$ is the Planck function. This greybody peaks at $\sim$45 K and has a luminosity of $4 \times 10^{10} L_{\odot}$ (from [Telesco & Harper 1980] corrected by distance). However, at higher frequencies, a simple greybody emission cannot explain observations, and an excess appears at near IR wavelengths. [Lindner 2003] proposed a dust cloud model in which an envelope of dust grains surrounds a luminous source. Each concentric shell decreases its density with increasing radius and has its own temperature and associated flux. As a simpler but still accurate approximation, an addition of just one secondary greybody is enough to fit the data well. The temperature of this greybody is warmer ($T \simeq 200$ K) than the main one, and it has a smaller luminosity of $7 \times 10^{9} L_{\odot}$. Small changes in the warm greybody luminosity or maximum of the peak are possible with results similar to the ones presented here, and they have been explored. The fit to the IR data is quite good, as can be seen in Figure 5.3.

The model discussed in this work yields inverse Compton fluxes of just a few percent or less than the upper limits at X-ray energies, see e.g., [Persic *et al.* 2008] and references therein. The diffuse emission is overwhelmed by emission from compact objects.

Gamma-ray predictions

Figure 5.4 shows the gamma-ray differential flux that results from this model coming from the central region of M82, together with the sensitivity curves of possible instruments observing it. The goodness of this prediction is that it is consistent with the remaining range of the electromagnetic spectrum: the particles generating this emission, both hadrons and leptons, are the same ones generating the radiation seen at lower energies. The model confirms that there is not an expectation for detection by EGRET, consistent with EGRET upper limit by [Torres *et al.* 2004], and the stacking analysis of EGRET data by [Cillis *et al.* 2005]. Nonetheless, it predicts M82 as a source for *Fermi*. The total flux estimations at high and very high energies are as follows:

- for $E > 100\,\mathrm{MeV}$, 2.6×10^{-8} $(8.3 \times 10^{-9})\,\mathrm{cm^{-2}\,s^{-1}}$,
- for $E > 100\,\mathrm{GeV}$, 8.8×10^{-12} $(2.8 \times 10^{-12})\,\mathrm{cm^{-2}\,s^{-1}}$,

with the parenthesis representing the results obtained with the lower energy cutoff and lower supernova explosion rate. Separate contributions are plotted from each gamma-ray channel: neutral pion decay, bremsstrahlung and inverse Compton (against CMB, far and near IR photon densities). Finally, Figure 5.4 also presents neutrino fluxes coming from the inner part of the starburst galaxy. The separate contribution of each neutrino process can be seen, together with the total flux. As in the previous case, parenthesis represent the results obtained with the lower energy cutoff and lower supernova explosion rate. The total flux estimations at high and very high energies are as follows:

- for $E > 100\,\mathrm{GeV}$, 1.2×10^{-11} $(3.9 \times 10^{-12})\,\mathrm{cm^{-2}\,s^{-1}}$,
- for $E > 1\,\mathrm{TeV}$ 3.8×10^{-13} $(9.9 \times 10^{-14})\,\mathrm{cm^{-2}\,s^{-1}}$.

Consequently, only if the highest end of the predictions happens to be a realistic representation of the galaxy, the MAGIC telescope could detect it above 300 GeV with 5σ in 50 h. Although the time required by MAGIC alone would be unrealistic in order to obtain a detection for the lowest end of the predictions, with the upcoming arrival of MAGIC II, the time to expend on this source could be affordable. The actual estimations for MAGIC II sensitivity are a factor of 2 to 3 better than for MAGIC I, so the flux coming from the starburst galaxy would be detected within 50h. Similar estimations would apply for the VERITAS array. But indeed, the instrument of choice to deeply study this source would be the forthcoming Cerenkov Telescope Array (CTA). Presenting an instrument acceptance extending both to the lower and higher energy ends compared to the previous telescopes, with a 1 TeV sensitivity one order of magnitude or more better than present Cherenkov experiments, M82 should be a bright source for CTA, if this model is a realistic representation of this object. Witch this observatory, studies on the possible cutoff in the proton spectra could be made, although M82 would still look as a point like source.

The dependence of these results on the initial injection slope p has been explored by enforcing the latter to be different. This dependece is not found to be relevant, within a reasonable range. In Figure 5.5, this is shown by analyzing the predictions of the present model for a -2.3 average injection slope. Both the multi-wavelength predictions in radio-IR and the gamma-ray emission are displayed. No relevant differences (within uncertainties) are found in the parameters that give rise to these curves.

Equipartition estimates

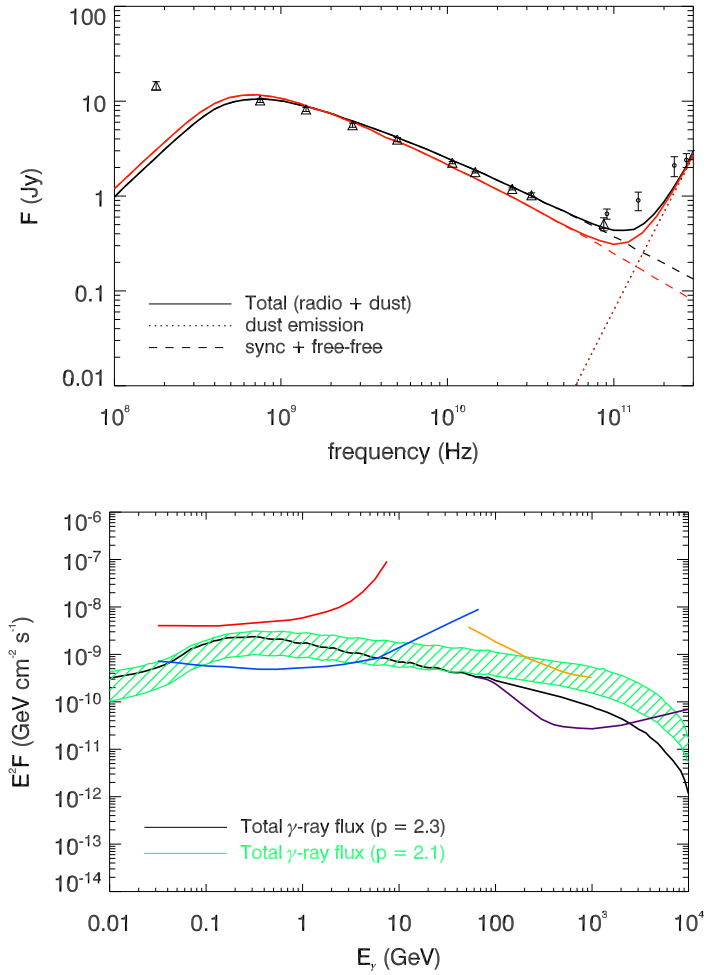

Figure 5.5: Comparison of the multi-wavelength predictions for different initial spectral slope in the injection, see Figure 5.3 for further details. The black curve correspond to the model with proton injection spectrum $p = 2.1$ and magnetic field $B = 130\mu$G, whereas the red curve correspond to the results of modelling with $p = 2.3$ and $B = 170\mu$G. The gamma-ray emission from the -2.3 model in the case of the highest SN explosion rate is shown against those obtained with the harder injection (the green shadow, coming from the uncertainties described before). Main differences appear at high energies.

It has already been mentioned that care should be exercised with equipartition estimates and even more after the work done by [Beck & Krause 2005], where it was shown that the usual formula to compute the equipartition field[2] may be of limited practical use. This formula is based on the ratio $\mathcal{K}$ of the total energies of cosmic ray protons and electrons, which is generally computed

[2]The equipartition field is sometimes referred as the minimum-energy estimate of total magnetic fields strengths from radio synchrotron intensities

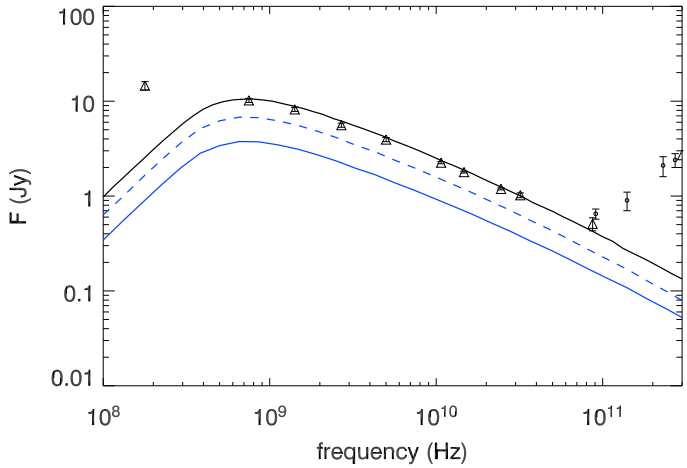

Figure 5.6: Different contributions to the radio emission (synchrotron + free-free) by the steady primary-only (blue) and secondary-only (yellow) electron population, also compared to the total radio emission of the whole electron population (black).

without a full model of the system. In addition to other non-trivial technical problems mentioned by Beck & Krause, if energy losses of electrons are important, the number density between these particles increases with particle energy and the equipartition field may be significantly underestimated. The correct value can be computed only by constructing a model of gas density and cosmic ray propagation. [Beck & Krause 2005] already emphasize that starburst galaxies – and regions of high star formation rate in the central regions and massive spiral arms of galaxies – have high gas densities and mostly flat radio spectra, thus non-thermal bremsstrahlung and other losses are important. Since the loss rate increases linearly with gas density n, the proton-to-electron ratio also increases with gas density. In addition, protons are also subject to energy-dependent losses or escape (e.g., diffusion timescales differ). Thus, the ratio N_p/N_e depends really on energy, and any equipartition formula will not cope. Using the steady population of relativistic particles that have been found as a result of this model, the energy content in such component can be determined. From this point, equipartition is *imposed* in order to see how the magnetic field behaves. The obtained value is then compared to the output of the model. The result is 150 μG, which is close (but not the same) to the estimation by [Weaver *et al.* 2002], and of the same order as the magnetic field from the model, 120 μG.

Neutrino predictions

[Loeb & Waxman 2006] have suggested that hadronic processes in starbursts can produce a large enough background of diffuse high energy neutrinos to be

observable with the ICECUBE experiment. They arrive to this conclusion – criticized by [Stecker 2007] – starting, essentially, from two assumptions and making order-of-magnitude estimations thereafter:

1. protons lose essentially all of their energy to pion production, and
2. a lower limit to the energy loss rate of the protons can be obtained from the synchrotron radio flux, by assuming that all of the radiating electrons (and positrons) come from pion decay.

Even when photo-dissociation in starbursts is a minor effect [Anchordoqui *et al.* 2008], the 1^{st} assumption is arguable, as [Stecker 2007] emphasized, because particles are subject to diffusion and convection by winds in addition to pion losses, i.e., the galaxy is not a complete calorimeter, especially at the highest energies. The 2^{nd} assumption is arguable because synchrotron radiating electrons are not only secondary particles, but the primaries too. Figure 5.6 quantifies this effect for M82 and compares the contribution to the synchrotron radiation of the inner starburst if only-primary or only-secondary electrons are considered. From $E_e - m_e \sim 10^{-1}$ to $\sim$ 100 GeV, the secondary population of electrons slightly dominates, see Figure 5.2 (left), with the primary population contributing significantly. Therefore, it would not be very accurate to normalize the whole radio emission to the secondaries alone (or primaries alone), and then use this to fix the energy loss rate of protons, from where one can estimate the neutrino emission. This study presents the first full neutrino emission computation from a starburst galaxy which is self-consistent with the emission at all electromagnetic frequencies included in the same model. Given the detail needed for such a description, a generalization of the present results for M82 to all the starbursts is not recommended. However, if this is done, and if it is supported by basic assumptions on the starbursts number density within the horizon, the neutrino diffuse emission would be below the Waxman-Bahcall limit[3].

The sky-average sensitivity of the current ICECUBE installation (IC-22, with 22 strings) at 90%C.L. to a generic E^{-2} flux of ν_μ is $1.3(2.0) \times 10^{-11}\,\mathrm{TeV}^{-1}\,\mathrm{cm}^{-2}\,\mathrm{s}^{-1}\ (E/\mathrm{TeV})^{-2}$ depending on the analysis [Bazo Alba *et al.* 2009]. This is not enough to detect M82 directly (see Figure 5.4). In fact, using the present estimation of the neutrino flux from M82 and following the comments made by [Anchordoqui *et al.* 2004], less than 2 events per year would be expected in the full ICECUBE facility. A more definitive

[3] [Waxman & Bahcall 1999] show that cosmic-ray observations set a model-independent upper bound of $\mathrm{E}_\nu^2\Phi_\nu < 2\times10^{-8}\,\mathrm{GeV\,cm^{-2}\,s^{-1}sr^{-1}}$ to the intensity of high-energy neutrinos produced by photo-meson (or pp) interactions in sources of size not much larger than the proton photo-meson (or pp) mean-free-path. The bound applies, in particular, to neutrino production by either AGN jets or GRBs. This upper limit is two orders of magnitude below the flux predicted in some popular AGN jet models, but is consistent with their predictions from GRB models. Their upper bound is stated in eq. (3) and is illustrated in fig. 1 [Waxman & Bahcall 1999].

assessment of its sensitivity to such a signal will need to await further refinement of angular and energy resolutions, via improved knowledge of the detector response.

5.4 Discovery of HE and VHE emission from starbursts

5.4.1 Gamma-ray emission detected from M82

Recently, VHE gamma-ray emission coming from M82 was claimed by VERITAS [Acciari *et al.* 2009a]. Meanwhile, the HE regime was covered by the *Fermi* telescope, also detecting emission from the same galaxy in the first year of observations [Abdo *et al.* 2010c]. In Figure 5.7, this data is displayed, together with the spectral energy distribution (SED) of the model presented in this Chapter. A separate contribution is shown coming from each gamma-ray generator: neutral pion (π^0) decay, bremsstrahlung and inverse Compton radiation. The latter was computed having the cosmic microwave background (CMB), far and near infrared (IR) photon densities as targets altogether, see Figure 5.8. The prediction (green shade region) is perfectly compatible with the observational data presented both at HE and VHE, within errors. The *Fermi* LAT and VERITAS data allow to further precise the original predictions. Therefore, a range of parameters and some specific outputs (red and black solid curves) are explored to better constrain the model to the observed results, see Table 5.1. As can be seen, π^0 decay contribution dominates at VHE energies.

5.4.2 NGC 253, confronted with the model

The also near, barred-spiral starburst galaxy NGC 253 has been deeply studied through the years. The distance has been subject of uncertainty, its value ranging from 2.5 Mpc [Turner & Ho 1985, Mauersberger *et al.* 1996], going up to 3.3 Mpc [Mouhcine *et al.* 2005], 3.5 Mpc [Rekola *et al.* 2005], and even 3.9 Mpc, according to the detection of the red giant branch [Karachentsev *et al.* 2003]. Its continuum spectrum peaks in the far IR, at about 100 μm, with a high luminosity of $4 \times 10^{10} L_{\odot}$, [Telesco & Harper 1980, Rice *et al.* 1988, Melo *et al.* 2002]. Its inner (100 pc) region is characterized, as well as M82, by starburst activity [Paglione *et al.* 1996, Domingo-Santamaría & Torres 2005].

The integral flux published by H.E.S.S. constrains previous predictions for NGC 253 at the VHE regime. Moreover, the first results from the *Fermi* telescope add more information to the spectrum of the galaxy at lower energies. A set of curves for the SED are specifically plotted in Figure 5.9 to achieve this low flux, exploring the uncertainties in the distance to this galaxy and subsequent ranges in the magnetic field and diffusive timescale.

Apart from diffusing away during 10^{6-7} yrs (see Table 5.2), particles can escape the inner starburst convectively, carried away by winds ($\sim 300\,\mathrm{km\,s^{-1}}$), and through pion collisions with ambient gas, in even shorter timescales of around a few 10^5 yrs.

Table 5.1: Physical parameters used in the multi-wavelength model of M82, presented in the previous section and in [de Cea del Pozo *et al.* 2009b], together with specific values that try to match the emission from the VERITAS detection. In any case, the (small) variations explored below are within the former predictions of the original model. The list of parameters is divided in sections: observational values, derived from observational values, obtained from modelling, and assumed. SB stands for starburst.

Physical parameters	**From 2009 model**	**VERITAS-driven model**
Distance	$(3.9 \pm 0.3_{stat} \pm 0.3_{sys})$ Mpc	...
Inclination	$(77 \pm 3)^\circ$	...
Radius SB	300 pc	...
Radius Disk	7 kpc	...
Height SB	200 pc	...
Gas Mass SB	$2 \times 10^8 M_\odot$ (H_2)	...
Gas Mass Disk	7×10^8 $M_\odot$ (HI), 1.8×10^9 $M_\odot$ (H_2)	...
IR Luminosity	4×10^{10} $L_\odot$	...
SN explosion rate	$0.3\,\mathrm{yr}^{-1}$ ($0.1\,\mathrm{yr}^{-1}$)	$0.2\,\mathrm{yr}^{-1}$ | $0.3\,\mathrm{yr}^{-1}$
SN explosion energy	10^{51} erg	...
SN energy transferred to CR	10%	10% | 5%
Convective velocity	$600\,\mathrm{km\,s}^{-1}$	...
Dust temperature	45 K	...
Ionized temperature	10000 K	...
Uniform density SB	$\sim 180\,\mathrm{cm}^{-3}$	...
Dust emissivity index	1.5	...
Emission measure	$5 \times 10^5\,\mathrm{pc\,cm}^{-6}$	...
Magnetic field	120 μG (270 μG)	170 μG | 210 μG
Proton to electron primary ratio	50 (30)	...
Slope of primary injection spectrum	2.1	...
E_{max} for primaries	10^6 GeV	...
Diffusion coeficient slope	0.5	...
Diffusive timescale	$1 - 10$ Myr	...

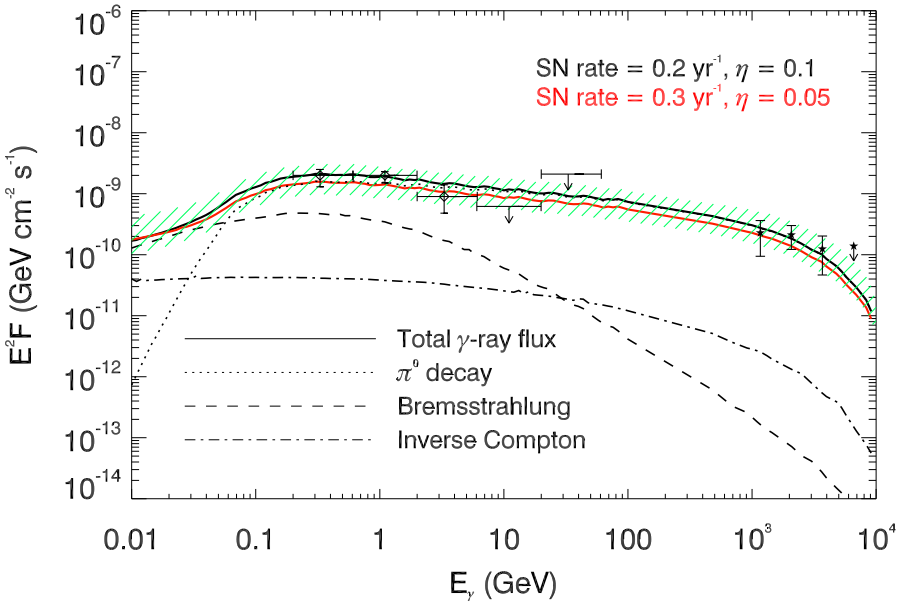

Figure 5.7: Energy distribution of the differential gamma-ray fluxes of M82, exploring a range of uncertainties in supernova explosion rate and efficiency to inject energy from SN to CR. The shaded green area corresponds to the original model presented in this Chapter and [de Cea del Pozo *et al.* 2009b]. Data points and upper limit correspond to both VERITAS (stars) and *Fermi* (diamonds) detections.

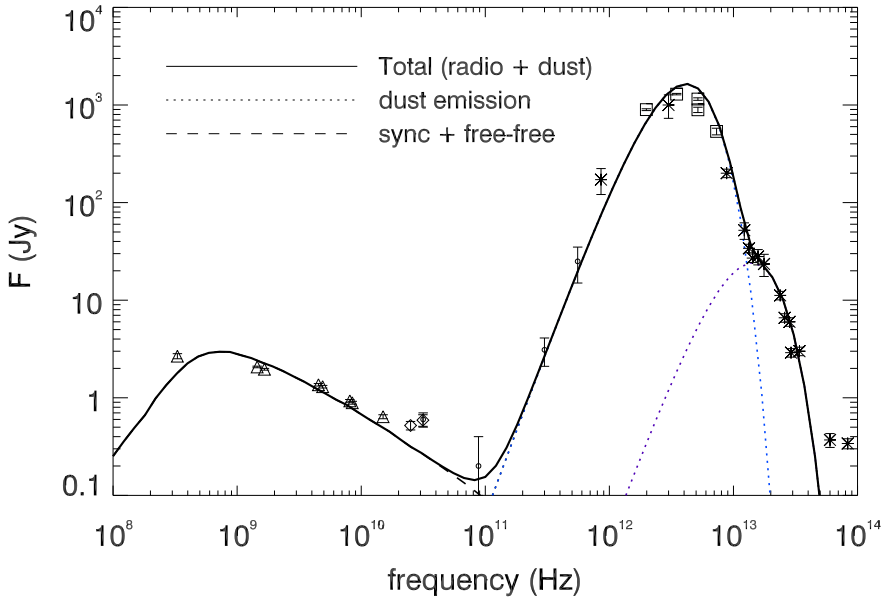

Figure 5.8: Multifrequency spectrum of NGC 253 from radio to infrared. The observational data points correspond to: [Carilli 1996] (triangles), [Elias *et al.* 1978] (circles), [Rieke *et al.* 1973] (asterisks), [Ott *et al.* 2005] (diamonds) and [Telesco & Harper 1980] (squares), and references therein. The results from modelling correspond to: synchrotron plus free-free emission (dashed), dust emission (dotted) splitted in a cool (blue, $T_{cold} = 45\,K$) and a warm (purple, $T_{warm} \sim 200\,K$) component, and the total emission from radio and IR emission (solid).

The diffusion timescale of the particle depends on the energy. As the timescale decreases, the slope of the gamma-ray spectrum becomes steeper (the losses are higher). The diffusion coefficient associated is $\sim 10^{26-27}\,cm^{-2}\,s^{-1}$ at $1 - 10\,GeV$, compared to the $\sim 10^{28}\,cm^{-2}\,s^{-1}$ value in our Galaxy.

5.5 Concluding remarks

The multi-wavelength model presented in this Chapter explains reasonably well both the HE and VHE emission coming from the two closest starburst galaxies M82 and NGC 253, within a range of the explored parameters already mentioned. Every component of the emission can be tracked to one and the same original CR population. Moreover, this CR population results as a consequence of all electromagnetic and hadronic channels from the primary and subsequently-produced secondary particles.

CR enhancement present in these starburst galaxies is reflected in the high energy density values that can be obtained from the steady proton population. Above a proton energy of $\sim 1500\,GeV$ (corresponding to $E_\gamma \sim 250\,GeV$), the energy density is around $10\,eV\,cm^{-3}$ for M82 and similar value for NGC 253. Now that the VHE

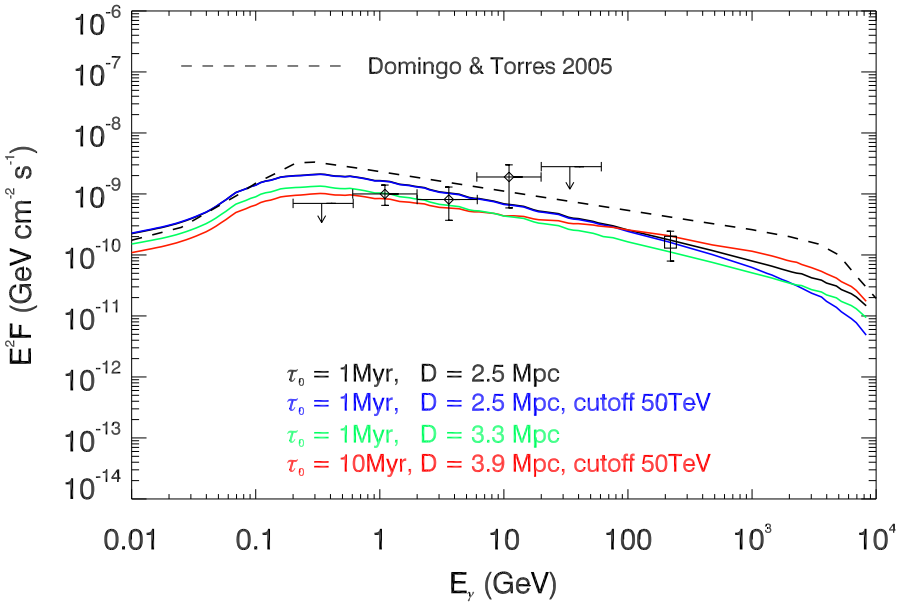

Figure 5.9: Energy distribution of the differential gamma-ray fluxes of NGC 253, exploring the uncertainty in distance, a range of timescale diffusion (τ_0) and possible cutoffs in the proton injection spectrum. The original model from [Domingo-Santamaría & Torres 2005] is also shown for comparison, as well as data points from *Fermi* detection (diamonds) and the integral flux from the H.E.S.S. detection (square), transformed in differential flux (assuming a range of injection spectra).

Table 5.2: Physical parameters used in the multiwavelength model of NGC 253, as presented both in the previous [Domingo-Santamaría & Torres 2005] study and in this section, but exploring some variations allowed within the model in order to match the emission from the H.E.S.S. detection. The list of parameters is divided in sections: observational values, derived from observational values, obtained from modelling, and assumed. SB stands for starburst.

Physical parameters	**From 2005 model**	**H.E.S.S.-driven model**
Distance	2.5 Mpc	2.6 Mpc | 3.9 Mpc
Inclination	78°	...
Radius SB	100 pc	...
Radius Disk	1 kpc	...
Height SB	70 pc	...
Gas Mass SB	3×10^7 $M_\odot$	...
Gas Mass Disk	2.5×10^8 $M_\odot$	
IR Luminosity	$(2-4) \times 10^{10}$ $L_\odot$	...
SN explosion rate	$0.08\,yr^{-1}$	...
SN explosion energy	10^{51} erg	...
Convective velocity	$300\,km\,s^{-1}$	...
Dust temperature	50 K	45 K
Ionized temperature	10000 K	...
Uniform density SB	$\sim 600\,cm^{-3}$	...
Dust emissivity index	1.5	...
Emission measure	5×10^5 pc cm^{-6}	...
Magnetic field	300 μG	200 μG | 270 μG
Proton to electron primary ratio	50	30
Slope of primary injection spectrum	2.3	2.1
E_{max} for primaries	10^6 GeV	...
Diffusion coefficient slope	0.5	...
Diffusive timescale	10 Myr	1 Myr | 10 Myr

regime has been finally achieved by ground-based telescopes, and *Fermi* has proven that detections are possible from lower energies ($\sim 100\,\mathrm{MeV}$), a full and clear picture of gamma-ray emission is begining to appear.

PART II:

Observations using the MAGIC experiment,
and simulations of future observations using CTA

Chapter 6

Analysis of MAGIC data

Contents

The atmosphere blocks most of the radiation that arrives to Earth, which otherwise would be harmful for life. In Astronomy, this implies that most of the observations above ultraviolet (UV) radiation, for instance, need to be carried out from space. However, the atmosphere can also act as a calorimeter and thus allow the indirect detection of very energetic particles, cosmic and gamma rays. The MAGIC (Major Atmospheric Gamma-ray Imaging Cherenkov) telescopes, among other ground-based experiments, profits from this circumstance using the Cherenkov technique.

6.1 Cherenkov technique and telescopes

Cosmic rays that arrive to Earth collide with the nuclei present in the atmosphere. The secondary particles produced interact again with other atmosperic nuclei, generating a cascade of particles, also defined as EAS, extended atmospheric showers, [Longair 1992]. This collision process continues, losing energy in each step, until the critical energy for creating particles is reached. By the time the radiation arrives to the ground level, it can be detected by imaging atmospheric Cherenkov telescopes (IACT) as Cherenkov light.

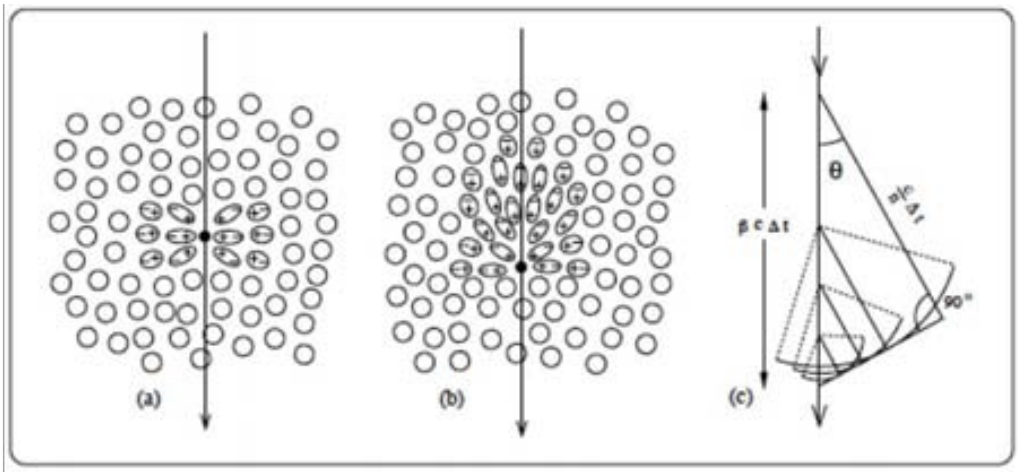

Figure 6.1: Polarization of the medium by a charged particle with (a) low velocity, $v < c/n$, and (b) high velocity, $v > c/n$. Huygens construction of Cherenkov wavefront in (c)

6.1.1 Cherenkov light

The Cherenkov effect ([Cherenkov 1934], [Tamm & Frank 1937]) takes place when a charged particle travels at a speed larger than c in a transparent medium ($v = \beta c, \beta > 1/n$), disrupting the local electromagnetic field. The light emission results from the re-orientation of the instantaneous electric dipoles induced by the particle in the medium. When the distortion travels faster than the generated photons, the wavefronts along the trajectory can sum coherently (according to Huygens construction, see Figure 6.1) and, if the medium is transparent, the light propagates at an angle θ_c:

$$cos\theta_c = \frac{1}{\beta n}. \tag{6.1}$$

The energy threshold for the charged particles to emit Cherenkov light is:

$$E_{th} = \frac{m_0 c^2}{\sqrt{1-\beta_{min}^2}} = \frac{m_0 c^2}{\sqrt{1-1/n^2}} \tag{6.2}$$

where m_0 is the rest mass of the particle.

The number of Cherenkov photons emitted per track length by a charged particle is given by [Yao *et al.* 2006]:

$$\frac{d^2N}{dxd\lambda} = \frac{2\pi\alpha Z^2}{\lambda^2}\left(1 - \frac{1}{(\beta n)^2}\right) \tag{6.3}$$

where α is the fine structure constant. From this equation, it appears that most of the Cherenkov photons are emitted at short wavelenghts and their number

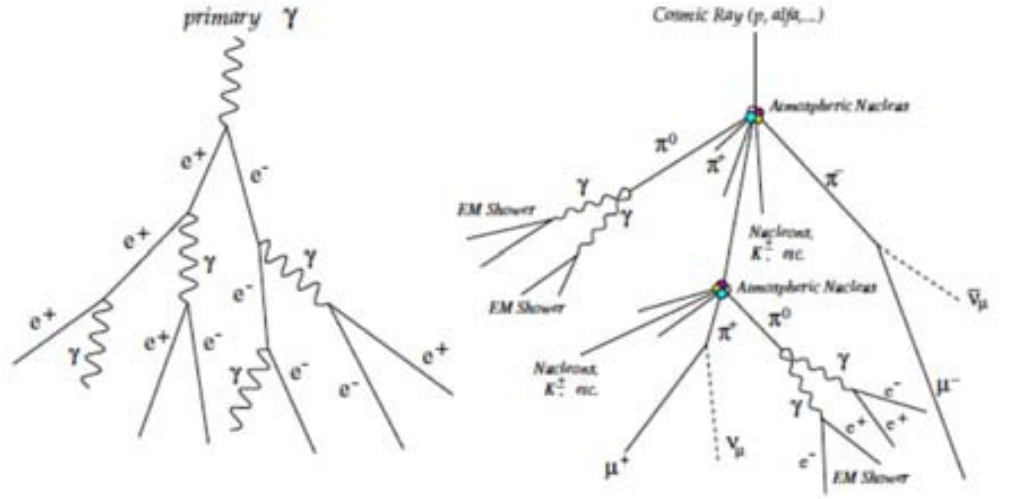

Figure 6.2: Scheme of a γ-ray induced electromagnetic shower (right) and a hadron-induced shower (left) developing in the atmosphere

decreases when going from ultraviolet to optical light. The main source of attenuation (between 15 and 2 km above sea level) is the Rayleigh scattering, in which photons are scattered by polarizable air molecules with a smaller size than the photons wavelenght. Another important contribution comes from the Mie scattering, produced when photons interact with small dust particles suspended in the air. Finally, Cherenkov photons can be absorbed by the ozone layer (for $\lambda < 290$ nm) in the upper part of the atmosphere.

The previously defined Cherenkov angle θ_c can be expressed as a function of the altitude. Since the refraction index is not constant in the atmosphere, the relationship is such that θ increases with decreasing height. Therefore, when the light emitted at different heights reaches the ground, a light pool is created: the photons arrive at a similar distance from the axis of the shower of particles, and the projected cones of light that should be rings become smeared out. The Cherenkov light density is constant up to 120 m away from the shower axis, where the sudden drop occurs.

6.1.2 Hadronic and electromagnetic showers

In order to produce this Cherenkov light, very energetic cosmic and gamma rays are needed. Depending on the nature of the primary particle, the development of the shower can be very different (i.e., Figure 6.2).

If the primary particle is a gamma-ray, the cascade will be an electromagnetic one. When a photon interacts with one atmospheric nucleus, an electron-positron pair is generated. These secondary particles loose energy producing less energetic photons through bremsstrahlung. The shower keeps developing, quite symmetri-

cally, alternating between pair production and bremsstrahlung, until a critical energy is reached, 83 MeV, below which the main energy loss is due to ionization. This point (usually between 7 and 13 km above sea level) coincides with the shower maximum, and after that, the cascade dies out. Due to the relativistic energies involved, the particles from a γ-induced shower are strongly colimated along the incident direction.

On the other hand, when cosmic rays (usually protons) hit the atmosphere, many different process and types of secondary particles are involved. These hadronic cascades can generate pions (90%), kaons and antiprotons (10%) when interacting with atmospheric nuclei, and in subsequent steps, muons and neutrinos, among other particles. The hadronic core of the shower continues to interact until the energy threshold for pion production is reached (1 GeV), then the ionization process becomes dominant and the cascade dies out. The majority of secondary particles are pions, and therefore can initiate an electromagnetic sub-shower. In their neutral form, those pions decay mainly in two photons. The charged pions decay in muons and neutrinos. The latter will not interact due to their low cross-section, whereas muons interact almost exclusively through ionization and, thanks to their long lifetimes, usually reach the ground before decaying. Hadrons are able to transfer significant momenta to the secondary generated particles, thus widening the tranverse evolution of the shower. Another important characteristic is that the arrival directions for the hadronic showers are isotropic, contrary to γ-induced showers, which originally come from the pointed astronomical source. These, together with morphological and timing differences, are important features when discriminating gammas from hadrons detected with IAC telescopes.

6.1.3 Imaging Air Cherenkov Technique

The goal of the imaging air Cherenkov (IAC) telescopes is to detect, at ground level, very energetic photons coming from astronomical objects, using the Cherenkov effect. These telescopes collect Cherenkov light on a reflecting surface (mirror) and focus it on a detector (camera). The detector's instrumentation converts the photons into electric pulses and later saves these as a geometrical projection of the atmospheric showers.

The image of the air shower is the key of the IAC technique. It contains information about the longitudinal development of the cascade of particles through the number of photons and arrival time of the images. Cherenkov photons emitted at different heights reach the camera at different positions, see Figure 6.3. When pointing to a possible γ-ray source, the most energetic secondary particles (located at the top of the shower) will hit closely to the central part of the camera. Meanwhile, the less energetic lower part of the shower will form images away from the center of the camera. The amount of detected Cherenkov light is an estimator of the total number of secondaries, and therefore, of the energy of the primary particle. Moreover, the orientation and shape of the image of the shower is a good indicator of the incoming direction and the nature of that primary particle. For instance and as explained

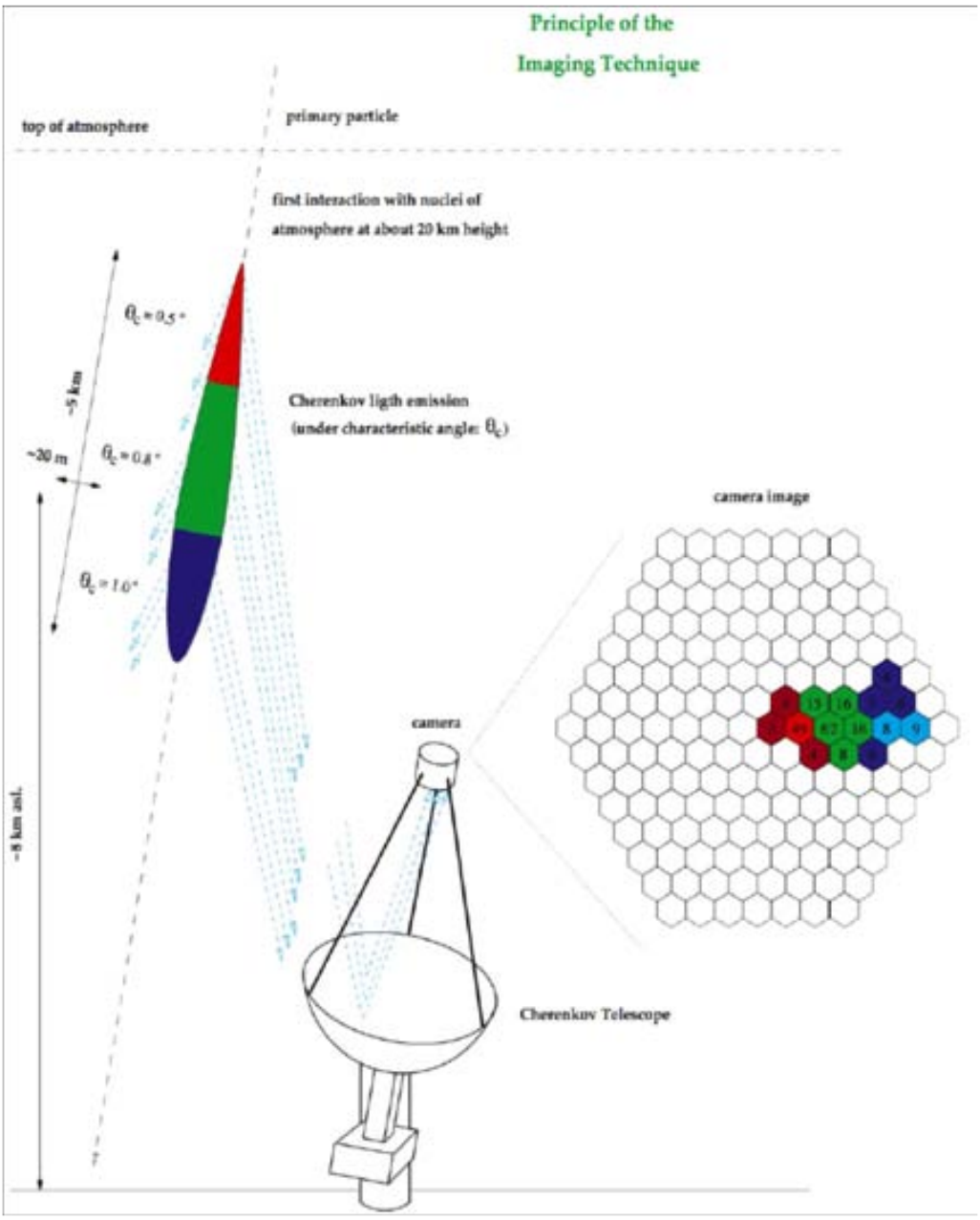

Figure 6.3: Image formation scheme in the camera of an IAC telescope. The values are referred to a 1 TeV γ-induced shower. The blue part is the image head whereas the red part is the image tail. The numbers in the pixels correspond to the number of incident photons. [Tescaro 2010]

in 6.1.2, arrival directions of the hadronic showers are uniformly distributed along the detector and their projected image is wide spread, while γ-ray shower images have nice elliptical shape and their axis point to the center of the camera. This morphological differences help rejecting hadronic events from the background.

In order to extract γ-ray induced showers from the background, an energy threshold is imposed to the primary photon:

$$E_{th} \sim \sqrt{\frac{\phi\Omega\tau}{\varepsilon A}} \tag{6.4}$$

The energy threshold is inversely proportional to the square root of the quantum efficiency of the detector (ε) and the mirror surface (A). It also depends on the solid angle subtended by the mirror (Ω), the integration time of the signals in the camera (τ) and the background light from the night sky (ϕ, which main sources are stars, airglow, zodiacal light, artificial man-made light or even moon light). Therefore, IAC telescopes need large mirror surfaces and high sensitivity photodetectors.

6.2 The MAGIC telescopes

Since the fall of 2009, the MAGIC experiment, seen in Figure 6.4, observes gamma-ray sources with two 17-m diameter IAC telescopes. They are located at the Observatorio del Roque de los Muchachos, in La Palma, Canary Islands, Spain ($28°N17°W$, 2200m above sea level). Their design mainly fulfills two aims: achieving the lowest energy threshold (of 50 GeV for standard observations, or even 25 GeV with a special trigger setup), and a fast repositioning (an average of 30 seconds takes to point the telescopes from one point to another in the sky). The earliest operations started in 2004 with one single-dish telescope (MAGIC-I), and lately the instrument was upgraded to stereoscopic observing mode by adding a second - in many ways, "clone" - telescope (MAGIC-II) at ~ 85 m from the first one. In doing so, the system improved the sensitivity, the primary energy reconstruction and the source position determination. A list and description of the characteristics of the MAGIC experiment is presented in the following sections.

6.2.1 Structure and reflector

Light carbon fiber reinforced tubes support the structure of both telescopes and allow for a fast repositioning in any direction of the sky, for instance, in case of gamma-ray burst (GRB) alerts. The drive system also provides a high degree of pointing accuracy. Each telescope has two motors of 11 kW of power each in the azimuth axis and one for the zenith movement. The mentioned pointing quality is reinforced with a starguider system. It consists on a CCD camera placed at the center of the reflector, with a 4.6° field of view (FOV), thus imaging partially the camera and a portion of the sky. Using six LEDs on the camera as a reference system, the starguider compares the position of detected stars with a catalogue. In

Figure 6.4: Picture of the two MAGIC telescopes: MAGIC-I (left) and MAGIC-II (right)

this way, corrections for possible mispointing can be later applied during the analysis of the data.

The reflector has a parabolic curvature in order to minimize the arrival time spread and improve the signal to noise ratio. As it was previously stated, both telescope dishes have 17 m of diameter, with a total reflective surface of 239 m^2 and $(80-85)\%$ of reflectivity in the range from 250 to 650 nm. MAGIC-I has 49.5 cm $\times$ 49.5 cm spherical mirrors, while MAGIC-II has 1 m $\times$ 1 m mirror elements, which doubles the size of the former. Despite the rigidity of the structure, the reflector surface can suffer distortions depending on the pointing position of the telescopes, therefore a re-adjusting needs to be done by the active mirror control (AMC). Each mirror panel has a laser at the center and two mechanical actuators. A camera records the image formed by the lasers when pointing to the closed camera, and the alignment of the mirrors is completed via software orders to the motors.

6.2.2 Camera

The camera receives the Cherenkov light, collected in the reflector surface, and converts the signal into photoelectrons. The design of the camera is such that it attempts to have a large FOV ($\sim 3.5°$) and a fine pixelization (to improve the gamma/hadron separation). Photomultiplier tube (PMT) cameras for both telescopes are slightly different. In the case of MAGIC-I, it has hexagonal shape and consists of 397 small (30 mm diameter) inner PMTs, surrounded by 180 big-

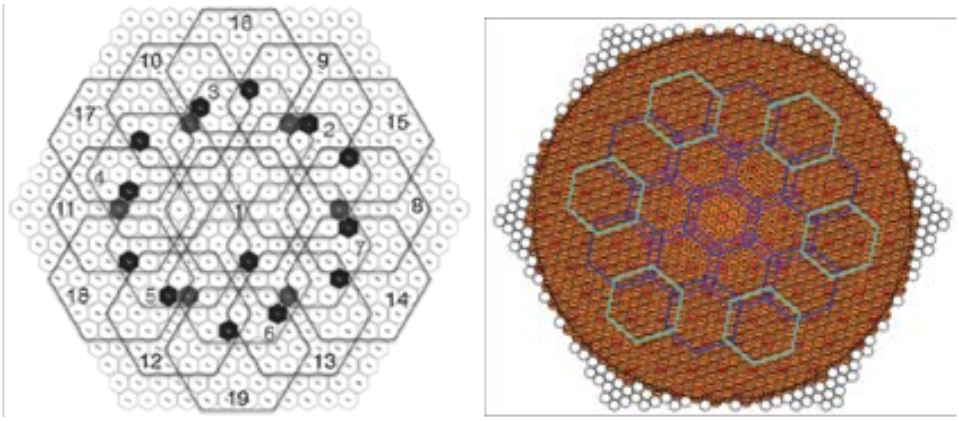

Figure 6.5: Scheme for the standard trigger configuration in MAGIC I (left) and II (right) cameras ([Meucci *et al.* 2007], [Cortina *et al.* 2009]).

ger (60 mm diameter) PMTs. Meanwhile, MAGIC-II camera has a circular shape and 1039 medium (25 mm diameter) PMTs. To improve the quantum efficiency (QE) and compensate the dead space between the edges of the rounded PMTs, each one is surrounded by hexagonal-shaped, non-imaging light concentrators (Winston Cone); in addition, the hemispherical entrance window is coated with a milky lacquer doped with a wavelenght shifter. Temperature and humidity inside the camera are controlled by a water cooling system.

6.2.3 Readout, trigger and data adquisition

All the electronics of the MAGIC system are kept in a facility 150 m away from the telescopes, in order to avoid extra weight to the camera and keep it safe from bad weather conditions. The electronic signal is converted into an optical one and travels from the camera to the readout system via optical fibers. When the signal is received, it is transformed into an electric current by means of a photodiode, and split in two signals. One part is digitized with a multiplex 2GSamples/s Flash Analog-to-Digital-Converter (FADC) and kept in a ring buffer for MAGIC-I. For MAGIC-II, the Cherenkov pulses are sampled by low-power Domino Ring Sampler chips, working at 2GSamples/s, and stored again in a ring buffer. The other part of the electronic signal is sent to the trigger system.

Only a certain -inner- region of each camera (see Figure 6.5) is considered for the trigger, which in turn has different decision levels. The first level (L0T) is a discriminator: if the analog signal of one pixel exceeds a certain threshold (which depends on light conditions), the channel signal goes to the next level. For L1T, if close packed next-neighbour (3, 4 or 5 NN) pixels have a signal in a short ($2-5$ ns) time window, the charge is recorded (in mono-observations). There is a L2T that would allow further online pattern recognition later in the analysis, but it has not been implemented. The actual standard mode of operation, i.e., stereoscopic, requires a L3T: if the signal is detected at both telescopes in a certain time window,

then the events are recorded.

For some dedicated observations (like pulsar observations), there is another option, called the analog sum trigger [Aliu *et al.* 2008a], that lowers the energy threshold down to 25 GeV. It consists of a linear sum of the signals of large patches of pixels. This time, the trigger area is not an inner circle but a centered doughnut shape.

In case the trigger occurs, the digitization process stops and the information contained in the ring buffers is kept in a disc. The raw data are stored by the data adquisition (DAQ) system in run files of 2GB maximum. All files are transferred to the data center Port d'Informacio Cientifica (PIC, htt://magic.pic.es) in Barcelona.

6.2.4 Calibration

An optical calibration system is needed to determine how to convert FADC counts into a number of photoelectrons (phe). In order to achieve this, a set of different LEDs (emitting at 370, 460 and 520 nm) are fired onto the camera to uniformly illuminate it. When the signal is triggered, the calibration events are recorded in dedicated runs, and can be later used in the analysis chain to correct for gain variations.

6.2.5 Observation modes

The MAGIC telescopes can observe in two modes: *on-off* and *wobble*. On the one hand, to observe a source in *on-off* mode, the telescopes first point to source position in the sky (ON), and then, to a dark region of the sky (with no-known gamma-ray source and similar zenith and general conditions), in order to substract the background (OFF). On the other hand, if the *wobble* mode [Fomin *et al.* 1994] is chosen, two opposite directions in the sky, 0.4 degrees away from the source, are observed during 20 minutes each. For *wobble* mode observations, the ON region is defined around the source position in the camera, while the OFF region is centered at a position opposite to the source with respect to the camera center (so-called, the anti-source position). The standard MAGIC analysis uses also two additional OFF regions corresponding to the source position rotated by $\pm 90^{\circ}$ with respect to the camera center, see Figure 6.6. The standard observation mode in MAGIC is the *wobble* mode because, despite the lower sensitivity, it saves observation time and provides a better background estimation.

6.3 Analysis method

The final goals of the data analysis software of a ground-based Cherenkov telescope are: distinguishing between gamma-like and background-like events, determining the energy of the primary γ-ray (to derive the energy spectrum of the detected emission), calculating the incoming direction of the gamma shower to estimate the

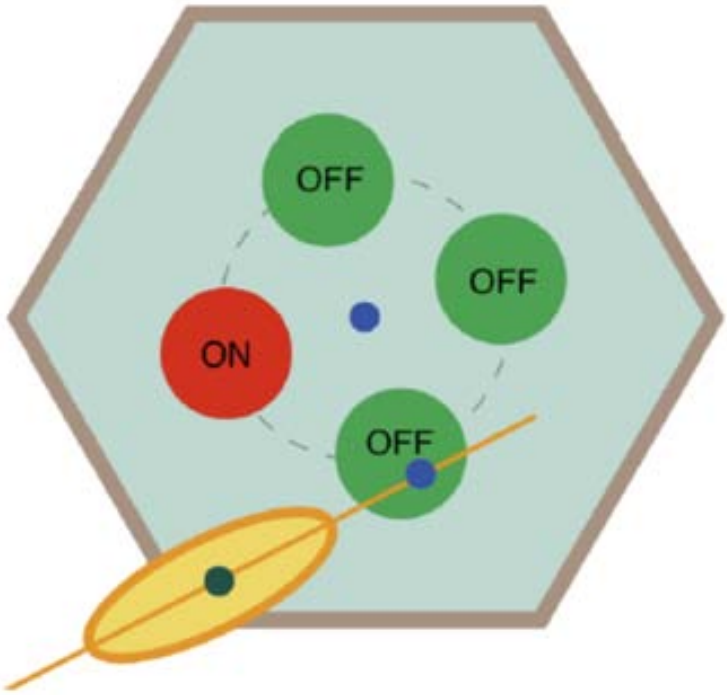

Figure 6.6: Sketch of the definition of the signal (ON) and background (OFF) regions in *wobble* observations. The anti-source is the OFF position located symmetrically to the ON position (the red circle) with respect to the center [Mazin 2007].

position of the emitting source, and determining the arrival time of each γ-ray candidate to produce light curves.

In this section, the analysis technique used in MAGIC will be described in detail. The MARS software package (MAGIC Analysis and Reconstruction Software, [Moralejo *et al.* 2009]) is a collection of programs for the analysis of the MAGIC data, written in C++, in the ROOT framework maintained at CERN. Each program correspond to a certain step in the analysis procedure:

- *callisto*: performs the signal extraction and calibration steps.
- *star*: carries out the image cleaning and calculates the image parameters.
- *osteria*: is in charge of the training of the Random Forest.
- *melibea*: applies the trained matrices to calculate the *hadronnes* parameter and the estimated energy of each event.
- *fluxlc*: calculates the energy spectrum, the effective area and the light curve of the source.
- *celestina/caspar*: produces a skymap of the excess events of the region of the sky that contains the source.

The reconstruction of gamma ray initiated air shower characteristics requires detailed Monte Carlo (MC) simulations of the shower development and of the response of the telescope. In the MAGIC analysis, MC gamma showers are also used to optimize the cuts for background rejection and to estimate the effective collection area after all cuts, which allows converting excess events into a physical flux of γ-rays. The MC simulation program of MAGIC uses the software CORSIKA 6.019 [Heck *et al.* 1998]. Gamma showers are simulated, under the US standard atmosphere, and the output Cherenkov photons that arrive to ground level are recorded. As a second step, the so-called *reflector* program first computes the Cherenkov light attenuation in the atmosphere, and subsequently, the reflexion of the photons on the dish mirrors is simulated. Next, the *camera* program simulates the response of the telescope PMTs and both trigger and DAQ systems. *Camera* also performs a smearing of the arrival directions according to the optical point spread function (PSF) of the telescope. After this point, the simulated events are ready to be used in the MAGIC analysis chain. In the present Thesis, analysis of sources observed in both mono and stereo mode are presented. The analysis chain is introduced in what follows.

Signal extraction and calibration

The Cherenkov photon flashes produce very short signal pulses when they reach the PMTs, which are digitized and stored in the raw data. The reconstruction of this information is called signal extraction. Once the number of counts is recovered, the calibration consists in converting these into number of photoelectrons (phe). Thus, dedicated calibration files are recorded as

explained in 6.2.4 (see also [Gaug 2006]). Up to this point, analyzers can obtain this information directly from the data center at PIC, without personally running the programs or executables.

Image cleaning

At this stage, pixels which contain no signal from the gamma showers are recognized and eliminated. Only the shower image survives. The standard method cleans the image in two steps: first, it selects groups of at least two pixels (*core*) with a phe content higher than a minimum value q_1, then, pixels sorrounding it (*boundary*) can be added if they exceed a signal q_2 and if they also have at least another boundary pixel exceeding q_2. Next, the mean arrival time of all core pixels is calculated. Only those core pixels inside the timing coincidence window (δt_1) are kept, and similarly (δt_2) for the boundary pixels. The usual image cleaning setting used in MAGIC-I analysis has $q_1 = 6$ phe, $q_2 = 3$ phe, $\delta t_1 = 4.5$ ns and $\delta t_2 = 1.5$ ns [Oya 2010]. When arrival time information is not used, a harder image cleaning is applied (e.g. $q_1 = 10$ phe and $q_2 = 5$ phe, which is the one used in MAGIC-II).

Image parameters

The cleaned images can be characterized by the so-called Hillas parameters [Hillas 1985], that are related to the statistical moments of the images up to third order. For a graphical interpretation of some of these, see Figure 6.7. The following parameters are independent of the position of the source in the camera:

- *SIZE:* Total number of phe in the image. It is roughly proportional to the primary particle energy for a fixed impact parameter (distance of the shower from the telescope axis, a.k.a. IP) of the shower.
- *LENGTH:* Second moment of the light distribution along the major image axis.
- *WIDTH:* Second moment of the light distribution along the minor image axis.
- *CONC[N]:* Fraction of the total amount of phe contained in the N most luminous pixels. Usually, N = 2.
- *leakage:* Fraction of the light of the image contained in pixels that belong to the outermost ring of pixels of the camera. It is useful for recognizing images partially outside the camera.
- *M3Long:* Longitudinal third moment of the distribution of the charge along the major axis. It is used to resolve the head/tail degeneracy.
- *time RMS:* It is the RMS of the arrival times of all pixels that survived the image cleaning, and measures the time spread of the arrival times.

The following image parameters are dependent on the position of the source in the camera:

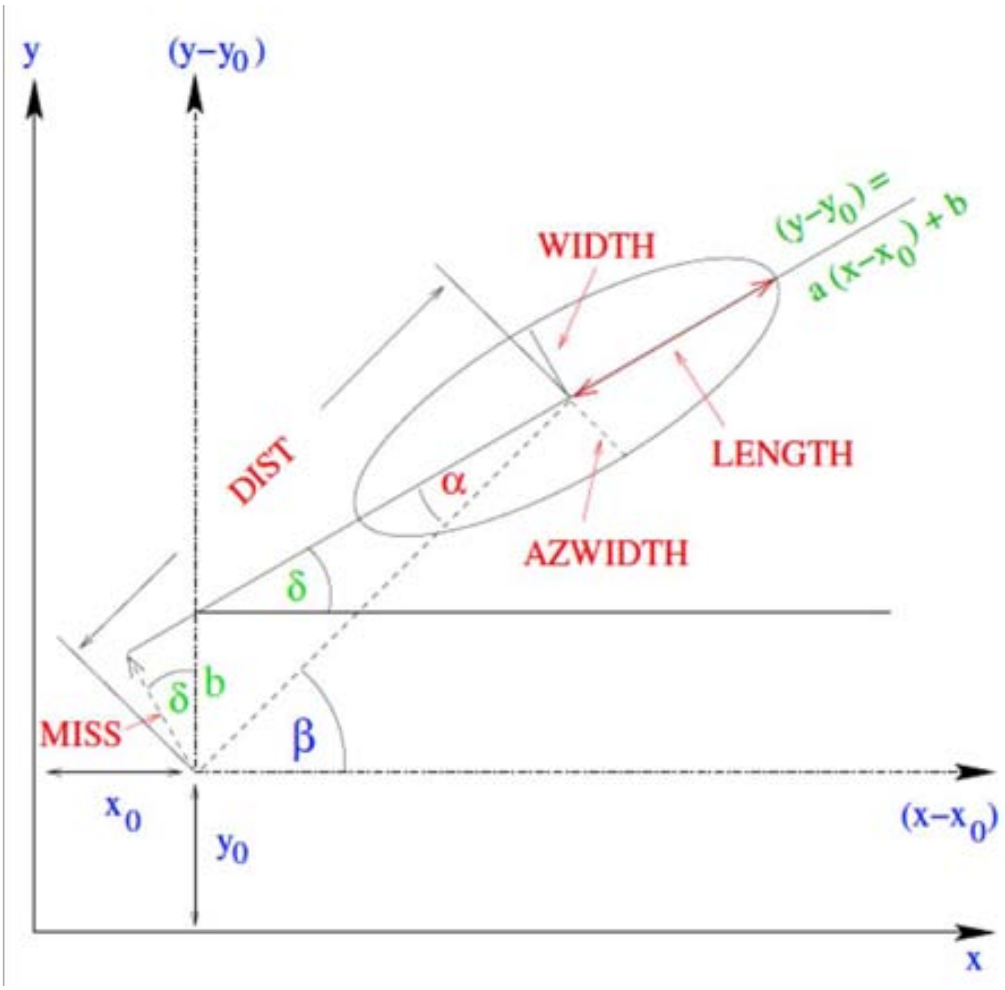

Figure 6.7: Graphical representation of some of image parameters described in the text. The nominal position of the observed source is (x_0, y_0) [Mankuzhiyil 2010].

- *alpha:* Angle (α) between the direction of the major axis and the line connecting the image centroid with the source position. Images from γ-ray showers from the source will have small *alpha* values.
- *Dist:* Distance between the image centroid and the source position in the camera. It is correlated to the impact parameter of the shower.
- *time gradient:* It measures the magnitude of the time profile of the event. This parameter is obtained from the slope of the linear fit applied on the arrival time versus the space coordinate along the major axis.

Note that the time-related image parameters are not exactly Hillas parameters, but are used to enhance the analysis performance [Tescaro *et al.* 2007], [Aliu *et al.* 2009]. There is also another parameter, *Disp*, that allows to produce sky-plots even with a stand-alone Cherenkov telescope and will be introduced in 6.3.1.

Quality selection

Since observations with a Cherenkov telescope are performed under partially controlled conditions, data quality selection cuts need to be done before starting the analysis of any astronomical object. The most reliable and effective parameter is the trigger rate. Since the CR flux is dominated by the constant isotropic hadron background, the trigger rate is expected to be constant during the observation time. Therefore, a cut on the event trigger rate is an effective quality cut to avoid, for instance, bad weather condictions like clouds or dust in the air (*calima*).

A typical MAGIC analysis usually includes a few hours of observation of the Crab Nebula source. These observations are chosen as close as possible to the observation period and zenith angle of the analyzed source. Given the strong and steady signal from the Crab Nebula (considered a standard candle in γ-ray Astronomy), these data are considered as a test sample where to check the consistency and sensitivity of the current analysis.

6.3.1 Mono observations

The tasks that are going to be explained below try to estimate the main characteristics of the primary particle that originated the air shower: the nature, energy and direction of the primary γ-ray. The corresponding programs in MARS are *osteria* and *melibea*.

Background rejection

In order to discriminate images of gamma showers from the much more abundant images of hadronic origin, as well as those from isolated muons and fluctuations of the night sky background, previously described image parameters are used (also others like the zenith distance). MAGIC analysis makes use of the *Random Forest* (RF) method for this task. The RF method uses a *forest*

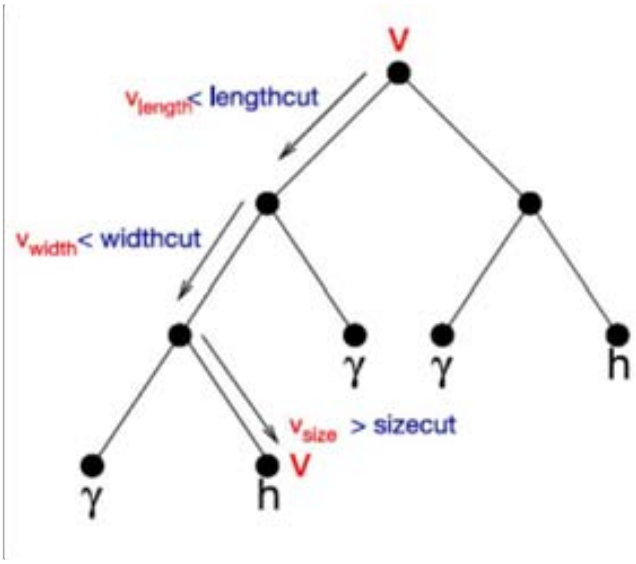

Figure 6.8: Sketch of a *tree* structure for the classification of an event v via size, length and width. The decision path through the *tree*, leading to classification of the event as hadron can be followed [Errando 2009].

of decision *trees* to classify each event. The decision *trees* are created (trained) from MC simulated γ-ray events and real events from hadron events from unaltered data samples (sometimes, also off-data samples). The individual *trees* are grown by using a list of image parameters with a proven discrimination power and finding adequate cuts on these parameters (see Figure 6.8). From the training sample, a binary decision *tree* can be constructed, subdividing the parameter space in two parts, and iteratively repeating the process. The procedure stops when a sub sample composed only by gammas or by hadrons is found (a *leaf* of the *tree* is reached). The ending *leaf* is labeled as a 0 (gamma) or 1 (hadron).

The background rejection takes place after the training. Each event is passed through all decision *trees* and they will score 0 or 1, depending on the reached *leaf* label. A mean score is computed averaging over all the different separation *tree* results. This average is called *hadronness* (h) and represents a sort of probability for the event to be a hadron (h close to 1) or a gamma (h close to 0). There are two kinds of parameters used to train the h parameter: parameters which have power to discriminate between hadrons and γs (*WIDTH, LENGTH, CONC, Dist, M3Long, time RMS* and *time Gradient*) and, also, *SIZE* and *zenith distance* because the rest of parameters depend strongly on the size of the shower images. Including these last two, the cuts in RF can be scaled dynamically with the geometry of the shower image.

Energy reconstrucion

The energy of the γ-ray events is also reconstructed by the Random Forest

method, using training MC γ-ray samples. A MC simulated γ-ray sample with a known primary γ-ray energy is filled in bins of logarithmic energy. The classiffier will be trained to accommodate each event in a particular energy bin. After this, each tree will assign a specific energy range to each event, that will be analogous to the previously described *hadronness* parameter. The parameters used normally are *WIDTH, LENGTH, SIZE, log(SIZE/(WIDTH LENGTH)), CONC, leakage, ZD, Dist* and *time Gradient*, being the last two source position dependent. The obtained energy resolution is about 20% for energies from 100 GeV to 10 TeV, increasing at lower energies and decreasing for higher ones. The energy of the γ-rays is usually overestimated at low energies ($<$100 GeV) and underestimated at higher energies ($>$10 TeV). The finite resolution and bias require that the energy estimation is later corrected by the spectrum unfolding, using a migration matrix.

Analysis approaches (α and θ^2)

The analyzer can either decide to go for an *alpha*-type analysis or a *theta*-square-type analysis. *Alpha* has already been described with the image parameters. *Theta*, (θ), is the angular distance in the sky between the expected emitting position and the reconstructed incoming direction of the recorded shower. An excess of events at small values of *alpha* or θ^2 is expected, as the γ-ray shower images will be oriented towards the center of the camera. The *alpha*-analysis approach is suitable when the emitting source can be considered as point-like. If the point-like source has very well known sky coordinates a source-dependent analysis can be performed: a priori assumptions about the location of the source are done. The advantages are that, by using some extra image parameters (like *M3long* or the *time gradient*), a better background rejection and an enhanced sensitivity in the analysis are achieved. The θ^2-analysis is, instead, more suitable when the source of gamma rays is extended or when the position of a point-like source is not well known. A source-independent analysis allows the production of sky maps showing the excess of gamma rays in the observation field, but no assumptions about the source location are done, resulting in a less sensitive analysis. In the case of a single dish telescope, the reconstruction of the primary gamma direction is done through the so-called *Disp* method.

Once this step of the analysis is reached, the signal may have been found as arriving from the pointed source. If the signal is strong enough, both a spectrum and a light curve can be calculated with *fluxlc*. If it is not statistically meaningful, differential or integral upper limits on the gamma-ray flux can be set. There is also the possibility of producing a skymap, by projecting the arrival directions of the selected gamma-ray candidates into celestial coordinates.

Spectrum

The differencial energy spectrum of a source is defined as the number of γ-rays arriving to Earth, per unit of energy, time and area:

$$\frac{dF}{dE} = \frac{dN_\gamma}{dt dA_{eff} dE} \tag{6.5}$$

Here N_γ is the number of detected γ-rays and t the exposure time. The effective collection area, A_{eff}, is the area in which air showers can be observed by the telescope, folded with the efficiency of all the cuts applied in the analysis (ε_γ). It increases with the zenithal angle (specially above 45 degrees). This cut efficiency can be estimated using MC gamma rays, and is defined as the number of produced gammas divided by the number of events that survive the analysis cuts. Loose background rejection cuts are applied in order to compute the spectrum because they reduce the effect of systematic uncertainties and provide larger statistic of excess events.

Due to the finite resolution of the detector and the bias introduced in the energy estimation, the measured spectra become distorted. The unfolding procedure tries to correct this distortion. Those biases are due to the fact that the true energy of the incoming gamma-rays is not measured but indirectly estimated. Several unfolding methods can be chosen in the MAGIC analysis, differing from the algorithm used for the calculation of the true distribution [Albert *et al.* 2007c]. An agreement within the different methods is required to trust the obtained results.

The *light curves* are plots where the integral gamma-ray flux above a certain energy is shown as function of the observation epoch. Cuts used for the *light curve* are the same as for the spectrum calculation.

Skymap

As mentioned previously, sky maps are calculated by reconstructing the arrival directions of the gamma-like showers in camera coordinates and projecting them into celestial coordinates. The arrival direction of the gamma-ray images is estimated using the *Disp* method ([Lessard *et al.* 2001], [Domingo-Santamaría *et al.* 2005]). The method assumes that the arrival direction of the primary particle lies on the major axis of the shower. The *Disp* parameter is defined as the angular distance between the reconstructed source position in the camera and the center of gravity of the shower image. The parameterization used to calculate *Disp* is optimized using a MC gamma-ray sample, and is a function of the image parameters. One important degeneracy in the *Disp* method are the two solutions found for a source location: one in the head of the image and another in the tail. The *M3long* parameter is used to choose and place the source position always closer to the head of the image. The program used to perform skymaps is called *celestina*. It produces sky plots with three background estimation methods, on-off, *wobble* and model, depending on the observation mode (the latter serves for both). Recently, two -simpler- programs have replaced *celestina*: *caspar* and *zinc*. *Zinc* is to the *celestina* model skyplots what *caspar* is to the *celestina* wobble skyplots. In

the present work, when observations in wobble mode are presented, *caspar* is the chosen program to reproduce skymaps, and the background estimation was done from the same data set. However, in one set of observations, the *celestina* program has been used (on-off observations, see next Chapter for details), due to the fact that *zinc* was still not available at that moment. After the background is built, a map of excess events is generated by subtracting the distribution of background events to the γ-ray candidates. The excess map is smoothed using the PSF of the telescope.

6.3.2 Stereo observations

Since fall 2009, MAGIC-II has joined its twin Cherenkov telescope MAGIC-I in the observing duty. The two telescopes can be operated independently or in stereoscopic mode. The stereoscopic mode leads to a better reconstruction of the image parameters and a stronger background suppression. When an image of the shower is obtained with the two telescopes, image parameters are individually obtained from the signal of each telescope, and then combined to calculate stereo parameters. The incoming direction of the shower (i.e., the source position) is obtained from the intersection of the major axes of the two images of the shower. In addition, the height of the shower maximum can also be estimated.

The stereo analysis, therefore, uses the θ^2-approach as the standard one. The rest of the chain consists basically on duplicating each step: two calibration, two random forests and two star files are generated, both for the data and the MC. After that, a new program called *SuperStar* is used to convert two star files with individual-image parameters to a Stereo-Parameter file. It performs the stereoscopic reconstruction of the shower parameters (direction, ground impact, altitude) and can also reconstruct the energy from look-up tables. Then, modified versions (to make use of the stereo parameters) of *melibea, fluxlc* and *caspar/zinc* complete the analysis method.

Chapter 7

Two Milagro-detected, Bright Fermi Sources in the Region of SNR G65.1+0.6

Contents

7.1 Motivation

Since the launch of the *Fermi* satellite and the publication of new source list, several proposals were presented by the different IAC telescope collaborations to carry out a follow up of these sources up to the highest energies. In February 2009, the *Fermi* collaboration published a list of the most significant gamma-ray sources above 100 MeV, detected by the large area telescope (LAT) within 3 months of observation [Abdo *et al.* 2009c]. Among the galactic sources detected by LAT, 34 were within the field of view of the Milagro gamma-ray observatory ([Abdo *et al.* 2009i] and references within). The sensitivity of this instrument peaks in the energy range $10 - 50\,\mathrm{TeV}$. Consequently, the Milagro collaboration re-analysed their previous skymap looking for counterparts [Abdo *et al.* 2009i], and claimed 14 new sources with confidence levels above $3\,\sigma$. Since many of them were positionally coincident with *Fermi* pulsars, they are mostly believed to be Pulsar Wind Nebula (PWN), or similar sources.

The MAGIC telescope (described in the previous Chapter) is a well-suited instrument to study the energy range between *Fermi* and Milagro. To select possible candidates for MAGIC, an interpolation of the fluxes given by both experiments was calculated in two different ways. The Fermi Bright Source List provides an integral value above 1 GeV, whereas the Milagro sources are listed together with their differential flux points normalized at 35 TeV. Firstly, a power law interpolation

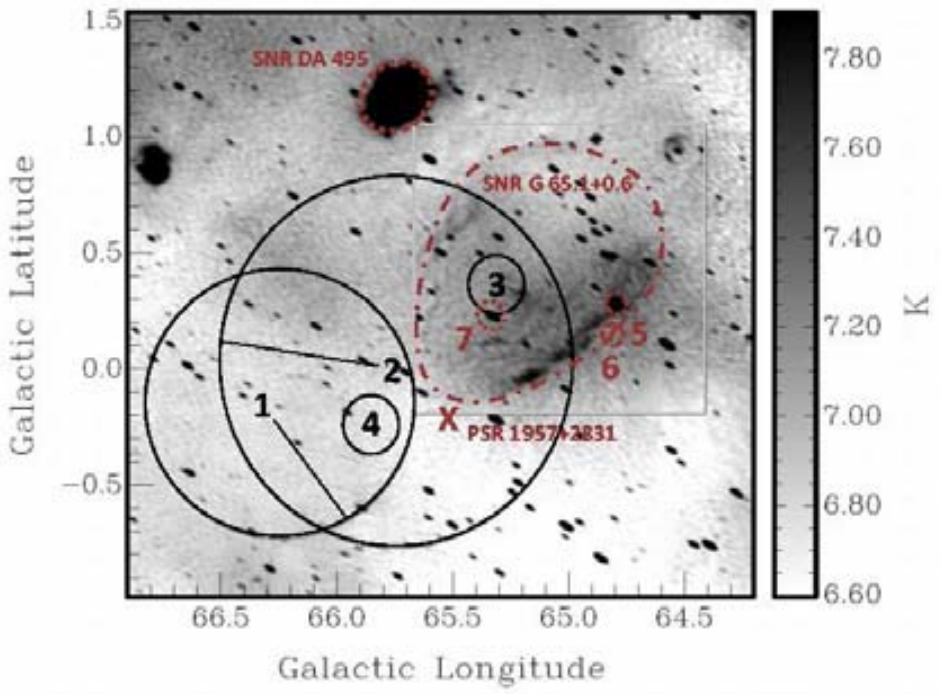

Figure 7.1: Radio image of the region around SNR G65.1+0.6. The numbered objects are: (1) 3EG J1958+2909, (2) 2 CG 065+00, (3) 0FGL J1954+2838, (4) 0FGL J1958.1+2848, (5) region of different spectral index, (6) IRAS 19520+2759, (7) bright compact radio object.

can be done from these two values, resulting in a flux value at 1 TeV and a spectral index. Since the *Fermi* flux is likely to contain both pulsar and steady emission, this value is probably an overestimation. Thus, a second flux estimation may be done by extrapolating the Milagro value to 1 TeV, assuming a power law index of 2.1. The expected flux range optimal for MAGIC observations lies in between these estimated values. Looking for interesting sources, those that were already observed by MAGIC were ruled out (i.e. those in the H.E.S.S. scan of the galactic plane), together with the ones that were below the threshold sensitivity. An interesting object that did not fulfill these characteristics appears in the region of SNR G56.1+06. It turned out to be the pulsar 0FGL J1954.4+2838, with a calculated flux range of $2\% - 4.9\%$ of Crab.

In fact, this region is densely populated, as can be seen in Figure 7.1, and the objects it contains and their likely associations is still a matter of debate. G65.1+0.6 (dash-dotted shape) is a faint supernova remnant (SNR) first reported by [Landecker *et al.* 1990]. In [Tian & Leahy 2006], a distance of 9.2 kpc and a Sedov age of $40 - 140$ kyr were suggested. Despite its distance, it is a very extended object ($90' \times 50'$). Very close to the already mentioned *Fermi* source (labeled 3 in the Figure 7.1), there is a strong compact radio object (7). In the southern rim of the shell, a region with different spectral indexes (5), originally thought to be an extra-

galactic object [Seiradakis *et al.* 1985], can be found. Also, the nearby pulsar PSR 1957+2831 (X) may be associated to the remnant [Tian & Leahy 2006], due to the compatibility of its characteristic age. Looking at longer wavelenghts, the infrared source IRAS 19520+2759 (6) has been suggested to be at a similar distance of the SNR and, given that it has associated a CO line, a H_2O and OH maser emission, an interaction between the molecular cloud and the remnant could be a possible scenario [Arquilla & Kwok 1987].

The gamma-ray emission in the region of G65.1+0.6 was first detected by the COS-B satellite [Swanenburg *et al.* 1981] as 2CG065+00, and later confirmed by the EGRET satellite (3EG J1958+2909) in [Hartman *et al.* 1999], where a possible extension or multiple sources were denoted. But it was only recently that *Fermi* could clarify their signal as caused by the two sources 0FGL J1954 + 2838 and 0FGL J1958.1 + 2848 (3 and 4 in Figure 7.1).

Observing the SNR G65.1+06 region, MAGIC was expected to deliver the following scientific results:

- Establishing the location of the $\gamma-$ray source with a resolution exceeding the one of *Fermi*. This might clarify whether the origin of the radiation comes from inside the shell, or even from a compact object.

- Obtaining a complete spectrum, together with *Fermi* and Milagro results, to characterize the source at very high energies. On the one hand, the result may shed some light to confirm the SNR as the source of the emission. On the other hand, if no signal is found, it would imply that the Milagro object is not identical to the *Fermi* Bright source. For instance, Milagro could be seeing the interaction between the SNR and the molecular cloud. In this case, one of the pulsars (1957+2831 or 1954+2838) may not belong to G65.1+0.6.

- Profiting from the inclusion of other objects in the field of view of the camera to obtain hints to other detections. These other objects are a pulsar, the rim of the SNR and the infrared region, among others.

The results of the study of this region were published in the Astrophysical Journal in 2010 [Aleksić *et al.* 2010], and the PhD student is one of the corresponding co-authors in this paper.

7.2 Observations

The observations were centered on the Fermi Bright source 0FGL J1954.4 + 2838 (from now on referred as $J1954_0$) in July and August 2009. The observations were carried out in wobble mode (see previous Chapter, or [Fomin *et al.* 1994]), which yielded two datasets with offsets of $\pm 0.4^\circ$ in RA from this source, see Figure 7.2. The wobble position was alterned every 20 min, and the data were taken at zenith angles between 0 and 40 degrees. At the time, the MAGIC-II telescope was still

under comissioning, therefore the analysis performed here uses only the data from the stand-alone MAGIC-I telescope.

Summer observation time at the MAGIC site usually implies calima: dust suspended in the atmosphere coming from the Sahara desert, that interferes with the quality of the data taking. Therefore, from the total amount of time observed, only 24.7 hours survived the quality selection cuts. Those cuts were applied to the data runs mainly based on the steadiness of the event rate after image cleaning, but also considering a few parameters that characterize the transparency of the atmosphere, such as the sky temperature and humidity. An additional cut removed the events with a total charge (*size*) of less than 100 photoelectrons, thus providing a better background rejection.

As it was previously stated, this region included other interesting objects. Specifically, there was another *Fermi* source, 0FGL $J1958.1+2848$ (shortly referred as $\mathrm{J1958_0}$), in the field of view of one of the two wobble positions. 12.6 hours of effective observation time were analyzed for this object.

7.3 Data analysis

Each data set was analyzed in the MARS analysis framework (see previous Chapter, [Moralejo *et al.* 2009]), standard software for the analysis of MAGIC data. To look for the signal coming from the two Milagro-detected *Fermi* sources, a standard analysis was performed, using θ^2 plots and skymaps. It shall be noted, though, that when the 1-year catalog of *Fermi* sources [Abdo *et al.* 2010a] was released, the exact coordinates of both now identified pulsars (1FGL J1954.3 + 2836 and 1FGL J1958.6 + 2845, in short J1954 and J958, respectively) changed respect to the ones given in the previous Fermi Bright Source list (0FGL J1954 + 2838 and 0FGL J1958.1 + 2848, named in this text $\mathrm{J1954_0}$ and $\mathrm{J958_0}$, respectively). The whole analysis had to be repeated, this time using the latest more accurate source positions.

Both sources had to be analized differently. In the case of J1954, a standard wobble analysis could be done: in such case, the exposure inhomogeneities cancel out when comparing the photon flux from the source to the one on the opposite side of the camera (called anti-source, see Figure 7.2). However, for J1958, a wobble analysis using only one of the two wobble positions does not guarantee this cancelation. Therefore, the analysis was done in ON/OFF mode, using the near wobble sample as ON-source data and the far wobble sample as OFF-source data. Having the OFF-source at the same position in relative camera coordinates as the source in the ON sample, the exposure inhomogeneities may cancel out.

Figure 7.3 shows the θ^2 distributions for each source, where the values in the horizontal axis represent the squared angular distances between photon directions and the source position. In the case of having a very high energy (VHE) gamma-ray emission coming from the observed source, an excess is expected to appear for low θ^2 values, see section 6.3.1. This excess comes from substracting the background

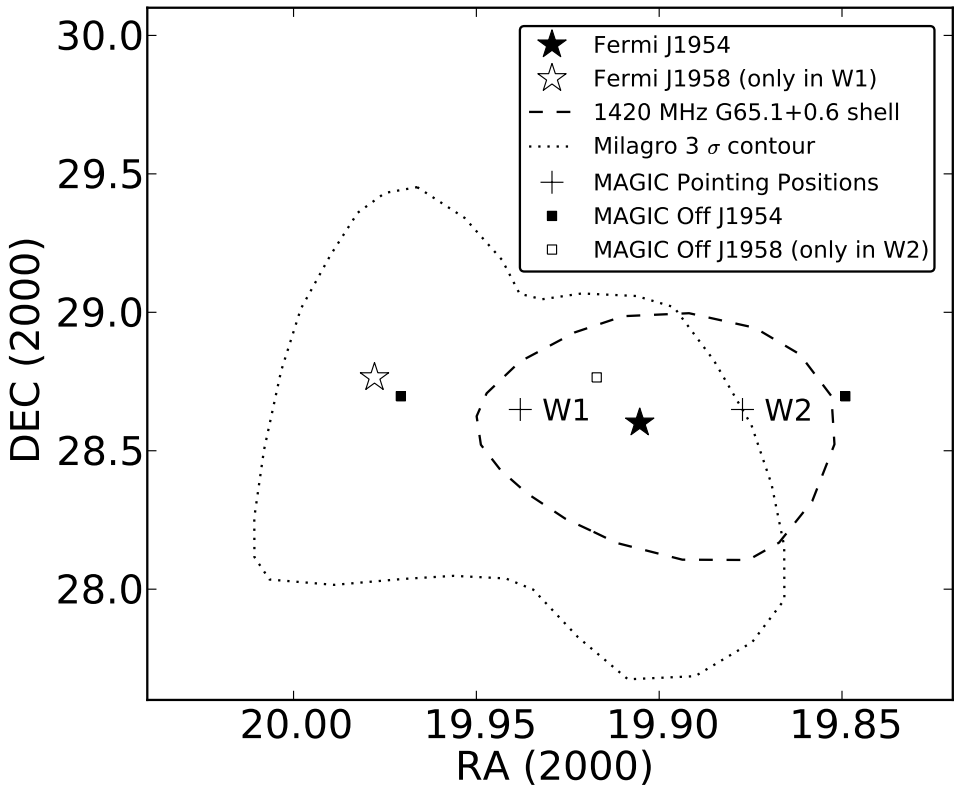

Figure 7.2: Observation setup for the two *Fermi* sources J1954 and J1958 in the context of SNR G65.1+0.6 and a Milagro significance contour. J1958 appears only in one wobble position (W1), so the OFF data is taken from the other wobble sample, using the same position relative to the pointing direction. The outline of the remnant is taken from the radio map in [Landecker *et al.* 1990]. The extension of the Milagro significance contour [Abdo *et al.* 2009i] is compatible with their point spread function.

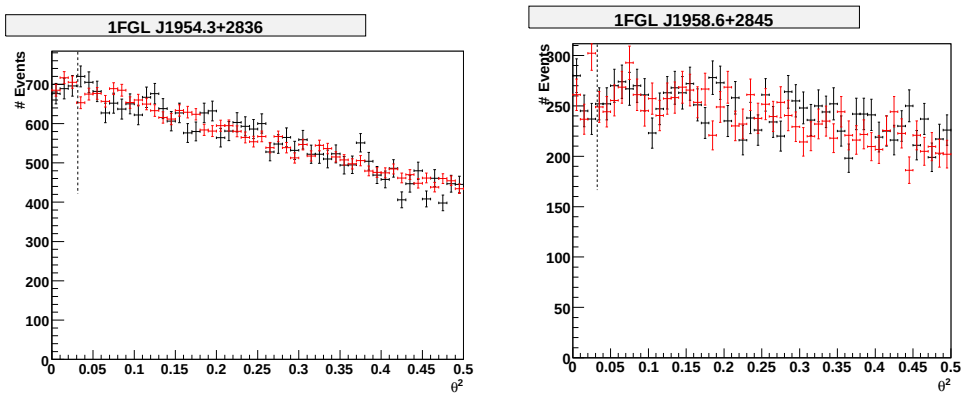

Figure 7.3: Plots showing the θ^2 distributions for J1954 (left) and J1958 (right). The shapes of the ON and OFF distributions agree well with each other in both sources, which means there is no $\gamma-$ray signal. The dashed lines indicate the signal regions.

to the number of events around the source position (ON events), having previously estimated the background by counting the events around the anti-source position (OFF events). The number of OFF regions explored in the analysis of J1954 was one and three, although only the last option is shown in the Figure 7.3. Therefore, the unlikely case of an emission occuring by chance at both ON and OFF locations at a similar flux level is discarded. Furthermore, a cut in *hadronnes* of 0.1 was applied to improve the background estimation and determine the signal region separately in both sources. No significant signal could be found in any of the sources.

In order to find a signal using a blind search (i.e., regardless of the source position), skymaps in a region of $2.8° \times 2.0°$ were drawn in different energy ranges. The same cuts in *hadronnes* (0.1) and size (100) as in the θ^2 plots were applied to the maps. Figure 7.4 shows the skymap for both sources above 200 GeV. No significant signal could be found in any of the skyplots in either of the sources.

7.4 Upper limits on the gamma-ray flux

Since no signal could be retrieved from the SNR G65.1+0.6 region, upper limits were calculated of the integral and differential flux. To obtain the differential upper limit (u.l.) values, the data was divided into three bins of estimated energy (starting from 120 GeV, going to 375 GeV, then 2.8 TeV and finally 12 TeV). From the θ^2-plots, an event number upper limit was calculated at 95% confidence level (c.l.) for each bin, using the method described in [Rolke *et al.* 2005]. An efficiency systematic error of 30% was assumed [Albert *et al.* 2008b]. To calculate the flux upper limit, the number of events per energy bin is established to be:

$$N = t_{eff} \int \Phi(E) A_{eff}(E) dE \tag{7.1}$$

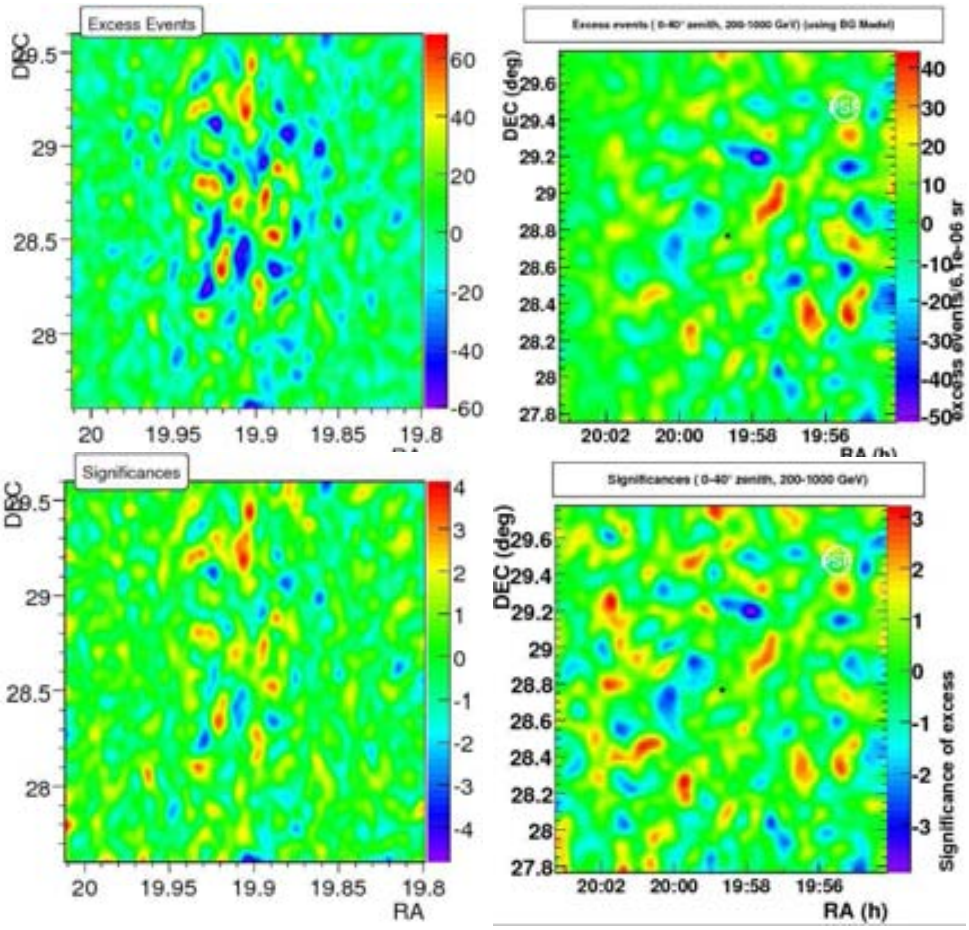

Figure 7.4: Skymaps of the excess events (top) and significance (bottom) for J1954 (left) and J1958 (right). The black star shows the center of the pointed source, the white circle represents the MAGIC point spread function (PSF) at mid energies. The distribution of significances are well-fitted with a simple gaussian.

Table 7.1: Differential upper limits for both sources, for the present crosscheck analysis.

Source Name	Extension (deg)	$E_{\rm med}$ (GeV)	Significance (σ)	$F_{95\%}$ ($10^{-12}\,{\rm TeV}^{-1}{\rm cm}^{-2}{\rm s}^{-1}$)
1FGL J1954.3+2836	≤ 0.08	221	-1.4	25
		980	-1.0	0.5
		5686	+2.2	0.022
1FGL J1958.6+2845	≤ 0.08	221	-1.0	76
		966	-0.9	0.71
		5123	+0.7	0.033

where Φ is the flux (photons per unit of time, energy and area), t_{eff} is the effective time of observation and A_{eff} is the effective area after cuts. To simulate this A_{eff}(E), a power law energy spectrum with a photon index of -2.1 is assumed for each energy bin:

$$\Phi = K \left(\frac{E}{E_0} \right)^{-2.1} \tag{7.2}$$

where K is a normalization factor. The influence of the photon index is minor, since the energy ranges are sufficiently small. Once the upper limit is derived from the number of events (N_{ul}), the conversion to flux upper limits uses (in each energy bin):

$$K \leq \frac{N_{ul}}{t_{eff} \int (E/E_0)^{-2.1} A_{eff}(E) dE} \tag{7.3}$$

The mean $\gamma-$ray energy in each bin of reconstructed energies, after all cuts, can be obtained through Monte Carlo simulations, since the data can only be selected by an estimated energy.

Until this point, the analysis was performed assuming the sources were point-like, i.e. the extension was supposed similar or smaller than the PSF of MAGIC (defined as the sigma of a two dimensional Gaussian function). For this case, it was considered to be 0.08°. In this particular region, though, $\gamma-$rays may come from an extended source (a PWN or the shell of the SNR). Therefore, another upper limit for the flux was calculated, assuming an extension of 0.3°. This particular value was chosen because the biggest TeV PWNe have sizes of few tens of parsecs, which at the distance of G65.1+0.6 would be within this radius. Increasing the signal integration radius, more background events are included and that leads, thus, to higher upper limits. The derived 95% c.l. flux upper limits are summarized in Table 7.1. The differences between the limits of J1954 and J1958 are all compatible within the statistical fluctuations.

Also, an integral upper limit above 200 GeV was derived for each source. The results were 3×10^{-13} TeV^{-1} cm^{-2} s^{-1} for J1954 and 4×10^{-13} TeV^{-1} cm^{-2} s^{-1} for J1958, which can also be translated in commonly used units as 3% and 2% of Crab Nebula flux, respectively.

Table 7.2: Characteristic parameters of the two Fermi pulsars 1FGL $J1954.3+2836$ and 1FGL $J1958.6+2845$, refereed as J1954 and J1958, respectively. See references in the text.

Parameters	1FGL J1954.3+2836	1FGL J1958.6+2845
Age (kyr)	69.5	21
Period (ms)	290	92.7
Spin-down luminosity (erg/s)	10.48×10^{35}	3.39×10^{35}
Energy cut-off (GeV)	2.9	1.2

7.5 Interpretation and discussion

When the 1-year *Fermi* Catalog was released, J1954 and J958 could be reported as $\gamma-$ray pulsars thanks to a blind search ([Saz Parkinson *et al.* 2010], [Abdo *et al.* 2009d] and [Abdo *et al.* 2010b]). They appeared to be normal *Fermi* pulsars, as can be seen in their characteristic parameters listed in the table 7.2. Before this happened, significances of $4.3\,\sigma$ for $J1954_0$ and $4.0\,\sigma$ for $J1958_0$ were claimed as detections by Milagro [Abdo *et al.* 2009i]. Given that the angular resolution of Milagro is about $0.4° - 1.0°$, those values are still correct for the 1-year catalog positions of the sources, which are offset by $\leq 0.1°$. Flux values were determined for a characteristic median energy of 35 TeV. As it is shown in Figure 7.1, the region of SNR G65.1+0.6 is densely populated, and Milagro sources could be associated with the *Fermi* pulsars, a possible extragalactic source, a molecular cloud interacting with the SNR or a radio compact object (see section 7.1 for further details). However, the most likely assumption was that they were indeed related to the objects observed by *Fermi*, i.e., that they were PWNe or, in the case of J1954, the shell of the SNR, which surrounds the pulsar. Gamma-rays at TeV energies could also be produced in an interaction of the shell with a coincident molecular cloud, such as the infrared source IRAS 19520+2759 (figure 7.1).

The upper limits calculated on the flux at 1 TeV, at the maximum of the MAGIC sensitivity, present values of 3% and 2% of Crab for J1954 and J1958, respectively. Therefore, the photon index in the energy range of 1 to 35 TeV must be harder than 2.2 for J1954, and 2.1 for J1958, if an association between the Milagro and the *Fermi* objects is assumed and they are treated as point-like objects. The spectral energy distribution (SED) would be thus likely to peak at energies greater than 1 TeV. On the other hand, if an extension up to 0.3° is assumed, the corresponding flux limits in Crab Nebula units are 14% for J1954 and 3% for J1958. In this extended case, the photon indices would be limited to values inferior to 2.6 and 2.2, respectively.

A complete SED, covering from the *Fermi* to the Milagro energies, can be constructed by adding the MAGIC upper limits (see Figure 7.5). From this general picture, it can be stated that the most likely scenario to explain the gamma ray emission detected by Milagro might be the presence of two PWNe, associated with the *Fermi* pulsars. Given the old ages of the pulsars (see table 7.2), it is reasonable

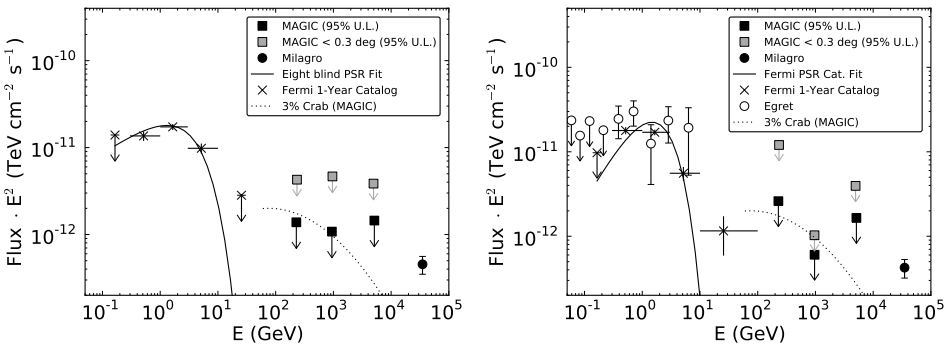

Figure 7.5: Compilation of flux measurements and upper limits for: (left) 1FGL J1954.3+2836 from *Fermi* [Saz Parkinson *et al.* 2010, Abdo *et al.* 2010a] , (right) 1FGL J1958.6+2845 from EGRET [Hartman *et al.* 1999], *Fermi* [Abdo *et al.* 2010b, Abdo *et al.* 2010a], together with MAGIC and Milagro [Abdo *et al.* 2009i] data. The 3% fraction of the MAGIC Crab spectrum [Albert *et al.* 2008b] is shown for comparison.

to expect an inverse compton component that dominates their energy outflows, and consequently the VHE emission to be extended [de Jager & Djannati-Ataï 2009], [Tanaka & Takahara 2009].

7.6 Conclusions

After the analysis of nearly 25 hours of good quality data in the region of the SNR G65.1+0.6, no significant γ-ray emission could be found in the MAGIC energy range (from hundreds of GeV to several TeV). In that same region, the Milagro collaboration had reported the emission of γ-rays, with a median energy of 35 TeV, and the *Fermi* satellite had detected two pulsars, 1FGL J1954.3 + 2836 and 1FGL J1958.6 + 2845. The lack of detection with the MAGIC-I telescope, both using the a-priori source-position analysis and a skymap of the area, yielded three differential flux upper limits for each source.

In the light of MAGIC results, the flux upper limits support the scenario in which the multi-TeV emission measured by Milagro is caused by a different mechanism than the emission detected by *Fermi*. Taking into account the ages of the pulsars and the SNR, the existence of two old PWNe – powered by the two GeV pulsars – is one of the likely scenarios.

Chapter 8

Simulations of CTA response to particular science cases

Contents

The CTA experiment (Cherenkov Telescope Array) [1] has been defined as the next generation of telescopes using the Cherenkov technique. In the energy range of few TeVs, the CTA sensitivity will improve by one order of magnitude compared to the previous generation experiments (like MAGIC or H.E.S.S.). In addition, the energy range will also be expanded, from 0.01 to 100 TeV, thanks to the large number of different sized Cherenkov telescopes. Furthermore, an improvement regarding the angular resolution is expected by achieving a better resolution and higher photon statistics that can refine the imaging of the air showers. In order to achieve full-sky coverage, two arrays will be built: one in the northern and one in the southern hemisphere. The northern site is planned to focus on extragalactic sources, whereas the southern one will take care of the galactic sources, specially since it will cover the central galactic plane. CTA is planned as an open observatory, with transparent access to data, analysis tools and user training. The main design work has been perfomed [Hofmann *et al.* 2010], and now it is facing the prototyping and construction phases. Simulations of CTA response to interesting science cases are presented below.

8.1 Sorting out different layouts and configurations for CTA

At an early stage of the design of the CTA array, several layouts were generated, each of them with different distributions and types of telescopes. These configurations

[1] http://www.cta-observatory.org/

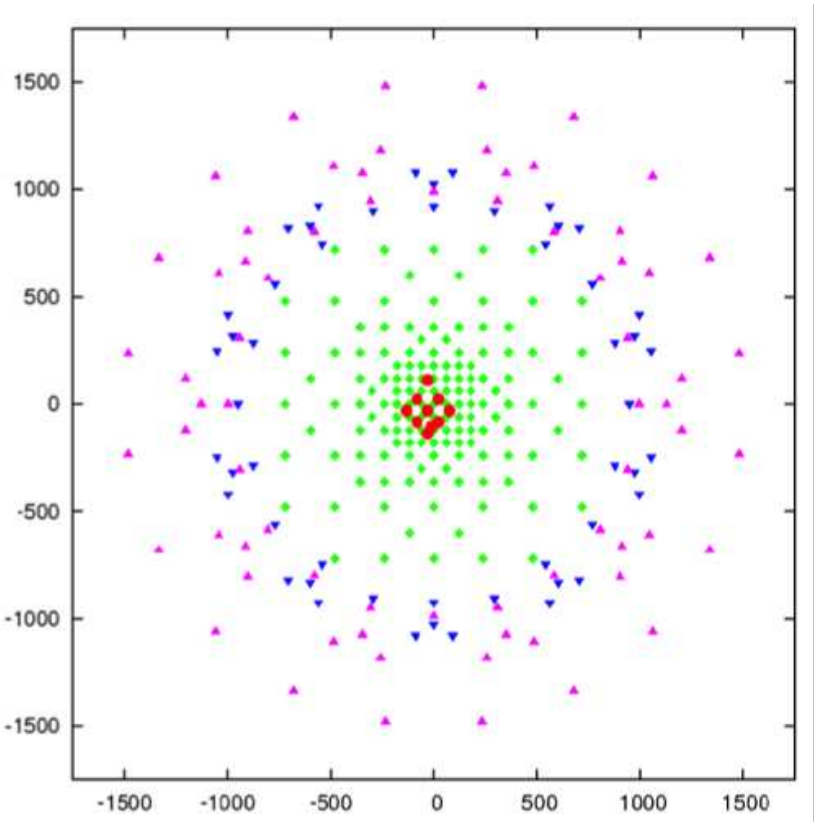

Figure 8.1: Konrad Bernlöhrs adapted layout of the original ultra-CTA (from Padova 2008 CTA meeting). Four types of telescopes are plotted, see table 8.1 for details, being 1 = red, 2 = green, 3 = blue and 4 = magenta.

Table 8.1: Main characteristics of different types of telescopes for CTA.

	Area	Diameter	F.o.V.	Pixels
1	$412\,\mathrm{m}^2$	23 m	5°	0.09°
2	$100\,\mathrm{m}^2$	11 m	8°	0.18°
3	$37\,\mathrm{m}^2$	7 m	10°	0.25°
4	$100\,\mathrm{m}^2$	11 m	10°	0.18°

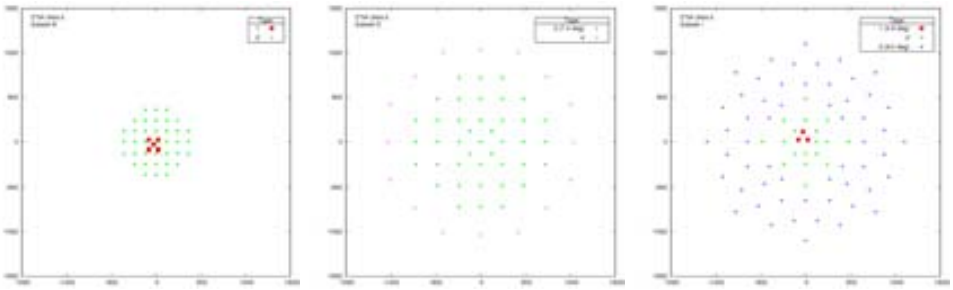

Figure 8.2: Layout configurations of the three representatives: B (left), D (center), I (right). The types of telescopes corresponds to the ones detailed in Table 8.1, being 1 (red), 2 (green), 3 (blue), 4 (magenta), the number in brackets corresponds to the field of view of each telescope.

of CTA were originally taken as subsets of the so-called ultra-CTA (see Figure 8.1), and were selected ensuring a similar construction cost. The initial studies for the Physics group started with these 11 configurations (named from A to K). The very first step consisted on grouping and comparing all of them in order to understand their intrinsic characteristics and make any subsequent analysis easier. The final goal was to work only with one representative configuration from each group, and analyze different sources with these representatives.

All the configurations were classified, in a first approximation, by looking at the differential sensitivity, and maximizing their response at low energies (LE), high energies (HE) and over the whole energy range. In the end, three simulated configurations were chosen from each group with the following characteristics:

- Compact distribution with bigger telescopes, optimized at LE.
- Extended distribution with mid-size telescopes, optimized at HE.
- Mix of the previous two: optimized over the whole energy range.

The choices were validated comparing each representative to the rest of the configurations of their respective groups. Then, deviations from the representative were calculated, quantifying the goodness of the representative with respect to the others in the same group.

Finally, comparing the angular and energy resolution, the chosen configurations were still good representatives at LE, HE and over the whole energy range, see Figures 8.4 and 8.5. Once the configurations were successfully classified, the three representatives (B, D, I) were used to simulate the spectra and light curves of specific sources, which could be interesting cases for CTA.

8.2 A brief look at starting-up tools

In the following sections, the simulated response of CTA has been calculated using the following macros provided by Daniel Mazin:

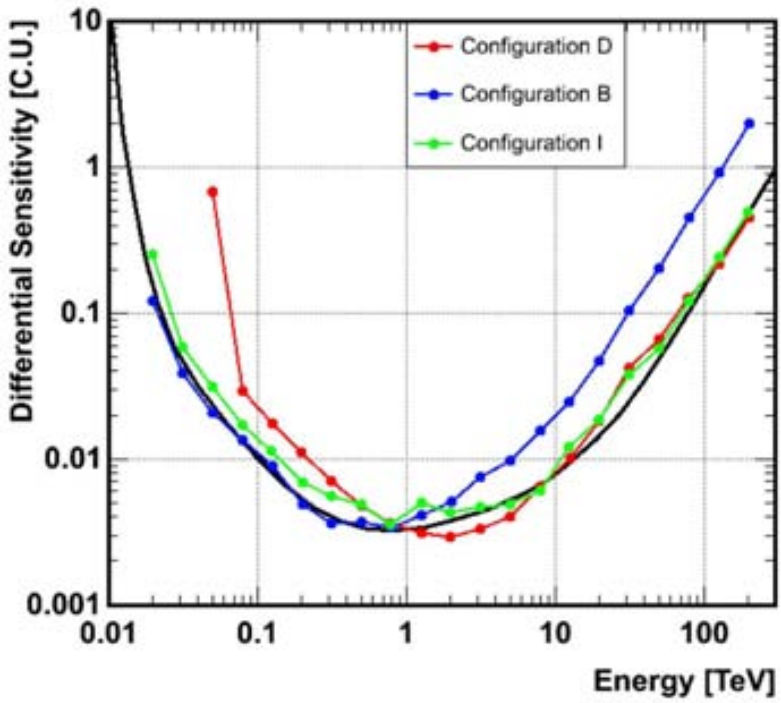

Figure 8.3: Differential sensitivity of the three representative configurations: D (red), B (blue), I (green), in Crab units (C.U.) for 50 hours of observation.

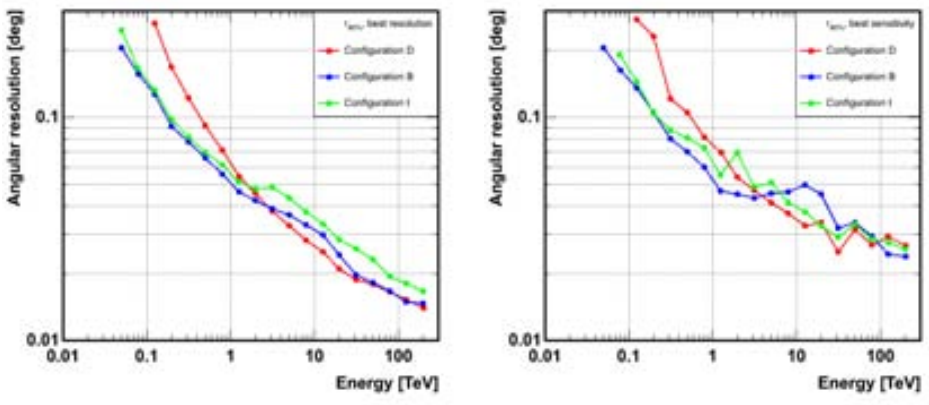

Figure 8.4: Angular resolution (80% containment radius) of the three representative configurations, see Figure 8.3, for best resolution (left) and best sensitivity (right).

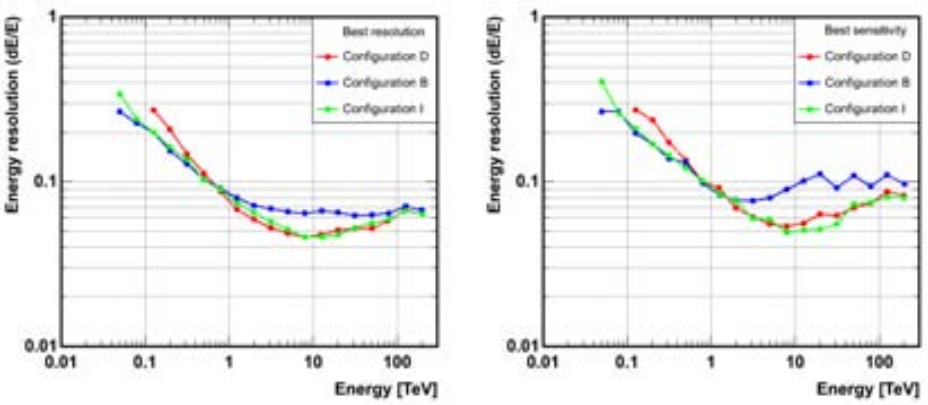

Figure 8.5: Energy resolution of the three representative configurations, see Figure 8.3, for best resolution (left) and best sensitivity (right).

- *makeCTAspec.C*: Simulates CTA spectral points for a given source,
- *testCTA.C*: Calls previous macro and draws the spectrum.

Moreover, the simulations depend on the layout configurations. Their performance files contain information on the effective area, the differential sensitivity, the background rate and the angular resolution (68% and 80% containment).

The main ingredients for the program *makeCTAspec.C* are the intrinsic spectral shape and flux of the chosen source, the afforementioned effective area and the observational time. In the case of sources outside our Galaxy, the extragalactic background light (EBL) attenuation can be taken into account. The selection criteria for data points require more than 3 sigma, a number of excess events greater than 10 and the excess 1% above the background signal. If the number of excess events or significance is too low, the spectrum is re-binned. Additionally, the ON events are calculated randomly according to the Poisson statistics with a given mean value. In the case of an extended source, the background flux is integrated. When the simulation is completed, the macro provide the differential energy spectrum and the integral flux in a specific energy range. On the other hand, *testCTA.C* handles the user interface, by introducing the actual configuration file of the CTA performance, the function of the source spectrum, the observation time and the size of the source extension. Also, attenuation can be applied if needed, as well as redefining the energy range.

The use of these tools, thus, provide CTA simulated data points for the spectral energy distribution of different interesting sources, as shown in subsequent sections.

8.3 Spectral studies

Every simulated layout for CTA provides different advantages and disadvantages when observing different objects in the sky. Actually testing the behaviour of in-

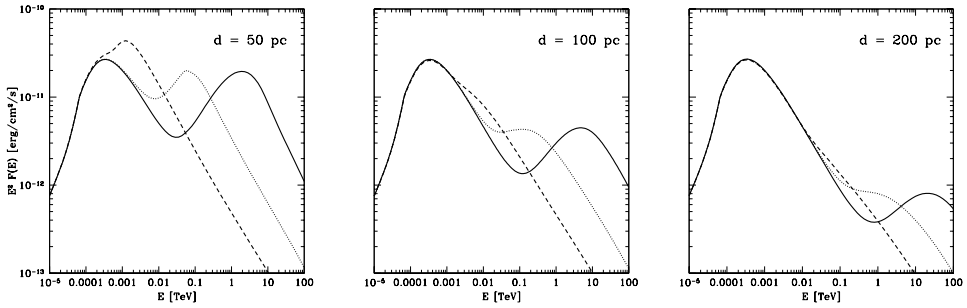

Figure 8.6: Total gamma ray emission from a molecular cloud of mass $10^5 M_\odot$ located at a distance of 1 kpc. The distance between the molecular cloud and the SNR is 50, 100 and 200 pc for left, center and right panel, respectively. The solid, dotted, and dashed lines refer to the emission at 2000, 8000 and 32000 years after the SN explosion. Private communication from S. Gabici, based on figure 5 from [Gabici *et al.* 2009].

teresting gamma-ray sources with CTA simulations will help to choose which one of those configurations is favoured. In the next sections, initial spectral studies on different objects are shown in order to obtain estimations for unexplored energy ranges, new spectral features and model validations. These objects are in a certain way related to cosmic ray diffusion, either in our galaxy (IC 443, molecular clouds close to supernova remnants) or in others (starburst galaxies M82 and NGC 253). The case of IC 443 is detailed in the next Chapter.

8.3.1 Molecular clouds illuminated by CR from nearby SNR

Non-thermal emission is expected to come from molecular clouds, due to interactions of cosmic rays (CR) penetrating the cloud. This emission would be enhanced if the molecular cloud is in the proximity of a supernova remnant (SNR) [Gabici *et al.* 2009], [Rodríguez Marrero *et al.* 2009]. The CR spectrum has two contributions:

- Galactic background: characterized by a steep spectrum, steady in time, that peaks in the GeV energy region;
- Runaway CRs from SNR: present a hard spectrum, variable in time. This second peak appears at TeV energies and moves to lower and lower energies: the higher the energy, the earlier and faster CRs diffuse away.

When superimposing both contributions, a curious concave spectra appears. This V-shape is reflected in gamma-rays, given that above 100 MeV, the spectrum is dominated by emission coming from neutral pion decay ($\pi_0 \rightarrow \gamma\gamma$). If joint observations of *Fermi* and ground based Cherenkov telescopes were carried out, the detection of such a shape could prove the presence of a CR accelerator close to molecular clouds.

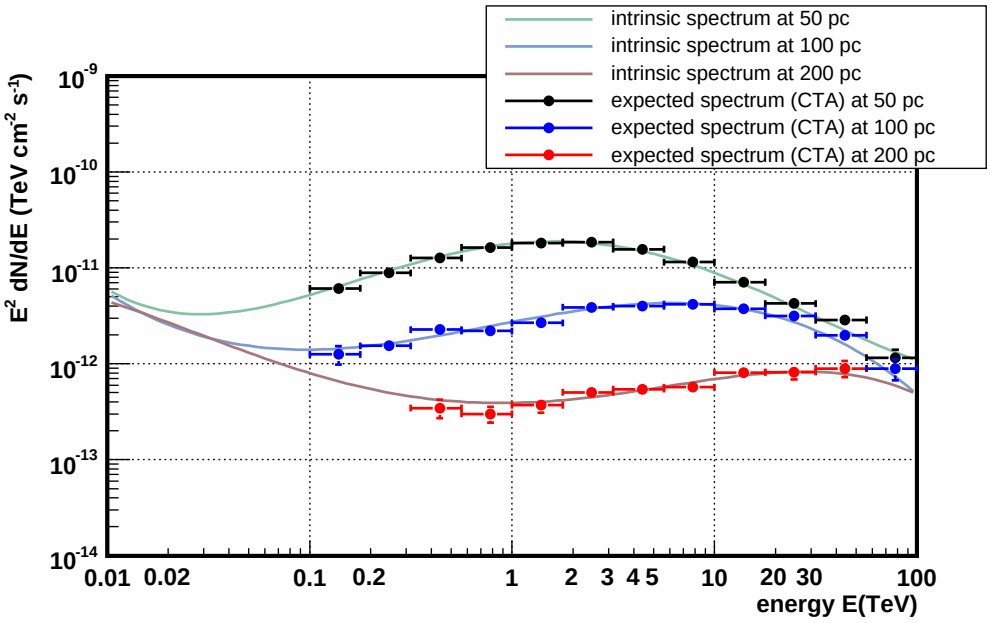

Figure 8.7: Gamma-ray emission from a molecular cloud of $10^5 M_\odot$ illuminated by an accelerator (which explosion occurred 2000 yrs ago) and simulated with layout configuration I, for 20 hours of observation. The molecular cloud is located at a distance of 1 kpc from the observer and placed at different distances from the accelerator: 50 (black), 100 (blue), 200 (red) pc.

One of the theoretical studies on this topic, by [Gabici *et al.* 2009], was used in the present work to simulate a response with CTA. In Figure 8.6, the gamma emission coming from a molecular cloud near a SNR is plotted. The molecular cloud, located at 1 kpc from the observer, has a mass of $10^5 M_\odot$. Considering that the main bulk of gamma-ray emission comes from π_0 decay, the curves show the flux at different epochs after the supernova (SN) explosion and at different separations from the accelerator. The larger this separation is between the molecular cloud and the SNR, the lower is the level of CR flux that comes from the accelerator, as seen in the panels from left to right. There is also an evolution in time, proportional to the square of the separation. In each panel, the peak moves to lower and lower energies with time (from right to left) due to the fact that CR with lower and lower energies can progressively reach the cloud.

Considering a fixed time since the SN exploded (2000 years, solid curve in Figure 8.6), different separations between the SNR and the cloud are simulated in Figure 8.7. Observing 20 hrs, peculiar features in the spectra can already be seen at the CTA sensitivity. A broad distribution with big telescopes at the center (I) appears as the best choice to cover low and high energies. An additional component should arise at lower energies (*Fermi* range) due to the contribution of CR from galactic background.

CTA will be able to distinguish molecular clouds illuminated by escaping cosmic rays from a nearby SNR. The expected softening at lower energies, however, is hardly reachable, leaving the whole V-shape spectrum to be obtained by a combination of *Fermi* and CTA data. In order to get enough statistics, from 20 to 30 hours of observation time are needed. Moreover, the configuration I seems more suitable to allow a better understanding of every possible feature in the spectra.

Promising as these results appear, there are however some caveats inherent to the model. Despite the large mass of the simulated cloud, these type of objects tend to be even more massive and extended. Therefore treating the source as point-like may be a bit optimistic. Also, the largest separation of the cloud and the SNR, 200 pc, is translated in angular distance in the sky as $\sim$ 6 degrees, which is larger than the average detectors' field of view. Thus, the association between target and accelerator becomes more difficult. Finally, the distance at which the molecular cloud is located probably will need to be readjusted, given that there are not so many candidates at 1 kpc. W28, an already detected gamma-ray source, is considered a possible association of a molecular cloud and a SNR and it is located at 1.5 kpc.

8.3.2 Starburst galaxies M82 & NGC 253

Starburst galaxies are characterized by an enhanced star formation and supernova (SN) explosion rate. Since SNe are believed to accelerate cosmic rays, whenever they are found in dense environments, like the central regions of starburst galaxies, gamma-ray emission has been predicted to appear as a result of proton-proton interaction and subsequent neutral pion decay. Recently, two of their most representative members, M82 and NGC 253, have been detected at GeV -TeV energies. In the lower energies, the *Fermi* satellite was responsible of the detection of both galaxies above 100 MeV [Abdo *et al.* 2010c]. At higher energies, both Cherenkov array experiments VERITAS and H.E.S.S. detected M82 above 700 GeV [Acciari *et al.* 2009a] and NGC 253 above 220 GeV [Acero *et al.* 2009], respectively. See table 8.2 for details on those detections.

The very long observational time required to detect these two starburst galaxies by ground based gamma-ray experiments (more than a hundred hours), disesteemed further studies on these interesting objects. However, since these two galaxies are the closest ones to us (therefore, easier to resolve), a deeper knowledge will shade some light on CR diffusion and gamma-ray absorption, among other spectral pecularities. Hopefully, CTA will help in these aspects and may also open the door for future population studies on these and other related objects, like globular clusters.

As a first approach to the problem, a simulation of the spectra of both galaxies was performed using H.E.S.S. and VERITAS data. The model explained in Chapter 5, see also [Domingo-Santamaría & Torres 2005], [de Cea del Pozo *et al.* 2009b], has been taken as input. In Figure 8.8, the curves that arise from the modeling of both spectra are shown, together with the data points obtained by the different gamma-ray telescopes. For M82 (left), the space parameter studied (green shaded region

Table 8.2: Summary of the observational detections of M82 and NGC 253 by *Fermi* (at high energies, HE), VERITAS and H.E.S.S. (very high energies, VHE). The energy thresholds for the integral flux calculations are: above 100 MeV in the case of *Fermi* LAT observations, above 700 GeV for VERITAS, and above 220 GeV for H.E.S.S.

		M 82	NGC 253
HE	Significance (σ)	6.8 (*Fermi*)	4.8 (*Fermi*)
	Time observed	1 year	1 year
	Integral flux (10^{-8} cm^{-2}s^{-1})	$1.6 \pm 5_{stat} \pm 0.3_{sys}$	$0.6 \pm 0.4_{stat} \pm 0.4_{sys}$
	Differential photon index	$2.2 \pm 0.2_{stat} \pm 0.05_{sys}$	$1.95 \pm 0.4_{stat} \pm 0.05_{sys}$
VHE	Significance (σ)	4.8 (VERITAS)	5.2 (H.E.S.S.)
	Time observed	137 hrs	119 hrs
	Integral flux (10^{-13} cm^{-2}s^{-1})	$3.7 \pm 0.8_{stat} \pm 0.7_{sys}$	$5.5 \pm 1.0_{stat} \pm 2.8_{sys}$
	Differential photon index	$2.5 \pm 0.6_{stat} \pm 0.2_{sys}$	-

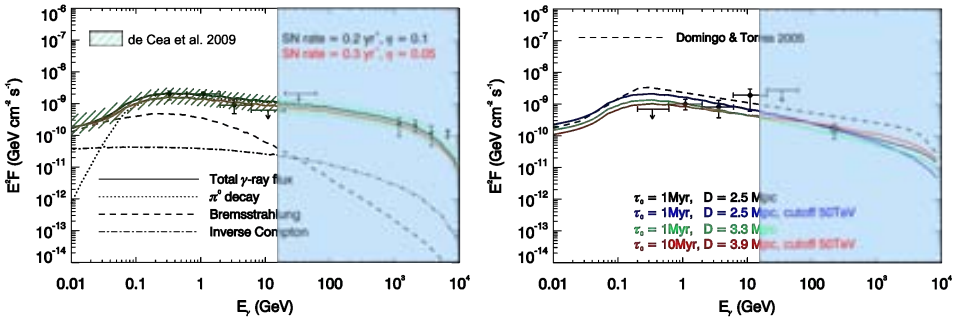

Figure 8.8: Spectral modeling of the gamma-ray emission of the two closest starburst galaxies M82 (left) and NGC 253 (right). The overlaid blue box corresponds to the range of energies that CTA is predicted to observe (from a few tens of GeV to $\sim$ 100 TeV). Data points in both plots correspond to detections by *Fermi* (diamond), VERITAS (star) and H.E.S.S. (square). Figures taken from [de Cea del Pozo *et al.* 2009a]. For a complete explanation, see Chapter 5.

from [de Cea del Pozo *et al.* 2009b]) satisfactorily explains the detected high and very high energy emission coming from the galaxy. One of the possible curves in that region, stating a rate of 0.2 supernova explosions per year (solid black), is used as input for the simulation. In the case of NGC 253 (right), given the uncertainty in the distance to the galaxy (from 2.5 up to 3.9 Mpc), a set of curves can account for the flux at these high energies [de Cea del Pozo *et al.* 2009a]. The curve selected for the simulation corresponds to a distance of 3.9 Mpc (solid red), given that it has the highest flux normalization at the CTA energy range.

Simulating 30 hours of observation with CTA, the spectrum of the starburst galaxy M82 is clearly seen in Figure 8.9. Three different array configurations were tested: the three representatives extracted in section 8.1. The compact configuration (B) gives slightly better coverage at lower energies (0.1 TeV), whereas the more extended configurations (D or I) cover nicely the last part of the spectrum (up to 10 TeV). In each case, a much better reconstructed spectrum is achieved, compared to the existing data points from *Fermi* and VERITAS (in grey).

However, when studying the case of NGC 253, 30 hours were not enough to obtain a confident detection of the galaxy. Indeed, at least 50 hours of observation appear to be the estimated time to guarantee a detection and reconstruction of the spectrum of this source, as seen in Figure 8.10. Again, the three representatives were tested (but only one is shown), and the best results are obtained when using an extended array configuration (either I or D). Although surprising as it may seem that the H.E.S.S. integral data point is below the CTA sensitivity, it should be reminded that a special analysis technique called model analysis[2] was used to obtain such detection.

The results for NGC 253 were not as promising as for M82, regarding a statisically well reconstructed spectrum in a reasonable time (around 30 hours). Nonetheless, it seems that CTA will be able to detect starburst galaxies. For a better understanding of all possible spectral features, configuration D or I seem more suitable, i.e., extended array configurations with or without bigger telescopes at the center that provide a good reconstruction of low energy gamma showers. Future works on this topic could be determining how far away CTA can detect other starburst galaxies, so that a population study can be performed.

8.4 Future work

The CTA observatory will open a wider range of energies (from tens of GeV to tens of TeV) to study gamma-ray astronomy, providing better sensitivity and angular resolution. A thorough study is intended to be carried out, among other topics, on the

[2]The Model Analysis is based on a comparison and fit of observed air shower images with a precomputed library of images [de Naurois & Rolland 2009]. It was trained with simulated gamma rays and with real cosmic-ray data from background fields [Ohm *et al.* 2009]. The algorithm yields an improvement by a factor 1.5 to 1.7 in the statistical significance of faint sources compared with the standard image analysis [Aharonian *et al.* 2006a], [Acero *et al.* 2009], as verified with a number of other gamma-ray sources.

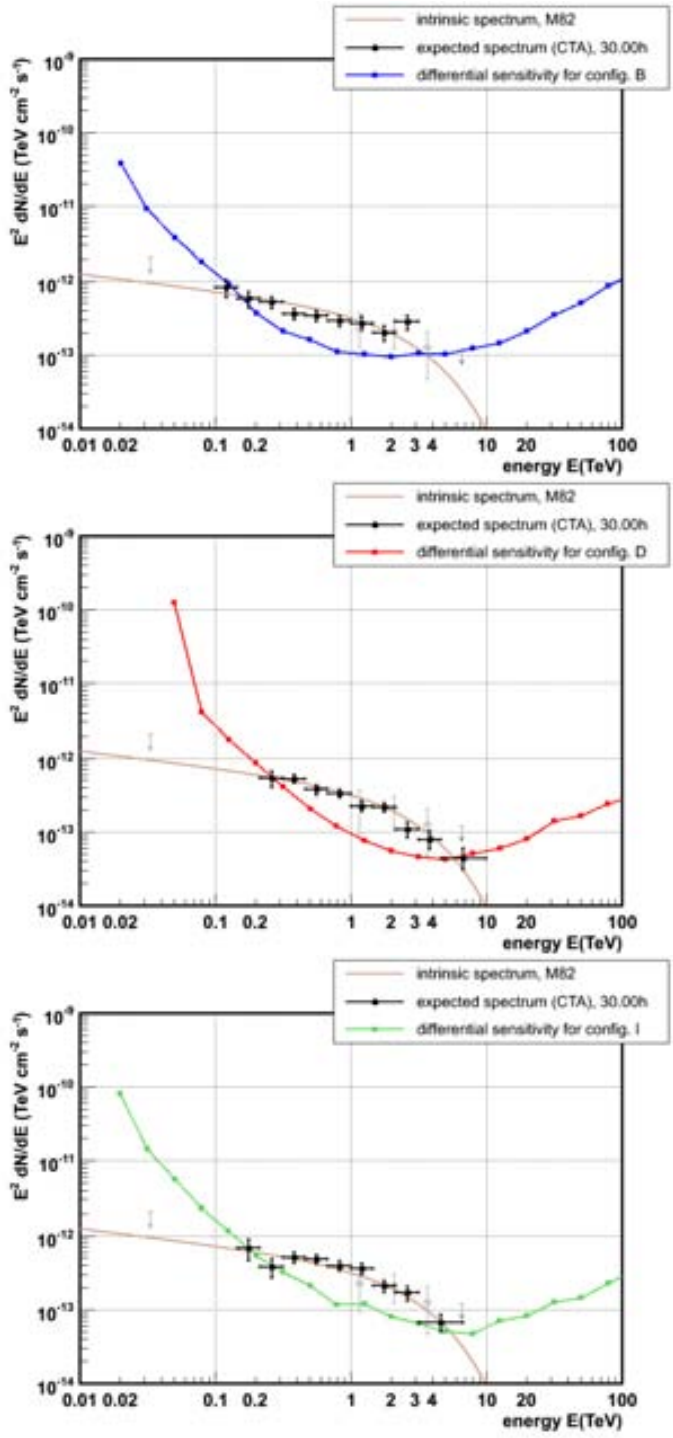

Figure 8.9: M82 spectrum as simulated for CTA for 30 hrs with configuration B (top), D (center), I (bottom). The grey points correspond to observational data: at lower energies, an upper limit (68% c.l.) from *Fermi*, and at higher energies, the differential data points and an upper limit (99% c.l.) from VERITAS.

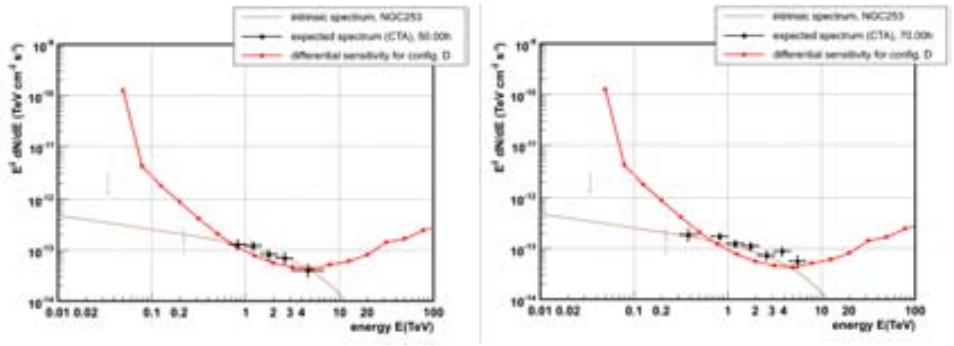

Figure 8.10: NGC 253 spectrum as simulated for CTA in 50 (left) and 70 hours (right) with configuration D. The observational data (grey) corresponds to an upper limit (68% c.l.) from *Fermi*; and H.E.S.S. integral data point (converted to differential flux)

origin of Galactic CR, their propagation within galaxies, and their interaction with the environment. For a long time, supernova remnants (SNR) have been thought to be the sources of CR. To test this hypothesis with CTA, population studies are needed in order to increase the number of detected SNR and improve statistics on these objects. In addition to this issue, a discussion on source confussion (due to the large number of sources to be detected in the galactic plane) should be addressed. Another test on the SNRs as the origin of CRs could be done by improving the quality of the spatial correlation studies between γ-rays and X-rays, and between γ-rays and gas distribution at SNRs. This last probe is yet to be carried out with CTA.

If SNRs are indeed responsible for the origin of galactic CRs, then the most extended explanation for their acceleration is via diffusive shock acceleration (DSA). To better understand this proccess with CTA, some studies have been already performed on the cutoff region in SNR gamma ray spectra (from IC 443, see next Chapter, and also RX J1713.7-3946 [Aharonian *et al.* 2004a]). The detection of very high energy photons (i.e. significantly above 10 TeV) from any SNR would help to discriminate between hadronic and leptonic models, since the Klein-Nishina effect would dramatically suppress the gamma ray flux due to inverse Compton in this energy domain. Another topic that would shed some light on this aspect is spatially resolving the spectra of SNRs possible thanks to the improved angular resolution.

To better understand CR propagation it will be useful to study molecular clouds that present gamma-ray emission coming both from the CR background and nearby accelerators (i.e. SNRs). In the first case, the so-called passive molecular clouds could be used to trace the spatial distribution of CRs in the Galaxy [Gabici 2008, Aharonian 2001, Issa & Wolfendale 1981, Casanova *et al.* 2010]. The case of molecular clouds associated with SNR has been presented in section 8.3.1. These studies are important because the detection of the gamma ray radiation com-

ing from these molecular clouds might constitute an indirect evidence for the acceleration of CRs at SNRs and, since the characteristics of the radiation are expected to depend on the CR diffusion coefficient, these studies might be used to constrain its value in the vicinity of CR accelerators. Another interesting work related to this issue would be studying the case in which the accelerator is placed inside the molecular cloud.

Finally, regarding the studies on starburst galaxies, as previously mentioned, a breakthrough would come from the discovery of more sources of this type, given the improvement in sensitivity. In any case, it will also be important to explore the already detected starburst galaxies, not only their spectra (as in section 8.3.2) but also their extension and morphology. Regarding further spectra features, any steepening at the highest energies could explain extra complexity in the radiative particle distribution, as presently needed to explain observational data and, ultimately, put limits on particle acceleration in these systems. Last, investigating flux variability would give reliability to CR-related emission scenarios in any extragalactic source.

Chapter 9

IC 443 in MAGIC stereo and prospects with CTA

Contents

As already introduced in Chapters 3 and 4, IC 443 is a well known supernova remnant (SNR) in gamma-ray astronomy. One of the most striking facts is that the centroids of these detections at high and very high energies do not coincide, as can be seen in Figure 9.2. There is a clear displacement between the MAGIC/VERITAS source and the EGRET/*Fermi* one. The EGRET central position is located directly towards the center of the radio shell of the SNR, where the *Fermi* source 0FGL J0617.4+2234 is also located. Meanwhile, the MAGIC source is (in Galactic coordinates) south of it, close but beyond the 95% confidence level (c.l.) contour of the EGRET detection (black contours in Figure 9.1). As noted in [Albert *et al.* 2007b], the MAGIC source centroid is positionally coincident with a giant cloud in front of the SNR (see also ^{12}CO contours in Figure 9.1). If the *Fermi* source is taken as reference, the centroid is displaced 0.05 degrees from EGRET, 0.15 degrees from MAGIC, and 0.12 degrees from VERITAS centroids.

Not only is there a difference in the position, but there also seems to be a break in the spectrum between these two ranges of energies. If an extrapolation of the spectrum of the EGRET/*Fermi* source is performed into the VHE regime, a higher flux and harder spectrum than the one observed by MAGIC is obtained. In fact, such a change appears to be reflected on the *Fermi* data. For a spectral energy distribution (SED) from 200 MeV up to 50 GeV, it seems better explained with, for instance, a broken power law that rolls over at about 3 GeV, steepening at the highest energies to match in slope the one that is found by MAGIC.

The region of the sky in which IC443 can be found contains a pulsar wind nebula (PWN) CXOU J061705.3+222127 [Olbert *et al.* 2001], [Bocchino & Bykov 2001]. However, in all energy bands, the centroid of the correspondingly detected sources is inconsistent with this PWN (and the putative pulsar). For instance, the centroid of the PWN is 0.26 degrees from the *Fermi* LAT centroid. Given the above factors, a possible way of explaining a relation between the MAGIC source and the SNR is

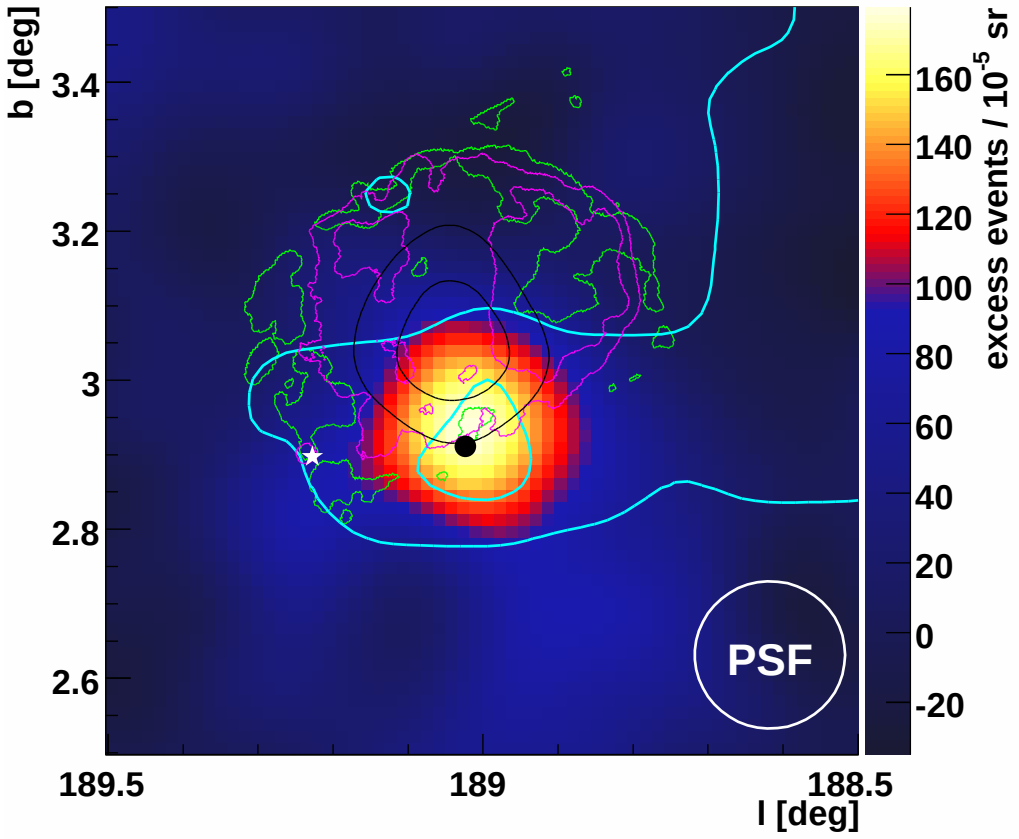

Figure 9.1: Sky map of gamma-ray candidate events (background subtracted) in the direction of MAGIC J0616+225 for an energy threshold of about 150 GeV in galactic coordinates. Overlayed are ^{12}CO emission contours (cyan) showing the position of their maxima coinciding with the MAGIC detection, and contours of 20 cm VLA radio data (green), X-ray contours from Rosat (pu^{12}rple) and gamma-ray contours from EGRET (black). The white star denotes the position of the pulsar CXOU J061705.3+222127. The black dot shows the position of the 1720 MHz OH maser. The white circle shows the MAGIC I PSF of $\sigma = 0.1°$. From [Albert *et al.* 2007b]

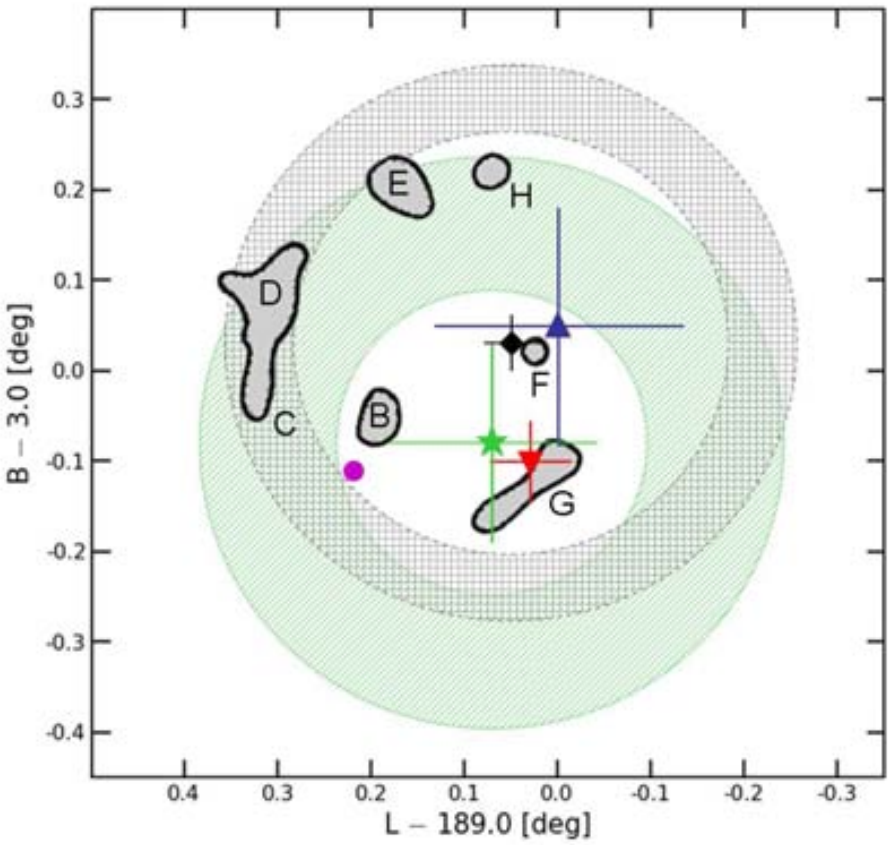

Figure 9.2: Locations and extensions of the 4 gamma-ray sources. Centroid positions are marked with different symbols: EGRET (blue triangle), MAGIC (red downside triangle), VERITAS centroid (green star) and *Fermi* LAT (black diamond). The respective localization errors are shown as crosses. Best-fit spatial extensions of the *Fermi* (cross-hatched band) and VERITAS (striped green band) sources are drawn as rings with radii of θ_{68}^{ext} and widths of $\pm 1\,\sigma$ error. The PWN location is shown as a magenta dot. Contours are the locations and shapes of the local shocked molecular clouds taken from [Huang *et al.* 1986]. Figure taken from [Abdo *et al.* 2010g]

achieved through the diffusion of cosmic rays (CR). MAGIC J0616+225 is consistent with the interpretation of CR interacting with the giant molecular cloud lying in front of the remnant, producing no counterpart at lower energies. In the model by [Torres *et al.* 2008], the nearby EGRET/*Fermi* source can be produced by the same accelerator, and in this case, a co-spatial MAGIC source is not expected. For further details on the model, see Chapters 3 and 4.

In order to further bridge the energy gap between *Fermi* and MAGIC, a proposal for observing IC443 with MAGIC stereo system was made. Details of the proposal and subsequent analysis are explained in the following sections.

9.1 Proposal and observations with MAGIC stereo

As it has been previously stated, MAGIC I observations yield to the detection of a new source of gamma-rays, J0616+225. This source is located at (RA,DEC)=($06^{\mathrm{h}}16^{\mathrm{m}}43^{\mathrm{s}}$,+22°31'48"), with a statistical positional error of 1.5', and a systematic error of 1'. A simple power law was fitted to the measured spectral points through:

$$\frac{\mathrm{d}N_\gamma}{\mathrm{d}A\mathrm{d}t\mathrm{d}E} = (1.0 \pm 0.2) \times 10^{-11} \left(\frac{E}{0.4\,\mathrm{TeV}}\right)^{-3.1\pm0.3} \mathrm{cm}^{-2}\mathrm{s}^{-1}\mathrm{TeV}^{-1} \tag{9.1}$$

with quoted errors being statistical. The integral flux of MAGIC J0616+225 above 100 GeV is about 6.5% of the Crab Nebula.

MAGIC observations in stereo mode could provide, together with *Fermi*, continuous coverage of the source from 100 MeV up. It should be noted, though, that by the time the proposal was made, no *Fermi* results were released. The intended aims, back then, were as follows:

- To analyze the position of the source as a function of different low-to-high energy cuts. Thus, checking whether the source moves towards the center (outskirts) of the SNR with lower (higher) energy threshold.
- To find whether the spectrum of the MAGIC detection becomes harder as the energy threshold decreases.
- To extract morphological information (i.e., the extension of the source) and investigate a possible dependency on the energy threshold.

The whole proposal was driven by the already explained scenario in which CR would escape from the SNR and interact with the molecular cloud in front of it. The molecular cloud environment surrounding IC 443 and its possible connection with the EGRET gamma-ray source was studied by e.g., [Torres *et al.* 2003]. There is a large amount of molecular mass ($\sim 10^4\,\mathrm{M}_\odot$) consistent with the distance to the SNR, corresponding to a velocity range of -20 to 20 km/s. The highest CO intensity detected is directly superimposed on the central position of the MAGIC source.

According to that scenario, the displacement between EGRET and MAGIC sources would have a physical origin. Such displacement would come from the different properties of the proton spectrum at different locations, which in turn is produced by the diffusion of CRs from the accelerator (IC 443) to the target. Specific predictions for future observations can be made as a result of the model presented by [Torres *et al.* 2008]. At high energies, a morphological and spectral change from the position of the cloud (i.e. the center of MAGIC J0616+225) towards the center of IC 443 should be seen. At a morphological level, when observing at lower and lower energies, the radiation will be detected closer to the position of the SNR shell. At a spectral level: sufficient statistics should show that the lower the gamma-ray energy, the harder the spectrum is. Measurements by MAGIC stereo and *Fermi* could lead to the empirical determination of the diffusion coefficient in the medium.

Originally, the observations were planned during winter 2009 - 2010, but due to bad weather conditions, only a small fraction of the granted time was spent on the data taking between January and February 2010. A preliminar analysis of the data is presented below.

9.2 Analysis and results

Stereoscopic observations were carried out in wobble mode, at two positions 0.4° away from the center. The reason for this observational mode was that the sky region around the source has a relatively high and non-uniform level of background light. Within a distance of ∼1.5° from the source, there are two bright stars, one of them is brighter than 8 mag, eta Gem with 3.28 mag, and the other (a bit further away) is mu Gem, with 2.88 mag. By choosing one of the two wobble off-positions coinciding with the brigthest star (eta Gem), a similar sky brightness distribution can be achieved in both wobble positions.

Although the source could be observed at good low zenith angles from November 2009 onwards, the stereoscopic mode in MAGIC was still under comissioning. The start of the data taking was then postponed until December 2009. By that time, observations of the Crab Nebula (standard candle in gamma-ray astronomy) would have been perfomed and analysed, and a deeper knowledge about the new system could have been achieved. However, due to bad weather, only 7 hours were observed between January and February 2010. The proposal was re-submitted in the next cycle (2010 - 2011) to obtain more observational time, but unfortunately no more time was granted.

The observations were taken at zenith angles below 30°, to achieve the necessary low energy threshold this study requires. At La Palma, IC 443 culminates at about 6° zenith angle (ZA). Since the already detected spectrum was found to be steep ($\Gamma = -3.1 \pm 0.3$), the intended study can better benefit from low energy threshold (thus the low zenith angle) and greater senstivity (granted by the new stereoscopic system).

Given the small amount of time observed (5 hours after quality cuts), the

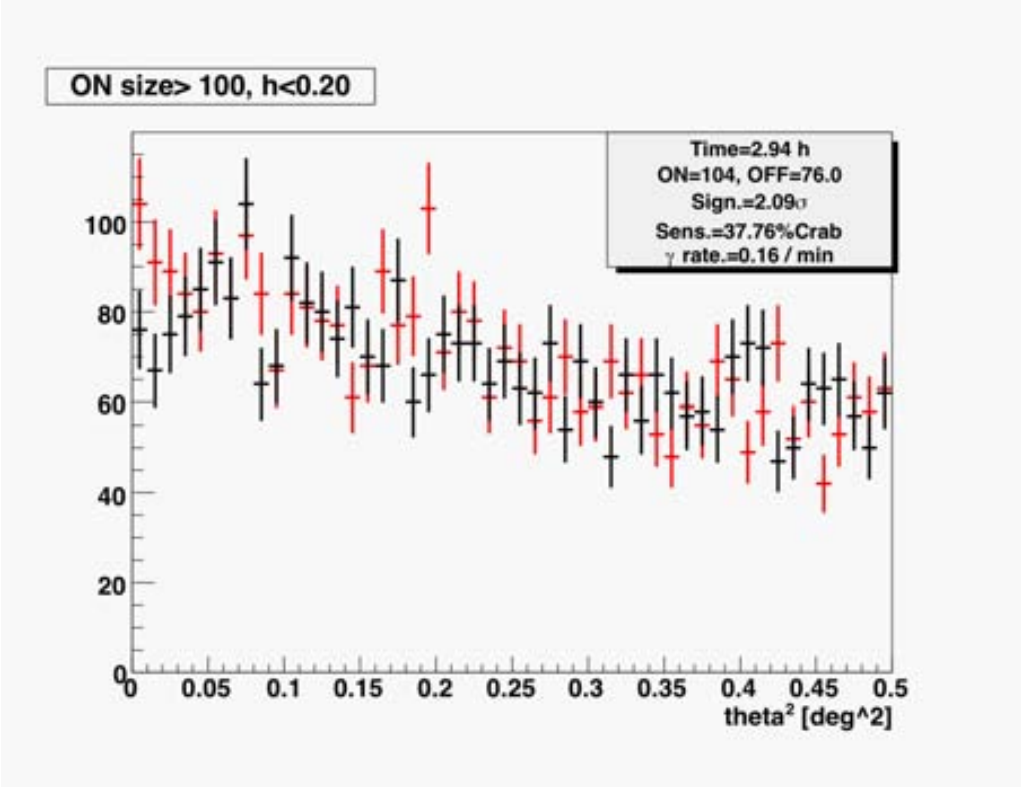

Figure 9.3: Plot showing the θ^2 distribution for the MAGIC source in the region of IC 443. The shapes of the ON and OFF distributions agree well with each other. A hint of signal is already seen in barely 3 hours of observations.

originally planned study could not be performed, and a quick analysis was carried out. The data collected was analyzed in the MARS analysis framework ([Moralejo *et al.* 2009]), standard software for the analysis [1] of MAGIC data. Due to the novelty of the stereo system, the analysis tools used were still under development by that time.

In order to look for gamma-rays coming from the pointed source, standard cuts for stereo were applied in *hadronness* and *size* (0.2 and 100, respectively). In the θ^2 distribution [2] from Figure 9.3, an excess at lower angles can barely be seen, implying that a hint of signal ($2\,\sigma$) can be detected. However, it is not enough for a spectral reconstruction, nor the detailed study in the spectrum and morphology (in bins of energy). The gamma-ray hint of signal is positionally coincident with the previously published MAGIC J0616+225 source. A skymap above 200 GeV, with the same cuts as the θ^2 plot, can be seen in Figure 9.4.

[1] An example of one analysis of MAGIC data can be found at [Aleksić *et al.* 2010]
[2] a definition can be found in section 7.3

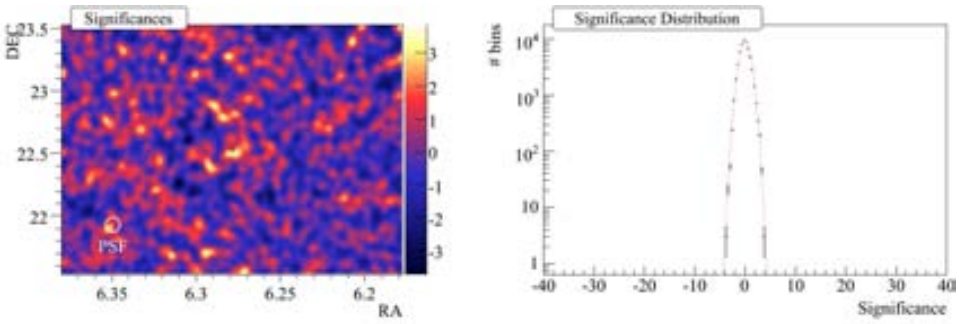

Figure 9.4: Skymap (map of significances) of the SNR IC 443 (left) and distribution of significances (right) of the same region. The black cross marks the position of the MAGIC source J0616+225. The white circle shows the PSF of the MAGIC stereo system.

Table 9.1: Power law (p.l.) index for MAGIC-like or VERITAS-like spectrum for IC 443, when simulating CTA response for 50 hrs in configuration I.

	Observed p. l. index	CTA simulated p. l. index
MAGIC-like spectrum	3.1 ± 0.3	3.14 ± 0.04
VERITAS-like spectrum	2.99 ± 0.38	2.98 ± 0.03

9.3 IC443 as seen in CTA

Having in mind similar goals as in the MAGIC stereo proposal (see section 9.1), a preliminar spectral study on IC 443 was performed for CTA. The response of the instrument was simulated using the tools and the three representative layout configurations described in the previous Chapter 8. The energy range that CTA would cover goes from a few GeVs to hundreds of TeVs. Initially, the observed spectra (by satellite and ground based telescopes) were used as the *intrinsic* one, specifically the ones from the MAGIC and VERITAS experiments and the second part of the broken power-law provided by the *Fermi* satellite. The defined energy range was from 0.02 to 0.07 TeV for the *Fermi* spectrum, and from 0.07 to 7 TeV for the MAGIC and VERITAS spectra. The CTA response was simulated using *Fermi*/MAGIC and *Fermi*/VERITAS spectra to see if CTA can distinguish them. Every *intrinsic* power law has different index: 2.56 ± 0.11 for *Fermi*, 3.1 ± 0.3 for MAGIC and 2.99±0.38 for VERITAS. As seen in Figure 9.5, depending on the choice made for the intrinsic spectrum, CTA will be able to distinguish whether the power law index is similar to the MAGIC's or the VERITAS's slope, when extrapolated to higher energies. This can also be verified in table 9.1, where the specific numbers derived from Figure 9.5 are shown.

In the simulations, several realistic observational times were tested to establish when new results would be achievable. In order to have better resolution at low

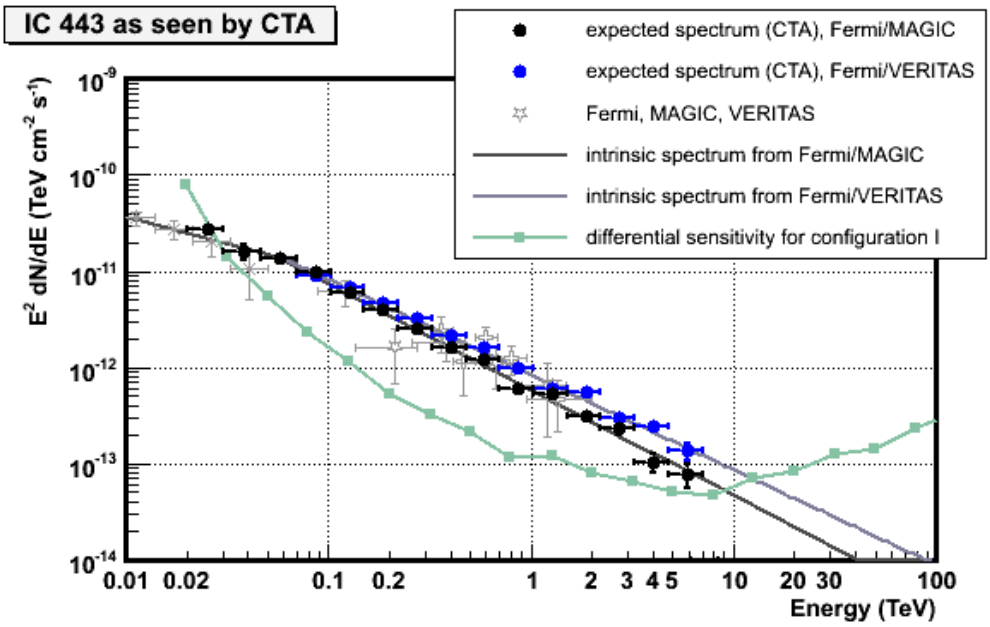

Figure 9.5: CTA simulated spectrum of IC 443 with configuration I (green curve) and 50 hours. The input spectra (grey lines) correspond: at lower energies to the power law published from *Fermi* above 3 GeV, whereas at higher energies the power law index is taken from the measurements by MAGIC and VERITAS. The grey symbols show the actual data from previous experiments. The simulated data points for CTA above 100 GeV can be fitted to a power law, which index depends on the assumed initial spectra (black dots for MAGIC, blue ones for VERITAS).

Table 9.2: Statistics of two fittings to the spectrum for IC 443, when simulating CTA response for 20 hrs in configuration I. The simulated data points use the intrinsic spectra from Figure 9.6: a power law with a cut off at a few TeV. The two fittings, then, are a power law with or without a cut off. The first number is the fit probability, which values should be in the range between $5 - 60\%$, the closest to 50%, the better. The second set of numbers represents the reduced χ^2 (defined as χ^2 divided by the number of degrees of freedom), and for a good fit, it should be closer to 1.

	Cut-off at 5 TeV	Cut-off at 10 TeV
Power law fit	2.21%	9.69%
	19.38 / 9	14.79 / 9
Power law + cut-off fit	61.09%	39.7%
	6.38 / 8	8.38 / 8

energies (several GeV), CTA needs at least 20 hours of observation time, independently of the layout of the used configuration. On the other hand, at high energies (several TeV), CTA needs more than 10 hours to achieve better results than with already operating experiments. At these energies, the compact configuration (B) is not as useful as the other more extended configurations (I or D).

Another interesting point focuses on whether CTA could distinguish the existence of a cut-off in the power law spectrum above the energies of MAGIC and VERITAS. The last data points measured by ground based telescopes are between 1 and 2 TeV. If a cut-off was to be found close to this energy, it could be detected easier by an extended configuration as, for example, configuration D (with the best sensitivity in this energy range). However, a higher cut-off (above 10 TeV) fitting is hard to discriminate from a simple power-law fitting, independently of the used configuration, see Figure 9.6. To obtain enough statistics, more than 20 hours of observation time are needed. But even in that case, distinguishing between a power-law and a power-law with a cut-off fit is not guaranteed, as can be seen in table 9.2.

In conclusion, the prospects of having CTA as the next generation of Cherenkov telescopes will bring a solution to some interesting physics cases. In the case of the IC 443 spectrum, CTA will be able to present major coverage of the spectrum – than the one presentely achieved by MAGIC or VERITAS – and with more accuracy (improving 10% the error bars). With already merely $20 - 30$ hours of observation time, new and meaningful results could be achieved with enough statistics. However, if a cut-off were to appear above 5 TeV, CTA might not be able to distinguish it from a simple power-law. For a better understanding of all its possible spectra features, an array configuration with an extended distribution but also with big size telescopes seems more suitable for all this kind of studies (like the configuration I).

The next step leading to an understanding of the neighbourhood around the

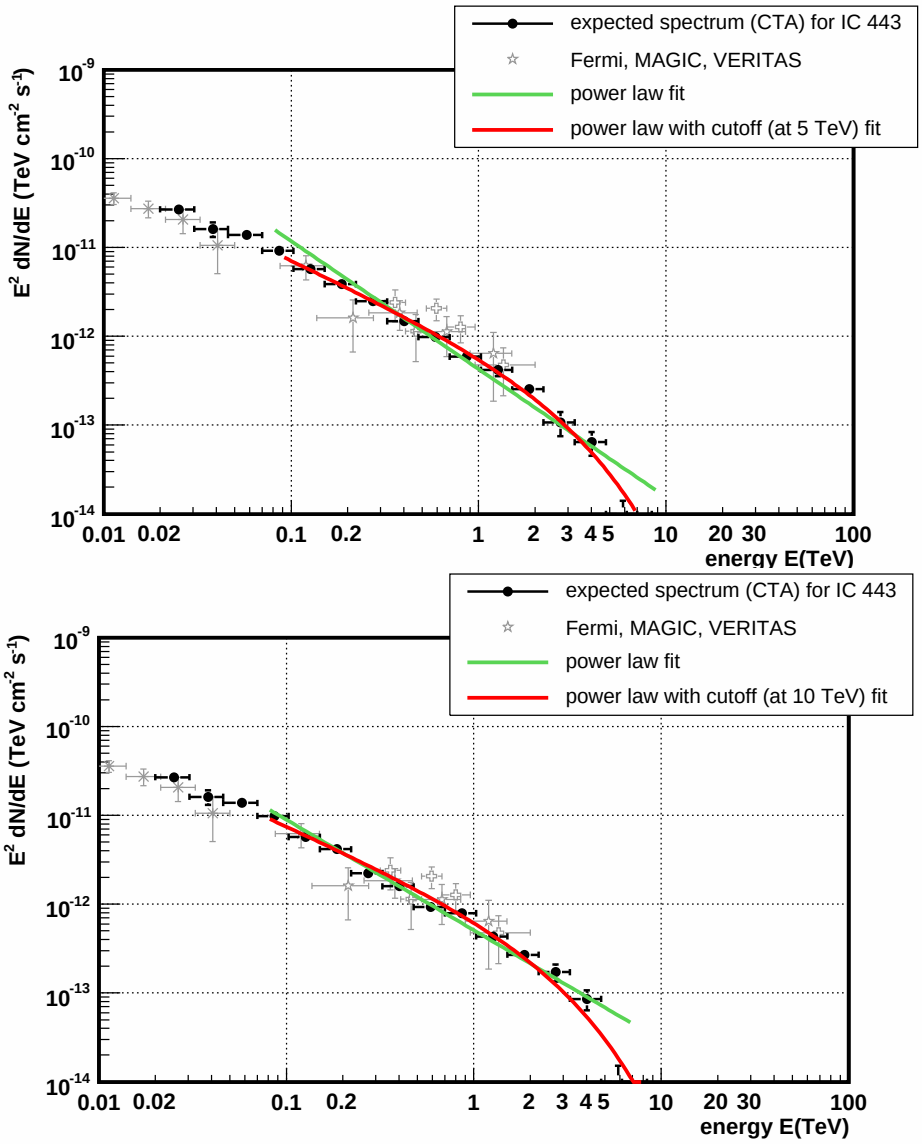

Figure 9.6: The spectrum of IC443 is simulated with layout CTA-I for 50 hours of observation, assuming an input spectrum in the form of a power law with a cut off of 5 (top) and 10 (bottom) TeV. The power law index is the one published by MAGIC (-3.1). The highest energy cut-off that could be resolved is at 5 TeV, at higher energies (i.e. 10 TeV) a fitting with power law with a cut off (red) is statistically undistinguishable from a simple power law (green) in the observed CTA range of energies.

SNR IC 443 will be a morphological study and an actual check of a possible energy dependence.

Chapter 10

Conclusions and future work

10.1 Final remarks

One of the most distinguishing aspects on studies about diffuse emission is that some spectral signatures may serve as an identification of the underlying mechanism producing the gamma rays. In other words, they may help to discern which kind of accelerator and under which diffusion properties cosmic rays (CRs) propagate.

Following the topic on CR diffusion, in Chapters 3 and 4, a theoretical model has been presented explaining the phenomenology around the SNR IC 443 at energies above 100 MeV, placing an emphasis on the displacement between the sources at high and very high energy (HE and VHE respectively). The displacement is generated by the different properties of the proton spectrum at different locations, i.e., how separated are the SNR and the molecular cloud in front of it. These differences are produced by the diffusion of CRs from the accelerator (IC 443) to the target. The VHE source discovered by the MAGIC telescope is interpreted as a delayed TeV emission of CRs diffusing from the SNR. Whereas the HE source can be explained as produced by the same accelerator, without producing a co-spatial VHE source. Some of the predictions made before the *Fermi* telescope was launched were correctly fulfillen. At a morphological level, when the energy is lower, the gamma-ray radiation has been detected closer to the SNR shell. At a spectral level, sufficient statistics have shown that the spectrum gets harder when going towards lower gamma-ray energies.

However, the *Fermi* results have extended the energy domain of the SED much beyond what was possible for its predecessor. The spectrum appears harder than what was previously suggested, presenting an almost flat SED up to 10 GeV, with a roll-over in the spectrum between 10 and 100 GeV. The original parameters of the model needed a sligth modification in their values: mainly, the location and masses of the overtaken clouds. The combined spectra measured by VHE and *Fermi* telescopes can be explained in a scenario where a giant cloud produces a peak at about the *Fermi* spectral turnover. The distance between the cloud and the SNR shell is smaller than previously predicted and the CR are affected by a faster diffusion. The diffusion coefficient is lower and the cosmic-ray density is higher than the Earth-values of both magnitudes. Nonetheless, there are left some uncertainties in the amount and the localization of the target molecular mass, and the density of this molecular material. Those caveats should be addressed in subsequent studies on this an similar sources, like the southern W28 detected by H.E.S.S., or the northern W51C reported by MAGIC and VERITAS.

In Chapter 5, a model for starburst galaxies is presented and succesfully confirmed by the more recent observations. Such galaxies have an enhancement both in the star formation and supernova (SN) explosion rate, and dense environments at their centers. Very energetic gamma rays are produced due to CRs interactions with ambient nuclei and subsequent π^0 decay. The main model described multi-frequency (from radio to near infrared) and multi-messenger (neutrinos) predictions for the photon emission coming from the central region of M82. The model presented is consistent along the electromagnetic spectrum, and allows to track the emission to one and the same original cosmic-ray population. This population is a consequence of every leptonic and hadronic channel, including both primary and secondary particles. The model explains reasonably well both the HE and VHE emission coming from the two closest starburst galaxies M82 and NGC 253, within a range of the explored parameters already mentioned. Now, the opportunity to continue working in these objects is open, and further studies on CR enhancement, X-ray predictions, and features in the spectra below 300 GeV and above 1 TeV are expected.

10.2 Future work

The Thesis concludes with a few initial studies on key objects with the forthcoming Cherenkov Telescope Array (CTA) in Chapter 8:

- The ability to distinguish molecular clouds illuminated by escaping cosmic rays from a nearby SNR, although the whole V-shape spectrum has to be obtained by a combination of *Fermi* and CTA data. The caveats of this study are a consequence of the theoretical model behind it: such large masses for molecular clouds tend to be extended and morphological studies are required. Also, a range of uncertainty is needed for both distances and mass of molecular clouds, because association between SNR and molecular clouds gets harder the wider the separation.

- Concerning starburst galaxies, a much better reconstructed spectrum should be achieved, compared to the existing one for M82. Further studies are expected to report on the possible cutoff in the proton spectra aroung TeV energies. However, the other candidate from this source-class, NGC 253, is not so easily detected, therefore an effort should be made towards achieving an analysis, like the H.E.S.S model analysis that guaranteed its detection. Once this is accomplished, diffuse radiation from other starburst galaxies – placed further away – may be detected, so that a population study can be initiated.

- The study on SNR IC 443 tried to stablish the energy dependence of the gamma-ray centroid, the photon index of the spectrum and the extension. In the spectral study it could be seen that the existing statistics on photon index were significantly improved. However, the opposite happened respect to the

possibility to distinguish a cut-off over few TeVs, where sufficient statistics were not achieved.

CTA will have better sensitivity (one order of magnitud at 1 TeV) and better angular resolution. This is right now the future of the ground-based astronomy at the highest energies. The window will be open to unveil the origin of CR and the SNR as their main accelerator. On the latter objects, population studies and spectral studies looking for a cut-off (to disentangle hadronic/leptonic models) are expected to become common. Related with this topic, the natural targets for these accelerators, the molecular clouds nearby, will also be studied. Other projects await, like multifrequency (X-ray, gas) and multi-messenger (neutrinos) observations and models, together with morphological and extension-related studies, where a dependency on the energy might be tested. To avoid the source confussion, more detailed diffusion skymaps will be developed. And with respect to extragalactic sources, like the starburst galaxies, extension and morphology will be explored, apart from detailed spectra and variability tests (like in blazar and other active galactic nuclei objects).

All and all, this Thesis is just the tip of the iceberg: the field is wide and many prospects for future work will continue to open as our understanding on gamma-ray astronomy progresses. The studies presented in this Thesis simply represent a starting point, and even more exciting topics lay ahead. The journey has just begun...

Bibliography

[Abdo *et al.* 2008] A. A. Abdo, M. Ackermann, W. B. Atwood, L. Baldini, J. Ballet, G. Barbiellini, M. G. Baring, D. Bastieri, B. M. Baughman, K. Bechtol and 175 coauthors. *The Fermi Gamma-Ray Space Telescope Discovers the Pulsar in the Young Galactic Supernova Remnant CTA 1.* Science, vol. 322, no. 5905, pages 1218–1221, 2008. (Cited on page 11.)

[Abdo *et al.* 2009a] A. A. Abdo, M. Ackermann, M. Ajello, B. Anderson, W. B. Atwood, M. Axelsson, L. Baldini, J. Ballet, G. Barbiellini, M. G. Baring and 170 coauthors. *Detection of 16 Gamma-Ray Pulsars Through Blind Frequency Searches Using the Fermi LAT.* Science, vol. 325, no. 5942, pages 840–844, 2009. (Cited on page 11.)

[Abdo *et al.* 2009b] A. A. Abdo, M. Ackermann, M. Ajello, K. Asano, W. B. Atwood, M. Axelsson, L. Baldini, J. Ballet, G. Barbiellini, M. G. Baring and 199 coauthors. *A limit on the variation of the speed of light arising from quantum gravity effects.* Nature, vol. 462, no. 7271, pages 331–334, 2009. (Cited on page 13.)

[Abdo *et al.* 2009c] A. A. Abdo, M. Ackermann, M. Ajello, W. B. Atwood, M. Axelsson, L. Baldini, J. Ballet, D. L. Band, G. Barbiellini, D. Bastieri and 200 coauthors. *Fermi/Large Area Telescope Bright Gamma-Ray Source List.* Astrophysical Journal Supplement, vol. 183, no. 1, pages 46–66, 2009. (Cited on page 101.)

[Abdo *et al.* 2009d] A. A. Abdo, M. Ackermann, M. Ajello, W. B. Atwood, M. Axelsson, L. Baldini, J. Ballet, G. Barbiellini, M. G. Baring, D. Bastieri and 192 coauthors. *Detection of 16 Gamma-Ray Pulsars Through Blind Frequency Searches Using the Fermi LAT.* Science, vol. 325, no. 5942, pages 840–844, 2009. (Cited on page 109.)

[Abdo *et al.* 2009e] A. A. Abdo, M. Ackermann, M. Ajello, W. B. Atwood, M. Axelsson, L. Baldini, J. Ballet, G. Barbiellini, M. G. Baring, D. Bastieri and 192 coauthors. *A Population of Gamma-Ray Millisecond Pulsars Seen with the Fermi Large Area Telescope.* Science, vol. 325, no. 5942, pages 848–852, 2009. (Cited on page 11.)

[Abdo *et al.* 2009f] A. A. Abdo, M. Ackermann, M. Ajello, W. B. Atwood, M. Axelsson, L. Baldini, J. Ballet, G. Barbiellini, D. Bastieri, B. M. Baughman and 157 coauthors. *Detection of High-Energy Gamma-Ray Emission from the Globular Cluster 47 Tucanae with Fermi.* Science, vol. 325, no. 5942, pages 844–848, 2009. (Cited on page 11.)

[Abdo *et al.* 2009g] A. A. Abdo, M. Ackermann, M. Ajello, M. Axelsson, L. Baldini, J. Ballet, G. Barbiellini, D. Bastieri, B. M. Baughman and 167 coauthors. *Modulated High-Energy Gamma-Ray Emission from the Microquasar Cygnus X-3.* Science, vol. 326, no. 5959, pages 1512–1516, 2009. (Cited on page 10.)

[Abdo *et al.* 2009h] A. A. Abdo, M. Ackermann, M. Arimoto, K. Asano, W. B. Atwood, M. Axelsson, L. Baldini, J. Ballet, D. L. Band, G. Barbiellini and 244 coauthors. *Fermi Observations of High-Energy Gamma-Ray Emission from GRB 080916C.* Science, vol. 323, no. 5922, pages 1688–1692, 2009. (Cited on page 13.)

[Abdo *et al.* 2009i] A. A. Abdo, B. T. Allen, T. Aune, D. Berley, C. Chen, G. E. Christopher, T. DeYoung, B. L. Dingus, R. W. Ellsworth, M. M. Gonzalez and 20 coauthors. *Milagro Observations of Multi-TeV Emission from Galactic Sources in the Fermi Bright Source List.* Astrophysical Journal Letters, vol. 700, no. 2, pages 127–131, 2009. (Cited on pages 101, 105, 109, 110 and 175.)

[Abdo *et al.* 2010a] A. A. Abdo, M. Ackermann, M. Ajello, A. Allafort, E. Antolini, W. B. Atwood, M. Axelsson, L. Baldini, J. Ballet, G. Barbiellini and 225 coauthors. *Fermi Large Area Telescope First Source Catalog.* Astrophysical Journal Supplement, vol. 188, no. 2, pages 405–436, 2010. (Cited on pages 104, 110 and 175.)

[Abdo *et al.* 2010b] A. A. Abdo, M. Ackermann, M. Ajello, W. B. Atwood, M. Axelsson, L. Baldini, J. Ballet, G. Barbiellini, M. G. Baring, D. Bastieri and 207 coauthors. *The First Fermi Large Area Telescope Catalog of Gamma-ray Pulsars.* Astrophysical Journal Supplement, vol. 187, no. 2, pages 460–494, 2010. (Cited on pages 109, 110 and 175.)

[Abdo *et al.* 2010c] A. A. Abdo, M. Ackermann, M. Ajello, W. B. Atwood, M. Axelsson, L. Baldini, J. Ballet, G. Barbiellini, D. Bastieri, K. Bechtol and 161 coauthors. *Detection of Gamma-Ray Emission from the Starburst Galaxies M82 and NGC 253 with the Large Area Telescope on Fermi.* The Astrophysical Journal Letters, vol. 709, no. 2, pages L152–L157, 2010. (Cited on pages 13, 58, 74 and 118.)

[Abdo *et al.* 2010d] A. A. Abdo, M. Ackermann, M. Ajello, W. B. Atwood, L. Baldini, J. Ballet, G. Barbiellini, D. Bastieri, B. M. Baughman, K. Bechtol and 172 coauthors. *Fermi Gamma-Ray Imaging of a Radio Galaxy.* Science, vol. 328, no. 5979, pages 725–728, 2010. (Cited on page 12.)

[Abdo *et al.* 2010e] A. A. Abdo, M. Ackermann, M. Ajello, W. B. Atwood, L. Baldini, J. Ballet, G. Barbiellini, D. Bastieri, K. Bechtol, R. Bellazzini and 206 coauthors. *Gamma-Ray Emission Concurrent with the Nova in the Symbiotic Binary V407 Cygni.* Science, vol. 329, no. 5993, pages 817–821, 2010. (Cited on page 9.)

[Abdo *et al.* 2010f] A. A. Abdo, M. Ackermann, M. Ajello, L. Baldini, J. Ballet, G. Barbiellini, M. G. Baring, D. Bastieri, B. M. Baughman, K. Bechtol and 171 coauthors. *Gamma-Ray Emission from the Shell of Supernova Remnant W44 Revealed by the Fermi LAT.* Science, vol. 327, no. 5969, pages 1103–1106, 2010. (Cited on pages 9 and 169.)

[Abdo *et al.* 2010g] A. A. Abdo, M. Ackermann, M. Ajello, L. Baldini, J. Ballet, G. Barbiellini, D. Bastieri, B. M. Baughman, K. Bechtol, R. Bellazzini and 162 coauthors. *Observation of Supernova Remnant IC 443 with the Fermi Large Area Telescope.* Astrophysical Journal, vol. 712, no. 1, pages 459–468, 2010. (Cited on pages 42, 43, 45, 127 and 177.)

[Abdo *et al.* 2010h] A. A. Abdo, M. Ackermann, M. Ajello, L. Baldini, J. Ballet, G. Barbiellini, D. Bastieri, B. M. Baughman, K. Bechtol, R. Bellazzini and 170 coauthors. *PSR J1907+0602: A Radio-Faint Gamma-Ray Pulsar Powering a Bright TeV Pulsar Wind Nebula.* The Astrophysical Journal, vol. 711, no. 1, pages 64–74, 2010. (Cited on page 43.)

[Abdo *et al.* 2010i] A. A. Abdo, D. Parent, J. E. Grove, G. A. Caliandro, M. Roberts, S. Johnston and M. Chernyakova. *Fermi LAT Detection of GeV Gamma-Ray Emission from the Binary System PSRB1259-63.* The Astronomer's Telegram, vol. 3085, pages 1–+, 2010. (Cited on page 10.)

[Abdo *et al.* 2011] A. A. Abdo, M. Ackermann, M. Ajello, A. Allafort, L. Baldini, J. Ballet, G. Barbiellini, D. Bastieri, K. Bechtol, R. Bellazzini and 158 coauthors. *Gamma-Ray Flares from the Crab Nebula.* Science, vol. 331, no. 6018, pages 739–742, 2011. (Cited on page 10.)

[Acciari *et al.* 2009a] V. A. Acciari, E. Aliu, T. Arlen, T. Aune, M. Bautista, M. Beilicke, W. Benbow, D. Boltuch, S. M. Bradbury and 83 coauthors. *A connection between star formation activity and cosmic rays in the starburst galaxy M82.* Nature, vol. 462, no. 7274, pages 770–772, 2009. (Cited on pages 13, 74 and 118.)

[Acciari *et al.* 2009b] V. A. Acciari, E. Aliu, T. Arlen, T. Aune, M. Bautista, M. Beilicke, W. Benbow, S. M. Bradbury, J. H. Buckley, V. Bugaev and 82 coauthors. *Observation of Extended Very High Energy Emission from the Supernova Remnant IC 443 with VERITAS.* Astrophysical Journal Letters, vol. 698, no. 2, pages L133–L137, 2009. (Cited on page 41.)

[Acciari *et al.* 2009c] V. A. Acciari, E. Aliu, T. Arlen, M. Bautista, M. Beilicke, W. Benbow, S. M. Bradbury, J. H. Buckley, V. Bugaev, Y. Butt and 383 coauthors. *Radio Imaging of the Very-High-Energy γ-Ray Emission Region in the Central Engine of a Radio Galaxy.* Science, vol. 325, no. 5939, pages 444–447, 2009. (Cited on page 12.)

[Acero *et al.* 2009] F. Acero, F. Aharonian, A. G. Akhperjanian, G. Anton, U. Barres de Almeida, A. R. Bazer-Bachi, Y. Becherini, B. Behera, K. Bernlöhr, and 161 coauthors. *Detection of Gamma Rays from a Starburst Galaxy.* Science, vol. 326, no. 5956, pages 1080–1082, 2009. (Cited on pages 13, 118 and 120.)

[Aharonian & Atoyan 1996] F. A. Aharonian and A.M. Atoyan. *On the emissivity of π^0-decay gamma radiation in the vicinity of accelerators of galactic cosmic rays.* Astronomy and Astrophysics, vol. 309, pages 917–928, 1996. (Cited on pages 20, 21, 22, 35, 45, 51, 52, 53 and 172.)

[Aharonian *et al.* 2003] F. Aharonian, A. Akhperjanian, M. Beilicke, K. Bernlöhr, H.-G. Börst, H. Bojahr, O. Bolz, T. Coarasa, J. L. Contreras, J. Cortina and 43 coauthors. *Is the giant radio galaxy M 87 a TeV gamma-ray emitter?* Astronomy and Astrophysics, vol. 403, pages L1–L5, 2003. (Cited on page 12.)

[Aharonian *et al.* 2004a] F. A. Aharonian, A. G. Akhperjanian, K.-M. Aye, A. R. Bazer-Bachi, M. Beilicke, W. Benbow, D. Berge, P. Berghaus, K. Bernlhr, O. Bolz and 90 coauthors. *High-energy particle acceleration in the shell of a supernova remnant.* Nature, vol. 432, no. 7013, pages 75–77, 2004. (Cited on page 122.)

[Aharonian *et al.* 2004b] F. A. Aharonian, A. G. Akhperjanian, K.-M. Aye, A. R. Bazer-Bachi, M. Beilicke, W. Benbow, D. Berge, P. Berghaus, K. Bernlöhr, O. Bolz and 90 coauthors. *High-energy particle acceleration in the shell of a supernova remnant.* Nature, vol. 432, no. 7013, pages 75–77, 2004. (Cited on pages 9 and 169.)

[Aharonian *et al.* 2005a] F. Aharonian, A. G. Akhperjanian, K.-M. Aye, A. R. Bazer-Bachi, M. Beilicke, W. Benbow, D. Berge, P. Berghaus, K. Bernlöhr, C. Boisson and 92 coauthors. *Discovery of the binary pulsar PSR B1259-63 in very-high-energy gamma rays around periastron with HESS.* Astronomy and Astrophysics, vol. 442, pages 1–10, 2005. (Cited on page 10.)

[Aharonian *et al.* 2005b] F. A. Aharonian, A. G. Akhperjanian, K.-M. Aye, A. R. Bazer-Bachi, M. Beilicke, W. Benbow, D. Berge, P. Berghaus, K. Bernlöhr, C. Boisson and 90 coauthors. *A New Population of Very High Energy Gamma-Ray Sources in the Milky Way.* Science, vol. 307, no. 5717, pages 1938–1942, 2005. (Cited on page 10.)

[Aharonian *et al.* 2005c] F. A. Aharonian, A. G. Akhperjanian, K.-M. Aye, A. R. Bazer-Bachi, M. Beilicke, W. Benbow, D. Berge, P. Berghaus, K. Bernlöhr, C. Boisson and 93 coauthors. *Discovery of Very High Energy Gamma Rays Associated with an X-ray Binary.* Science, vol. 309, no. 5735, pages 746–749, 2005. (Cited on page 10.)

[Aharonian *et al.* 2006a] F. Aharonian, A. G. Akhperjanian, A. R. Bazer-Bachi, M. Beilicke, W. Benbow, D. Berge, K. Bernlhr, C. Boisson, O. Bolz, V. Borrel and 97 coauthors. *Observations of the Crab nebula with HESS.* Astronomy and Astrophysics, vol. 457, no. 3, pages 899–915, 2006. (Cited on page 120.)

[Aharonian *et al.* 2006b] F. Aharonian, A. G. Akhperjanian, A. R. Bazer-Bachi, M. Beilicke, W. Benbow, D. Berge, K. Bernlöhr, C. Boisson, O. Bolz, V. Borrel and 105 coauthors. *Energy dependent $\gamma-$ray morphology in the pulsar wind nebula HESS J1825-137.* Astronomy and Astrophysics, vol. 460, no. 2, pages 365–374, 2006. (Cited on page 43.)

[Aharonian *et al.* 2006c] F. A. Aharonian, A. G. Akhperjanian, A. R. Bazer-Bachi, M. Beilicke, W. Benbow, D. Berge, K. Bernlhr, C. Boisson, O. Bolz, V. Borrel and 96 coauthors. *First detection of a VHE gamma-ray spectral maximum from a cosmic source: HESS discovery of the Vela X nebula.* Astronomy and Astrophysics, vol. 448, no. 2, pages L43–L47, 2006. (Cited on page 25.)

[Aharonian *et al.* 2006d] F. A. Aharonian, A. G. Akhperjanian, A. R. Bazer-Bachi, M. Beilicke, W. Benbow, D. Berge, K. Bernlöhr, C. Boisson, O. Bolz, V. Borrel and 113 coauthors. *Fast Variability of Tera-Electron Volt γ Rays from the Radio Galaxy M87.* Science, vol. 314, no. 5804, pages 1424–1427, 2006. (Cited on page 12.)

[Aharonian *et al.* 2006e] F. A. Aharonian, A. G. Akhperjanian, A. R. Bazer-Bachi, M. Beilicke, W. Benbow, D. Berge, K. Bernlöhr, C. Boisson, O. Bolz, V. Borrel and 92 coauthors. *Discovery of very-high-energy γ-rays from the Galactic Centre ridge.* Nature, vol. 439, no. 7077, pages 695–698, 2006. (Cited on page 10.)

[Aharonian *et al.* 2006f] F. A. Aharonian, A. G. Akhperjanian, A. R. Bazer-Bachi, M. Beilicke, W. Benbow, D. Berge, K. Bernlöhr, C. Boisson, O. Bolz, V. Borrel and 92 coauthors. *A low level of extragalactic background light as revealed by γ-rays from blazars.* Nature, vol. 440, no. 7087, pages 1018–1021, 2006. (Cited on page 11.)

[Aharonian *et al.* 2009] F. A. Aharonian, A. G. Akhperjanian, G. Anton, U. Barres de Almeida, A. R. Bazer-Bachi, Y. Becherini, B. Behera, W. Benbow, K. Bernlöhr, C. Boisson and 149 coauthors. *Detection of very high energy radiation from HESS J1908+063 confirms the Milagro unidentified source MGRO J1908+06.* Astronomy and Astrophysics, vol. 499, no. 3, pages 723–728, 2009. (Cited on page 43.)

[Aharonian 2001] F. A. Aharonian. *Gamma Rays From Molecular Clouds.* Space Science Review, vol. 99, no. 1, pages 187–196, 2001. (Cited on page 122.)

[Akyüz *et al.* 1991] A. Akyüz, A. Brouillet and M.E. Özel. *M82 in gamma-rays.* Astronomy and Astrophysics, vol. 248, no. 2, pages 419–420, 1991. (Cited on page 63.)

[Albert *et al.* 2006] J. Albert, E. Aliu, H. Anderhub, P. Antoranz, A. Armada, M. Asensio, C. Baixeras, J. A. Barrio, M. Bartelt, H. Bartko and 138 coauthors. *Variable Very-High-Energy Gamma-Ray Emission from the Microquasar LS I +61 303.* Science, vol. 312, no. 5781, pages 1771–1773, 2006. (Cited on page 10.)

[Albert *et al.* 2007a] J. Albert, E. Aliu, H. Anderhub, P. Antoranz, A. Armada, C. Baixeras, J. A. Barrio, H. Bartko, D. Bastieri, J. K. Becker and 130 coauthors. *Very High Energy Gamma-Ray Radiation from the Stellar Mass Black Hole Binary Cygnus X-1.* The Astrophysical Journal, vol. 665, pages L51–L54, 2007. (Cited on page 10.)

[Albert *et al.* 2007b] J. Albert, E. Aliu, H. Anderhub, P. Antoranz, A. Armada, C. Baixeras, J. A. Barrio, H. Bartko, D. Bastieri, J. K. Becker and 131 coauthors. *Discovery of Very High Energy Gamma Radiation from IC 443 with the MAGIC Telescope.* Astrophysical Journal, vol. 664, no. 2, pages L87–L90, 2007. (Cited on pages 34, 35, 125, 126 and 177.)

[Albert *et al.* 2007c] J. Albert, E. Aliu, H. Anderhub, P. Antoranz, A. Armada, C. Baixeras, J. A. Barrio, H. Bartko, D. Bastieri, J. K. Becker and 134 coauthors. *Unfolding of differential energy spectra in the MAGIC experiment.* Nuclear Instruments and Methods in Physics Research A, vol. 583, pages 494–506, 2007. (Cited on page 99.)

[Albert *et al.* 2008a] J. Albert, E. Aliu, H. Anderhub, L. A. Antonelli, P. Antoranz, M. Backes, C. Baixeras, J. A. Barrio, H. Bartko and 140 coauthors. *Very-High-Energy gamma rays from a Distant Quasar: How Transparent Is the Universe?* Science, vol. 320, no. 5884, pages 1752–1754, 2008. (Cited on page 12.)

[Albert *et al.* 2008b] J. Albert, E. Aliu, H. Anderhub, P. Antoranz, A. Armada, C. Baixeras, J. A. Barrio, H. Bartko, D. Bastieri, J. K. Becker and 132 coauthors. *VHE -Ray Observation of the Crab Nebula and its Pulsar with the MAGIC Telescope.* Astrophysical Journal, vol. 674, no. 2, pages 1037–1055, 2008. (Cited on pages 106, 110 and 175.)

[Aleksić *et al.* 2010] J. Aleksić, L. A. Antonelli, P. Antoranz, M. Backes, J. A. Barrio, D. Bastieri, J. Becerra González, W. Bednarek, A. Berdyugin, K. Berger and 137 coauthors. *MAGIC Upper Limits for two Milagro-detected, Bright Fermi Sources in the Region of SNR G65.1+0.6.* Astrophysical Journal, vol. 725, no. 2, pages 1629–1632, 2010. (Cited on pages 16, 103 and 130.)

[Aliu *et al.* 2008a] E. Aliu, H. Anderhub, L. A. Antonelli, P. Antoranz, M. Backes, C. Baixeras, J. A. Barrio, H. Bartko, D. Bastieri, J. K. Becker and 139 coauthors. *Observation of Pulsed -Rays Above 25 GeV from the Crab Pulsar with MAGIC.* Science, vol. 322, no. 5905, page 1221, 2008. (Cited on page 91.)

[Aliu *et al.* 2008b] E. Aliu, H. Anderhub, L. A. Antonelli, P. Antoranz, M. Backes, C. Baixeras, J. A. Barrio, H. Bartko, D. Bastieri, J. K. Becker and 139 coauthors. *Observation of Pulsed γ-Rays Above 25 GeV from the Crab Pulsar with MAGIC.* Science, vol. 322, no. 5905, pages 1221–1223, 2008. (Cited on page 11.)

[Aliu *et al.* 2009] E. Aliu, H. Anderhub, L. A. Antonelli, P. Antoranz, M. Backes, C. Baixeras, J. A. Barrio, H. Bartko, D. Bastieri, J. K. Becker and 137 coauthors. *Improving the performance of the single-dish Cherenkov telescope MAGIC through the use of signal timing.* Astroparticle Physics, vol. 30, no. 6, pages 293–305, 2009. (Cited on page 96.)

[Anchordoqui *et al.* 2003] L. A. Anchordoqui, D. F. Torres, T. P. McCauley, G. E. Romero and F. A. Aharonian. *Neutrinos from Accreting Neutron Stars.* The Astrophysical Journal, vol. 589, no. 1, pages 481–486, 2003. (Cited on page 55.)

[Anchordoqui *et al.* 2004] L.A. Anchordoqui, H. Goldberg, F. Halzen and T. J. Weiler. *Neutrino bursts from Fanaroff Riley I radio galaxies.* Physics Letters B, vol. 600, no. 3-4, pages 202–207, 2004. (Cited on page 73.)

[Anchordoqui *et al.* 2008] L.A. Anchordoqui, D. Hooper, S. Sarkar and A. M. Taylor. *High energy neutrinos from astrophysical accelerators of cosmic ray nuclei.* Astroparticle Physics, vol. 29, no. 1, pages 1–13, 2008. (Cited on pages 57 and 73.)

[Arquilla & Kwok 1987] R. Arquilla and S. Kwok. *CO observations of IRAS Circular No. 9 sources 19520 + 2759 and 01133 + 6434 - Regions of star formation.* Astronomy and Astrophysics, vol. 173, no. 2, pages 271–278, 1987. (Cited on page 103.)

[Asaoka & Aschenbach 1994] I. Asaoka and B. Aschenbach. *An X-ray study of IC443 and the discovery of a new supernova remnant by ROSAT.* Astronomy and Astrophysics, vol. 284, no. 2, pages 573–582, 1994. (Cited on page 33.)

[Atoyan *et al.* 1995] A. M. Atoyan, F. A. Aharonian and H. J. Völk. *Electrons and positrons in the galactic cosmic rays.* Physical Review D (Particles, Fields, Gravitation, and Cosmology), vol. 52, no. 6, pages 3265–3275, 1995. (Cited on page 21.)

[Baring *et al.* 1999] M. G. Baring, D. C. Ellison, S. P. Reynolds, I. A. Grenier and P. Goret. *Radio to Gamma-Ray Emission from Shell-Type Supernova Remnants: Predictions from Nonlinear Shock Acceleration Models.* The Astrophysical Journal, vol. 513, no. 1, pages 311–338, 1999. (Cited on page 19.)

[Bartel *et al.* 1987] N. Bartel, M. I. Ratner, A. E. E. Rogers, I. I. Shapiro, R. J. Bonometti, N. L. Cohen, M. V. Gorenstein, J. M. Marcaide and R. A. Pre-

ston. *VLBI observations of 23 hot spots in the starburst galaxy M82.* Astrophysical Journal, vol. 323, no. 1, pages 505–515, 1987. (Cited on page 66.)

[Bartko & Bednarek 2008] H. Bartko and W. Bednarek. *Gamma-ray emission from PWNe interacting with molecular clouds.* Monthly Notices of the Royal Astronomical Society, vol. 385, no. 3, pages 1105–1109, 2008. (Cited on pages 39 and 43.)

[Bazo Alba *et al.* 2009] J. L. Bazo Alba, R. Abbasi, Y. Abdou, M. Ackermann, J. Adams, J. Aguilar, M. Ahlers, K. Andeen, J. Auffenberg, X. Bai, M. Baker and 240 coauthors. *Search for neutrino point sources with IceCube 22-strings.* Nuclear Physics B Proceedings Supplements, vol. 188, pages 267–269, 2009. (Cited on page 73.)

[Beck & Krause 2005] R. Beck and M. Krause. *Revised equipartition and minimum energy formula for magnetic field strength estimates from radio synchrotron observations.* Astronomische Nachrichten, vol. 326, no. 6, pages 414–427, 2005. (Cited on pages 71 and 72.)

[Becker 2008] J. K. Becker. *High-energy neutrinos in the context of multimessenger astrophysics.* Physics Reports, pages 173–246, March 2008. (Cited on pages 2 and 169.)

[Bell 1978] A. R. Bell. *The acceleration of cosmic rays in shock fronts. II.* Monthly Notices of Royal Astronomical Society, vol. 182, pages 443–455, 1978. (Cited on pages 19 and 61.)

[Berezhko *et al.* 2006] E. G. Berezhko, L. T. Ksenofontov and H. J. Völk. *Gamma-ray emission expected from Kepler's supernova remnant.* Astronomy and Astrophysics, vol. 452, no. 1, pages 217–221, 2006. (Cited on page 61.)

[Berezinskii *et al.* 1990] V. S. Berezinskii, S. V. Bulanov, V. A. Dogiel and V. S. Ptuskin. Ginzburg, V. L., Amsterdam, North-Holland, 1990. (Cited on pages 50 and 62.)

[Bertsch *et al.* 1993] D. L. Bertsch, T. M. Dame, C. E. Fichtel, S. D. Hunter, P. Sreekumar, J. G. Stacy and P. Thaddeus. *Diffuse Gamma-Ray Emission in the Galactic Plane from Cosmic-Ray, Matter, and Photon Interactions.* Astrophysical Journal, vol. 416, pages 587–600, 1993. (Cited on page 20.)

[Blattnig *et al.* 2000a] S. R. Blattnig, S. R. Swaminathan, A. T. Kruger, M. Ngom and J. W. Norbury. *Parametrizations of inclusive cross sections for pion production in proton-proton collisions.* Physical Review D, id.094030, vol. 62, no. 9, 2000. (Cited on page 51.)

[Blattnig *et al.* 2000b] S. R. Blattnig, S. R. Swaminathan, A. T. Kruger, M. Ngom, J. W. Norbury and R. K. Tripathi. *Parameterized Cross Sections for Pion*

Production in Proton-Proton Collisions. Technical Report, NASA/TP-2000-210640, vol. 1, 2000. (Cited on page 51.)

[Blom *et al.* 1999] J. J. Blom, T. A. Paglione and A. Carramiñana. *Diffuse Gamma-Ray Emission from Starburst Galaxies and M31.* The Astrophysical Journal, vol. 516, no. 2, pages 744–749, 1999. (Cited on pages 57 and 59.)

[Bocchino & Bykov 2000] F. Bocchino and A. M. Bykov. *Hard X-ray emission from IC443: evidence for a shocked molecular clump?* Astronomy and Astrophysics, vol. 362, pages L29–L32, 2000. (Cited on page 33.)

[Bocchino & Bykov 2001] F. Bocchino and A. M. Bykov. *The plerion nebula in IC 443: The XMM-Newton view.* Astronomy and Astrophysics, vol. 376, pages 248–253, 2001. (Cited on pages 33, 39 and 125.)

[Bocchino & Bykov 2003] F. Bocchino and A. M. Bykov. *XMM-Newton study of hard X-ray sources in IC 443.* Astronomy and Astrophysics, vol. 400, pages 203–211, 2003. (Cited on page 33.)

[Braun & Strom 1986] R. Braun and R. G. Strom. *The structure and dynamics of evolved supernova remnants - The IC 443 complex.* Astronomy and Astrophysics, vol. 164, no. 1, pages 193–207, 1986. (Cited on page 31.)

[Bressan *et al.* 2002] A. Bressan, L. Silva and G. L. Granato. *Far infrared and radio emission in dusty starburst galaxies.* Astronomy and Astrophysics, vol. 392, pages 377–391, 2002. (Cited on page 68.)

[Brown & Marscher 1977] R. L. Brown and A. P. Marscher. *Energetic secondary electrons in dense interstellar clouds.* Astrophysical Journal, vol. 212, no. 1, pages 659–663, 1977. (Cited on page 59.)

[Butt *et al.* 2003] Y. M. Butt, D. F. Torres, J. A. Combi, T. Dame and G. E. Romero. *Molecular Beam Dumps as Tracers of Hadronic Cosmic Ray Sources: the Case of SNR IC 443.* In XXIInd Moriond Astrophysics Meeting, pages 323–331. arXiv:astro-ph/0206132v2, 2003. (Cited on pages 33, 37 and 45.)

[Bykov *et al.* 2000] A. M. Bykov, R. A. Chevalier, D. C. Ellison and Yu. A. Uvarov. *Nonthermal Emission from a Supernova Remnant in a Molecular Cloud.* The Astrophysical Journal, vol. 538, no. 1, pages 203–216, 2000. (Cited on page 37.)

[Bykov *et al.* 2005] A. M. Bykov, F. Bocchino and G. G. Pavlov. *A Hard Extended X-Ray Source in the IC 443 Supernova Remnant Resolved by Chandra: A Fast Ejecta Fragment or a New Pulsar Wind Nebula?* The Astrophysical Journal, vol. 624, no. 1, pages L41–L44, 2005. (Cited on page 33.)

[Bykov *et al.* 2008] A. M. Bykov, A. M. Krassilchtchikov, Yu. A. Uvarov, H. Bloemen, F. Bocchino, G. M. Dubner, E. B. Giacani and G. G. Pavlov. *Isolated X-Ray-Infrared Sources in the Region of Interaction of the Supernova Remnant IC 443 with a Molecular Cloud.* The Astrophysical Journal, vol. 676, no. 2, pages 1050–1063, 2008. (Cited on page 33.)

[Carilli 1996] C. L. Carilli. *Free-free absorption towards the nucleus of NGC 253: further evidence for high pressures in the starburst nucleus.* Astronomy and Astrophysics, vol. 305, pages 402–, 1996. (Cited on pages 77 and 174.)

[Casanova *et al.* 2010] S. Casanova, F. A. Aharonian, Y. Fukui, S. Gabici, D. I. Jones, A. Kawamura, T. Onishi, G. Rowell, H. Sano, K. Torii and H. Yamamoto. *Molecular Clouds as Cosmic-Ray Barometers.* Publications of the Astronomical Society of Japan, vol. 62, no. 3, pages 769–777, 2010. (Cited on pages 19 and 122.)

[Casasola *et al.* 2004] V. Casasola, D. Bettoni and G. Galletta. *The gas content of peculiar galaxies: Strongly interacting systems.* Astronomy and Astrophysics, vol. 422, pages 941–950, 2004. (Cited on page 63.)

[Cavasinni *et al.* 2006] V. Cavasinni, D. Grasso and L. Maccione. *TeV neutrinos from supernova remnants embedded in giant molecular clouds.* Astroparticle Physics, vol. 26, no. 1, pages 41–49, 2006. (Cited on page 55.)

[Cherenkov 1934] P. A. Cherenkov. *Visible emission of clean liquids by action of gamma radiation.* Doklady Akademii Nauk SSSR Ser. A, vol. 2, pages 451–455, 1934. (Cited on page 84.)

[Chevalier 1999] R. A. Chevalier. *Supernova Remnants in Molecular Clouds.* The Astrophysical Journal, vol. 511, no. 2, pages 798–811, 1999. (Cited on page 33.)

[Cillis *et al.* 2005] A. N. Cillis, D. F. Torres and O. Reimer. *EGRET Upper Limits and Stacking Searches of Gamma-Ray Observations of Luminous and Ultraluminous Infrared Galaxies.* The Astrophysical Journal, vol. 621, no. 1, pages 139–145, 2005. (Cited on page 69.)

[Claussen *et al.* 1997] M. J. Claussen, D. A. Frail, W. M. Goss and R. A. Gaume. *Polarization Observations of 1720 MHz OH Masers toward the Three Supernova Remnants W28, W44, and IC 443.* Astrophysical Journal, vol. 489, pages 143–159, 1997. (Cited on page 31.)

[Corbet *et al.* 2011] R. H. D. Corbet, C. C. Cheung, M. Kerr, R. Dubois, D. Donato, G. A. Caliandro, M. J. Coe, P. G. Edwards, M. D. Filipovic, J. L. Payne and J. Stevens. *1FGL J1018.6-5856: a New Gamma-ray Binary.* The Astronomer's Telegram, vol. 3221, pages 1–+, 2011. (Cited on page 10.)

[Cornett *et al.* 1977] R. H. Cornett, G. Chin and G. R. Knapp. *Observations of CO emission from a dense cloud associated with the supernova remnant IC 443.* Astronomy and Astrophysics, vol. 54, no. 3, pages 889–894, 1977. (Cited on pages 33, 34 and 44.)

[Cortina *et al.* 2009] J. Cortina, F. Goebel, T. Schweizer and for the MAGIC Collaboration. *Technical Performance of the MAGIC Telescopes.* In Proc. 31^{st} International Cosmic Ray Conference. (Łódź, Poland). arXiv: astro-ph/0907.1211v1, 2009. (Cited on pages 90 and 174.)

[Crutcher *et al.* 1978] R. M. Crutcher, D. H. Rogstad and K. Chu. *Aperture-synthesis observations of H I in the galaxy M82.* Astrophysical Journal, vol. 225, no. 1, pages 784–789, 1978. (Cited on page 63.)

[Crutcher 1988] R. M. Crutcher. Dickman, R. and Snell, R. and Young, J. Eds., New York, Springer, 1988. (Cited on page 68.)

[Crutcher 1994] R. M. Crutcher. *Clouds, cores and low mass stars.* In Proceedings of the 4th Haystack Observatory, volume 65 of *Astronomical Society of the Pacific Conference Series*, page 87. Clemens, D. P. and Barvainis, R., 1994. (Cited on page 68.)

[Crutcher 1999] R. M. Crutcher. *Magnetic Fields in Molecular Clouds: Observations Confront Theory.* The Astrophysical Journal, vol. 520, no. 2, pages 706–713, 1999. (Cited on page 68.)

[De Angelis 2011] A. De Angelis. *Recent results from VHE gamma astrophysics related to fundamental physics and cosmic rays.* ArXiv e-prints, 2011. (Cited on pages 8 and 179.)

[de Cea del Pozo *et al.* 2009a] E. de Cea del Pozo, D. F. Torres, A. Y. Rodríguez and O. Reimer. *Model analysis of the very high energy detections of the starburst galaxies M82 and NGC 253.* In Proc. 1^{st} Fermi Symposium (Washington, DC). arXiv: astro-ph/0912.3497v2, 2009. (Cited on pages 16, 58, 119, 120 and 176.)

[de Cea del Pozo *et al.* 2009b] E. de Cea del Pozo, D. F. Torres and A. Y. Rodríguez Marrero. *Multi-messenger model for the starburst galaxy M82.* The Astrophysical Journal, vol. 698, no. 2, pages 1054–1071, 2009. (Cited on pages 16, 58, 75, 76, 118, 120, 174 and 179.)

[de Grijs *et al.* 2001] R. de Grijs, R. W. O'Connell and J. S. III Gallagher. *The Fossil Starburst in M82.* The Astronomical Journal, vol. 121, no. 2, pages 768–792, 2001. (Cited on page 66.)

[de Jager & Djannati-Ataï 2009] O.C. de Jager and A. Djannati-Ataï. Neutron stars and pulsars, volume 357. Astrophysics and Space Science Library, (Berlin) Springer, 2009. (Cited on page 110.)

[de Naurois & Rolland 2009] M. de Naurois and L. Rolland. *A high performance likelihood reconstruction of -rays for imaging atmospheric Cherenkov telescopes.* Astroparticle Physics, vol. 32, no. 5, pages 231–252, 2009. (Cited on page 120.)

[De Noyer & Frerking 1981] L. K. De Noyer and M. A. Frerking. *Some new results on shock chemistry in IC 443.* Astrophysical Journal, vol. 246, pages L37–L40, 1981. (Cited on pages 33 and 44.)

[Dermer 1986] C. D. Dermer. *Secondary production of neutral pi-mesons and the diffuse galactic gamma radiation.* Astronomy and Astrophysics, vol. 157, no. 2, pages 223–22, 1986. (Cited on page 46.)

[Dickman *et al.* 1992] R. L. Dickman, R. L. Snell, L. M. Ziurys and Y.-L. Huang. *Structure and kinematics of dense gas associated with the supernova remnant IC 443.* Astrophysical Journal, vol. 400, no. 1, pages 203–213, 1992. (Cited on pages 33, 34 and 44.)

[Dogel & Sharov 1990] V. A. Dogel and G. S. Sharov. *Manifestations of cosmic ray acceleration in giant molecular clouds.* Astronomy and Astrophysics, vol. 229, no. 1, pages 259–271, 1990. (Cited on page 19.)

[Domingo-Santamaría & Torres 2005] E. Domingo-Santamaría and D. F. Torres. *High energy -ray emission from the starburst nucleus of NGC 253.* Astronomy and Astrophysics, vol. 444, no. 2, pages 403–415, 2005. (Cited on pages 20, 51, 57, 58, 61, 63, 68, 74, 78, 79, 118, 174 and 179.)

[Domingo-Santamaría *et al.* 2005] E. Domingo-Santamaría, J. Flix, J. Rico, V. Scalzotto and W. Wittek. *The DISP analysis method for point-like or extended gamma source searches/studies with the MAGIC Telescope.* In Proc. of the 29th International Cosmic Ray Conference, Pune (India), volume 5, page 363. Mumbai: Tata Institute of Fundamental Research, 2005. (Cited on page 99.)

[Drury *et al.* 1994] L. O'C. Drury, F. A. Aharonian and H. J. Völk. *The gamma-ray visibility of supernova remnants. A test of cosmic ray origin.* Astronomy and Astrophysics, vol. 287, pages 959–971, 1994. (Cited on pages 19 and 59.)

[Elias *et al.* 1978] J. H. Elias, D. J. Ennis, D. Y. Gezari, M. G. Hauser, J. R. Houck, K. Y. Lo, K. Matthews, D. Naduea, G. Neugebauer, M. W. Werner and W. E. Westbrook. *1 millimeter continuum observations of extragalactic objects.* Astrophysical Journal, vol. 220, no. 1, pages 25–41, 1978. (Cited on pages 77 and 174.)

[Errando 2009] M. Errando. *Discovery of very high energy gamma-ray emission from 3C 279 and 3C 66A/B with the MAGIC telescope.* PhD thesis, Univ. Autonoma de Barcelona, 2009. (Cited on pages 97 and 175.)

[Everett *et al.* 2008] J. E. Everett, E. G. Zweibel, R. A. Benjamin, D. McCammon, L. Rocks and J. S. III Gallagher. *The Milky Way's Kiloparsec-Scale Wind: A Hybrid Cosmic-Ray and Thermally Driven Outflow.* The Astrophysical Journal, vol. 674, no. 1, pages 258–270, 2008. (Cited on page 59.)

[Fatuzzo & Melia 2003] M. Fatuzzo and F. Melia. *A Kinship Between the EGRET Supernova Remnants and Sagittarius A East.* The Astrophysical Journal, vol. 596, no. 2, pages 1035–1043, 2003. (Cited on page 59.)

[Fazio 1967] G. G. Fazio. *Gamma Ratiation from Celestial Objects.* Annual Review of Astronomy and Astrophysics, vol. 5, page 481, 1967. (Cited on page 59.)

[Fesen & Kirshner 1980] R. A. Fesen and R. P. Kirshner. *Spectrophotometry of the supernova remnant IC 443.* Astrophysical Journal, vol. 242, no. 1, pages 1023–1040, 1980. (Cited on page 31.)

[Fichtel *et al.* 1976] C. E. Fichtel, D. A. Kniffen, D. J. Thompson, G. F. Bignami and C. Y. Cheung. *Significance of medium-energy gamma-ray astronomy in the study of cosmic rays.* Astrophysical Journal, vol. 208, no. 1, pages 211–219, 1976. (Cited on page 20.)

[Fomin *et al.* 1994] V. P. Fomin, A. A. Stepanian, R. C. Lamb, D. A. Lewis, M. Punch and T. C. Weekes. *New methods of atmospheric Cherenkov imaging for gamma-ray astronomy. I. The false source method.* Astroparticle Physics, vol. 2, no. 2, pages 137–150, 1994. (Cited on pages 91 and 103.)

[Förster *et al.* 2003] N.M. Förster, M. Sauvage, V. Charmandaris, O. Laurent, P. Gallais, I. F. Mirabel and L. Vigroux. *ISOCAM view of the starburst galaxies M82, NGC253, and NGC1808.* Astronomy and Astrophysics, vol. 399, pages 833–855, 2003. (Cited on pages 66 and 173.)

[Freedman *et al.* 1994] W. L. Freedman, S. M. Hughes, B. F. Madore, J. R. Mould, M. G. Lee, P. Stetson, R. C. Kennicutt, A. Turner, L. Ferrarese, H. Ford and 5 coauthors. *The Hubble Space Telescope Extragalactic Distance Scale Key Project. 1: The discovery of Cepheids and a new distance to M81.* Astrophysical Journal, Part 1, vol. 427, no. 2, pages 628–655, 1994. (Cited on page 62.)

[Funk *et al.* 2008] S. Funk, O. Reimer, D. F. Torres and J. A. Hinton. *The GeV-TeV Connection in Galactic γ-ray sources.* The Astrophysical Journal, vol. 679, no. 2, pages 1299–1314, 2008. (Cited on pages 20, 22, 35, 67, 169 and 173.)

[Gabici & Aharonian 2007] S. Gabici and F. A. Aharonian. *Searching for Galactic Cosmic-Ray Pevatrons with Multi-TeV Gamma Rays and Neutrinos.* The Astrophysical Journal, vol. 665, no. 2, pages L131–L134, 2007. (Cited on pages 19, 22, 28, 35, 37, 40 and 45.)

[Gabici *et al.* 2009] S. Gabici, F. A. Aharonian and S. Casanova. *Broad-band non-thermal emission from molecular clouds illuminated by cosmic rays from nearby supernova remnants.* Monthly Notices of the Royal Astronomical Society, vol. 396, no. 3, pages 1629–1639, 2009. (Cited on pages 19, 28, 54, 116, 117 and 176.)

[Gabici 2008] S. Gabici. *Gamma Ray Astronomy and the Origin of Galactic Cosmic Rays.* In XXI European Cosmic Ray Symposium. arXiv: astro-ph/0811.0836, 2008. (Cited on page 122.)

[Gaensler *et al.* 2006] B. M. Gaensler, S. Chatterjee, P. O. Slane, E. van der Swaluw, F. Camilo and J. P. Hughes. *The X-Ray Structure of the Pulsar Bow Shock G189.22+2.90 in the Supernova Remnant IC 443.* The Astrophysical Journal, vol. 648, no. 2, pages 1037–1042, 2006. (Cited on page 33.)

[Gaisser *et al.* 1995] T. K. Gaisser, F. Halzen and T. Stanev. *Particle astrophysics with high energy neutrinos [Erratum: 1996PhR...271..355G].* Physics Reports, vol. 258, pages 173–236, 1995. (Cited on page 55.)

[Gaisser *et al.* 1998] T. K. Gaisser, R. J. Protheroe and T. Stanev. *Gamma-Ray Production in Supernova Remnants.* Astrophysical Journal, vol. 492, no. 1, pages 219–227, 1998. (Cited on pages 19, 37 and 39.)

[Gallagher & Smith 2005] J. S. Gallagher and L. J. Smith. *Observational Ponderings on Disk-Halo Interfaces.* In Extra-Planar Gas, volume 331 of *Astronomical Society of the Pacific Conference Series*, pages 147–154. R. Braun, 2005. (Cited on page 59.)

[Gaug 2006] M. Gaug. *Calibration of the MAGIC telescope and Observation of Gamma Ray Bursts.* PhD thesis, Univ. Autonoma de Barcelona, 2006. (Cited on page 94.)

[Ginzburg & Syrovatskii 1964] V. L. Ginzburg and S. I. Syrovatskii. The origin of cosmic rays. New York: Macmillan, 1964. (Cited on pages 2, 21, 35, 59 and 61.)

[Green 2004] D. A. Green. *Galactic supernova remnants: an updated catalogue and some statistics.* Bulletin of the Astronomical Society of India, vol. 32, pages 335–370, 2004. (Cited on page 31.)

[Halzen & Klein 2010] F. Halzen and S. R. Klein. *Invited Review Article: IceCube: An instrument for neutrino astronomy.* Review of Scientific Instruments, vol. 81, no. 8, pages 081101–+, 2010. (Cited on page 14.)

[Halzen 2006] F. Halzen. *Astroparticle physics with high energy neutrinos: from AMANDA to IceCube.* The European Physical Journal C, vol. 46, no. 3, pages 669–687, 2006. (Cited on page 54.)

[Hartman *et al.* 1999] R.C. Hartman, D. L. Bertsch, S. D. Bloom, A. W. Chen, P. Deines-Jones, J. A. Esposito, C. E. Fichtel, D. P. Friedlander, S. D. Hunter, L. M. McDonald and 17 coauthors. *The Third EGRET Catalog of High-Energy Gamma-Ray Sources*. Astrophysical Journal Supplement Series, vol. 123, no. 1, pages 79–202, 1999. (Cited on pages 5, 12, 34, 43, 103, 110 and 175.)

[Heck *et al.* 1998] D. Heck, J. Knapp, J. N. Capdevielle, G. Schatz and T. Thouw. Forschungszentrum Karlsruhe, Hannover (Germany), 1998. (Cited on page 93.)

[Hermsen 1990] W. Hermsen. *Highlights from the COS-B mission*. Advances in Space Research, vol. 10, pages 69–79, 1990. (Cited on page 4.)

[Hess 1912] V. Hess. *Uber Beobachtungen der durchdringenden Strahlung bei sieben Freiballonfahrten*. Physikalische Zeitschrift, vol. 13, pages 1084–1091, 1912. (Cited on page 1.)

[Hewitt *et al.* 2006] J. W. Hewitt, F. Yusef-Zadeh, M. Wardle, D. A. Roberts and N. E. Kassim. *Green Bank Telescope Observations of IC 443: The Nature of OH (1720 MHz) Masers and OH Absorption*. The Astrophysical Journal, vol. 652, no. 2, pages 1288–1296, 2006. (Cited on page 31.)

[Hillas 1985] A.M. Hillas. *Cerenkov light images of EAS produced by primary gamma*. In F. C. Jones, editeur, International Cosmic Ray Conference, volume 3, pages 445–448, 1985. (Cited on page 94.)

[Hofmann *et al.* 2010] W. Hofmann, M. Martinez and the CTA consortium. *Design Concepts for the Cherenkov Telescope Array*. eprint arXiv:1008.3703v2, 2010. (Cited on page 111.)

[Holder *et al.* 2005] J. Holder, H. M. Badran, G. Blaylock, I. H. Bond, P. J. Boyle, S. M. Bradbury, J. H. Buckley, K. Byrum, D. A. Carter-Lewis, O. Celik and 63 coauthors. *Recent Observations of IC443 with the Whipple 10m Telescope*. In High Energy Gamma-Ray Astronomy: 2^{nd} International Symposium. Heidelberg (Germany), volume 745 of *AIP Conference Proceedings*, pages 275–280. New York: American Institute of Physics, 2005. (Cited on page 34.)

[Huang *et al.* 1986] Y.-L. Huang, R. L. Dickman and R. L. Snell. *IRAS sources associated with shocked gas regions in IC 443*. Astrophysical Journal, Part 2 - Letters to the Editor, vol. 302, pages L63–L66, 1986. (Cited on pages 34, 127 and 177.)

[Hughes *et al.* 1994] D.H. Hughes, W.K. Gear and E.I. Robson. *The Submillimetre Structure of the Starburst Nucleus in M82 - a Diffraction-Limited 450-MICRON Map*. Monthly Notices of the Royal Astronomical Society, vol. 270, no. 3, page 641, 1994. (Cited on pages 66 and 173.)

[Humensky & the VERITAS Collaboration 2008] T. B. Humensky and the VERITAS Collaboration. *Observation of the Supernova Remnant IC 443 with VERITAS*. In Proc. of the 30^{th} International Cosmic Ray Conference.Mérida, Yucatán, Mexico, volume 2, pages 835–838. Universidad Nacional Autónoma de México, Mexico City, Mexico, 2008. (Cited on page 34.)

[Issa & Wolfendale 1981] M. R. Issa and A. W. Wolfendale. *Gamma rays from the cosmic ray irradiation of local molecular clouds*. Nature, vol. 292, pages 430–433, 1981. (Cited on page 122.)

[Kamae *et al.* 2005] T. Kamae, T. Abe and T. Koi. *Diffractive Interaction and Scaling Violation in pp–>π^0 Interaction and GeV Excess in Galactic Diffuse Gamma-Ray Spectrum of EGRET*. The Astrophysical Journal, vol. 620, no. 1, pages 244–256, 2005. (Cited on page 51.)

[Karachentsev *et al.* 2003] I. D. Karachentsev, E. K. Grebel, M. E. Sharina, A. E. Dolphin, D. Geisler, P. Guhathakurta, P. W. Hodge, V. E. Karachentseva, A. Sarajedini and P. Seitzer. *Distances to nearby galaxies in Sculptor*. Astronomy and Astrophysics, vol. 404, pages 93–111, 2003. (Cited on page 74.)

[Kelner *et al.* 2006] S. R. Kelner, F. A. Aharonian and V. V. Bugayov. *Energy spectra of gamma rays, electrons, and neutrinos produced at proton-proton interactions in the very high energy regime*. Physical Review D, vol. 74, no. 3, page 034018, 2006. (Cited on pages 20, 52, 53, 54, 59 and 172.)

[Keohane *et al.* 1997] J. W. Keohane, R. Petre, E. V. Gotthelf, M. Ozaki and K. Koyama. *A Possible Site of Cosmic Ray Acceleration in the Supernova Remnant IC 443*. Astrophysical Journal, vol. 484, pages 350–359, 1997. (Cited on page 33.)

[Khelifi 2003] B. Khelifi. *Recherche de sources gamma par un methode de Maximum de Vraisemblance: Application aux AGN et aux sources galactiques suivis par le telescope CAT*. PhD thesis, University of Caen, France, 2003. (Cited on page 34.)

[Klein *et al.* 1988] U. Klein, R. Wielebinski and H.W. Morsi. *Radio continuum observations of M82*. Astronomy and Astrophysics, vol. 190, no. 1, pages 41–46, 1988. (Cited on pages 66 and 173.)

[Kronberg & Sramek 1985] P.P. Kronberg and R.A. Sramek. *Discovery of new variable radio sources in the nucleus of the nearby galaxy Messier 82*. Science, vol. 227, pages 28–31, 1985. (Cited on page 66.)

[Kronberg & Wilkinson 1975] P. P. Kronberg and P. N. Wilkinson. *High-resolution, multifrequency radio observations of M82*. Astrophysical Journal, vol. 200, no. 1, pages 430–438, 1975. (Cited on page 66.)

[Kronberg *et al.* 1985] P.P. Kronberg, P. Biermann and F.R. Schwab. *The nucleus of M82 at radio and X-ray bands - Discovery of a new radio population of supernova candidates.* Astrophysical Journal, vol. 291, no. 1, pages 693–707, 1985. (Cited on page 66.)

[Lamb & Macomb 1997] R. C. Lamb and D. J. Macomb. *Point Sources of GeV Gamma Rays.* Astrophysical Journal, vol. 488, pages 872–880, 1997. (Cited on pages 34 and 43.)

[Landecker *et al.* 1990] T.L. Landecker, M. Clutton-Brock and C.R. Purton. *G 65.1+0.6 - A new supernova remnant of low surface brightness.* Astronomy and Astrophysics, vol. 232, no. 1, pages 207–214, 1990. (Cited on pages 102, 105 and 175.)

[Lasker *et al.* 1990] B. M. Lasker, C. R. Sturch, B. J. McLean, J. L. Russell, H. Jenkner and M. M. Shara. *The Guide Star Catalog. I - Astronomical foundations and image processing.* Astronomical Journal, vol. 99, pages 2019–2058, 1990. (Cited on pages 31, 32, 34 and 170.)

[Leahy 2004] A. D. Leahy. *1420 and 408 MHz Continuum Observations of the IC 443/G189.6+3.3 Region.* The Astronomical Journal, vol. 127, no. 4, pages 2277–2283, 2004. (Cited on page 31.)

[Lessard *et al.* 2001] R. W. Lessard, J. H. Buckley, V. Connaughton and S. Le Bohec. *A new analysis method for reconstructing the arrival direction of TeV gamma rays using a single imaging atmospheric Cherenkov telescope.* Astroparticle Physics, vol. 15, no. 1, pages 1–18, 2001. (Cited on page 99.)

[Lindner 2003] J. Lindner. *Dusty galaxies: modelling spectral energy distributions.* Canadian Undergraduate Physics Journal, vol. 2, no. 1, pages 7–12, 2003. (Cited on page 69.)

[Lipari 1993] P. Lipari. *Tev muons in hadronic showers.* Astroparticle Physics, vol. 1, no. 4, pages 399–415, 1993. (Cited on page 55.)

[Loeb & Waxman 2006] A. Loeb and E. Waxman. *The cumulative background of high energy neutrinos from starburst galaxies.* Journal of Cosmology and Astroparticle Physics, vol. 5, no. 003, pages 2–8, 2006. (Cited on pages 57 and 72.)

[Longair 1992] M. S. Longair. volume 1. Cambridge University Press, Cambridge, UK, 1992. (Cited on page 83.)

[Longair 1994] M. S. Longair. volume 2. Cambridge University Press, 2^{nd} ed., Cambridge, UK, 1994. (Cited on page 61.)

[Lozinskaya 1981] T. A. Lozinskaya. *The radio brightness-diameter relation for supernova remnants - Some new distance calibrators.* Soviet Astronomy Letters, vol. 7, pages 17–19, 1981. (Cited on page 33.)

[Mankuzhiyil 2010] Nijil Mankuzhiyil. *MAGIC gamma-ray observations of distant AGN and a study of source variability and the extragalactic background light using Fermi and air Cherenkov telescopes.* PhD thesis, University of Udine, 2010. (Cited on pages 95 and 174.)

[Mannheim & Schlickeiser 1994] K. Mannheim and R. Schlickeiser. *Interactions of cosmic ray nuclei.* Astronomy & Astrophysics, vol. 286, pages 983–996, 1994. (Cited on page 61.)

[Maraschi *et al.* 1968] L. Maraschi, G. C. Perola and S. Schwarz. *X-ray flux and anisotropy produced by galactic cosmic-ray electrons.* Il Nuovo Cimento B Series 10, vol. 53, no. 2, pages 443–458, 1968. (Cited on page 59.)

[Mariotti 2011] M. Mariotti. *MAGIC confirms VHE gamma-ray emission from HESS J0632+057 between 7-9 Feb 2011.* The Astronomer's Telegram, vol. 3161, pages 1–+, 2011. (Cited on page 10.)

[Markoff *et al.* 1999] S. Markoff, F. Melia and I. Sarcevic. *High-Energy Emission from Relativistic Particles in Sagittarius A*.* The Astrophysical Journal, vol. 522, no. 2, pages 870–878, 1999. (Cited on page 59.)

[Marscher & Brown 1978] A. P. Marscher and R. L. Brown. *Energetic secondary electrons and the nonthermal galactic radio background - A probe of the magnetic field in interstellar clouds.* Astrophysical Journal, vol. 221, no. 1, pages 588–597, 1978. (Cited on page 59.)

[Mauersberger *et al.* 1996] R. Mauersberger, C. Henkel, R. Wielebinski, T. Wiklind and H.-P. Reuter. *Molecular distribution and kinematics in nearby galaxies. I. NGC 253.* Astronomy and Astrophysics, vol. 305, pages 421–434, 1996. (Cited on page 74.)

[Mayya *et al.* 2005] Y. D. Mayya, L. Carrasco and A. Luna. *The Discovery of Spiral Arms in the Starburst Galaxy M82.* The Astrophysical Journal, vol. 628, no. 1, pages L33–L36, 2005. (Cited on page 62.)

[Mayya *et al.* 2006] Y. D. Mayya, A. Bressan, L. Carrasco and L. Hernandez-Martinez. *The Star Formation History of the Disk of the Starburst Galaxy M82.* The Astrophysical Journal, vol. 649, no. 1, pages 172–180, 2006. (Cited on page 63.)

[Mazin 2007] D. Mazin. *A study of very high energy gamma-ray emission from AGNs and constraints on the extragalactic background light.* PhD thesis, Technische Universität München, 2007. (Cited on pages 92 and 174.)

[McLeod *et al.* 1993] K. K. McLeod, G. H. Rieke, M. J. Rieke and D. M. Kelly. *M82 - The saga continues.* Astrophysical Journal, vol. 412, no. 1, pages 111–126, 1993. (Cited on page 66.)

[Melo *et al.* 2002] V. P. Melo, A. M. Pérez García, J. A. Acosta-Pulido, C. Muñoz Tuñón and J. M. Rodríguez Espinosa. *The Spatial Distribution of the Far-Infrared Emission in NGC 253.* The Astrophysical Journal, vol. 574, no. 2, pages 709–718, 2002. (Cited on page 74.)

[Meucci *et al.* 2007] M. Meucci, R. Paoletti, R. Pegna, A. N. Stamerra Turini, D. Corti, M. Mariotti and the MAGIC Collaboration. *The trigger system of the MAGIC telescope: on-line selection strategies for Cherenkov telescopes.* IEEE Trans. Nucl. Sci., vol. 54, no. 2, pages 404–409, 2007. (Cited on pages 90 and 174.)

[Moiseev *et al.* 2007] A. A. Moiseev, R. C. Hartman, J. F. Ormes, D. J. Thompson, M. J. Amato, T. E. Johnson, K. N. Segal and D. A. Sheppard. *The anti-coincidence detector for the GLAST large area telescope.* Astroparticle Physics, vol. 27, no. 5, pages 339–358, 2007. (Cited on page 20.)

[Montmerle 1979] T. Montmerle. *On gamma-ray sources, supernova remnants, OB associations, and the origin of cosmic rays.* Astrophysical Journal, vol. 231, no. 1, pages 95–110, 1979. (Cited on page 19.)

[Moralejo *et al.* 2009] A. Moralejo, M. Gaug, E. Carmona, P. Colin, C. Delgado, S. Lombardi, D. Mazin, V. Scalzotto, J. Sitarek, D. Tescaro and for the MAGIC collaboration. *MARS, the MAGIC Analysis and Reconstruction Software.* In Proc. 31^{st} International Cosmic Ray Conference (Łódź, Poland). arXiv: astro-ph/0907.0943, 2009. (Cited on pages 93, 104 and 130.)

[Moskalenko & Strong 1998] I. Moskalenko and A. Strong. *Production and Propagation of Cosmic-Ray Positrons and Electrons.* Astrophysical Journal, vol. 493, pages 694–715, 1998. (Cited on page 59.)

[Mouhcine *et al.* 2005] M. Mouhcine, H. C. Ferguson, R. M. Rich, T. M. Brown and T. E. Smith. *Halos of Spiral Galaxies. I. The Tip of the Red Giant Branch as a Distance Indicator.* The Astrophysical Journal, vol. 633, no. 2, pages 810–820, 2005. (Cited on page 74.)

[Mufson *et al.* 1986] S. L. Mufson, M. L. McCollough, J. R. Dickel, R. Petre, R. White and R. Chevalier. *A multiwavelength investigation of the supernova remnant IC 443.* Astronomical Journal, vol. 92, pages 1349–1357, 1986. (Cited on page 33.)

[Naito & Takahara 1994] T. Naito and F. Takahara. *High energy gamma-ray emission from supernova remnants.* Journal of Physics G: Nuclear and Particle Physics, vol. 20, no. 3, pages 477–486, 1994. (Cited on page 19.)

[Nolan *et al.* 2003] P. L. Nolan, W. F. Tompkins, I. A. Grenier and P. F. Michelson. *Variability of EGRET Gamma-Ray Sources.* The Astrophysical Journal,, vol. 597, no. 1, pages 615–627, 2003. (Cited on page 34.)

[O'Connell & Mangano 1978] R. W. O'Connell and J. J. Mangano. *The central regions of M82.* Astrophysical Journal, vol. 221, no. 1, pages 62–79, 1978. (Cited on page 62.)

[Ohm *et al.* 2009] S. Ohm, C. van Eldik and K. Egberts. *γ/hadron separation in very-high-energy γ-ray astronomy using a multivariate analysis method.* Astroparticle Physics, vol. 31, no. 5, pages 383–391, 2009. (Cited on page 120.)

[Olbert *et al.* 2001] C. M. Olbert, C. R. Clearfield, N. E. Williams, J. W. Keohane and D. A. Frail. *A Bow Shock Nebula around a Compact X-Ray Source in the Supernova Remnant IC 443.* Astrophysical Journal, vol. 554, no. 2, pages L205–L208, 2001. (Cited on pages 33, 39, 43 and 125.)

[Ong 2011] R. A. Ong. *VERITAS Reports Increased Activity of HESS J0632+057 in Very High Energy Gamma Rays.* The Astronomer's Telegram, vol. 3153, pages 1–+, 2011. (Cited on page 10.)

[Ormes *et al.* 1988] J. F. Ormes, M. E. Ozel and D. J. Morris. *On the high-energy gamma-ray signature of cosmic-ray sources.* The Astrophysical Journal, vol. 334, pages 722–733, 1988. (Cited on pages 25 and 37.)

[Orth & Buffington 1976] C. D. Orth and A. Buffington. *Secondary cosmic-ray electrons and positrons from 1 to 100 GeV in the upper atmosphere and interstellar space, and interpretation of a recent positron flux measurement.* Astrophysical Journal, vol. 206, no. 1, pages 312–332, 1976. (Cited on page 59.)

[Ott *et al.* 2005] J. Ott, A. Weiß, C. Henkel and F. Walter. *The Temperature Distribution of Dense Molecular Gas in the Center of NGC 253.* The Astrophysical Journal, vol. 629, no. 2, pages 767–780, 2005. (Cited on pages 77 and 174.)

[Oya 2010] I. Oya. *Observations of Active Galactic Nuclei with the MAGIC Telescope.* PhD thesis, Univ. Complutense de Madrid, 2010. (Cited on page 94.)

[Paglione *et al.* 1996] T. A. D. Paglione, A. P. Marscher, J. M. Jackson and D. L. Bertsch. *Diffuse Gamma-Ray Emission from the Starburst Galaxy NGC 253.* Astrophysical Journal, vol. 460, pages 295–302, 1996. (Cited on pages 57, 59, 63 and 74.)

[Pavlidou & Fields 2001] V. Pavlidou and B. Fields. *Diffuse Gamma Rays from Local Group Galaxies.* The Astrophysical Journal, vol. 558, no. 1, pages 63–71, 2001. (Cited on page 63.)

[Persic *et al.* 2008] M. Persic, Y. Rephaeli and Y. Arieli. *Very-high-energy emission from M 82.* Astronomy and Astrophysics, vol. 486, no. 1, pages 143–149, 2008. (Cited on pages 57, 63, 64 and 69.)

[Punch *et al.* 1992] M. Punch, C. W. Akerlof, M. F. Cawley, M. Chantell, D. J. Fegan, S. Fennell, J. A. Gaidos, J. Hagan, A. M. Hillas, Y. Jiang, A. D.

Kerrick, R. C. Lamb, M. A. Lawrence, D. A. Lewis, D. I. Meyer, G. Mohanty, K. S. O'Flaherty, P. T. Reynolds, A. C. Rovero, M. S. Schubnell, G. Sembroski, T. C. Weekes and C. Wilson. *Detection of TeV photons from the active galaxy Markarian 421.* Nature, vol. 358, no. 6386, pages 477–478, 1992. (Cited on page 7.)

[Ramaty & Lingenfelter 1966] R. Ramaty and R. E. Lingenfelter. *Galactic Cosmic-Ray Electrons.* Journal of Geophysical Research, vol. 71, pages 3687–+, 1966. (Cited on page 59.)

[Ranalli *et al.* 2008] P. Ranalli, A. Comastri, L. Origlia and R. Maiolino. *A deep X-ray observation of M82 with XMM-Newton.* Monthly Notices of the Royal Astronomical Society, vol. 386, no. 3, pages 1464–1480, 2008. (Cited on page 62.)

[Reimer 2001] O. Reimer. *Gamma-Ray Properties of Unidentified EGRET Sources.* In The Nature of Unidentified Galactic High-Energy Gamma-Ray Sources. Tonantzintla, Puebla, Mexico, volume 267 of *Astrophysics and Space Science Library*, pages 17–34. Kluwer Academic Publishers Dordrecht, 2001. (Cited on page 40.)

[Rekola *et al.* 2005] R. Rekola, M. G. Richer, Marshall L. McCall, M. J. Valtonen, J. K. Kotilainen and Chris Flynn. *Distance to NGC 253 based on the planetary nebula luminosity function.* Monthly Notices of the Royal Astronomical Society, vol. 361, no. 1, pages 330–336, 2005. (Cited on page 74.)

[Rho *et al.* 2001] J. Rho, T. H. Jarrett, R. M. Cutri and W. T. Reach. *Near-Infrared Imaging and [O I] Spectroscopy of IC 443 using Two Micron All Sky Survey and Infrared Space Observatory.* The Astrophysical Journa, vol. 547, no. 2, pages 885–898, 2001. (Cited on page 31.)

[Rice *et al.* 1988] W. Rice, C. J. Lonsdale, B. T. Soifer, G. Neugebauer, E. L. Kopan, Lawrence A. Lloyd, T. de Jong and H. J. Habing. *A catalog of IRAS observations of large optical galaxies.* Astrophysical Journal Supplement Series, vol. 68, pages 91–127, 1988. (Cited on page 74.)

[Rieke *et al.* 1973] G. H. Rieke, D. A. Harper, F. J. Low and K. R. Armstrong. *350-MICRON Observations of Sources in H II Regions, the Galactic Center, and NGC 253.* Astrophysical Journal, vol. 183, pages L67–L71, 1973. (Cited on pages 77 and 174.)

[Rieke *et al.* 1980] G. H. Rieke, M. J. Lebofsky, R. I. Thompson, F. J. Low and A. T. Tokunaga. *The nature of the nuclear sources in M82 and NGC 253.* Astrophysical Journal, vol. 238, no. 1, pages 24–40, 1980. (Cited on page 66.)

[Rodríguez Marrero *et al.* 2008] A. Y. Rodríguez Marrero, D. F. Torres, E. de Cea del Pozo, O. Reimer and A. N. Cillis. *Diffusion of Cosmic*

Rays and the Gamma-Ray Large Area Telescope: Phenomenology at the 1-100 GeV Regime. The Astrophysical Journal, vol. 689, no. 1, pages 213–218, 2008. (Cited on pages 16, 19 and 20.)

[Rodríguez Marrero *et al.* 2009] A. Y. Rodríguez Marrero, D. F. Torres and E. de Cea del Pozo. *The GeV to TeV view of SNR IC443: predictions for Fermi.* In 6^{th} Workshop on Science with the New Generation of High Energy Gamma-Ray Experiments (SciNeGHE '08). arXiv: astro-ph/0901.2615v1, 2009. (Cited on pages 16, 28, 38, 45, 48, 116 and 171.)

[Rolke *et al.* 2005] W. A. Rolke, A. M. López and J. Conrad. *Limits and confidence intervals in the presence of nuisance parameters.* Nuclear Instruments and Methods in Physics Research Section A, vol. 551, no. 2-3, pages 493–503, 2005. (Cited on page 106.)

[Romero *et al.* 1999] G. E. Romero, P. Benaglia and D. F. Torres. *Unidentified 3EG gamma-ray sources at low galactic latitudes.* Astronomy and Astrophysics, vol. 348, pages 868–876, 1999. (Cited on page 40.)

[Rosado *et al.* 2007] M. Rosado, L. Arias and P. Ambrocio-Cruz. *Kinematics of the Molecular Hydrogen Associated with the Supernova Remnant IC 443.* The Astronomical Journal, vol. 133, no. 1, pages 89–98, 2007. (Cited on pages 33, 34 and 50.)

[Sabatini *et al.* 2010] S. Sabatini, M. Tavani, E. Striani, A. Bulgarelli, V. Vittorini, G. Piano, E. Del Monte, M. Feroci, F. de Pasquale, M. Trifoglio and 51 coauthor. *Episodic Transient Gamma-ray Emission from the Microquasar Cygnus X-1.* The Astrophysical Journal Letters, vol. 712, pages L10–L15, 2010. (Cited on page 10.)

[Sakai & Madore 1999] S. Sakai and B. F. Madore. *Detection of the Red Giant Branch Stars in M82 Using the Hubble Space Telescope.* The Astrophysical Journal, vol. 526, no. 2, pages 599–606, 1999. (Cited on page 62.)

[Saz Parkinson *et al.* 2010] P.M. Saz Parkinson, M. Dormody, M. Ziegler, P. S. Ray, A. A. Abdo, J. Ballet, M. G. Baring, A. Belfiore, T. H. Burnett, G. A. Caliandro and 27 coauthors. *Eight -ray Pulsars Discovered in Blind Frequency Searches of Fermi LAT Data.* Astrophysical Journal, vol. 725, no. 1, pages 571–584, 2010. (Cited on pages 109, 110 and 175.)

[Seiradakis *et al.* 1985] J. H. Seiradakis, W. Reich, W. Sieber, R. Schlickeiser and H. Kühr. *An extended extragalactic radio source behind the Milky Way.* Astronomy and Astrophysics, vol. 143, no. 2, pages 478–480, 1985. (Cited on page 103.)

[Seta *et al.* 1998] M. Seta, T. Hasegawa, T. M. Dame, S. Sakamoto, T. Oka, T. Handa, M. Hayashi, J.-I. Morino, K. Sorai and K. S. Usuda. *Enhanced*

CO J=(2-1)/J=(1-0) Ratio as a Marker of Supernova Remnant − Molecular Cloud Interactions: The Cases of W44 and IC 443. The Astrophysical Journal, vol. 505, no. 1, pages 286–298, 1998. (Cited on pages 33 and 44.)

[Smith *et al.* 1991] P. A. Smith, P. W. J. L. Brand, C. M. Mountain, P. J. Puxley and N. Nakai. *The (C-12)O to H2 ratio in the centre of M82.* Monthly Notices of the Royal Astronomical Society, vol. 252, pages 6P–11P, 1991. (Cited on page 63.)

[Stecker 1970] F. W. Stecker. *The Cosmic γ-Ray Spectrum from Secondary Particle Production in Cosmic-Ray Interactions.* Astrophysics and Space Science, vol. 6, no. 3, pages 377–389, 1970. (Cited on page 59.)

[Stecker 1977] F. W. Stecker. *Observations of galactic gamma-rays and their implications for galactic structure studies.* Astrophysical Journal, vol. 212, no. 1, pages 60–70, 1977. (Cited on page 59.)

[Stecker 2007] F. W. Stecker. *Upper Limits to Fluxes of Neutrinos and Gamma-Rays from Starburst Galaxies.* Journal of Physics: Conference Series, vol. 60, no. 1, pages 215–218, 2007. (Cited on pages 57 and 73.)

[Stephens & Badhwar 1981] S. A. Stephens and G. D. Badhwar. *Production spectrum of gamma rays in interstellar space through neutral pion decay.* Astrophysics and Space Science, vol. 76, no. 1, pages 213–233, 1981. (Cited on page 51.)

[Strickland *et al.* 1997] D. K. Strickland, T. J. Ponman and I. R. Stevens. *ROSAT observations of the galactic wind in M 82.* Astronomy and Astrophysics, vol. 320, pages 378–394, 1997. (Cited on page 62.)

[Strong & Moskalenko 1998] A. Strong and I. Moskalenko. *Propagation of Cosmic-Ray Nucleons in the Galaxy.* The Astrophysical Journal, vol. 509, no. 1, pages 212–228, 1998. (Cited on page 59.)

[Sturner *et al.* 1997] S. J. Sturner, J. G. Skibo, C. D. Dermer and J. R. Mattox. *Temporal Evolution of Nonthermal Spectra from Supernova Remnants.* Astrophysical Journal, vol. 490, no. 2, pages 619–632, 1997. (Cited on page 19.)

[Swanenburg *et al.* 1981] B.N. Swanenburg, K. Bennett, G. F. Bignami, R. Buccheri, P. Caraveo, W. Hermsen, G. Kanbach, G. G. Lichti, J. L. Masnou, H. A. Mayer-Hasselwander and 4 coauthors. *Second COS B catalog of high-energy gamma-ray sources.* Astrophysical Journal, Part 2 - Letters to the Editor, vol. 243, pages L69–L73, 1981. (Cited on page 103.)

[Tabatabaei *et al.* 2007] F. S. Tabatabaei, R. Beck, E. KrÃ$\frac{1}{4}$gel, M. Krause, E. M. Berkhuijsen, K. D. Gordon and K. M. Menten. *High-resolution radio continuum survey of M 33. II. Thermal and nonthermal emission.* Astronomy and Astrophysics, vol. 475, no. 1, pages 133–143, 2007. (Cited on page 68.)

[Tamm & Frank 1937] I. E. Tamm and I. M. Frank. *Coherent radiation of fast electrons in a medium.* Doklady Akademii Nauk SSSR, vol. 14, page 107, 1937. (Cited on page 84.)

[Tanaka & Takahara 2009] S. J. Tanaka and F. Takahara. *A Model of the Spectral Evolution of Pulsar Wind Nebulae.* In Proc. 1^{st} Fermi Symposium (Washington, DC). arXiv: astro-ph/1001.2360, 2009. (Cited on page 110.)

[Tatischeff & Hernanz 2007] V. Tatischeff and M. Hernanz. *Evidence for Nonlinear Diffusive Shock Acceleration of Cosmic Rays in the 2006 Outburst of the Recurrent Nova RS Ophiuchi.* The Astrophysical Journal, vol. 663, pages L101–L104, 2007. (Cited on page 10.)

[Tatischeff & Hernanz 2008] V. Tatischeff and M. Hernanz. *Evidence for Nonlinear Diffusive Shock Acceleration of Cosmic Rays in the 2006 Outburst of RS Ophiuchi.* In RS Ophiuchi (2006) and the Recurrent Nova Phenomenon, volume 401 of *Astronomical Society of the Pacific Conference Series*, pages 328–+. A. Evans, M. F. Bode, T. J. O'Brien, & M. J. Darnley, 2008. (Cited on page 10.)

[Tavani *et al.* 2010] M. Tavani, A. Giuliani, A. W. Chen, A. Argan, G. Barbiellini, A. Bulgarelli, P. Caraveo, P. W. Cattaneo, V. Cocco, T. Contessi and 52 coauthors. *Direct Evidence for Hadronic Cosmic-Ray Acceleration in the Supernova Remnant IC 443.* Astrophysical Journal Letters, vol. 710, no. 2, pages L151–L155, 2010. (Cited on page 42.)

[Telesco & Harper 1980] C. M. Telesco and D. A. Harper. *Galaxies and far-infrared emission.* Astrophysical Journal, vol. 235, no. 1, pages 392–404, 1980. (Cited on pages 69, 74, 77 and 174.)

[Telesco *et al.* 1991] C. M. Telesco, M. Joy, K. Dietz, R. Decher and H. Campins. *Infrared mapping of M82 - A starburst in an edge-on barred galaxy.* Astrophysical Journal, vol. 369, no. 1, pages 135–146, 1991. (Cited on page 62.)

[Tescaro *et al.* 2007] D. Tescaro, H. Bartko, N. Galante, F. Göbel and the MAGIC Collaboration. *Study of the performance and capability of the new ultra-fast 2 GSample/s FADC data acquisition system of the MAGIC telescope.* ArXiv: astro-ph/0709.1410, 2007. (Cited on page 96.)

[Tescaro 2010] D. Tescaro. *TeV gamma-ray observations of nearby Active Galactic Nuclei with the MAGIC telescope: exploring the high energy region of the multiwavelength picture.* PhD thesis, Univ. Autonoma de Barcelona, 2010. (Cited on pages 87 and 174.)

[Tian & Leahy 2006] W.W. Tian and D.A. Leahy. *Association Of The SNR G65.1+0.6 And The PSR J1957+2831.* Bulletin of the American Astronomical Society, vol. 455, page 1053, 2006. (Cited on pages 102 and 103.)

[Torres & Domingo-Santamaría 2005] D. F. Torres and E. Domingo-Santamaría. *Some Comments on the High Energy Emission from Regions of Star Formation Beyond the Galaxy.* Modern Physics Letters A, vol. 20, no. 37, pages 2827–2843, 2005. (Cited on pages 60 and 173.)

[Torres *et al.* 2001a] D. F. Torres, G. E. Romero, J. A. Combi, P. Benaglia, H. Andernach and B. Punsly. *A variability analysis of low-latitude unidentified gamma-ray sources.* Astronomy and Astrophysics, vol. 370, pages 468–478, 2001. (Cited on page 34.)

[Torres *et al.* 2001b] D. R. Torres, M. E. Pessah and G. E. Romero. *On the time variability of Gamma-ray sources: a numerical analysis of variability indices.* Astronomische Nachrichten, vol. 322, no. 4, pages 223–227, 2001. (Cited on page 40.)

[Torres *et al.* 2003] D. F. Torres, Gustavo E. Romero, T. M. Dame, J. A. Combi and Y. M. Butt. *Supernova remnants and $\gamma-$ray sources.* Physics Reports, vol. 382, no. 6, pages 303–380, 2003. (Cited on pages 31, 32, 33, 40, 44, 128 and 170.)

[Torres *et al.* 2004] D. F. Torres, O. Reimer, E. Domingo-Santamaría and S. W. Digel. *Luminous Infrared Galaxies as Plausible Gamma-Ray Sources for the Gamma-Ray Large Area Space Telescope and the Imaging Atmospheric Cerenkov Telescopes.* The Astrophysical Journal, vol. 607, no. 2, pages L99–L102, 2004. (Cited on pages 57, 63 and 69.)

[Torres *et al.* 2008] D. F. Torres, A. Y. Rodríguez Marrero and E. de Cea del Pozo. *MAGIC J0616+225 as delayed TeV emission of cosmic rays diffusing from the supernova remnant IC 443.* Monthly Notices of the Royal Astronomical Society: Letters, vol. 387, no. 1, pages L59–L63, 2008. (Cited on pages 16, 22, 25, 31, 35, 128 and 129.)

[Torres *et al.* 2010] D. F. Torres, A.Y. Rodríguez Marrero and E. de Cea Del Pozo. *The GeV to TeV connection in the environment of SNR IC 443.* Monthly Notices of the Royal Astronomical Society, vol. 408, no. 2, pages 1257–1266, 2010. (Cited on pages 16, 41, 49 and 172.)

[Torres 2004] D. F. Torres. *Theoretical Modeling of the Diffuse Emission of Gamma Rays from Extreme Regions of Star Formation: The Case of ARP 220.* The Astrophysical Journal, vol. 617, no. 2, pages 966–986, 2004. (Cited on pages 45, 57, 58, 63 and 68.)

[Troja *et al.* 2006] E. Troja, F. Bocchino and F. Reale. *XMM-Newton Observations of the Supernova Remnant IC 443. I. Soft X-Ray Emission from Shocked Interstellar Medium.* The Astrophysical Journal, vol. 649, no. 1, pages 258–267, 2006. (Cited on pages 33 and 34.)

[Turner & Ho 1985] J. L. Turner and P. T. P. Ho. *The 1 parsec radio core and possible nuclear ejection in NGC 253.* Astrophysical Journal, vol. 299, no. 2, pages L77–L81, 1985. (Cited on page 74.)

[Völk *et al.* 1989] H. J. Völk, U. Klein and R. Wielebinski. *M82, the Galaxy, and the dependence of cosmic ray energy production on the supernova rate.* Astronomy and Astrophysics, vol. 213, no. 1, pages L12–L14, 1989. (Cited on page 68.)

[Völk *et al.* 1996] H. J. Völk, F. A. Aharonian and D. Breitschwerdt. *The Nonthermal Energy Content and Gamma-Ray Emission of Starburst Galaxies and Clusters of Galaxies.* Space Science Reviews, vol. 75, no. 1, pages 279–297, 1996. (Cited on pages 63 and 64.)

[Volkova 1980] L. V. Volkova. *Energy Spectra and Angular Distributions of Atmospheric Neutrinos.* Sov. J. Nucl. Phys., vol. 31, pages 784–, 1980. (Cited on page 55.)

[Wang *et al.* 1992] Z. R. Wang, I. Asaoka, S. Hayakawa and K. Koyama. *Hard X-rays from the supernova remnant IC 443.* Astronomical Society of Japan, Publications, vol. 44, no. 3, pages 303–308, 1992. (Cited on page 33.)

[Waxman & Bahcall 1999] E. Waxman and J. Bahcall. *High energy neutrinos from astrophysical sources: An upper bound.* Physical Review D, vol. 59, no. 2, pages 023002–+, 1999. (Cited on page 73.)

[Weaver *et al.* 2002] K. A. Weaver, T. M. Heckman, D. K. Strickland and M. Dahlem. *Chandra Observations of the Evolving Core of the Starburst Galaxy NGC 253.* The Astrophysical Journal, vol. 576, no. 1, pages L19–L23, 2002. (Cited on page 72.)

[Weekes *et al.* 1989] T. C. Weekes, M. F. Cawley, D. J. Fegan, K. G. Gibbs, A. M. Hillas, P. W. Kowk, R. C. Lamb, D. A. Lewis, D. Macomb, N. A. Porter, P. T. Reynolds and G. Vacanti. *Observation of TeV gamma rays from the Crab nebula using the atmospheric Cerenkov imaging technique.* Astrophysical Journal, vol. 342, no. 1, pages 379–395, 1989. (Cited on page 7.)

[Weiß *et al.* 2001] A. Weiß, N. Neininger, S. HÃ$\frac{1}{4}$ttemeister and U. Klein. *The effect of violent star formation on the state of the molecular gas in M 82.* Astronomy and Astrophysics, vol. 365, pages 571–587, 2001. (Cited on page 63.)

[Wild *et al.* 1992] W. Wild, A. I. Harris, A. Eckart, R. Genzel, U. U. Graf, J. M. Jackson, A. P. G. Russell and J. Stutzki. *A multi-line study of the molecular interstellar medium in M 82's starburst nucleus.* Astronomy and Astrophysics, vol. 265, no. 2, pages 447–464, 1992. (Cited on page 63.)

[Yao *et al.* 2006] W. M. Yao, C. Amsler, D. Asner, R. M. Barnett, J. Beringer, P. R. Burchat, C. D. Carone, C. Caso, O. Dahl and 160 co authors. *Review*

of Particle Physics. Journal of Physics G Nuclear Physics, vol. 33, no. 1, page 1232, 2006. (Cited on page 84.)

[Young & Scoville 1984] J. S. Young and N. Z. Scoville. *Molecular clouds in M82.* Astrophysical Journal, vol. 287, no. 1, pages 153–166, 1984. (Cited on page 63.)

[Zhang & Fang 2008] L. Zhang and J. Fang. *Nonthermal Emission from a Radio-bright Shell-Type Supernova Remnant IC 443.* The Astrophysical Journal, vol. 675, no. 1, pages L21–L24, 2008. (Cited on page 40.)

List of Figures

List of Tables

LaTeX template based on: http://olivier.commowick.org/thesis_template.php

Cover design: SaiSoto.